Doctoral School in Mathematics

A holistic multi-scale mathematical model of the murine extracellular fluid systems and study of the brain interactive dynamics

Christian Contarino

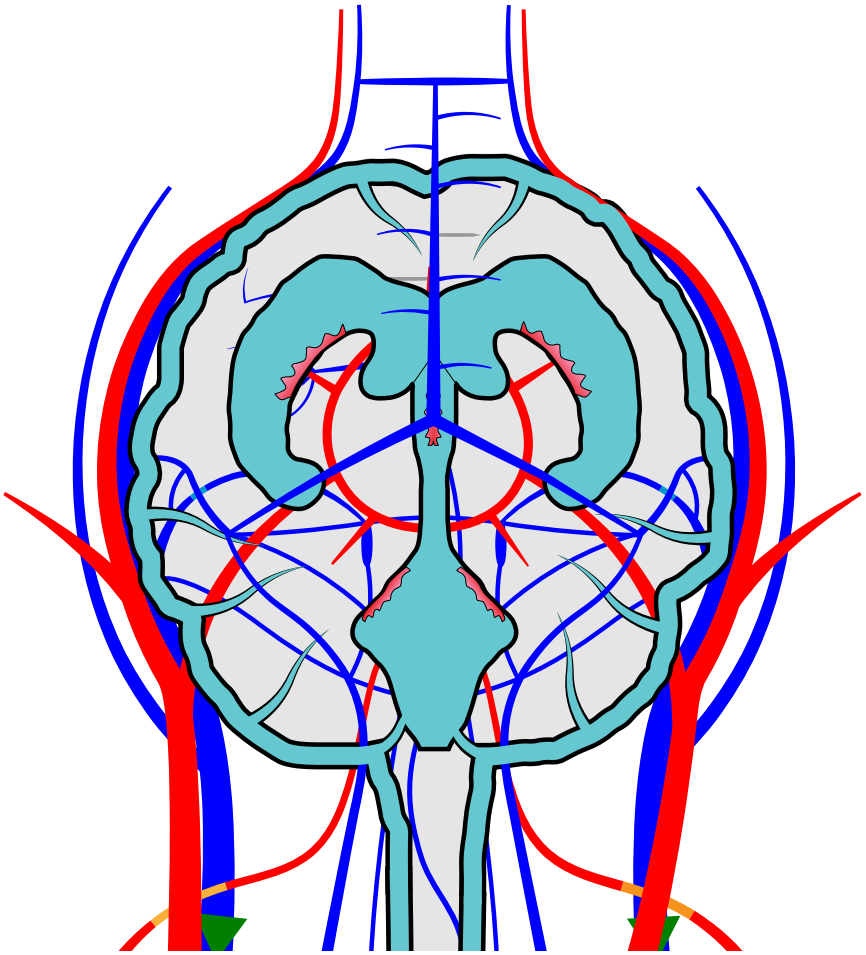

UNIVERSITÀ DEGLI STUDI
DI TRENTO

Dipartimento di Matematica

May 2018

Doctoral thesis in **Mathematics**, XXX cycle
Department of Mathematics, **University of Trento**
Academic year: 2016/2017
Supervisor: **Prof. Eleuterio F. Toro**, *University of Trento, Italy*

External examiner: **Prof. Vartan Kurtcuoglu**, *University of Zürich, Switzerland*
External examiner: **Prof. Roxana O. Carare**, *University of Southampton, England*

University of Trento
Trento, Italy
May, 2018

If you can dream it, you can do it.
Walt Disney

Abstract

Recent advances in medical science regarding the interaction and functional role of fluid compartments in the central nervous system have attracted the attention of many researchers across various disciplines. Neurotoxins are constantly cleared from the brain parenchyma through the intramural periarterial drainage system, glymphatic system and meningeal lymphatic system. Impairment of these systems can potentially contribute to the onset of neurological disorders.

The goal of this thesis is to contribute to the understanding of brain fluid dynamics and to the role of vascular pathologies in the context of neurological disorders. To achieve this goal, we designed the first multi-scale, closed-loop mathematical model of the murine fluid system, incorporating: heart dynamics, major arteries and veins, microcirculation, pulmonary circulation, venous valves, cerebrospinal fluid (CSF), brain interstitial fluid (ISF), Starling resistors, Monro-Kellie hypothesis, brain lymphatic drainage and the modern concept of CSF/ISF drainage and absorption based on the *Bulat-Klarica-Orešković* hypothesis. The mathematical model relies on one-dimensional Partial Differential Equations (PDEs) for blood vessels and on Ordinary Differential Equations (ODEs) for lumped parameter models. The systems of PDEs and ODEs are solved through a high-order finite volume ADER method and through an implicit Euler method. The computational results are validated against literature values and magnetic resonance flow measurements. Furthermore, the model is validated against *in-vivo* intracranial pressure waveforms acquired in healthy mice and in mice with impairment of the intracranial venous outflow. Through a systematic use of our computational model in healthy and pathological cases, we provide a complete and holistic neurovascular view of the main murine fluid dynamics. We propose a hypothesis on the working principles of the glymphatic system, opening a new door towards a comprehensive understanding of the mechanisms which link vascular and neurological disorders. In particular, we show how impairment of the cerebral venous outflow might potentially lead to accumulation of solutes in the parenchyma, by altering CSF and ISF dynamics.

This thesis also concerns the development of a high-order ADER-type numerical method for systems of hyperbolic balance laws in networks, based on a new implicit solver for the junction-generalized Riemann problem. The resulting ADER scheme can deal with stiff source terms and can be applied to non-linear systems of hyperbolic balance laws in domains consisting of networks of one-dimensional sub-domains. Also, we design a novel one-dimensional mathematical model for collecting lymphatics coupled with a Electro-Fluid-Mechanical Contraction (EFMC) model for dynamical contractions. The resulting mathematical model gives each lymphangion the autonomous capability to trigger action potentials based on local fluid-dynamical factors.

Preface

The research of this PhD thesis was carried out in the Department of Mathematics of the University of Trento under the supervision of Prof. Eleuterio F. Toro.

I sincerely thank Prof. J. Kipnis (Department of Neuroscience, University of Virginia, Charlottesville, USA) for the opportunity he gave me to visit his lab.

I sincerely thank Prof. E. M. Haacke (MR Research Facility, Wayne State University, Detroit, USA) for providing the software SPIN (Signal Processing in NMR, Detroit, MI) for blood and CSF MR-flow analysis.

In Chapter 4, Dr. I. Smirnov conducted the surgery and interventions, Dr. A. Louveau acquired the intracranial measurements.

Trento, May 2018
Christian Contarino

Acknowledgements

During the PhD journey, I encountered many challenges from both scientific and family point of views. Probably, the PhD journey has been one of the most significant experiences that allowed me to grow as a person and as a scientist. Nothing would have been possible without the help and support of many people I met during these three significant years. Every person, every chat, every moment of sharing allowed me to move forward and dream the life dream.

Nothing would have been possible without my family, from Danilo to my mother and father. You all believed, supported me and made many sacrifices to allow me to continue studying. Danilo, you are my supporting pillar and helped me in the most difficult situations. My mother taught me how important sacrifice is and what unlimited love is. My father taught me how to be strong and endure difficult situations.

I will always be grateful to my supervisor, Prof. Eleuterio F. Toro. You taught me the enthusiasm for research, believed in me, guided me through the PhD journey and changed my life several times. A wholehearted *thank*.

I will always be grateful to Dr Nivedita Agarwal. You taught me that we always have to fight for what we believe in and that nothing can stop us.

I will always be grateful to Federica Caforio. You taught me to never give up, that there will be always the third solution in the most difficult moments.

I will always be grateful to Simona Biancheri. You taught me how powerful words can be and you trusted me beyond the limits of life.

I wish to thank all fellows at the Department of Neuroscience of the University of Virginia in Charlottesville and all fellows at the Department of Mathematics of the University of Trento in Italy. I wish to thank all of my friends who believed in me and laughed with me even with the useless game "ce l'hai" which however has the incredible power to give a smile. *Thanks*.

I also thank the University of Trento, and in particular the Department of Mathematics, for providing the funding and the academic support to carry out my research. I wish to thank all professors at the University of Trento, in particular, Prof. Alberto Valli and Prof. Ana Alonso Rodriguez.

"Be the change you want to see in the world."

Contents

List of Figures

List of Tables

Papers published or submitted during the PhD candidature

- E. F. Toro, F. Borgioli, Q. Zhang, C. Contarino, L. O. Mueller and A. Bruno, *"Inner-ear circulation in humans is disrupted by extracranial venous outflow strictures: Implications for Ménière's disease"*, **Veins and Lymphatics**, 7 (2018): 10-21.
- C. Contarino, E. F. Toro, G. Montecinos, J. Kall and R. Borsche, *"Junction-generalized Riemann problem for stiff hyperbolic balance laws in networks: An implicit solver and ADER schemes"*, **Journal of Computational Physics**, 315 (2016): 409-433.
- M. Strocchi, C. Contarino, Q. Zhang, E. F. Toro and R. Bonmassari, *"A global mathematical model for the simulation of stenoses and bypass placement in the human arterial system"*, **Applied Mathematics and Computation**, 300 (2017): 21–39.
- C. Spiller, E. F. Toro, M. E. Vazquez and C. Contarino, *"On the exact solution of the Riemann problem for blood flow in human veins, including collapse"*, **Applied Mathematics and Computation**, 303 (2017): 178–189.
- S. Da Mesquita, A. Louveau, A. Vaccari, I. Smirnov, R. C. Cornelison, K. M. Kingsmore, C. Contarino, S. Onengut-Gumuscu, E. Farber, D. Raper, K. E. Var, W. Baker, N. Dabhi, G. Oliver, S. Rich, J. M. Munson, C. C. Overall, S. T. Acton and J. Kipnis, *"CNS-draining lymphatics play a key role in age-dependent cognitive decline and Alzheimer's disease pathology"*, **Nature**, Under review (2018).
- C. Contarino and E. F. Toro, *"A one-dimensional mathematical model of collecting lymphatics coupled with an electro-fluid-mechanical contraction model and valve dynamics"*, **Biomechanics and Modelling in Mechanobiology**, Under review (2018).
- N. Agarwal, C. Contarino, G. Rossi, C. Stegagno, L. Bertolasi and E. F. Toro, *"Intracranial fluid dynamics changes in idiopathic intracranial hypertension: pre and post therapy"*, **Current Neurovascular Research**, In press (2018).
- E. F. Toro, B. Thornber, Q. Zhang and C. Contarino, *"A one-dimensional computational model of the spinal cerebrospinal fluid"*, **Journal of Biomechanical Engineering**, Under review (2018).

Conference presentations during the PhD candidature

- C. Contarino, E. F. Toro, A. Louveau, S. Da Mesquita, D. Raper, I. Smirnov, N. Agarwal and J. Kipnis, *"The role of water dynamics in the glymphatic system through a holistic multi-scale mathematical model of the murine extracellular fluid systems"*, **Società Italiana di Matematica Applicata e Industriale (SIMAI) (scheduled) 2018**, Rome, Italy.
- C. Contarino, E. F. Toro, A. Louveau, S. Da Mesquita, D. Raper, I. Smirnov, N. Agarwal and J. Kipnis, *"A holistic multi-scale mathematical model of the murine fluid systems: understanding the pathophysiology of idiopathic intracranial hypertension"*, **International Association for Hydro-Environment Engineering and Research (IAHR) (scheduled) 2018**, Trento, Italy.
- C. Contarino, E. F. Toro, A. Louveau, S. Da Mesquita, D. Raper, I. Smirnov, N. Agarwal and J. Kipnis, *"A global, multi-scale mathematical model of the murine fluid systems: Application to idiopathic intracranial hypertension"*, **Istituto Nazionale di Alta Matematica (INdAM) Workshop 2018**, Rome, Italy.
- C. Contarino and E. F. Toro, *"Modelling the lymphatics: A 1D lymph flow model coupled to an electro-fluid-mechanical contraction model"*, **Computational and Mathematical Biomedical Engineering (CMBE) 2017**, Pittsburgh, United States.
- B. Thornber, Q. Zhang, C. Contarino and E. F. Toro, *"A one-dimensional computational model of the spinal cerebrospinal fluid"*, **Computational and Mathematical Biomedical Engineering (CMBE) 2017**, Pittsburgh, United States.
- C. Contarino and E. F. Toro, *"A one-dimensional mathematical model for dynamically contracting collecting lymphatics"*, **Società Italiana di Matematica Applicata e Industriale (SIMAI) 2016**, Milan, Italy.
- C. Contarino, E. F. Toro, G. I. Montecinos, R. Borsche and J. Kall, *"Junction-generalized Riemann problem for stiff hyperbolic balance laws in networks of blood vessels"*, **Società Italiana di Matematica Applicata e Industriale (SIMAI) 2016**, Milan, Italy.
- C. Contarino, E. F. Toro, G. I. Montecinos, R. Borsche and J. Kall, *"Junction-generalized Riemann problem for stiff hyperbolic balance laws in networks of blood vessels"*, **Platform for Advanced Scientific Computing (PASC) 2016**, Lausanne, Switzerland.
- C. Contarino and E. F. Toro, *"A first step towards a mathematical model for the human lymphatic system"*, **International Society for Neurovascular Disease (ISNVD) 2016**, New York, United States.
- C. Contarino, Q. Zhang, E. F. Toro and G. I. Montecinos, *"A first step towards a mathematical model for the human lymphatic system"*, **European Workshop on High Order Nonlinear Numerical Methods for Evolutionary PDEs: Theory and Applications (HONOM) 2015**, Trento, Italy.
- C. Contarino, Q. Zhang, E. F. Toro and G. I. Montecinos, *"Towards high-order methods for blood flow"*, **Computational and Mathematical Biomedical Engineering (CMBE) 2015**, Sancha, France.

Chapter 1

Introduction

1.1 Motivation and goals

In recent years, there have been several fundamental discoveries that have brought a lot of excitement in the field of neurological disorders. The meningeal lymphatic system is a complex network of lymphatic vessels which mainly drains immune cells and cerebrospinal fluid and is a key component of brain homeostasis [Louveau 2015, Louveau 2017, Absinta 2017]. Brain interstitial fluid and amyloid β drain from the parenchyma along the basement membranes of capillaries and arteries through intramural periarterial drainage pathways [Carare 2008]. Also, it has been shown that the brain is constantly cleared from neurotoxins through the so-called glymphatic system [Iliff 2012]. The glymphatic system consists of a trans-parenchymal cerebrospinal fluid (CSF) movement through glial cells from para-arterial CSF spaces to para-venous CSF spaces. Intracranial solutes and waste products are transported through the trans-parenchymal water movement towards para-venous CSF spaces and are drained into the venous system through arachnoid villi or meningeal lymphatics [Louveau 2017]. Thanks to this pseudolymphatic function of waste removal and to the trans-glial water movement, this system has been termed "glymphatic system". Impairment of the glymphatic system seems to correlate with amyloid β accumulation, a characteristic hallmark of Alzheimer's disease [Iliff 2012, Iliff 2014], with migraine [Schain 2017], and idiopathic intracranial hypertension [Bezerra 2018].

Despite the importance of the glymphatic system, it is not yet clear what are its driving forces. Originally, it was proposed that the glymphatic system was driven by bulk flow [Iliff 2012] and arterial pulsations [Iliff 2013]. In general, three possible mechanisms have been proposed: diffusion, advection (or bulk flow), and convection defined as a combination of diffusion and advection [Plog 2018]. In contrast with the original idea of Iliff et al. [Iliff 2013], Asgari et al. [Asgari 2016] showed through computational simulations that arterial pulsation is probably not the driving force of the glymphatic system. Also, Smith et al. [Smith 2017] showed that the glymphatic system is unlikely driven by bulk flows. Their results suggest that water movement in the cranial subarachnoid space is driven by convection, while that within the parenchyma is driven by diffusion. To date, however, there is not yet a conclusive explanation of the mechanisms which drive the glymphatic system.

Neurological disorders have been shown to correlate with vascular diseases. Zamboni et al.

[Zamboni 2008] described the so-called Chronic Cerebro-Spinal Venous Insufficiency (CCSVI) and suggested that it is associated with multiple sclerosis. The CCSVI is a condition characterized by obstructed blood flow in the major veins that drain the central nervous system and by iron accumulation [Singh 2009]. Although the relationship between CCSVI and multiple sclerosis is still debated [Kotsikoris 2013, Zamboni 2017], from the pioneering work of Zamboni there are a number of studies that have attempted to find possible connections between vascular pathologies and neurological disorders, as idiopathic Parkinson's disease [Liu 2014], idiopathic intracranial hypertension [Bateman 2008, Farb 2003], Ménière's disease [Toro 2018, Bruno 2014] and sudden sensorineural hearing loss [Alpini 2013]. It remains an open question whether there is a relationship between vascular pathologies and impairment of the glymphatic system, intramural periarterial system or meningeal lymphatic system.

Our goal is to provide some insights into the brain fluid dynamics through a computational model of the main murine extracellular fluid systems and attempt to answer the following question: can impairment of the vascular system provoke significant changes in the glymphatic system and potentially lead to accumulation of neurotoxins in the brain parenchyma?

1.2 State of the art

The human body has several interactive fluid systems [Levick 2009]. It includes the heart function, a network of arteries and veins connected through the microcirculation, the pulmonary circulation, the peripheral and brain interstitial fluid and the lymphatic system. In the following, we briefly review the mathematical models employed for the vascular, lymphatic and brain fluid systems and the numerical methodologies to solve the resulting set of differential equations.

1.2.1 The vascular system

Mathematical modelling has been widely used to understand the physiology and the pathophysiology of the human body. Several three-dimensional, zero-dimensional, one-dimensional and even multi-scale mathematical models have been proposed [Formaggia 1999, Olufsen 2000, Liang 2009a, Matthys 2007a, Müller 2013b, Müller 2014, Mynard 2015, Levitt 2016]. For a comprehensive review on the state of the art, refer to [Quarteroni 2017, Formaggia 2009, Shi 2011]. Liang et al. [Liang 2009b] constructed a multi-scale mathematical model of the cardiovascular system to understand the effect of arterial stenoses in the arterial tree. Müller et al. [Müller 2013b] built the first multi-scale, closed-loop mathematical model of the cardiovascular system which incorporated major arteries, major veins, microcirculation, pulmonary circulation and heart dynamics. The model was subsequently refined [Müller 2014] to include Starling resistors and a model of the intracranial dynamics based on the work of Ursino et al. [Ursino 1988]. The authors studied the impact of neck vein strictures on cerebral venous hemodynamics. Blanco et al. [Blanco 2015] built a mathematical model of the arterial tree with over 2000 vessels. Strocchi et al. [Strocchi 2017] studied the haemodynamical effect of stenoses and bypass placements. Regarding mathematical models of the murine cardiovascular system, the literature is quite scarce. Cuomo et al. [Cuomo 2015] modelled the main murine arterial tree using a validated fluid-solid interaction code. Aslanidou et al. [Aslanidou 2015] proposed a mathematical model of the murine arterial tree based on a network of one-dimensional

arterial vessels and validated it against *in-vivo* measurements performed on a cohort of mice.

1.2.2 The brain fluid systems

Brain fluid dynamics is a challenging issue for modellers. Brain fluids comprise arterial and venous blood, cerebrospinal fluid, interstitial fluid. Brain parenchyma has been modelled through three-dimensional poroelastic models [Chou 2016, Guo 2018, Chou 2014]. Brain fluid systems have been modelled through lumped parameter models [Ursino 1988, Gadda 2015, Gehlen 2017] and through multi-scale models [Müller 2014]. Ursino [Ursino 1988] proposed a mathematical model of the human intracranial hydrodynamics. The group of Linninger proposed a mathematical model of blood, cerebrospinal fluid and brain dynamics, including the Monro-Kellie doctrine [Linninger 2009]. The same group proposed a mathematical model of the intracranial fluid dynamics based on the *Bulat-Klarica-Orešković* hypothesis [Orešković 2017, Linninger 2017]. Gehlen et al. [Gehlen 2017] studied the effect of postural changes in the CSF dynamics through a lumped-parameter model of the CSF system and major compartments of the cardiovascular system.

1.2.3 The lymphatic system

The lymphatic system consists of a complex network of initial lymphatics, collecting lymphatics, trunks, lymph nodes, junctions and lymphatic valves. The lymphatic system functions in conjunction with other body fluid systems and with the immune system and carries excess interstitial fluid (ISF), excess proteins, metabolic waste and immune cells, facilitating immune responses. There is a substantial gap between mathematical models of the lymphatic system [Margaris 2012, Moore 2018] compared to those of the arterial system [Quarteroni 2017]. This gap relies on the range of scales of the lymphatic system and on the paucity of experimental data caused by the poor resolution and sensitivity of non-invasive imaging techniques of lymphatics [Munn 2014]. From the initial work of Reddy et al. [Reddy 1974], several mathematical models of the dynamics of collecting lymphatics [Venugopal 2007, Bertram 2011, Gajani 2015, Jamalian 2016, Caulk 2016, Kunert 2015], initial lymphatics [Roose 2012a, Roose 2012b] and lymph nodes [Cooper 2016, Jafarnejad 2015] have been proposed. MacDonald et al. [Macdonald 2008] performed experimental and in-silico computations of a single lymphangion in bovine collecting lymphatics. Bertram et al. [Bertram 2011] posed the basis for several other works and included at each step particular dynamics of lymphatics through experimental measurements [Bertram 2014b]. Jamalian et al. [Jamalian 2016] constructed a lumped-parameter model to simulate lymph transport in a network of rat lymphangions. Then, Jamalian and collaborators [Jamalian 2017] proved the existence of suction pressures in collecting lymphatics through computational modelling and experimental measurements. Caulk et al. [Caulk 2016] combined the lumped-parameter model described by Bertram et al. [Bertram 2014b] with their four-fibre family constitutive law proposed in [Caulk 2015] and studied the variation of muscle contractility in response to a sustained elevation in afterload [Caulk 2016]. To the best of our knowledge, to date there is yet no mathematical model of intracranial lymphatics. Also, a mathematical model of the interaction between arterial, venous interstitial fluid and lymphatic dynamics is still missing.

1.2.4 High-order numerical methods for partial differential equations

Many multi-scale mathematical models of the animal fluid system consist of sets of Partial Differential Equations (PDEs) and Ordinary Differential Equations (ODEs). Proper numerical schemes need to be employed for solving these equations. From the pioneering work of Toro et al. [Toro 2001], there have been several works on high-order ADER methods for both linear and non-linear systems of PDEs in one, two and three space dimensions using either Cartesian or unstructured meshes [Toro 2001, Schwartzkopff 2004, Titarev 2002, Dumbser 2007a, Dumbser 2014]. The ADER method is based on the solution of the generalized Riemann problem, for which several solvers have been proposed in the literature [Toro 2002, Castro 2008, Dumbser 2008, Montecinos 2014b, Toro 2015a]. The extension of the generalized Riemann problem for junctions has been proposed and used in the context of high-order numerical schemes [Borsche 2014a, Borsche 2016, Müller 2015a]. In a recent work, we extended the MT-TT and MT-HEOC solvers for junctions [Contarino 2016].

1.3 Contributions of this thesis

The main contributions of this thesis regard: 1) the development of a new high-order numerical method for junctions, 2) the design of a new mathematical model of one-dimensional collecting lymphatics and 3) the development of a holistic, multi-scale, closed-loop mathematical model of cerebral and peripheral murine extracellular fluid systems. In the present thesis, these topics are divided as listed below:

- In Chapter 2, we develop a high-order ADER-type numerical method for systems of hyperbolic balance laws in networks, based on a new implicit solver for the Junction-Generalized Riemann Problem (J-GRP). The resulting ADER scheme can deal with stiff source terms and can be applied to non-linear systems of hyperbolic balance laws in domains consisting of networks of one-dimensional sub-domains.
- In Chapter 3, we develop a novel one-dimensional mathematical model of collecting lymphatics coupled with a novel Electro-Fluid-Mechanical Contraction (EFMC) model for dynamical contractions and valve dynamics. The resulting mathematical model gives each lymphangion the autonomous capability to trigger action potentials based on local fluid-dynamical factors, such as circumferential stretch and wall-shear stress.
- In Chapter 4, based on a novel holistic, multi-scale, closed-loop mathematical model of the main murine fluid systems, we analyse the vascular blood dynamics of major vessels and the intracranial interaction of heart dynamics, arteries, veins, interstitial fluid and cerebrospinal fluid in healthy and pathological cases. We validate the mathematical model through MR-flow measurements and *in-vivo* intracranial pressure measurements acquired in healthy mice and in mice with an impairment of the cerebral venous outflow. Based on the computational results, we suggest a hypothesis on the working principles of the glymphatic system. Also, we show how impairment of the cerebral venous outflow might potentially lead to accumulation of solutes in the parenchyma, by altering CSF and ISF dynamics.

The goal of this thesis is reached in Chapter 4, which is based on the numerical methodologies explained in Chapter 2 and on existing literature of mathematical model of the human extracellular

fluid systems. One could have employed the mathematical model of Chapter 3 to construct a multi-scale mathematical model of the entire lymphatic system, coupled with the murine extracellular fluid system mathematical model presented in Chapter 4. However, there is still substantial work to be done to achieve such a subgoal. Chapter 3 is one of the bricks on which future work can build on to design a complete and physiologically based model of the lymphatic system.

Chapter 2

Junction-generalized Riemann problem for stiff hyperbolic balance laws in networks: An implicit solver and ADER schemes

2.1 Introduction

In recent years, suitable computational methods for non-linear systems of hyperbolic balance laws in domains consisting on networks of one-dimensional sub-domains, have been the subject of many publications. Related applications include gas flow in pipes [Banda 2006, Brouwer 2011, Bales 2009], traffic flow [Coclite 2002, Borsche 2014c, Bretti 2007], water flow [Borsche 2014b, Kesserwani 2008] and blood flow in the human circulation system [Müller 2013b, Müller 2014, Matthys 2007a, Formaggia 1999, Liang 2009b, Liang 2009a, Liang 2014, Mynard 2015, Olufsen 2000]. For a review of the subject see [Bressan 2014]. In all of these, the crucial point is the coupling of the information of the various one-dimensional sub-domains converging into a single junction. There exists a class of multi-scale methods that are based on the coupling between two or three-dimensional and one-dimensional equations. For the Euler equations, Hong and Kim [Hong 2011] described a strategy to simulate a network of pipes where the junction interfaces are modeled through the three-dimensional equations and normal averaged fluxes are used as boundary condition for the one-dimensional equations. Formaggia et al. [Formaggia 2001] proposed an approach to couple the three-dimensional and one-dimensional Navier-Stokes equations for flow problems in compliant vessels. Miglio et al. [Miglio 2005a, Miglio 2005b] coupled the two-dimensional and the one-dimensional Saint-Venant equations for water flow. With a multi-scale approach, one can maintain the information of the geometry such as angles and secondary flows, but as the number of junctions increases and the geometry becomes more complex, the computational cost can become too large, making a real simulation difficult or unfeasible. An example of a simpler model was described

by Fullana et al. [Fullana 2009] for blood flow that consists of ingoing and outgoing flows in a tank with a time-variable volume V, with a tube law analogous to the vessel tube law that relates pressure and volume. In this case, the choice of the tube law and parameters causes the numerical simulation to be parameter-dependent.

The coupling of different one-dimensional sub-domains at a junction has been formulated as an extended Riemann problem, see [Colombo 2008a, Colombo 2008b, Garavello 2006]. This formulation has several advantages. Firstly, it allows for a rigorous study of existence and uniqueness of solutions. Secondly, it can be used to numerically connect different tubes or channels, and can be combined with a numerical scheme for the interior part without additional computational costs compared to a multi-scale approach. Thirdly, it does not depend on additional parameters and the coupling conditions with no energy losses arise naturally from the PDEs themselves. The main disadvantage of this approach is the lack of geometrical information such as angles. For a rigorous mathematical study of existence and uniqueness of the Riemann problem solution at a junction under the assumption of subcritical flows, see Colombo et al. [Colombo 2008a, Colombo 2008b, Garavello 2006]. For the solution of the Riemann problem at a junction for arteries see [Sherwin 2003b], for arteries and veins refer to [Müller 2013b] and for gas pipes see [Banda 2006, Reigstad 2015].

A lot of research has been carried out in recent years in high-order ADER methods for both linear and non-linear systems in one, two and three space dimensions using either Cartesian or unstructured meshes, see for instance [Toro 2001, Schwartzkopff 2004, Schwartzkopff 2002, Titarev 2002, Titarev 2005, Dumbser 2007a, Dumbser 2014]. The building block of the ADER methodology is the solution of the Generalized Riemann Problem (GRP). Several solvers for the GRP have been proposed in the literature. The first one was proposed by Toro and Titarev [Toro 2002], called here the Toro-Titarev (TT) solver. Then, Castro and Toro [Castro 2008] reinterpreted, in the context of the GRP, the numerical scheme suggested by Harten et al. [Harten 1987] and proposed the HEOC solver. In the same study, the authors also proposed a different way to solve the GRP, which is analogous to the TT solver, and called it the Castro-Toro (CT) solver. Since all of these mentioned solvers are based on the explicit Taylor expansion combined with the Cauchy-Kowalewskaya procedure, they do not deal with stiff source terms. The first GRP solver that has allowed the proper treatment of stiff source terms was put forward by Dumbser, Enaux and Toro [Dumbser 2008], called here the DET solver. Subsequently, Montecinos and Toro [Montecinos 2014b] proposed an implicit solver, which is based on the implicit Taylor expansion combined with the Cauchy-Kowalewskaya procedure and is able to handle stiff source terms. The authors called it the MT-TT solver. More recently, they have formulated in [Toro 2015a] the implicit version of the HEOC solver and called it the MT-HEOC solver.

The extension of the Classical Riemann Problem (CRP) for junctions, which we call throughout this chapter the Junction-Classical Riemann Problem (J-CRP), has been studied and used in the context of low and high-order numerical schemes. A low order numerical treatment of junctions spoils the accuracy in space and time achieved by a high-order numerical scheme used within each subdomain of the network. Examples of this, in the context of human blood circulation simulated through a mathematical model, can be seen for instance in Müller and Toro [Müller 2013b, Müller 2014], Liang et al. [Liang 2009b, Liang 2009a, Liang 2014] and Mynard et al. [Mynard 2015]. First-order errors travel through the network of vessels with a damping effect for the pressure pulse-waves. Moreover, Borsche and Kall [Borsche 2014a] observed that the combination of schemes and

coupling conditions of different orders may modify the speed at which shocks pass the junction. To date, few studies have been done on the solution of the Junction-Generalized Riemann Problem (J-GRP), namely the extension of the GRP for junctions connecting one-dimensional sub-domains. The first high-order solvers of the J-GRP was put forward by Borsche and Kall [Borsche 2014a]. They generalized the TT and the CT solvers for the J-GRP. Then, Müller and Blanco [Müller 2015a] proposed an extension of the DET solver, which is able to deal with stiff source terms. In addition, Borsche and Kall [Borsche 2016] extended the HEOC solver for junctions.

The aim of this chapter is to extend the MT-HEOC solver for the GRP and construct a new implicit, semi-analytical solution of the J-GRP. Using the new MT-HEOC solver for the J-GRP, we design an ADER scheme that is globally explicit, locally implicit, free of any theoretical accuracy barrier in space and time, able to deal with stiff source terms and can be applied to non-linear systems of hyperbolic balance laws in domains consisting on networks of one-dimensional sub-domains. To validate the numerical methodology, we carry out a convergence rate study for a network of three vessels, propose a numerical experiment that assesses the ability of the numerical scheme to deal with stiff source terms and junctions, and implement the method for the physical model presented by Matthys et al. [Matthys 2007b] and further studied by Alastruey et al. [Matthys 2007a].

The rest of this chapter is structured as follows: in Section 2.2 we review the one-dimensional blood flow equations and explain the ADER finite volume scheme with different solvers for the GRP. We then describe a new methodology for solving the J-GRP. In Section 2.3 we propose two test problems in a network to verify the order of accuracy and the ability of the solver to deal with stiff source terms. We then show an application for a more complex network of 37 vessels and 21 junctions for which experimental results are available in the literature. Section 2.4 gives a summary and conclusions.

2.2 Methods

In this section we review the one-dimensional blood flow equations, briefly describe the ADER scheme with two different solvers for the GRP, formulate the J-GRP and propose a new methodology to accurately solve it.

2.2.1 One-dimensional blood flow equations

The one-dimensional blood flow equations for a compliant vessel are the following

$$\begin{cases} \partial_t A + \partial_x q = 0 \,, \\ \partial_t q + \partial_x \left(\alpha \frac{q^2}{A}\right) + \frac{A}{\rho} \partial_x p = -\frac{f}{\rho} \,, \end{cases} \tag{2.1}$$

where x is the space variable, t is time, α is the Coriolis coefficient assumed to be $\alpha = 1$, $A(x,t)$ is the cross-sectional area of the vessel, $q(x,t) = A(x,t)u(x,t)$ is the flow, $u(x,t)$ is the velocity, $p(x,t)$ is the pressure, ρ is the blood density (set to 1050 $^{kg}/_{m^3}$), $f(x,t) = \gamma\pi\mu\frac{q}{A}$ is the friction force per unit length of the tube with parameter γ chosen depending on the velocity profile and μ is the kinematic viscosity. There are two governing partial differential equations and three unknowns, namely $A(x,t)$, $q(x,t)$ and $p(x,t)$. For this reason, an extra relation is required to close the system,

the *tube law*, which relates pressure $p(x,t)$ and cross-sectional area $A(x,t)$. A purely elastic tube law reads

$$p(x,t) = K(x)\psi(A(x,t);A_0(x)) + p_e(x,t)\,, \tag{2.2}$$

with

$$\psi(A(x,t);A_0(x)) = \left[\left(\frac{A(x,t)}{A_0(x)}\right)^m - \left(\frac{A(x,t)}{A_0(x)}\right)^n\right], \tag{2.3}$$

where $p_e(x,t)$ is the external pressure, $A_0(x)$ is vessel cross-sectional area at equilibrium, $K(x)$ is the bending stiffness of the vessel wall, $m \geq 0$ and $n \leq 0$ are real numbers to be specified. For hyperbolicity m and n must satisfy additional constraints, see [Toro 2013]. For more information about the mathematical structure of the equations, see [Formaggia 2009, Toro 2013]. Relation (2.2) models a purely elastic behavior of the vessel wall. Other tube laws may also account for visco-elasticity, elastin and collagen, see [Matthys 2007a, Blanco 2014]. Practical choices for the parameters m, n and K are

$$K(x) = \begin{cases} K_a = \dfrac{E}{1-\nu^2}\left(\dfrac{h_0}{r_0}\right), & m = \dfrac{1}{2}\,, \quad n = 0 \quad \text{for arteries,} \\[2ex] K_v = \dfrac{E}{12(1-\nu^2)}\left(\dfrac{h_0}{r_0}\right)^3, & m \approx 10\,, \quad n = -3/2 \quad \text{for veins,} \end{cases} \tag{2.4}$$

where ν, h_0, r_0 are the Poisson ratio (set to $\nu = 0.5$), the wall-thickness at equilibrium and the cross-sectional radius at equilibrium. It is possible to write the blood flow equations in conservative form as follows:

$$\partial_t \mathbf{Q} + \partial_x \mathbf{F}(\mathbf{Q},x) = \mathbf{S}(\mathbf{Q},x)\,, \tag{2.5}$$

where

$$\mathbf{Q} = \begin{bmatrix} A \\ Au \end{bmatrix}, \quad \mathbf{F}(\mathbf{Q},x) = \begin{bmatrix} Au \\ Au^2 - \frac{K}{\rho}A_0\partial_{A_0}\Psi \end{bmatrix}, \tag{2.6}$$

$$\mathbf{S}(\mathbf{Q},x) = \begin{bmatrix} 0 \\ -\frac{1}{\rho}\left(f + A\partial_x p_e + \Psi\partial_x K + K\partial_x A_0 \partial_{A_0}\Psi\right) \end{bmatrix}, \tag{2.7}$$

with

$$\Psi = \Psi(A;A_0) = \int_A \psi(A;A_0)\mathrm{d}A = A_0\left(\frac{1}{m+1}\left(\frac{A}{A_0}\right)^{m+1} - \frac{1}{n+1}\left(\frac{A}{A_0}\right)^{n+1}\right), \tag{2.8}$$

and

$$\partial_{A_0}\Psi = \partial_{A_0}\Psi(A;A_0) = \partial_{A_0}\int_A \psi(A;A_0)\mathrm{d}A = -\left(\frac{m}{m+1}\left(\frac{A}{A_0}\right)^{m+1} - \frac{n}{n+1}\left(\frac{A}{A_0}\right)^{n+1}\right). \tag{2.9}$$

The constants arising from the integrals (2.8) and (2.9) are set to zero for consistency with (2.1) and (2.2), see [Elad 1991, Brook 1999, Toro 2016]. For a complete view of the mathematical analysis and derivation of the one-dimensional blood flow equations, refer to [Toro 2013, Formaggia 2009, Toro 2016].

2.2.2 ADER finite volume scheme

Consider the system of m hyperbolic balance laws

$$\partial_t \mathbf{Q} + \partial_x \mathbf{F}(\mathbf{Q}) = \mathbf{S}(\mathbf{Q}) \,. \tag{2.10}$$

By integrating (2.10) over the control volume $V = [x_{i-\frac{1}{2}}, x_{i+\frac{1}{2}}] \times [t^n, t^{n+1}]$ we obtain the exact formula

$$\mathbf{Q}_i^{n+1} = \mathbf{Q}_i^n - \frac{\Delta t}{\Delta x}\left(\mathbf{F}_{i+\frac{1}{2}} - \mathbf{F}_{i-\frac{1}{2}}\right) + \Delta t \mathbf{S}_i \,, \tag{2.11}$$

with definitions

$$\mathbf{Q}_i^n = \frac{1}{\Delta x}\int_{x_{i-\frac{1}{2}}}^{x_{i+\frac{1}{2}}} \mathbf{Q}(x, t^n)\mathrm{d}x \,, \tag{2.12}$$

$$\mathbf{F}_{i+\frac{1}{2}} = \frac{1}{\Delta t}\int_{t^n}^{t^{n+1}} \mathbf{F}(\mathbf{Q}(x_{i+\frac{1}{2}}, \tau))\mathrm{d}\tau \,, \quad \mathbf{S}_i = \frac{1}{\Delta t \Delta x}\int_{t^n}^{t^{n+1}}\int_{x_{i-\frac{1}{2}}}^{x_{i+\frac{1}{2}}} \mathbf{S}(\mathbf{Q}(x,\tau))\mathrm{d}x\mathrm{d}\tau \,. \tag{2.13}$$

Eq. (2.12) gives the spatial-integral average at time $t = t^n$ of the conserved variable $\mathbf{Q}$, (2.13) the time-integral average at interface $x = x_{i+\frac{1}{2}}$ of the physical flux $\mathbf{F}$ and the volume-integral average in V of the source term $\mathbf{S}$ respectively. Spatial mesh size and time step are $\Delta x = x_{i+\frac{1}{2}} - x_{i-\frac{1}{2}}$ and $\Delta t = t^{n+1} - t^n$ respectively. Finite volume methods depart from (2.10) to (2.13), where integrals are approximated, and then formula (2.11) becomes a *finite volume method*, where the approximated integrals (2.13) are called *numerical flux* and *numerical source*, respectively. The ADER finite volume schemes are one-step, fully discrete schemes, based on (2.11) with three main ingredients: a high-order spatial reconstruction (once per time step), the solution of the GRP at the cell interface to find the numerical flux and computation of the numerical source. The numerical flux is evaluated as time-integral average of the physical flux evaluated at the solution of the local GRP at the cell interface $x_{i+\frac{1}{2}}$ and the numerical source is computed as a high-order space-time integral of the source term within control volume V. See Toro et al. [Toro 2001], Chapter 19 and 20 of [Toro 2009] and references therein.

Generalized Riemann problem (GRP)

The Generalized Riemann Problem (GRP) is the following initial value problem

$$\left.\begin{array}{ll} \text{PDE:} & \partial_t \mathbf{Q} + \partial_x \mathbf{F}(\mathbf{Q}) = \mathbf{S}(\mathbf{Q}) \,, \quad x \in (-\infty, +\infty) \,, \quad t > 0 \,, \\ \text{IC:} & \mathbf{Q}(x,0) = \begin{cases} \mathbf{Q}_L(x) & x < 0 \,, \\ \mathbf{Q}_R(x) & x > 0 \,, \end{cases} \end{array}\right\} \tag{2.14}$$

where $\mathbf{Q}_L(x)$ and $\mathbf{Q}_R(x)$ are smooth vector-valued functions (e.g. polynomials of degree M) given by a reconstruction procedure. The particular case in which $\mathbf{Q}_L(x)$ and $\mathbf{Q}_R(x)$ are constant and $\mathbf{S}(\mathbf{Q}) = 0$ is called the *Classical Riemann Problem (CRP)*.

We are interested in finding the solution in time of problem (2.14) at the interface $x = 0$, which we denote with $\mathbf{Q}_{LR}(\tau)$, to evaluate the numerical flux $\mathbf{F}_{i+\frac{1}{2}}$, namely

$$\mathbf{F}_{i+\frac{1}{2}} = \frac{1}{\Delta t}\int_{t^n}^{t^{n+1}} \mathbf{F}(\mathbf{Q}_{LR}(\tau))\mathrm{d}\tau \,. \tag{2.15}$$

Several approaches have been proposed in the literature. There are two categories of GRP solvers: explicit and implicit. The first explicit solver for the GRP is the TT solver, proposed by Toro and Titarev [Toro 2002]. Then, Castro and Toro proposed both the CT and the HEOC solvers [Castro 2008]. The first implicit solver is the DET solver, proposed by Dumbser et al. [Dumbser 2008]. Then, implicit versions of TT and HEOC resulted in the MT-TT and the MT-HEOC solvers, both proposed by Montecinos and Toro [Montecinos 2014b, Toro 2015a]. For a comparison between different GRP solvers see [Montecinos 2012a]. For a study of analytical properties of the TT solver see Goetz and Iske [Goetz 2013]. Here we briefly present the HEOC approach in the explicit and implicit forms.

The Harten-Engquist-Osher-Chakravarthy (HEOC) solver

Castro and Toro [Castro 2008] reinterpreted the methodology proposed by Harten et al. [Harten 1987] in terms of a local GRP. The idea is to first evolve in time, independently, the left and right extrapolated values at the interface of the left and right reconstructed polynomials, up to a time τ and then solve a CRP with the resulting piece-wise constant data. Then the sought GRP solution at time τ is the Godunov state of the CRP solution, that is, the solution along the t-axis of the CRP. In what follows we describe the full procedure.

The GRP solution along the t-axis $\mathbf{Q}_{LR}(\tau)$ of (2.14) is found by solving the following CRP

$$\left.\begin{aligned} &\text{PDE:} && \partial_t \mathbf{Q} + \partial_x \mathbf{F}(\mathbf{Q}) = \mathbf{0}\,, \quad x \in (-\infty, +\infty)\,, \quad t > 0\,, \\ &\text{IC:} && \mathbf{Q}(x,0) = \begin{cases} \hat{\mathbf{Q}}_L(\tau) & x < 0\,, \\ \hat{\mathbf{Q}}_R(\tau) & x > 0\,, \end{cases} \end{aligned}\right\} \tag{2.16}$$

where the evolved vectors $\hat{\mathbf{Q}}_L(\tau)$ and $\hat{\mathbf{Q}}_R(\tau)$ are constant and given by applying a Taylor expansion around the initial points $\mathbf{Q}_L(0_-) = \lim_{x\to 0_-} \mathbf{Q}_L(x)$ and $\mathbf{Q}_R(0_+) = \lim_{x\to 0_+} \mathbf{Q}_R(x)$, respectively, evaluated at τ, that is

$$\left.\begin{aligned} \hat{\mathbf{Q}}_L(\tau) &= \mathbf{Q}_L(0_-) + \sum_{j=1}^{M} \frac{\tau^j}{j!} \partial_t^{(j)} \mathbf{Q}_L(0_-)\,, \\ \hat{\mathbf{Q}}_R(\tau) &= \mathbf{Q}_R(0_+) + \sum_{j=1}^{M} \frac{\tau^j}{j!} \partial_t^{(j)} \mathbf{Q}_R(0_+)\,. \end{aligned}\right\} \tag{2.17}$$

The Cauchy-Kowalewskaya procedure allows us to use the PDEs in (2.14) to express all time derivatives in (2.17) as functionals of space derivatives and of the source term $\mathbf{S}(\mathbf{Q})$, namely

$$\partial_t^{(j)} \mathbf{Q}(x,t) = \mathbf{G}^{(j)}\left(\mathbf{Q}(x,t), \ldots, \partial_x^{(j)} \mathbf{Q}(x,t)\right). \tag{2.18}$$

The polynomials $\mathbf{Q}_L(x)$ and $\mathbf{Q}_R(x)$ are defined on the left and right sides of the interface and are smooth away from 0 (locally the interface). This allows us to define limiting values from the left and right, at $t = 0$, of the spatial derivatives of the initial conditions, namely

$$\left.\begin{aligned} \partial_x^{(j)} \mathbf{Q}_L(0_-) &:= \lim_{x\to 0_-} \partial_x^{(j)} \mathbf{Q}_L(x)\,, \quad j = 1, \ldots, M\,, \\ \partial_x^{(j)} \mathbf{Q}_R(0_+) &:= \lim_{x\to 0_+} \partial_x^{(j)} \mathbf{Q}_R(x)\,, \quad j = 1, \ldots, M\,. \end{aligned}\right\} \tag{2.19}$$

Thus, time derivatives can be replaced by their respective Cauchy-Kowalewskaya functional $\mathbf{G}^{(j)}$, leading to

$$\left.\begin{aligned}\hat{\mathbf{Q}}_L(\tau) &= \mathbf{Q}_L(0_-) + \sum_{j=1}^{M} \frac{\tau^j}{j!}\mathbf{G}^{(j)}\Big(\mathbf{Q}_L(0_-),\ldots,\partial_x^{(j)}\mathbf{Q}_L(0_-)\Big)\,,\\ \hat{\mathbf{Q}}_R(\tau) &= \mathbf{Q}_R(0_+) + \sum_{j=1}^{M} \frac{\tau^j}{j!}\mathbf{G}^{(j)}\Big(\mathbf{Q}_R(0_+),\ldots,\partial_x^{(j)}\mathbf{Q}_R(0_+)\Big)\,.\end{aligned}\right\} \tag{2.20}$$

Eqs. (2.20) are final product of the *evolution stage*. The sought GRP solution along the t-axis at time $t=\tau$ is the Godunov state of the CRP with initial data given by (2.20) and self-similar solution $\mathbf{D}(x/t)$, that is

$$\mathbf{Q}_{LR}(\tau) = \mathbf{D}(0)\,. \tag{2.21}$$

Note that when solving the CRP (2.16) at time $t=\tau$, we change to local coordinates $\hat{x}=x$ and $\hat{t}=t-\tau$, and then for convenience we omit the "hats". This numerical solver for the GRP is called the *Harten-Engquist-Osher-Chakravarthy (HEOC)*. To evaluate the numerical flux $\mathbf{F}_{i+\frac{1}{2}}$, one has to calculate the solution of the GRP at the interface $x_{i+\frac{1}{2}}$ at different time-integration points, within the time step $0\le\tau\le\Delta t$. In the HEOC solver, for each time-integration point, one has to apply two Taylor expansions and solve a CRP. Moreover, the HEOC solver requires a robust and generally non-linear Riemann solver, which can be time-consuming; whereas the TT solver needs a single expansion right at the interface and uses a non-linear Riemann solver only once to compute the leading term. To solve the CRP we recommend the use of a non-linear complete approximate Riemann solver. Here for the two equation model, we use the Harten-Lax-van Leer (HLL) [Harten 1983]. For background on classical Riemann solvers, see [Toro 2009].

We now describe the implicit version of the HEOC solver, which uses the implicit Taylor series expansion instead of the explicit version.

The MT implicit Taylor series expansion

Toro and Montecinos proposed in [Toro 2015a, Montecinos 2014b] two methodologies for solving the GRP: the MT-TT and the MT-HEOC solvers. These solvers are the implicit versions of the TT and the HEOC solvers respectively, and are able to deal with stiff source terms. They are based on an implicit Taylor expansion in the evolution stage, which generates non-linear algebraic problems to be solved. For the MT-HEOC approach there are two possible schemes, namely *Reduced Implicit Taylor expansion Approach (RITA)* and *Complete Implicit Taylor expansion Approach (CITA)*. See [Toro 2015a] for details. Here we describe the RITA approach, insofar as it is simpler and there are less operations to be performed, when compared to CITA.

First of all, we apply an implicit Taylor expansion at position $x=0$ and time $t=\tau$,

$$\mathbf{Q}(0,\tau) = \mathbf{Q}(0,0_+) - \sum_{j=1}^{M} \frac{(-\tau)^j}{j!}\partial_t^{(j)}\mathbf{Q}(0,\tau)\,, \tag{2.22}$$

where the evolved vectors $\mathbf{Q}(0,\tau),\ldots,\partial_t^{(M)}\mathbf{Q}(0,\tau)$ are unknown. Then we use the Cauchy-Kowalewskaya procedure to convert time derivatives into functionals of space derivatives

$$\mathbf{Q}(0,\tau) = \mathbf{Q}(0,0_+) - \sum_{j=1}^{M} \frac{(-\tau)^j}{j!}\mathbf{G}^{(j)}\Big(\mathbf{Q}(0,\tau),\ldots,\partial_x^{(j)}\mathbf{Q}(0,\tau)\Big)\,. \tag{2.23}$$

Note that the Cauchy-Kowalewskaya functionals $\mathbf{G}^{(j)}$ are evaluated at the unknown evolved vectors $\mathbf{Q}(0,\tau),\ldots,\partial_x^{(j)}\mathbf{Q}(0,\tau)$. In Eqs. (2.23) there are $M+1$ vector unknowns and each one has m entries, thus the total number of unknowns is $m(M+1)$. Since we only have m equations in (2.23), we still need mM equations, which can be obtained by appling a time implicit Taylor expansion for the spatial derivatives $\partial_x^{(h)}\mathbf{Q}(0,\tau)$, with $h=1,\ldots,M$, leading to

$$\partial_x^{(h)}\mathbf{Q}(0,\tau)=\partial_x^{(h)}\mathbf{Q}(0,0_+)-\sum_{j=1}^{M-h}\frac{(-\tau)^j}{j!}\partial_t^{(j)}\partial_x^{(h)}\mathbf{Q}(0,\tau)\,,\quad h=1,\ldots,M\,. \tag{2.24}$$

Exchanging temporal and spatial derivatives and using the Cauchy-Kowalewskaya procedure, we obtain

$$\partial_x^{(h)}\mathbf{Q}(0,\tau)=\partial_x^{(h)}\mathbf{Q}(0,0_+)-\sum_{j=1}^{M-h}\frac{(-\tau)^j}{j!}\partial_x^{(h)}\mathbf{G}^{(j)}\left(\mathbf{Q}(0,\tau),\ldots,\partial_x^{(j)}\mathbf{Q}(0,\tau)\right),\quad h=1,\ldots,M\,. \tag{2.25}$$

The Mm and m equations obtained respectively by Eqs. (2.25) and (2.23) allow us to have the required number of equations, that is, $m(M+1)$. We introduce the notation

$$\left.\begin{aligned}&\mathbf{U}=[\mathbf{U}^0,\ldots,\mathbf{U}^M]\,,\quad \mathbf{U}^j=\partial_x^{(j)}\mathbf{Q}(0,\tau)\,,\quad j=0,\ldots,M\,,\\&\mathbf{U}_0=[\mathbf{U}_0^0,\ldots,\mathbf{U}_0^M]\,,\quad \mathbf{U}_0^j=\partial_x^{(j)}\mathbf{Q}(0,0_+)\,,\quad j=0,\ldots,M\,,\end{aligned}\right\} \tag{2.26}$$

where $\mathbf{U}$ is the vector of unknown and $\mathbf{U}_0$ is a known vector of the leading terms. Hence, rewriting Eqs. (2.23) and (2.25), we end up with the following problem: given $\mathbf{U}_0$, find $\hat{\mathbf{U}}$ such that

$$\mathbf{L}(\hat{\mathbf{U}};\mathbf{U}_0,\tau)=\hat{\mathbf{U}}-\mathbf{H}(\hat{\mathbf{U}};\mathbf{U}_0,\tau)=\mathbf{0}\,, \tag{2.27}$$

where

$$\mathbf{H}(\mathbf{U};\mathbf{U}_0,\tau)=\begin{bmatrix}\mathbf{U}_0^0-\displaystyle\sum_{j=1}^{M}\frac{(-\tau)^j}{j!}\mathbf{G}^{(j)}(\mathbf{U}^0,\ldots,\mathbf{U}^j)\\ \vdots\\ \mathbf{U}_0^h-\displaystyle\sum_{j=1}^{M-h}\frac{(-\tau)^j}{j!}\partial_x^{(h)}\mathbf{G}^{(j)}(\mathbf{U}^0,\ldots,\mathbf{U}^j)\\ \vdots\\ \mathbf{U}_0^M\end{bmatrix} \tag{2.28}$$

Once problem (2.27) is solved, evolved values $\mathbf{Q}(0,\tau),\ldots,\partial_x^{(M)}\mathbf{Q}(0,\tau)$ are known. Functionals $\mathbf{G}^{(j)}$ and their spatial derivatives can be found using symbolic manipulators in a preprocessing step. To find the root of $\mathbf{L}$, one can apply, for instance, a Newton or a Newton reduced-step method, see [Toro 2015a]. A possible guess value for a numerical method to find the solution of (2.27) is the vector of the leading terms, namely $\mathbf{U}_0$. The operator $\mathbf{L}(\hat{\mathbf{U}};\mathbf{U}_0,\tau)$ depends on the time τ and on the choice of $\mathbf{U}_0$, which will be different depending on the solver being used.

The implicit Montecinos-Toro HEOC (MT-HEOC) solver

The GRP solution along the t-axis $\mathbf{Q}_{LR}(\tau)$ of (2.14) is found by solving the following CRP

$$\left.\begin{array}{ll} \text{PDE:} & \partial_t \mathbf{Q} + \partial_x \mathbf{F}(\mathbf{Q}) = \mathbf{0}\,, \quad x \in (-\infty, +\infty)\,, \quad t > 0\,, \\ \text{IC:} & \mathbf{Q}(x,0) = \begin{cases} \hat{\mathbf{Q}}_L(\tau) & x < 0\,, \\ \hat{\mathbf{Q}}_R(\tau) & x > 0\,, \end{cases} \end{array}\right\} \tag{2.29}$$

where the evolved vectors $\hat{\mathbf{Q}}_L(\tau)$ and $\hat{\mathbf{Q}}_R(\tau)$ are constant and found by solving the following non-linear problems: find $\hat{\mathbf{U}}_L$ and $\hat{\mathbf{U}}_R$ such that

$$\mathbf{L}(\hat{\mathbf{U}}_L; \mathbf{U}_L, \tau) = \mathbf{0}\,, \quad \mathbf{L}(\hat{\mathbf{U}}_R; \mathbf{U}_R, \tau) = \mathbf{0}\,, \tag{2.30}$$

where the leading terms $\mathbf{U}_L$ and $\mathbf{U}_R$ are respectively

$$\left.\begin{array}{l} \mathbf{U}_L = [\mathbf{U}_L^0, \ldots, \mathbf{U}_L^M]\,, \quad \mathbf{U}_L^j = \partial_x^{(j)} \mathbf{Q}_L(0_-) = \lim\limits_{x \to 0_-} \partial_x^{(j)} \mathbf{Q}_L(x)\,, \quad j = 0, \ldots, M\,, \\ \mathbf{U}_R = [\mathbf{U}_R^0, \ldots, \mathbf{U}_R^M]\,, \quad \mathbf{U}_R^j = \partial_x^{(j)} \mathbf{Q}_R(0_+) = \lim\limits_{x \to 0_+} \partial_x^{(j)} \mathbf{Q}_R(x)\,, \quad j = 0, \ldots, M\,. \end{array}\right\} \tag{2.31}$$

The solution procedure of the non-linear problems (2.30) is termed here the *evolution stage*. Possible guess values for a numerical method to find the solutions of non-linear problems (2.30) are the reconstructed polynomials and their derivatives, namely $\mathbf{U}_L$ and $\mathbf{U}_R$. Once problems (2.30) are solved, then the evolved values $\hat{\mathbf{Q}}_L(\tau)$ and $\hat{\mathbf{Q}}_R(\tau)$ will be the first entries of $\hat{\mathbf{U}}_L$ and $\hat{\mathbf{U}}_R$ respectively, namely $\hat{\mathbf{U}}_L^0$ and $\hat{\mathbf{U}}_R^0$. The sought GRP solution along the t-axis at time $t = \tau$ is the Godunov state of the CRP (2.29) with initial data $\hat{\mathbf{Q}}_L(\tau)$ and $\hat{\mathbf{Q}}_R(\tau)$ and self-similar solution $\mathbf{D}(x/t)$, namely

$$\mathbf{Q}_{LR}(\tau) = \mathbf{D}(0)\,. \tag{2.32}$$

The MT-HEOC solver uses the implicit Taylor series expansion (2.30) in the evolution stage, instead of an explicit one (2.20). The use of the implicit approach in the evolution stage requires the solution of non-linear algebraic problem with $m(M+1)$ unknowns for each side of the interface and then the solution of a non-linear CRP. As for the HEOC solver, we can also use an approximate Riemann solver to find the solution of the CRP (2.29), such as the two-rarefaction [Toro 2009] or the HLL Riemann solvers [Harten 1983].

The PDEs of the CRP in (2.29) do not contain the source term $\mathbf{S}(\mathbf{Q})$. However, the influence of the source term is accounted for via the Cauchy-Kowalewskaya procedure through the functional $\mathbf{H}(\mathbf{U}; \mathbf{U}_0, \tau)$. The non-linear problems, which have to be solved in order to find the initial condition for the CRP, allow us to deal with stiff source terms, see [Montecinos 2014b, Toro 2015a] and [Montecinos 2012b].

2.2.3 The Junction-Generalized Riemann Problem (J-GRP)

We are concerned with the design of high-order numerical methods for solving hyperbolic balance laws in simplified domains consisting of networks of one-dimensional sub-domains that can be, for example, blood vessels, water channels or gas tubes. In our application we formulate the J-GRP in the context of one-dimensional blood flow equations. For this reason, we formulate the mathematical

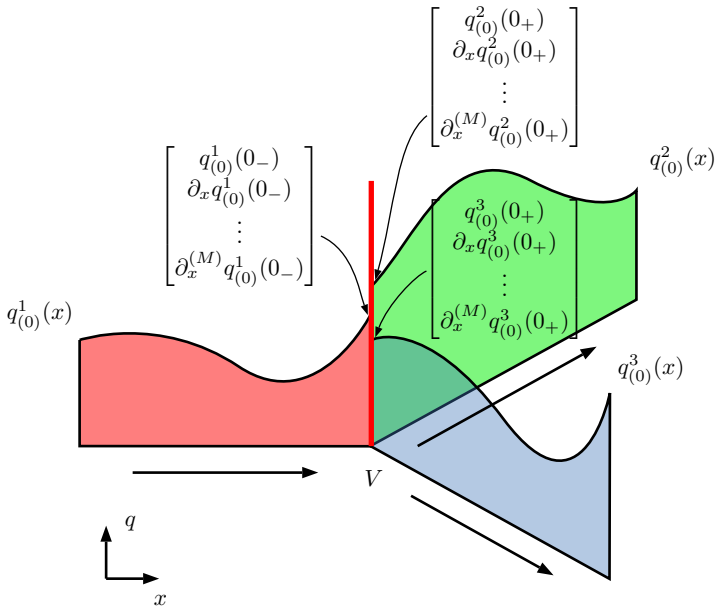

Figure 2.1: Illustration of an initial condition for a J-GRP with $N = 3$ vessels and vertex V for a single component $q_{(0)}(x,t)$ of the vector of unknowns $\mathbf{Q}_{(0)}(x,t)$. The data $q^1_{(0)}$, $q^2_{(0)}$ and $q^3_{(0)}$ are smooth away from vertex V and have one-sided spatial derivatives at V.

problem in terms of vessels. First, we define the J-GRP, then we explain how to solve the J-CRP for one-dimensional blood flow equations and propose a new solver for the J-GRP.

Consider a set of N vessels with the common vertex V. For the k-th vessel, variable x^k is the local coordinate and the vertex V is located in 0 without loss of generality. In each k-th vessel, consider the following initial value problem

$$\left.\begin{array}{ll} \text{PDEs:} & \partial_t \mathbf{Q}^k + \partial_x \mathbf{F}(\mathbf{Q}^k) = \mathbf{S}(\mathbf{Q}^k)\,, \quad x^k \in I_k = \left(a^k, b^k\right)\,, \quad t > 0\,, \\ \text{ICs:} & \mathbf{Q}^k(x^k,0) = \mathbf{Q}^k_{(0)}(x^k)\,, \end{array}\right\} \tag{2.33}$$

where either a^k or b^k is the local coordinate of vertex V, spatial domain I_k has length $L^k = |b^k - a^k|$ and the initial condition $\mathbf{Q}^k_{(0)}(x^k)$ is a smooth vector-valued function of the local coordinate x^k (e.g. polynomials of order M). Note that the material and geometrical properties can be different for each k-th vessel. The set of solutions $\mathbf{Q}^k(x^k,t)$, with $k = 1,\ldots,N$, has to satisfy the following coupling conditions at the common vertex V

$$\boldsymbol{\phi}(\mathbf{Q}^1(0,t),\ldots,\mathbf{Q}^N(0,t)) = \mathbf{0}\,, \quad t > 0\,, \tag{2.34}$$

where the vector $\boldsymbol{\phi}$ defines coupling conditions. We define as *Junction-Generalized Riemann Problem (J-GRP)* at the vertex V with N vessels, the set initial value problems (2.33), with $k = 1\ldots,N$, with constraints (2.34). Figure 2.1 illustrates a simple representation of a J-GRP. For the particular case in which $N = 2$, $b^1 = 0$ and $a^2 = 0$, we end up with a GRP with the jump discontinuity at the initial time located in $x = 0$. Therefore, the J-GRP is an extension of the GRP. In order to easy the notation in the following, we shall consider the local coordinate x^k without index.

We are interested in finding the solutions in time of problem (2.33) at the vertex V, which we denote with $\mathbf{Q}_V^k(\tau)$, for $k=1,\dots,N$, to evaluate the numerical flux $\mathbf{F}_V^k$ of the k-th vessel at the vertex V, namely

$$\mathbf{F}_V^k = \frac{1}{\Delta t}\int_{t^n}^{t^{n+1}} \mathbf{F}(\mathbf{Q}_V^k(\tau))\mathrm{d}\tau\,. \tag{2.35}$$

In the following we shall refer to these numerical fluxes at the vertex V as the *junction-numerical fluxes*. The main ingredient we require to solve the J-GRP is the related *classical* version with piece-wise constant data and no source terms.

The Junction-Classical Riemann Problem (J-CRP)

Consider the following set of initial value problems

$$\left.\begin{array}{lll} \text{PDEs:} & \partial_t\mathbf{Q}^k+\partial_x\mathbf{F}(\mathbf{Q}^k)=\mathbf{0}\,, \quad x\in I_k=\left(a^k,b^k\right)\,, \quad t>0\,, \\ \text{ICs:} & \mathbf{Q}^k(x,0)=\mathbf{Q}^k_{(0)}\,, \end{array}\right\} \quad k=1,\dots,N\,, \tag{2.36}$$

with coupling conditions ϕ

$$\phi(\mathbf{Q}^1(0,t),\dots,\mathbf{Q}^N(0,t))=\mathbf{0}\,, \quad t>0\,, \tag{2.37}$$

where $\mathbf{Q}^k_{(0)}$, with $k=1,\dots,N$, are constant vectors. We define as *Junction-Classical Riemann Problem (J-CRP)* at the vertex V with N vessels, the set initial value problems (2.36), with $k=1\dots,N$, with constraints (2.37).

The solution of a J-CRP is a set of self-similar functions $\mathbf{D}^k(x/t)$ defined for each k-th vessel. For a 2×2 hyperbolic balance law system in subcritical regime, we have a total number of $2N$ states. These $2N$ states arise from the N initial conditions $\mathbf{Q}^k_{(0)}$, with $k=1,\dots,N$, and N states $\mathbf{Q}^k_*$, with $k=1,\dots,N$, which are connected to the initial conditions through non-linear waves and among themselves by the coupling conditions ϕ. To completely solve the J-CRP, one has to find values $\mathbf{Q}^k_*$, with $k=1,\dots,N$, using both the structure of the waves (i.e. rarefactions or shocks) and the coupling conditions ϕ. The solutions along the t-axis $\mathbf{D}^k(0)$, with $k=1,\dots,N$, of the J-CRP, are termed here the *Godunov states*.

Here we present the solution of the J-CRP for the one-dimensional blood flow equations assuming subcritical flow. To the authors' knowledge, the complete solution of the J-CRP considering all possible wave-patterns is not available. This implies that we cannot handle supercritical and transcritical flows at junctions, which might be present in physiological situations due to vein collapse with discontinuous parameters in the human body, see [Siviglia 2013]. For the solution of the CRP for subcritical flows with discontinuous material properties for blood flow with $n=0$ and $m>0$ refer to [Toro 2011], and to [Toro 2013] with $n<0$ and $m>0$. For arteries, [Han 2014] solved in complete detail the CRP with discontinuous material properties. For the solution of the J-CRP in blood flow for subcritical flows with $n<0$ and $m>0$, see also [Müller 2015a]. See [Colombo 2008a, Colombo 2008b, Garavello 2006, Borsche 2014a] for the solution of the J-CRP using a more geometrical approach and for general conservation laws.

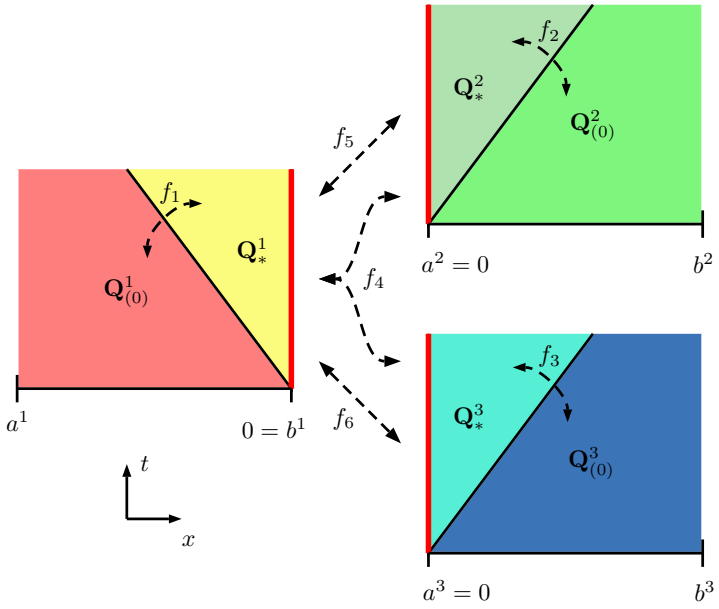

Figure 2.2: Representation of a J-CRP for a typical 2×2 non-linear system with $N = 3$ vessels, where $b^1 = 0$, $a^2 = 0$ and $a^3 = 0$ are the local coordinates of vertex V for the first, second and third vessel respectively. The non-linear function f_k connects the initial condition $\mathbf{Q}^k_{(0)}$ and unknown $\mathbf{Q}^k_*$ for $k = 1\dots,3$, f_4 connects all the unknowns $\mathbf{Q}^1_*, \mathbf{Q}^2_*, \mathbf{Q}^3_*$, while f_5 and f_6 connect the unknown $\mathbf{Q}^1_*$ to $\mathbf{Q}^2_*$ and $\mathbf{Q}^3_*$, respectively.

The coupling conditions that connect states $\mathbf{Q}^k_*$, with $k = 1,\dots,N$, among themselves are

$$\phi(\mathbf{Q}^1_*,\dots,\mathbf{Q}^N_*) = \begin{bmatrix} \sum_{k=1}^{N} g^k A^k_* u^k_* \\ p_t(A^1_*,u^1_*;K^1,A^1_0) - p_t(A^2_*,u^2_*;K^2,A^2_0) \\ \vdots \\ p_t(A^1_*,u^1_*;K^1,A^1_0) - p_t(A^N_*,u^N_*;K^N,A^N_0) \end{bmatrix} = \mathbf{0}\,, \tag{2.38}$$

where the vector of conserved variables $\mathbf{Q}$ is defined in (2.6), while K^k and A^k_0 are the material properties of the k-th vessel. The auxiliary function g^k indicates whether the k-th vessel has vertex V at a^k or b^k, and reads

$$g^k = \begin{cases} -1 & a^k = 0\,, \\ 1 & b^k = 0\,, \end{cases} \tag{2.39}$$

p_t denotes *total pressure*

$$p_t(A,u;K,A_0) = \frac{1}{2}\rho u^2 + p(A;K,A_0)\,, \tag{2.40}$$

and p is the pressure given in (2.2). The first component of ϕ assures conservation of mass, whereas all the remaining components, from the second to the N-th, guarantee equality of total pressure in all the vessels meeting at vertex V. Since the number of vectors $\mathbf{Q}^k_*$ is N and each vector has two

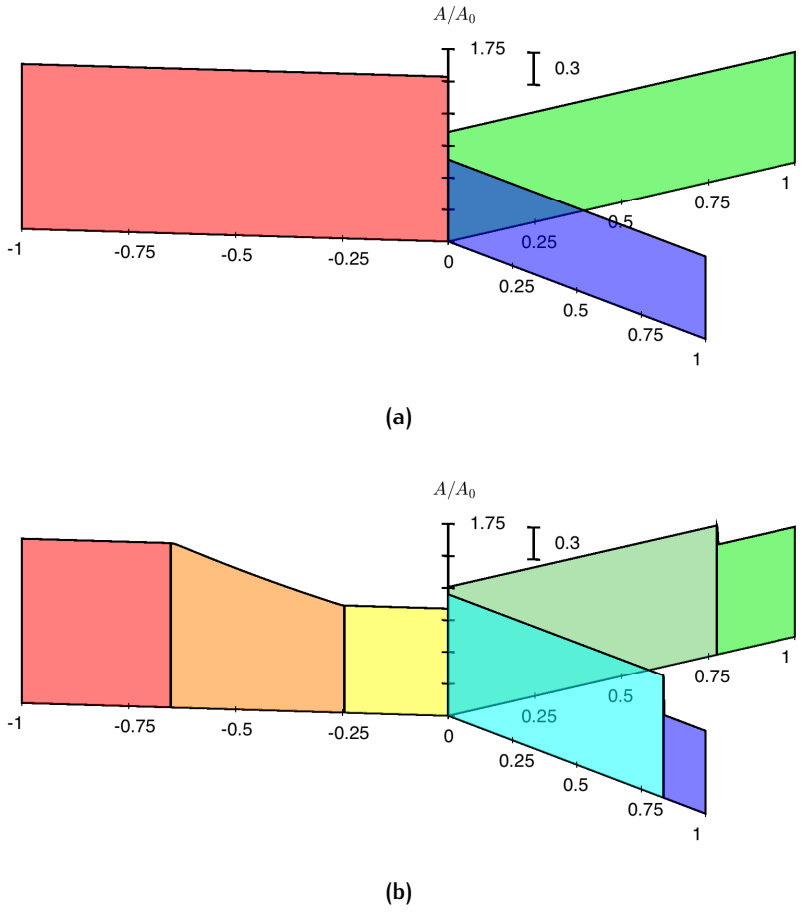

Figure 2.3: Example of a J-CRP. Piece-wise constant data are given for each vessel. Frames (a) and (b) depict the solution at initial and output time for a simple J-CRP respectively. A rarefaction wave propagates backward in the left sub-domain, whereas two shocks move forward in the others.

components A_*^k and $q_*^k = A_*^k u_*^k$, the total number of unknowns is $2N$. This means that we need a total number of $2N$ equations to close the system. The coupling conditions ϕ contain N equations, while the other N equations are obtained by connecting each state $\mathbf{Q}_*^k$ to the initial condition $\mathbf{Q}_{(0)}^k$ through non-linear waves for $k = 1,\dots,N$. The total number of equations are $2N$ and therefore the system is closed.

The non-linear relationship between $\mathbf{Q}_*^k$ and $\mathbf{Q}_{(0)}^k$, with $k = 1,\dots,N$, reads

$$u_*^k - u_{(0)}^k + g^k \beta(A_*^k; A_{(0)}^k, K^k, A_0^k) = 0\,, \quad k = 1,\dots,N\,, \tag{2.41}$$

where the non-linear function β is

$$\beta(A_*;A,K,A_0) = \begin{cases} \displaystyle\int_A^{A_*} \frac{c(\tau;K,A_0)}{\tau}\mathrm{d}\tau & \text{if } A_* \leq A\,, \quad \text{rarefaction wave,} \\ \displaystyle\sqrt{B(A_*;A,K,A_0)\frac{A_*-A}{A_*A}} & \text{if } A_* > A\,, \quad \text{shock wave.} \end{cases} \tag{2.42}$$

The wave speed is

$$c(A;K,A_0) = \sqrt{\frac{K}{\rho}\left(m\left(\frac{A}{A_0}\right)^m - n\left(\frac{A}{A_0}\right)^n\right)}\,, \tag{2.43}$$

and the function B is

$$B(A_*;A,K,A_0) = \frac{K}{\rho}\left(\frac{m}{m+1}\frac{A_*^{m+1}-A^{m+1}}{A_0^m} - \frac{n}{n+1}\frac{A_*^{n+1}-A^{n+1}}{A_0^n}\right). \tag{2.44}$$

Gathering the information coming from Eqs. (2.38) and (2.41) we end up with the following

Proposition 2.2.1. *The solution of the J-CRP with N vessels for subcritical flow is found by solving the following non-linear system*

$$\left.\begin{aligned} f_1(x_1,y_1;A^1_{(0)},u^1_{(0)}) &= y_1 - u^1_{(0)} + g^1\beta(x_1;A^1_{(0)},K^1,A^1_0) &&= 0\,,\\ &\vdots \\ f_N(x_N,y_N;A^N_{(0)},u^N_{(0)}) &= y_N - u^N_{(0)} + g^N\beta(x_N;A^N_{(0)},K^N,A^N_0) &&= 0\,,\\ f_{N+1}(x_1,\dots,x_N,y_1,\dots,y_N) &= g^1x_1y_1 + g^2x_2y_2 + \cdots + g^Nx_Ny_N &&= 0\,,\\ f_{N+2}(x_1,y_1,x_2,y_2) &= p_t(x_1,y_1;K^1,A^1_0) - p_t(x_2,y_2;K^2,A^2_0) &&= 0\,,\\ &\vdots \\ f_{2N}(x_1,y_1,x_N,y_N) &= p_t(x_1,y_1;K^1,A^1_0) - p_t(x_N,y_N;K^N,A^N_0) &&= 0\,, \end{aligned}\right\} \tag{2.45}$$

where the unknowns of the problem are

$$\mathbf{X} = [x_1,\dots,x_N] = [A^1_*,\dots,A^N_*]\,, \quad \mathbf{Y} = [y_1,\dots,y_N] = [u^1_*,\dots,u^N_*]\,, \tag{2.46}$$

with β and p_t defined in (2.42) and (2.40), respectively.

The k-th non-linear function f_k connects the initial condition $\mathbf{Q}^k_{(0)}$ to the unknown $\mathbf{Q}^k_*$ for $k = 1,\dots,N$, f_{N+1} connects all the unknowns $\mathbf{Q}^1_*\dots,\mathbf{Q}^N_*$, and f_{k+N} connects the unknown $\mathbf{Q}^1_*$ to the unknown $\mathbf{Q}^k_*$ for $k = 2,\dots,N$. We note that Proposition 2.2.1 is a generalization of Proposition 4.6 of [Toro 2011]. A J-CRP solver for 2 vessels with different parameters K, A_0 corresponds to the CRP solver with piece-wise constant parameters K,A_0 for a single vessel. As we have assumed subcritical flow, then the Godunov states of problem of the J-CRP will be $\mathbf{D}^k(0) = \mathbf{Q}^k_*$ for $k = 1,\dots,N$.

Sherwin et al. [Sherwin 2003a] solved the above system for blood flow assuming a two-rarefaction wave-pattern for the function β defined in (2.42), namely they assumed $A^* \leq A$. This hypothesis can be seen as an approximate J-CRP solver, through which numerical simulations show acceptable numerical results, see [Sherwin 2003a]. See also [Müller 2015a] for the first complete description of the solution of the J-CRP for blood flow, where both shocks and rarefaction waves are admitted for the genuinely non-linear characteristic fields.

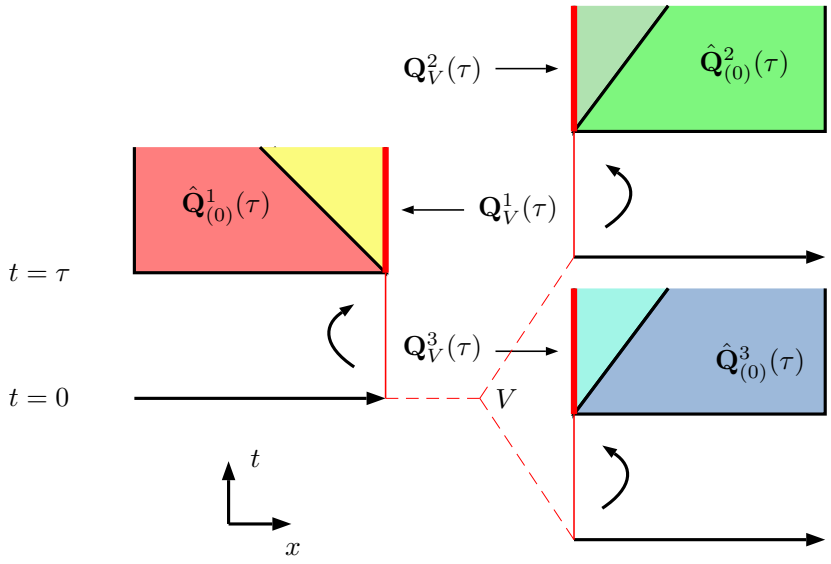

Figure 2.4: Illustration of the MT-HEOC solver for the J-GRP with $N=3$ vessels. The limiting values at vertex V are evolved separately up to time $t=\tau$. The sought solutions along the t-axis are the Godunov states of the J-CRP with these evolved states as initial data.

2.2.4 A new implicit J-GRP solver

Here we propose a new implicit solver for the J-GRP. Following the idea of the explicit HEOC solver for the J-GRP proposed in [Borsche 2016] and the implicit MT-HEOC solver for the GRP in [Toro 2015a], we propose to combine them and construct the MT-HEOC solver for the J-GRP.

The J-GRP solutions along the t-axis $\mathbf{Q}_V^k(\tau)$, with $k=1,\dots,N$, of (2.33) with coupling conditions ϕ are found by solving the following J-CRP at the vertex V with N vessels and coupling conditions ϕ

$$\left.\begin{array}{ll} \text{PDEs:} & \partial_t \mathbf{Q}^k + \partial_x \mathbf{F}(\mathbf{Q}^k) = \mathbf{0}\,, \quad x \in I_k = (a^k, b^k)\,, \quad t>0\,, \\ \text{ICs:} & \mathbf{Q}^k(x,0) = \hat{\mathbf{Q}}_{(0)}^k(\tau)\,. \end{array}\right\} \quad k=1,\dots,N\,, \tag{2.47}$$

where $\hat{\mathbf{Q}}_{(0)}^k(\tau)$, with $k=1,\dots,N$, are constant vectors. The evolved values $\hat{\mathbf{Q}}_{(0)}^k(\tau)$ are found by applying for each k-th vessel the implicit Taylor expansion at the vertex V up to time τ, that is, by solving the following non-linear problem: find $\hat{\mathbf{U}}_{(0)}^k$ such that

$$\mathbf{L}(\hat{\mathbf{U}}_{(0)}^k; \mathbf{U}_{(0)}^k, \tau) = \mathbf{0}\,, \tag{2.48}$$

where the leading term $\mathbf{U}_{(0)}^k$ is

$$\mathbf{U}_{(0)}^k = [\mathbf{U}_{(0)}^{k,0}, \dots, \mathbf{U}_{(0)}^{k,M}]\,, \quad \mathbf{U}_{(0)}^{k,j} = \begin{cases} \partial_x^{(j)} \mathbf{Q}_{(0)}^k(0_+) = \lim\limits_{x\to 0_+} \partial_x^{(j)} \mathbf{Q}_{(0)}^k(x)\,, & \text{if } a^k = 0\,, \\ \partial_x^{(j)} \mathbf{Q}_{(0)}^k(0_-) = \lim\limits_{x\to 0_-} \partial_x^{(j)} \mathbf{Q}_{(0)}^k(x)\,, & \text{if } b^k = 0\,, \end{cases} \quad j=0,\dots,M\,. \tag{2.49}$$

The solution procedure of the non-linear problems (2.48) is termed here the *evolution stage*. As in the MT-HEOC solver for the GRP, a possible initial guess for a numerical method to find solution of the non-linear problem (2.48) is $\mathbf{U}^k_{(0)}$. Once we solve problem (2.48), then the evolved vector $\hat{\mathbf{Q}}^k_{(0)}(\tau)$ will be the first entry of $\hat{\mathbf{U}}^k_{(0)}$, namely $\hat{\mathbf{U}}^{k,0}_{(0)}$. The sought J-GRP solutions along the t-axis at time $t=\tau$ are the Godunov states of the J-CRP (2.47) with initial data $\hat{\mathbf{Q}}^k_{(0)}(\tau)$, with $k=1,\dots,N$, and self-similar solutions $\mathbf{D}^k(x/t)$, namely

$$\mathbf{Q}^k_V(\tau)=\mathbf{D}^k(0)\,,\quad k=1,\dots,N\,. \tag{2.50}$$

Assuming subcritical flow, the values $\mathbf{Q}^k_V(\tau)$ are the N states $\mathbf{Q}^k_*$ described in Section 2.2.3, namely

$$\mathbf{Q}^k_V(\tau)=\mathbf{Q}^k_*\,,\quad k=1,\dots,N\,. \tag{2.51}$$

We call the present method the MT-HEOC solver for the J-GRP, which extends the MT-HEOC solver for the GRP to the J-GRP. In the evolution stage of the MT-HEOC solver for the GRP, one applies an implicit Taylor series expansion to the left and right boundary extrapolated values, up to time $t=\tau$; this part gives left and right evolved values that are the initial conditions for a CRP. The solution along the t-axis of the GRP at time $t=\tau$ is then the Godunov state of the CRP. The natural generalization of the evolution stage of the MT-HEOC solver for the J-GRP is to apply an implicit Taylor series expansion on each vessel at the vertex V up to time $t=\tau$; this part gives evolved values that are the initial conditions for a J-CRP. The solutions along the t-axis of the J-GRP at time $t=\tau$ are then the Godunov states of a J-CRP.

See Figure 2.4 for an illustration of the MT-HEOC solver for the J-GRP where we have $N=3$ vessels. We use the implicit Taylor expansion to evolve the extrapolated values and find the evolved values $\hat{\mathbf{Q}}^1_{(0)}(\tau),\hat{\mathbf{Q}}^2_{(0)}(\tau)$ and $\hat{\mathbf{Q}}^3_{(0)}(\tau)$. We then solve a J-CRP and find the solutions along the t-axis $\mathbf{Q}^1_V(\tau),\mathbf{Q}^2_V(\tau)$ and $\mathbf{Q}^3_V(\tau)$.

We point out that our new method requires the solution of a non-linear problem for each k-th vessel with a total number of N non-linear problems of $m(M+1)$ unknowns, where N, m and M are respectively the total number of vessels, the number of components of the conserved variable $\mathbf{Q}$ and the order of the polynomials obtained by a reconstruction procedure. We remark that implicit solvers for the GRP and J-GRP are more costly than explicit ones and should only be used for problems that are known or suspected to be stiff.

Spatial Reconstruction

The spatial reconstruction is a crucial ingredient of the ADER finite volume methods. In the presence of boundaries, one has to take into account the lack of information given by the limited space. For instance, for a junction of three vessels, we do not have enough data to apply a classical three stencils WENO reconstruction [Dumbser 2007a] near the boundaries.

Borsche and Kall in [Borsche 2014a] described a method that permits to fill the corresponding ghost cells using the information gained from the time derivatives of the Godunov states using either the Castro-Toro or the Toro-Titarev solver for the J-GRP. The same authors in [Borsche 2016] pointed out that in the explicit HEOC solver it is not possible to apply the same procedure as for the CT or the TT since we do not calculate the time derivatives of the Godunov states but rather directly evaluate the solutions of the J-GRP at time $t=\tau$. In the DET solver for the J-GRP, Müller and

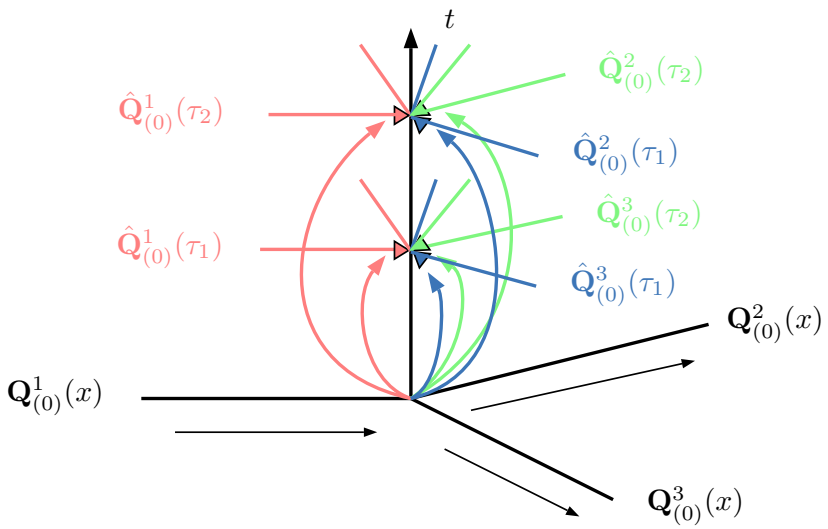

Figure 2.5: Three-vessel J-GRP using the MT-HEOC solver. In this illustration we use $N_{Gauss} = 2$ Gaussian quadrature points. We evolve the limiting value at vertex V up to time τ_1 for each vessel, and then solve a J-CRP. The solutions along the t-axis are used to approximate the junction-numerical flux in (2.52) for each vessel. We repeat the procedure for time τ_2.

Blanco [Müller 2015a] proposed to fill the ghost cells using the spatial derivatives obtained from the implicit Discontinuous Galerkin prediction for solving the GRP. In this way, the inverse Cauchy-Kowalewskaya functionals used by Borsche and Kall [Borsche 2014a] are avoided, and therefore the methodology can be applied to hyperbolic systems with non-invertible Jacobian matrices.

The MT-HEOC solver for the J-GRP gives more spatial information than its explicit version. In fact, by applying an implicit Taylor expansion, we evolve up to a certain time $t = \tau$ the extrapolated value of the reconstructed polynomial and its derivatives. Therefore, we should be able to apply the methodology proposed by Müller and Blanco [Müller 2015a]. As a matter of fact, the MT-HEOC solver replaces the numerical prediction of the DET solver with an implicit Taylor series expansion [Toro 2015a]. However, here we use a one-sided WENO reconstruction approach [Tan 2010], following the HEOC solver in [Borsche 2016]. The drawback of using a one-sided WENO reconstruction, compared to the use of filled ghost cells, is the requirement of a minimum number of cells for each sub-domain. Indeed, to apply a $k-$th order scheme, we require at least k computational cells for each sub-domain.

Algorithm for evolving the solution in the complete network

Here we provide an algorithm to evolve the solution in the complete network, from time t^n to t^{n+1}, using a high-order ADER scheme with the MT-HEOC solver for both the J-GRP and the GRP. To approximate the time integrals of the junction-numerical fluxes in (2.35), we use the classical Gaussian quadrature rule with N_{Gauss} time quadrature points.

1. For each vertex V with N connected vessels, compute the junction-numerical fluxes located

at the vertex V

$$\mathbf{F}_V^k = \frac{1}{\Delta t}\int_{t^n}^{t^{n+1}} \mathbf{F}(\mathbf{Q}_V^k(\tau))\mathrm{d}\tau \approx \sum_{h=1}^{N_{Gauss}} \omega_h \mathbf{F}(\mathbf{Q}_V^k(\tau_h)) \,, \quad k = 1,\dots,N \,, \tag{2.52}$$

applying the following procedure:

(a) for $k = 1,\dots,N$ use a WENO one sided reconstruction procedure to obtain polynomials $\mathbf{Q}_{(0)}^k(x)$ at the junction interface;

(b) for $h = 1,\dots,N_{Gauss}$

i. for $k = 1,\dots,N$, apply an implicit Taylor expansion for each extrapolated value at the junction and find the evolved values $\hat{\mathbf{Q}}_{(0)}^k(\tau_h)$, as explained in Section 2.2.2;

ii. solve J-CRP (2.36) with initial data given by $\hat{\mathbf{Q}}_{(0)}^k(\tau_h)$ with $k = 1,\dots,N$, as explained in Section 2.2.3 and find $\mathbf{Q}_V^k(\tau_h)$;

iii. for $k = 1,\dots,N$ evaluate the quantity $\mathbf{F}(\mathbf{Q}_V^k(\tau_h))$;

(c) For $k = 1,\dots,N$ evaluate junction-numerical flux $\mathbf{F}_V^k$ in (2.52).

2. Apply a high-order ADER scheme to compute the numerical fluxes across interior cell interfaces and the numerical sources within the cells for each k-th vessel.

3. Update the solution from time t^n to t^{n+1} according with finite volume formula (2.11) for each k-th vessel.

See Figure 2.5 for an illustration of step 1(b) of the proposed algorithm, which has advantages and disadvantages. As pointed out in Section 2.2.4, the main disadvantage is the lack of information needed to assign to the ghost cells outside the computational domain of each vessel. This can be overcome using a one-sided WENO reconstruction [Tan 2010]. The main advantage in a HEOC-type scheme is having to solve just two types of non-linear problems: one for the evolution stage and another for the interaction of the evolved states through the J-CRP. As noted by Borsche and Kall [Borsche 2016], a HEOC-type solver is easier to implement, as compared to one proposed earlier [Borsche 2014a]. It is worth noting that the ability of the present J-GRP solver to handle supercritical flows depends on that of its underlying J-CRP solver. Therefore, as long as we use a J-CRP that assumes subcritical flows, we will be unable to deal with trans and supercritical flows in networks.

2.3 Results

In this section we thoroughly assess the performance of the proposed methods. First, we perform an empirical convergence rate study of the proposed methods for a network of vessels with a single junction. Then, we assess the performance for a problem with stiff a source term. As a final test, we apply our mathematical model and described numerical method to the physical model of [Matthys 2007b] that consists of a network of 37 compliant silicon tubes (arteries) and 21 junctions. In the following, we shall refer to the solver of the J-GRP proposed by Borsche and Kall [Borsche 2014a] as the Borsche-Kall (BK) solver. Throughout this section, we shall also consider fully or partially high-order ADER methods. By *fully* high order we mean applying a high-order

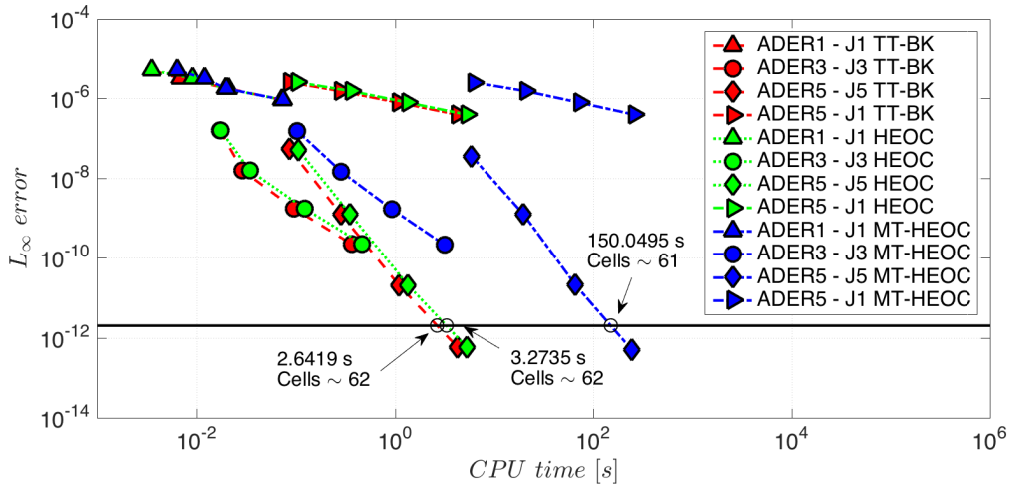

Figure 2.6: Efficiency plot: L_∞ errors against computational times. Comparison between first, third and fifth-order ADER schemes with TT-BK, HEOC and MT-HEOC solvers for GRP and J-GRP is shown. Results for the fifth-order ADER scheme in the interior of the domain with a first-order scheme at the junction are also shown. Numerical results were obtained with meshes of $10, 20, 40, 80$ cells. The intersections between the horizontal line $E = 2\times10^{-12}$ (prescribed error) and the fifth-order ADER schemes give the computational times and number of cells required to attain the prescribed error E.

ADER method within the domain coupled to a high-order numerical approximation at junctions. By *partially* high order we mean applying a high-order ADER method within the domain coupled to a first-order numerical approximation at junctions.

2.3.1 Empirical convergence rate studies

To assess the order of convergence of the ADER scheme with the MT-HEOC solver for both the J-GRP and the GRP when solving balance laws in networks of vessels, we designed a test which is highly sensitive to the numerical treatment of the J-GRP. From this test, we expect the order of the method to depend on the order of the approximation of the junction-numerical fluxes. For instance, using a fifth-order solver within the domain, that is, a fifth-order solver for the numerical fluxes across interior cell interfaces and for the numerical sources within each cell, and a first-order solver for the junction-numerical fluxes, we expect the global error of the method to be of order one.

Here we manufactured a problem with exact solution by prescribing the following smooth vector-valued function

$$\tilde{\mathbf{Q}}(x,t) = \begin{bmatrix} A(x,t) \\ A(x,t)u(x,t) \end{bmatrix} = \begin{bmatrix} \tilde{A} + \tilde{a}\sin(\frac{2\pi}{L}x + \phi)\cos(\frac{2\pi}{T_0}t) \\ 0 \end{bmatrix} . \tag{2.53}$$

Then, inserting it in (2.5), we obtained a modified non-linear system

$$\partial_t \tilde{\mathbf{Q}} + \partial_x \mathbf{F}(\tilde{\mathbf{Q}}, x) - \mathbf{S}(\tilde{\mathbf{Q}}, x) = \tilde{\mathbf{S}}(\tilde{\mathbf{Q}}, x, t) , \tag{2.54}$$

for which $\tilde{\mathbf{Q}}(x,t)$ is the exact smooth solution, and the explicit formula for $\tilde{\mathbf{S}}(\mathbf{Q},x,t)$ can be calculated by using a symbolic manipulator. The prescribed function $A(x,t)$ in (2.53) is product of trigonometric

Scheme	Cells	TT-BK E_∞	TT-BK O_∞	TT-BK $t_{CPU}[s]$	HEOC E_∞	HEOC O_∞	HEOC $t_{CPU}[s]$	MT-HEOC E_∞	MT-HEOC O_∞	MT-HEOC $t_{CPU}[s]$
ADER1 - J1	10	5.1069e-06		0.004	5.1069e-06		0.004	5.1069e-06		0.006
	20	3.2013e-06	0.6738	0.007	3.2013e-06	0.6738	0.009	3.2013e-06	0.6738	0.012
	40	1.7717e-06	0.8535	0.021	1.7717e-06	0.8535	0.020	1.7717e-06	0.8535	0.020
	80	9.2545e-07	0.9369	0.071	9.2545e-07	0.9369	0.072	9.2545e-07	0.9369	0.074
ADER2 - J2	10	5.4495e-07		0.011	5.0373e-07		0.010	5.1298e-07		0.019
	20	1.6146e-07	1.7549	0.015	1.6387e-07	1.6201	0.016	1.6506e-07	1.6359	0.038
	40	4.3208e-08	1.9018	0.039	4.3361e-08	1.9181	0.047	4.3429e-08	1.9263	0.134
	80	1.1546e-08	1.9039	0.143	1.1558e-08	1.9075	0.172	1.1544e-08	1.9116	0.521
ADER3 - J3	10	1.5862e-07		0.017	1.5711e-07		0.017	1.5346e-07		0.103
	20	1.5786e-08	3.3289	0.029	1.5482e-08	3.3431	0.034	1.4565e-08	3.3973	0.285
	40	1.7507e-09	3.1727	0.095	1.7299e-09	3.1618	0.122	1.6508e-09	3.1413	0.926
	80	2.2162e-10	2.9817	0.362	2.2288e-10	2.9564	0.464	2.1449e-10	2.9442	3.117
ADER4 - J4	10	5.8856e-08		0.017	5.5043e-08		0.017	6.7511e-08		0.416
	20	5.8862e-09	3.3218	0.044	5.8208e-09	3.2413	0.051	5.9532e-09	3.5034	1.343
	40	3.1375e-10	4.2296	0.154	3.1273e-10	4.2182	0.187	3.1478e-10	4.2413	4.209
	80	2.6169e-11	3.5837	0.585	2.6156e-11	3.5797	0.725	2.6347e-11	3.5786	14.342
ADER5 - J5	10	5.4857e-08		0.085	5.0963e-08		0.105	3.5734e-08		5.872
	20	1.2590e-09	5.4453	0.281	1.2550e-09	5.3437	0.349	1.2410e-09	4.8477	19.642
	40	2.0719e-11	5.9252	1.083	2.0704e-11	5.9217	1.340	2.0814e-11	5.8978	65.940
	80	5.7770e-13	5.1645	4.242	5.7776e-13	5.1633	5.261	5.0423e-13	5.3673	243.375
ADER2 - J1	10	3.5206e-06		0.009	3.4324e-06		0.011	3.4821e-06		0.021
	20	1.6697e-06	1.0762	0.014	1.6639e-06	1.0447	0.020	1.6657e-06	1.0638	0.035
	40	8.0363e-07	1.0550	0.037	8.0313e-07	1.0509	0.045	8.0332e-07	1.0521	0.132
	80	3.9097e-07	1.0395	0.142	3.9092e-07	1.0388	0.166	3.9081e-07	1.0395	0.519
ADER3 - J1	10	2.7055e-06		0.014	2.6961e-06		0.018	2.9330e-06		0.104
	20	1.5264e-06	0.8257	0.025	1.5261e-06	0.8210	0.032	1.5561e-06	0.9145	0.287
	40	7.7481e-07	0.9782	0.093	7.7475e-07	0.9781	0.120	7.7862e-07	0.9989	0.947
	80	3.8670e-07	1.0026	0.360	3.8668e-07	1.0026	0.467	3.8719e-07	1.0079	3.140
ADER4 - J1	10	2.5458e-06		0.020	2.5457e-06		0.018	2.5619e-06		0.400
	20	1.5196e-06	0.7444	0.041	1.5195e-06	0.7444	0.050	1.5187e-06	0.7544	1.365
	40	7.8148e-07	0.9595	0.146	7.8144e-07	0.9594	0.186	7.8118e-07	0.9591	4.385
	80	3.9079e-07	0.9998	0.575	3.9079e-07	0.9998	0.727	3.9072e-07	0.9995	15.030
ADER5 - J1	10	2.5562e-06		0.085	2.5544e-06		0.102	2.5320e-06		6.151
	20	1.5317e-06	0.7389	0.278	1.5315e-06	0.7381	0.359	1.5322e-06	0.7247	20.685
	40	7.8625e-07	0.9620	1.076	7.8618e-07	0.9620	1.341	7.8642e-07	0.9622	72.496
	80	3.9326e-07	0.9995	4.214	3.9324e-07	0.9995	5.249	3.9330e-07	0.9996	259.115

Table 2.1: Convergence rates study. The left column shows the various combinations of schemes used, the second column shows the meshes defined by the number of cells, the third to fifth columns show different GRP and J-GRP. For column TT-BK we show the L_∞ errors, the L_∞ order and the correspondent computational times in seconds; likewise for HEOC and the MT-HEOC. All numerical simulations were performed in an Intel Core i7-2600 with 4 cores (3.40 GHz clock speed). The code was not parallelized for these simulations. The order is spoiled when we use a first-order method at the junction.

functions, periodic in time and space with period T_0 and L respectively, and smooth at the junction,

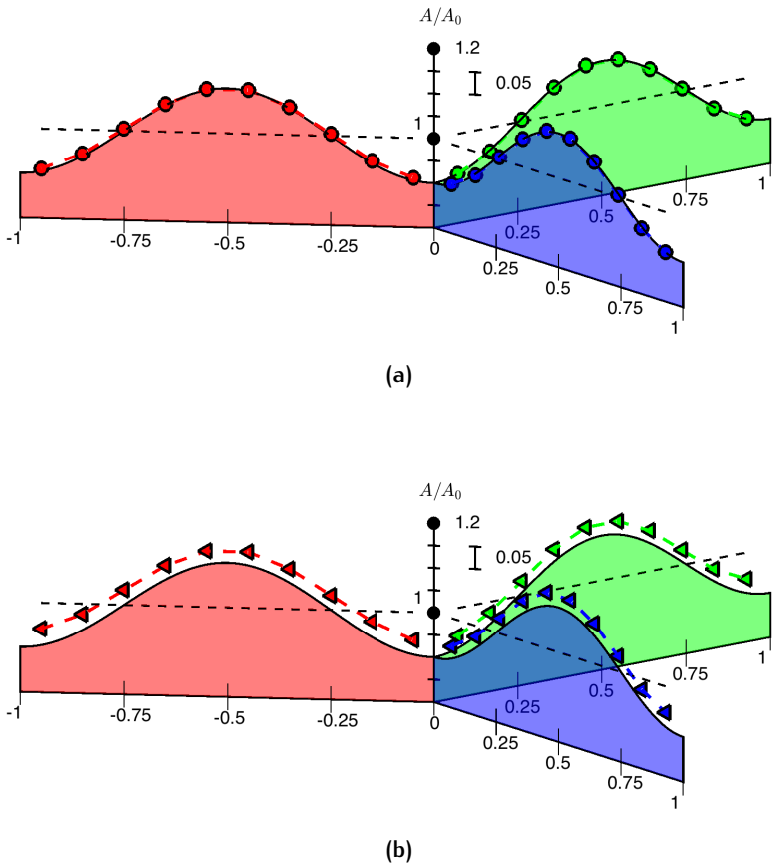

Figure 2.7: Illustration of the empirical convergence rate study. The normalized cross-sectional area $\frac{A}{A_0}$ is depicted in the z variable. The dotted and the shaded plot depict the numerical and the exact solution respectively. We used 10 cells for each vessel and we stopped the simulation after $100.5\ s$. The ADER scheme with the MT-HEOC solver was used. Frame (a): numerical solution obtained by the fully third-order scheme. Frame (b): numerical solution obtained by the partially third-order scheme.

namely it satisfies $\partial_x^{(j)} A(0,t) = \partial_x^{(j)} A(L,t)$ with $j = 0,\dots,M$ for any time. Moreover, as $A(0,t) = A(L,t) = \tilde{A}$ and $u(0,t) = u(L,t) = 0$, the prescribed functions $A(x,t)$ and $u(x,t)$ satisfy the coupling conditions ϕ for blood flow (2.38) for $t \geq 0$.

The empirical convergence rate test was performed on a network of $N = 3$ vessels with one junction. We considered the three vessels with local coordinate $[a^1,b^1] = [-1,0]$, and $[a^2,b^2] = [a^3,b^3] = [0,1]$, and vertex V located in 0. The initial condition for the numerical test was given by the described function $\tilde{\mathbf{Q}}(x,t)$ at time $t = 0$. We considered constant parameters K, A_0, external pressure $p_e = 0$ and friction resistance $f = 0$, so that the source term $\mathbf{S}(\mathbf{Q},x)$ was set to zero. Since the prescribed function $A(x,t)$ in (2.53) is periodic in space, we used periodic boundary conditions away from the junction. Vessel parameters are: $m = {}^1/_2$, $n = 0$, cross-sectional radius at

equilibrium $r_0 = 10\ mm$, cross-sectional area at equilibrium $A_0 = \pi r_0^2$, Young modulus $E = 0.4\ MPa$, wall-thickness at equilibrium $h_0 = 1.1\ mm$, length $L = 1\ m$. Computation parameters are: $T_0 = 1\ s$, $\tilde{A} = A_0$, $\tilde{a} = 0.1A_0$, $\phi = \frac{\pi}{2}$, output time $t_{end} = 0.5\ s$, Courant number coefficient $CFL = 0.9$. Since the three vessels have the same material properties and computation parameters, the smoothness at the junction of the prescribed function $A(x,t)$ is assured. We compared results given by the TT and the BK solver for the GRP and the J-GRP respectively, the HEOC and the MT-HEOC solver for both the GRP and the J-GRP. We used the HLL [Harten 1983] method to compute the numerical fluxes within each vessels, instead of solving exactly the CRP.

Table 2.1 shows empirical convergence rates for schemes of first to fifth accuracy in space and time. The first column of Table 2.1 shows the various combinations of schemes used, the second column shows the meshes defined by the number of cells, the third to fifth columns show different GRP and J-GRP. For column TT-BK, we show the L_∞ errors, the L_∞ order and the computational times in seconds; likewise for HEOC and the MT-HEOC. Orders from one to five are attained as desired. It is worth noting two points. First, the order of accuracy in space and time is spoiled whenever we use a first-order approximation of the junction-numerical fluxes. For instance, when we use the combination ADER5 - J1 with any of the solvers presented in Table 2.1, the accuracy decreases from five to one; likewise with other combinations. Therefore, even though we use a high-order scheme within each sub-domain but a first-order approximation of the junction-numerical fluxes, the overall accuracy in space-time is ruined. This means that low-order errors travel through the network when low-order schemes are used at junctions. Second, the implicit Taylor series expansion plays an important role in the computational cost. Indeed, there is a difference in the computational times between the numerical results obtained by using the explicit solvers TT-BK and HEOC, and the implicit solver MT-HEOC.

Figure 2.6 depicts L_∞ errors against computational times. Comparison between first, third and fifth-order ADER schemes with TT-BK, HEOC and MT-HEOC solvers for GRP and J-GRP are shown. Also shown are results for the fifth-order ADER scheme in the interior of the domain with a first-order scheme at the junction. For the computation we used meshes of $10, 20, 40, 80$ cells. The point of this figure is to assess the performance of the schemes by relating the error to the computational cost. For example, prescribing the error $E = 2 \times 10^{-12}$, the computational times needed for the ADER scheme to attain that specific error are $2.6419\ s$, $3.2735\ s$ and $150.0495\ s$ using respectively the TT-BK, HEOC and the MT-HEOC solvers. Note that a first-order method would have attained that error at the computational time of $\sim 130\ years$; such figure is obtained by extrapolation, which is probably an underestimate. These observations support the use of high-order methods for hyperbolic balance laws, when small errors are aimed for. The results also show that the combination ADER5 - J1 completely ruins the accuracy while maintaining the computational cost given by a fifth-order method. This suggests that the time to attain the above-mentioned error with a partially high-order method is even larger than that of a first-order method throughout. For instance, ADER5 - J1 with the implicit MT-HEOC solver would have attained that error at the computational time of $\sim 98\ centuries$.

Figure 2.7 depicts the normalized cross-sectional area $\frac{A}{A_0}$ for the exact solutions (shaded plot) and the numerical solutions (dotted line) for the three vessels at the output time. Frames 2.7a and 2.7b depict the numerical solutions from the fully and partially third-order ADER scheme with the MT-HEOC solver, respectively. The results show that a first order at the junction spoils the

accuracy throughout the space-time domain.

From the empirical convergence rate studies, we conclude that it is imperative to use high-order numerical schemes at junctions, in order to preserve the desired high-order of accuracy in the full computational domain.

2.3.2 A stiff problem for a junction

Following the work of Müller et al. [Müller 2012], we say that a source term is stiff when

$$\Delta x \frac{\max_i \left(|\beta_i|\right)}{\max_i \left(|\lambda_i|\right)} > 1 \,, \tag{2.55}$$

where Δx, β_i and λ_i are the spatial mesh size, the i-th eigenvalue of the Jacobian of the source term $\frac{\partial \mathbf{S}(\mathbf{Q})}{\partial \mathbf{Q}}$ and of the physical flux $\frac{\partial \mathbf{F}(\mathbf{Q})}{\partial \mathbf{Q}}$ respectively, see also [Dumbser 2008]. In the one-dimensional blood flow equations, assuming constant parameters and zero external pressure, source term (2.7) reads

$$\mathbf{S}(\mathbf{Q}) = \begin{bmatrix} 0 \\ -R\frac{q}{A} \end{bmatrix} \,, \tag{2.56}$$

where $R = \gamma\pi\frac{\mu}{\rho}$. The eigenvalues of (2.56) are $\beta_1 = 0$ and $\beta_2 = -\frac{R}{A}$. Condition (2.55) can be written as

$$\Delta x \frac{R}{A \max_i(|\lambda_i|)} > 1 \,. \tag{2.57}$$

As pointed out by Müller et al. [Müller 2012], source term (2.56) may become stiff under physiological conditions. If the cross-sectional area A approaches zero, then ratio (2.57) increases arbitrarily leading to a stiff problem. This happens routinely in veins: they are highly compliant and collapse easily under physiological situations.

To test the capability of the ADER scheme with the MT-HEOC solver for both the GRP and the J-GRP to deal with stiff source terms, we considered a network of $N = 3$ arteries with one junction. Although arteries do not collapse under physiological conditions because they are stiffer and designed to endure high pressure from the pumping action of the heart, we could still simulate a problem in the stiff regime assuming condition (2.57) and appropriately adjusting the cross-sectional area of the initial condition.

We considered three vessels with local coordinate $[a^1, b^1] = [-1, 0]$, and $[a^2, b^2] = [a^3, b^3] = [0, 1]$, and vertex V located in 0. The initial condition for the cross-sectional area A for the first vessel was

$$A(x,0) = 0.1A_0 + A_0 e^{-100\left(x-0.5\right)^2} \,, \tag{2.58}$$

while for the other vessels was $A(x,0) = 0.1A_0$. See Frame 2.8b shows $A(x,0)$ in the three vessels at the initial time. For each vessel we set $u(x,0) = 0$. Vessels parameters are: $m = {}^1/_2$, $n = 0$, length $L = 1$ m, cross-sectional radius at equilibrium $r_0 = 0.1$ mm, cross-sectional area at equilibrium $A_0 = \pi r_0^2$, Young modulus $E = 0.4$ MPa, wall-thickness at equilibrium $h_0 = 1.1$ mm, resistance defined in (2.56) $R = 8\pi\frac{\mu}{\rho}$ and dynamic viscosity $\mu = 2.5$ $mPas$. Computation parameters are: output time $t_{end} = 2$ s, 100 cells, Courant number coefficient $CFL = 0.9$. Transmissive boundary conditions was used away from the junction. With the given parameters, ratio (2.57) at the junction varies in time from 3 to 7 and results in a stiff problem.

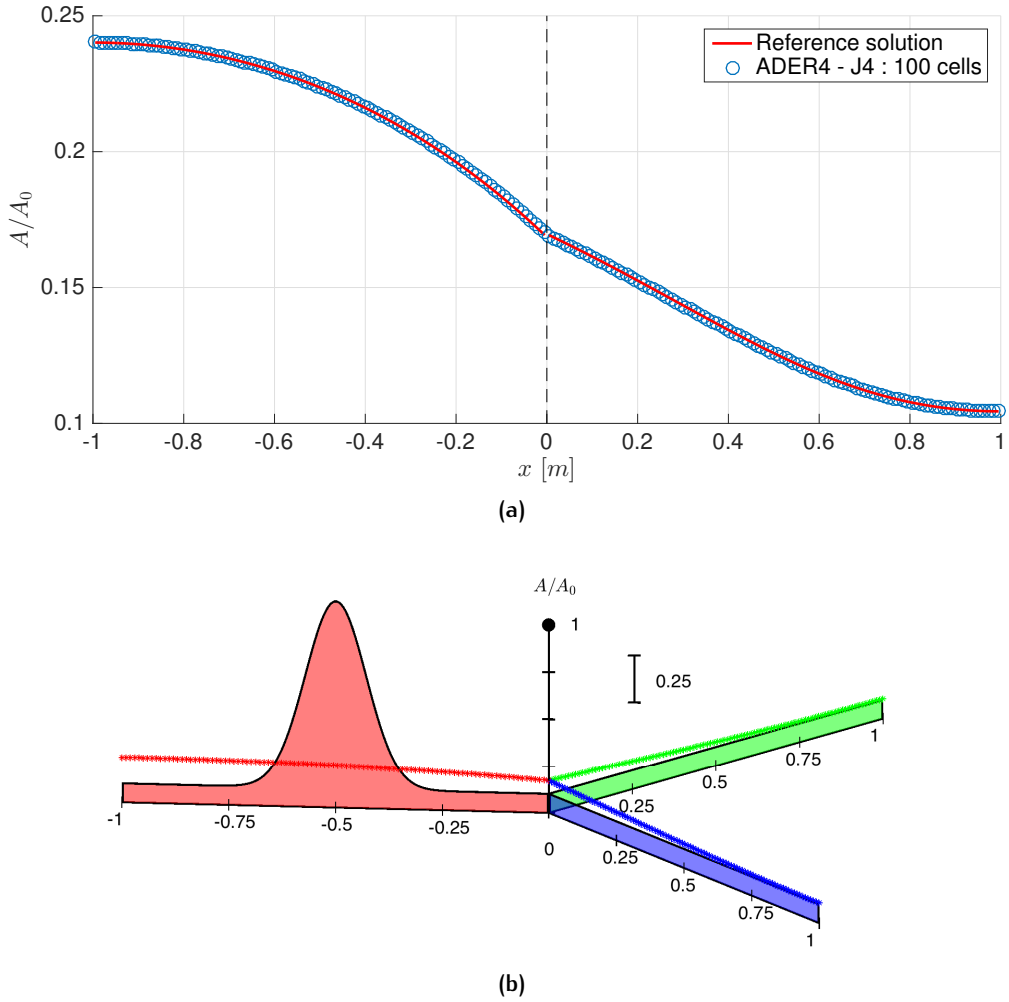

Figure 2.8: A stiff problem connecting three vessels at a single junction. The fourth-order ADER scheme with the MT-HEOC solver for both the GRP and J-GRP was used. Frame (a): the normalized cross-sectional area $\frac{A}{A_0}$ at the fixed time $t_{end} = 2\ s$ as a function of axial distance is depicted for each vessel. Note that the vertical line at $x = 0$ represents the junction position. The normalized cross-sectional area of one vessel is depicted in $[-1, 0]$, while the remaining two are coincident and are depicted in $[0, 1]$. The numerical solutions with 100 cells for each vessel is shown by ○, while a reference solution computed with a first-order method using 2000 cells for each vessel is shown by ——. Frame (b): illustration of the initial condition and computed results. The initial condition is depicted by the shaded graph, while the solution at the output time is shown by the single lines.

Frame 2.8a shows computed results for a fourth-order ADER scheme with the MT-HEOC solver for both the GRP and J-GRP. Satisfactory agreement is seen between the computed solution ○ and a reference solution obtained with a first-order method with a fine grid of 2000 cells ——. See legend of 2.8a for further information. It is worth remarking that for this test problem, if one uses an explicit solver for the J-GRP, the simulation fails after few time steps. This observation emphasizes

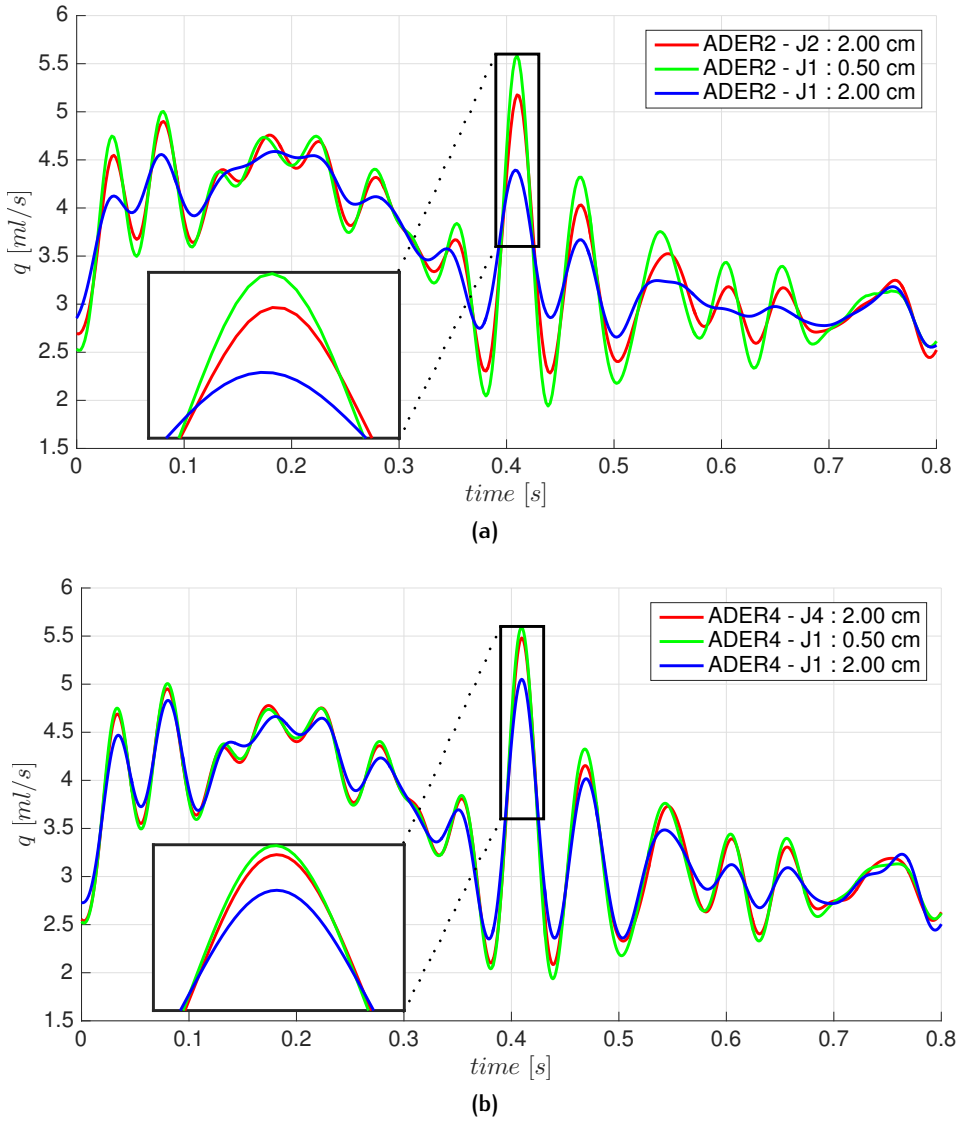

Figure 2.9: Computed flow $q(x,t)$ at midpoint of left renal artery. The ADER scheme with the MT-HEOC solver for both the GRP and J-GRP was used. Frame (a): comparison between fully and partially second-order methods with different mesh sizes. Frame (b): comparison between fully and partially fourth-order methods with different mesh sizes.

that in the stiff regime the use of a locally implicit solver is mandatory. See Frame 2.8b for an illustration of the initial condition and the computed results.

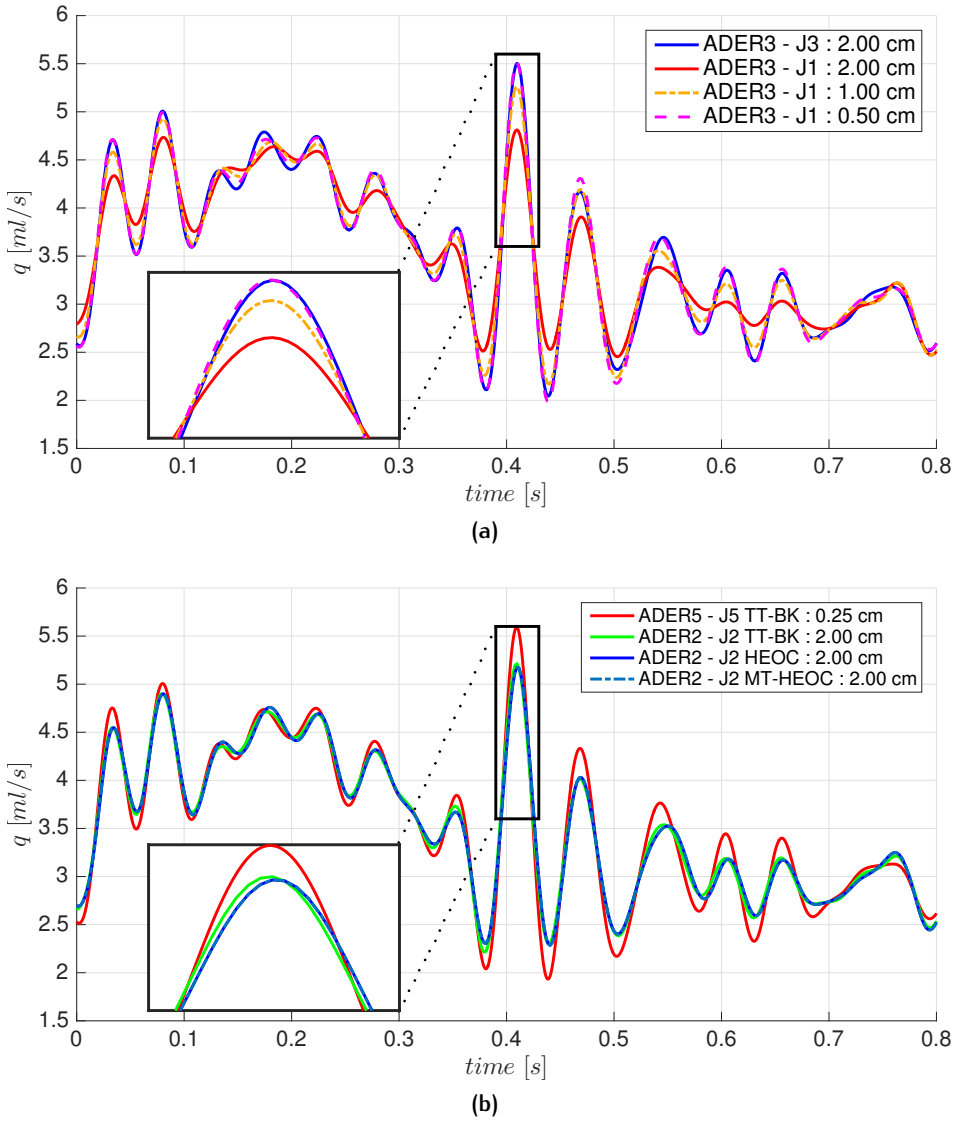

Figure 2.10: Computed flow $q(x,t)$ at midpoint of left renal artery. Frame (a): the ADER scheme with the MT-HEOC solver for both the GRP and J-GRP was used. Comparison between fully and partially third-order methods with different mesh sizes. Frame (b): comparison between fully second-order schemes with different solvers, with a fixed mesh size. A reference solution is also shown (ADER5 - J5 TT-BK : 0.25 cm).

2.3.3 Application to a network of arteries

In this section, we consider the model network of major arteries presented by Matthys et al. [Matthys 2007b], composed of 37 tubes that represent arteries, a pump that resembles the outflow of blood from the heart and terminal resistances. Mechanical properties of each vessel, terminal resistances, network geometry, and inflow measured at the root of ascending aorta are given in

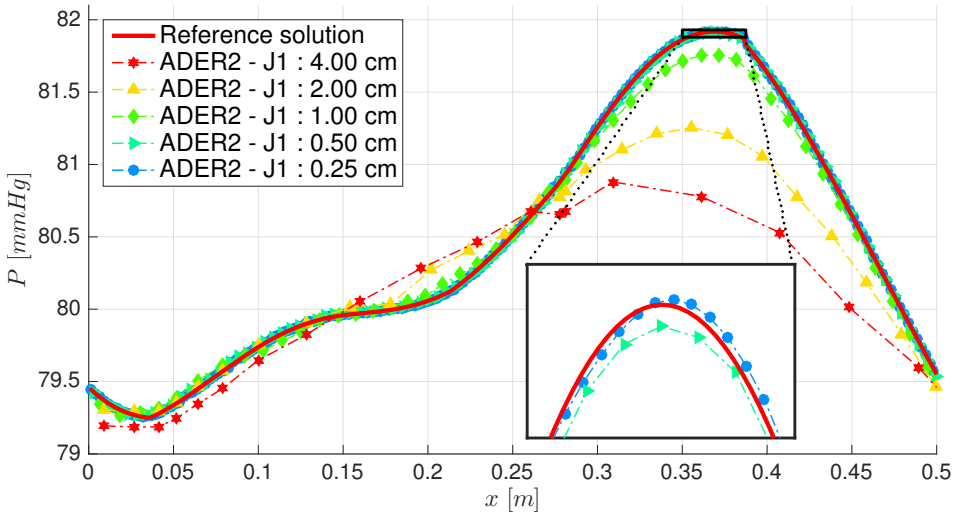

(a)

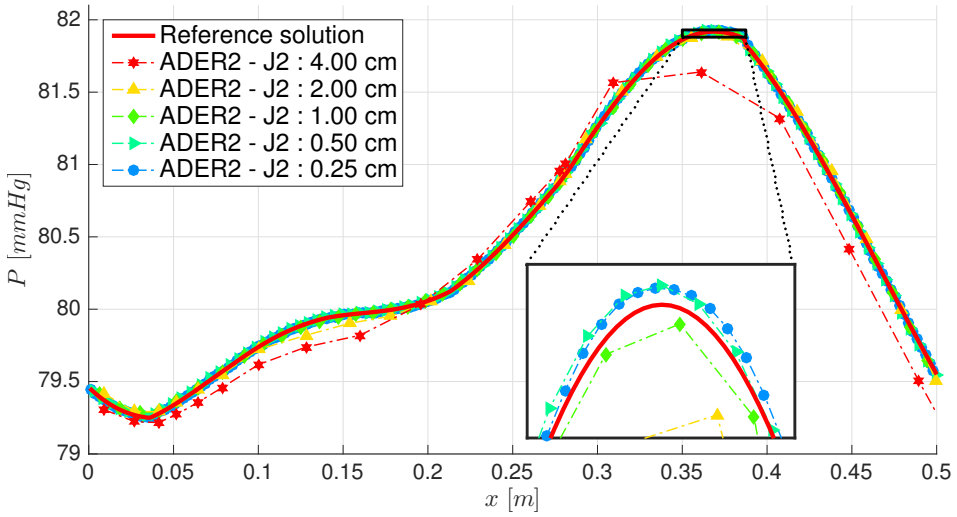

(b)

Figure 2.11: Computed pressure along the aorta and part of the right iliac femoral (vessel no. 1, 8, 10, 15, 17, 23, 25, 27, 28 of model in [Matthys 2007b]). The fully and partially second-order ADER schemes with the MT-HEOC solver were used. Mesh size runs from 0.25 *cm* to 4 *cm*. A reference solution from a fully fifth-order ADER scheme with a mesh size of 0.125 *cm* is depicted. Frame (a): numerical results with a fully second-order method are shown. Frame (b): numerical results with a partially second-order method are shown.

[Matthys 2007b, Matthys 2007a].

In the physical model of Matthys et al. [Matthys 2007b], the cross-sectional area at equilibrium A_0 varies along the vessel length and this requires the use of well-balanced schemes. Non well-balanced schemes may give wrong numerical results as pointed out in [Müller 2013c]. The current version of our scheme is not strictly well-balanced. Therefore, we have slightly modified the physical

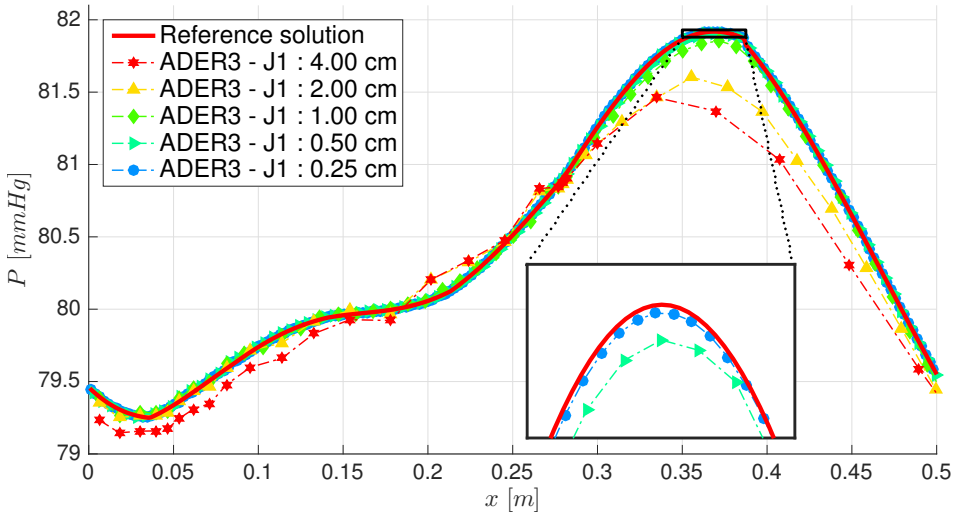

(a)

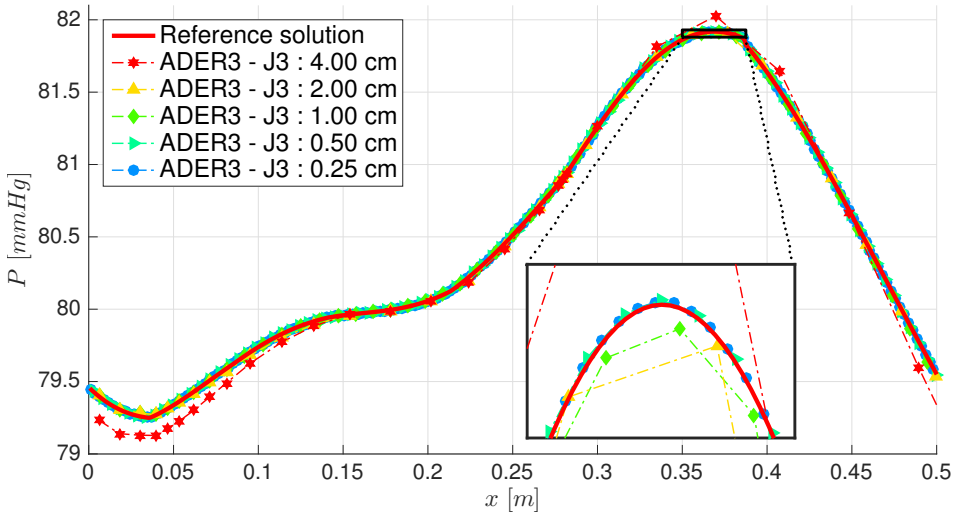

(b)

Figure 2.12: Computed pressure along the aorta and part of the right iliac femoral (vessel no. 1, 8, 10, 15, 17, 23, 25, 27, 28 of model in [Matthys 2007b]). The fully and partially third-order ADER schemes with the MT-HEOC solver were used. Mesh size runs from 0.25 cm to 4 cm. A reference solution from a fully fifth-order ADER scheme with a mesh size of 0.125 cm is also depicted. Frame (a): numerical results with a fully third-order method are shown. Frame (b): numerical results with a partially third-order method are shown.

model of Matthys et al. [Matthys 2007b] by neglecting the taper of tubes and taking mean values for parameters, for each vessel.

Computations were performed using $CFL = 0.9$, the inflow boundary condition and terminal resistances was treated as in [Matthys 2007a], and the tube law was purely elastic. The number of

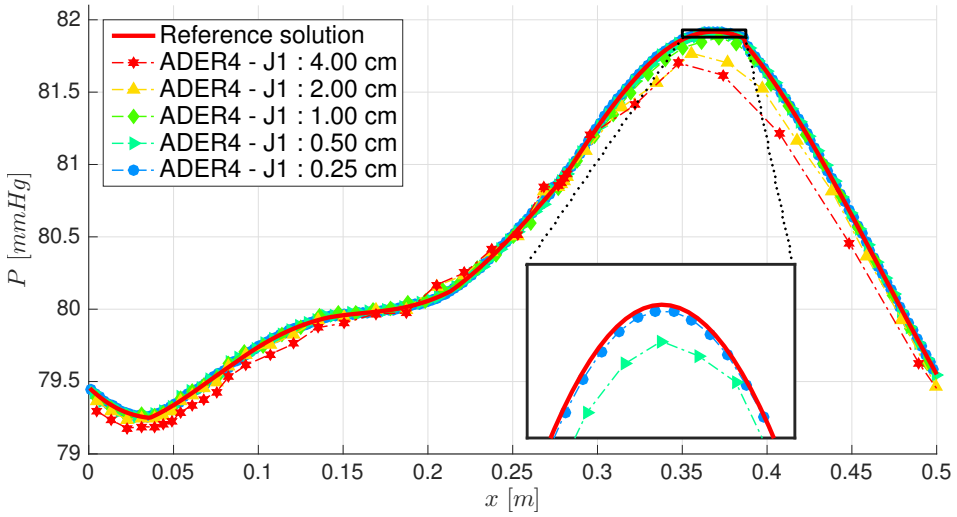

(a)

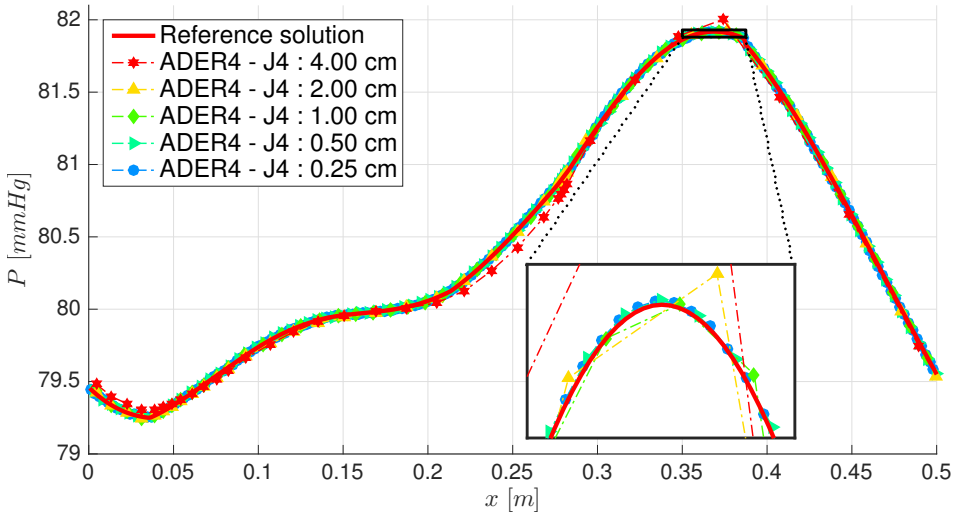

(b)

Figure 2.13: Computed pressure along the aorta and part of the right iliac femoral (vessel no. 1, 8, 10, 15, 17, 23, 25, 27, 28 of model in [Matthys 2007b]). The fully and partially fourth-order ADER schemes with the MT-HEOC solver were used. Mesh size runs from 0.25 cm to 4 cm. A reference solution from a fully fifth-order ADER scheme with a mesh size of 0.125 cm is also depicted. Frame (a): numerical results with a fully fourth-order method are shown. Frame (b): numerical results with a partially fourth-order method are shown.

cells M_{cells} for each vessel was chosen according to

$$M_{cells} = max(floor(L/\Delta x_{max}), ord) \,, \tag{2.59}$$

where L is the length of the vessel, Δx_{max} is the maximal space size (e.g. 0.02 m) and ord is the order

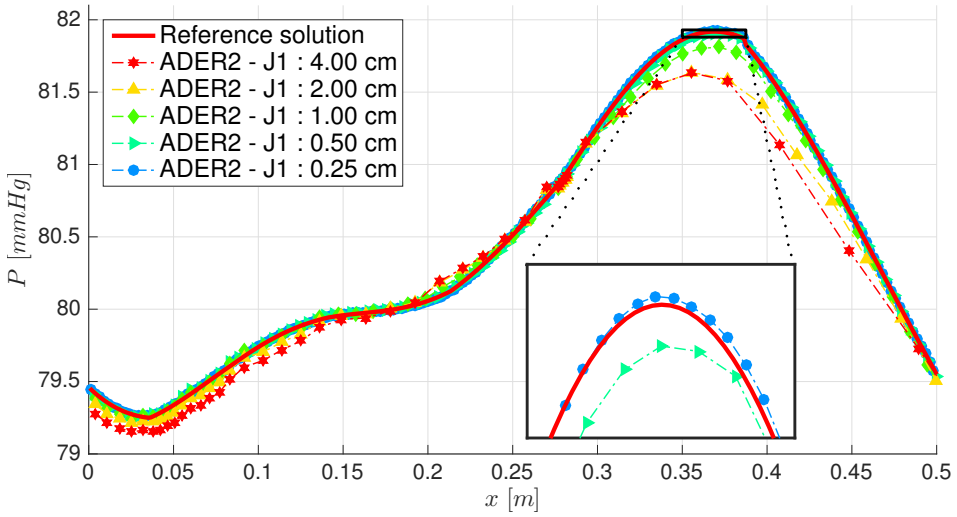

(a)

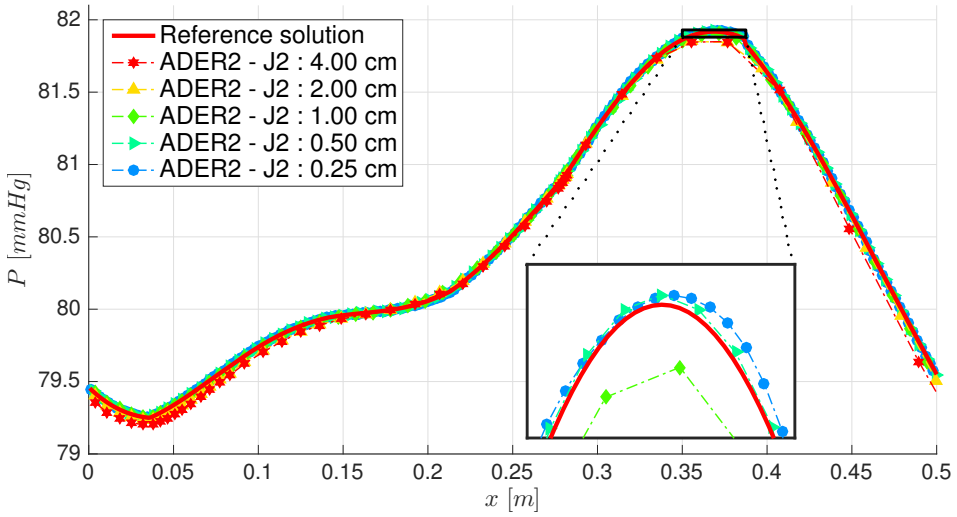

(b)

Figure 2.14: Computed pressure along the aorta and part of the right iliac femoral (vessel no. 1, 8, 10, 15, 17, 23, 25, 27, 28 of model in [Matthys 2007b]). The fully and partially second-order ADER schemes with the MT-HEOC solver were used. Mesh size runs from 0.25 cm to 4 cm. The minimum number of cells was 5. A reference solution from a fully fifth-order ADER scheme with a mesh size of 0.125 cm is depicted. Frame (a): numerical results with a fully second-order method are shown. Frame (b): numerical results with a partially second-order method are shown.

of the numerical method. Throughout the results we only refer, for instance, to 2 cm to indicate $\Delta x_{max} = 0.02\ m$. Numerical results obtained with fully and partially high-order methods with the same order of accuracy, have the same spatial mesh size. Accordingly to the above-mentioned criterion, the mesh is different for each order of accuracy. Therefore, caution is required in assessing

the numerical results obtained with different orders.

Another way to proceed with the assessment of results from high-order methods, in our case from one to five, is to impose a minimum number of cells which is common for all orders; in the present case the minimum is five. To do so we utilize the following procedure

$$M_{cells} = max(floor(L/\Delta x_{max}), 5) \; . \tag{2.60}$$

However there is a drawback with this approach. As the mesh is already fine enough, the differences between fully and partially high-order approximations are not clearly manifested in the results. In other words, the fine mesh has masked the high-order effect of the methods. Such phenomena is more evident for the schemes in the high-order range. Throughout this chapter, the default criterion is given by (2.59), unless specified.

Figures 2.9 and 2.10 show the computed flow $q(x,t)$ of the left renal artery after 20 cardiac cycles and the maximum flow peak at cardiac reference time 0.4 s. For Figure 2.9 and Frame 2.10a, we used ADER methods of different orders, with the MT-HEOC solver. Frame 2.9a compares fully and partially second-order methods. A first-order method at junctions spoils the accuracy in space and time with a damping effect for extrema. The fully second-order method with 2 cm —— is comparable with the partially second-order method with 0.5 cm ——. Similar results can be found for fully and partially fourth-order ADER methods in Frame 2.9b. Fully and partially third-order methods with different mesh sizes can be found in 2.10a. The partially third-order method requires a mesh size of 0.5 cm - - - to match the solution obtained with the fully third-order method with a mesh size of 2 cm ——, and the computational times per cardiac cycle are respectively 29.859 s and 9.556 s, see Table 2.2. The computational time of the partially third-order method is three times larger than the one of the fully third-order method. This observation emphasizes the better efficiency of high-order methods used at junctions. Frame 2.10b shows a comparison between different solvers. We compare the numerical results given by the TT-BK, the HEOC and the MT-HEOC solvers for the GRP and the J-GRP for a fixed mesh size of 2 cm. A reference solution given by the fifth-order ADER scheme with the TT-BK solver for the GRP and the J-GRP using a fine mesh size of 0.25 cm is also shown. All solvers give similar numerical results.

Figures 2.11 to 2.14 depict computed pressure in the aorta and part of the right iliac femoral, at the output time. Numerical results were obtained using ADER schemes of different orders, with the MT-HEOC solver. In Figure 2.14 the minimum number of cells was chosen accordingly to (2.60). A reference solution obtained using a fully fifth-order method with a fine mesh size of 0.125 cm is also shown. A first-order method at junctions spoils the accuracy of the numerical schemes insofar as first-order errors travel throughout the network of vessels with a damping effect for the pressure pulse-wave. Frames 2.11a and 2.11b show numerical results using fully and partially second-order methods, respectively. The second-order method at junctions improves the accuracy for pressure. A similar pattern is also seen with fully and partially third and fourth-order schemes; the numerical results are shown in Figures 2.12 and 2.13, respectively. The fully second and the partially fourth-order solvers using a mesh size of 2 cm are comparable. Computational times per cardiac cycle are respectively 1.621 s and 33.373 s, see Table 2.2. The computational time of the partially fourth-order method is 20 times larger than that for the fully second-order method. This suggests that accurate numerical results with less computational effort can be achieved by using high-order numerical methods at junctions. Frames 2.14a and 2.14b show numerical results using

	TT-BK		TT		HEOC				MT-HEOC			
cm	L_1	$t_{CPU}[s]$	L_1	$t_{CPU}[s]$	L_1	$t_{CPU}[s]$	L_1	$t_{CPU}[s]$	L_1	$t_{CPU}[s]$	L_1	$t_{CPU}[s]$
	ADER2 - J2		ADER2 - J1		ADER2 - J2		ADER2 - J1		ADER2 - J2		ADER2 - J1	
4.00	1.9259e-06	13.62	2.7016e-06	8.13	2.3375e-06	13.28	2.7015e-06	8.94	2.3385e-06	22.47	2.7011e-06	17.24
2.00	8.4894e-07	18.18	2.0112e-06	11.21	9.3598e-07	15.48	2.0112e-06	12.26	9.3386e-07	32.42	2.0115e-06	26.47
1.00	2.5310e-07	21.33	1.2044e-06	15.89	2.6439e-07	22.52	1.2044e-06	18.49	2.6125e-07	49.84	1.2023e-06	44.85
0.50	6.4895e-08	33.37	2.6798e-07	27.30	6.6194e-08	37.56	2.6797e-07	33.73	6.9441e-08	91.83	2.6526e-07	86.72
0.25	1.6004e-08	145.51	8.3692e-08	125.89	1.6343e-08	156.73	8.3690e-08	149.62	4.8067e-08	415.60	9.7928e-08	400.10
	ADER3 - J3		ADER3 - J1		ADER3 - J3		ADER3 - J1		ADER3 - J3		ADER3 - J1	
4.00	1.1156e-06	29.80	2.4775e-06	20.35	9.0297e-07	35.73	2.4775e-06	22.22	9.0297e-07	121.02	2.4775e-06	102.87
2.00	3.8831e-07	41.32	1.8020e-06	30.23	3.2900e-07	45.01	1.8020e-06	34.55	3.2899e-07	191.12	1.8020e-06	174.09
1.00	1.7415e-07	58.48	8.7341e-07	48.69	1.8747e-07	70.16	8.7339e-07	58.08	1.8744e-07	333.59	8.7336e-07	313.27
0.50	4.3286e-08	99.71	2.4397e-07	90.38	4.3579e-08	119.12	2.4396e-07	107.56	4.3567e-08	624.63	2.4394e-07	597.18
0.25	1.4918e-08	305.94	6.1851e-08	291.07	1.5206e-08	348.90	6.1850e-08	335.37	1.5195e-08	1953.85	6.1819e-08	1942.40
	ADER4 - J4		ADER4 - J1		ADER4 - J4		ADER4 - J1		ADER4 - J4		ADER4 - J1	
4.00	8.4933e-07	50.16	2.1885e-06	33.67	1.1062e-06	56.95	2.1885e-06	39.30	1.1062e-06	442.74	2.1885e-06	433.08
2.00	2.8120e-07	69.17	1.4788e-06	54.67	2.1396e-07	73.79	1.4788e-06	57.55	2.1396e-07	687.75	1.4788e-06	667.46
1.00	1.0004e-07	99.75	7.0308e-07	83.25	6.5577e-08	113.54	7.0306e-07	97.97	6.5577e-08	1194.90	7.0306e-07	1194.90
0.50	3.3719e-08	170.22	2.3124e-07	154.05	2.5942e-08	203.87	2.3123e-07	189.50	2.5942e-08	2315.43	2.3123e-07	2348.78
0.25	1.4633e-08	398.09	5.4277e-08	389.10	1.4077e-08	459.91	5.4276e-08	439.69	1.4077e-08	5399.23	5.4276e-08	5431.68
	ADER5 - J5		ADER5 - J1		ADER5 - J5		ADER5 - J1		ADER5 - J5		ADER5 - J1	
4.00	4.1746e-07	119.61	1.8771e-06	88.18	7.6933e-07	143.58	1.8770e-06	106.82	7.6933e-07	3834.08	1.8770e-06	3693.50
2.00	2.7524e-07	162.53	1.3384e-06	121.84	2.3790e-07	179.39	1.3384e-06	153.56	2.3790e-07	5064.60	1.3384e-06	5161.99
1.00	9.4003e-08	241.21	6.6951e-07	211.75	9.5565e-08	283.49	6.6950e-07	255.51	9.5565e-08	8564.96	6.6950e-07	9097.09
0.50	3.1106e-08	439.28	2.2883e-07	412.24	2.9227e-08	520.58	2.2882e-07	492.50	2.9227e-08	15949.96	2.2882e-07	16603.64
0.25	1.4652e-08	862.57	5.3384e-08	778.46	1.4200e-08	953.31	5.3383e-08	927.03	1.4200e-08	29192.95	5.3383e-08	29246.10

Table 2.2: Errors and computational times for a network of arteries. Left column shows the meshes defined by the maximum spatial mesh size Δx_{max}. Second to fourth columns show results different combinations of GRP and J-GRP solvers. Within every column we show L_1 errors and corresponding computational times for two combination of schemes. L_1 errors were evaluated considering the flows $q = Au$ in the whole arterial system; for a reference solution we used the fully fifth-order ADER scheme with a mesh size of 0.125 cm. All numerical simulations were performed in an Intel Core i7-2600 with 4 cores (3.40 GHz clock speed). The code was paralellized by means of *openMP*. Simulations were stopped after twenty cardiac cycles.

fully and partially second-order methods, respectively, where the minimum number of cells was 5. The numerical results are improved throughout. A second order method at junctions improves the accuracy for pressure, even though the differences are less significant than that depicted in Frames 2.11a and 2.11b.

Table 2.2 shows L_1 errors and computational times for schemes of order up to five in space and time using different combination of solvers. First-order methods at junctions coupled with high-order methods in the interior of the domain have larger errors compared to fully high-order methods. Computational times for the implicit solver MT-HEOC are larger compared to the explicit ones.

Figure 2.15 depicts L_1 errors against computational times. We compare ADER schemes of different orders, in all cases using the MT-HEOC solver. Errors of fully high-order methods (red-shaded colors) are always below to partially high-order methods (blue-shaded colors). It is worth noting that we formally do not preserve fully high-order accuracy in the whole arterial network due to our simple, low order, treatment of inflow boundary condition and terminal resistances. Consequently, the decreased rate of the fully fifth-order method is nearly equivalent to the fully second-order scheme. Nevertheless, the benefit of using high-order methods at junctions remains visible, but quite clearly, for a real application one must incorporate appropriate treatment of the inflow boundary and terminal resistances.

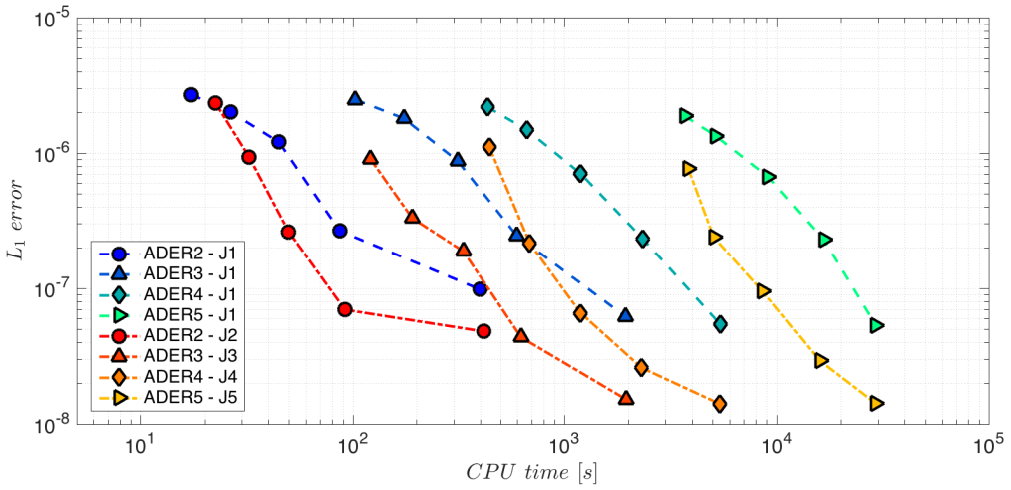

Figure 2.15: Efficiency plot for a network of arteries: L_1 errors against computational times. Comparison is shown between ADER schemes of different orders, used in conjunction with the MT-HEOC solver. L_1 errors were evaluated considering the flows $q = Au$ in the whole arterial system; for a reference solution we used the fully fifth-order ADER scheme with a mesh size of 0.125 cm. Blue-shaded and red-shaded colors refer to partial and fully high orders, respectively.

2.4 Summary and conclusions

Here we have proposed a new implicit solver for the Junction-Generalized Riemann Problem (J-GRP). This solver is an extension of the recently proposed Montecinos-Toro implicit solver for the GRP. We have then put together the two building blocks in the ADER framework to construct schemes of arbitrary accuracy in space and time for system of hyperbolic balance laws in networks. Specifically, we have applied the resulting methods to networks of blood vessels. To systematically assess convergence rates we have proposed a test problem with exact solution, consisting of three vessels connected at a single junction. Schemes of up to fifth order in space and time have been tested. The numerical experiments have shown that it is imperative to match the accuracy of the schemes at junctions to that in the interior of the domain. Otherwise the overall accuracy is lost. In addition, we have proposed a test problem for blood vessel networks in which there is a stiff source term. Our implicit method performed as expected, it endures the proposed test problem, while an explicit solver fails after few time steps. We have also deployed the present numerical techniques to simulate the physical model of 37 compliant silicon tubes (arteries) and 21 junctions proposed by Matthys et al. [Matthys 2007b]. Again, in this application it is clearly seen that the accuracy of the scheme at junctions is crucial to maintain the overall accuracy. Otherwise, low-order errors travel through the network of vessels with a damping effect, for example, for the pressure pulse-waves. The proposed methodology can be applied to more general network problems if high order of accuracy is desired.

Chapter 3

A one-dimensional mathematical model of collecting lymphatics coupled with an electro-fluid-mechanical contraction model and valve dynamics

3.1 Introduction

The lymphatic system is an intricate network of vessels and nodes which connect tissues to the bloodstream. The main functions of the lymphatic system comprise maintenance of tissue fluid balance through drainage of excess interstitial fluid, the transport of proteins and waste products, as well as the transport of immune cells [Swartz 2001]. The building block of collecting lymphatic vessels is the lymphangion: a mini-heart like, deformable vessel, which contracts and propels lymph into the next lymphangion, and has several mechanobiological auto-regulatory systems to provide optimal flow in various scenarios [Kunert 2015, Munn 2015]. The lymphangion is enclosed between valves which promote unidirectional flow. The frequency of lymphatic contractions depends on the circumferential stretch of the vessel wall and on the wall shear stress [Munn 2015, Telinius 2015, Gashev 2002]. For complete reviews of the mechanics of lymphangions and collectors, see [Munn 2015, Breslin 2014, Margaris 2012].

The lymphatic system has two different types of valves called primary and secondary valves. The former is located at the initial lymphatics at the level of the endothelium, while the latter is located between lymphangions in collectors [Schmid-Schönbein 2003, Bazigou 2013]. Primary and secondary lymphoedema, a lymphatic disease that leads to tissue swelling, is linked to lymphatic valve deficits [Kinmonth 1954, Mellor 2011, Herrick 2008, Noel 2001, Mihara 2012]. For instance, the lack of valves in lymphoedema distichiasis impairs lymphatic flow due to the inability to properly pump lymph forward [Mellor 2011, Petrova 2004, Sabine 2015, Bazigou 2013]. Also, chronic venous insufficiency leads to fibrotic lymph vessels due to hypertension, it compromises the functionality of lymphatic valves, and results in accumulation of fluid in tissues [Mortimer 2004, Rasmussen 2016]. Despite the connection between lymphatic valve deficits and lymphoedema, to the authors' knowl-

edge, the effect of non-functional valves in the lymphatic system has not been investigated and quantified. This is probably due to the difficulties in performing experiments on animal lymphatic valves, though the effects of genes mutations in engineered mice can be studied.

There is a substantial gap in the literature between mathematical models for the circulatory [Strocchi 2017, Liang 2009a, Müller 2014, Quarteroni 2016b], and lymphatic systems. The first reported attempt to construct a mathematical model for the lymphatic system is attributed to Reddy et al. [Reddy 1974]. In this work, the one-dimensional equations were written but the actual model implemented was zero dimensional. MacDonald et al. [Macdonald 2008] did further work based on this model. Extensive research has been carried out on the bases of lumped-parameter models [Venugopal 2007, Bertram 2011, Bertram 2014a, Bertram 2014b, Gajani 2015, Bertram 2016a, Jamalian 2016, Caulk 2016]. Jamalian et al. [Jamalian 2016] constructed a lumped-parameter model to simulate lymph transport in a network of rat lymphangions. Caulk et al. [Caulk 2016] combined the lumped-parameter model described by Bertram et al. [Bertram 2014b] with their four-fibre family constitutive law proposed in [Caulk 2015] and studied the variation of muscle contractility in response to a sustained elevation in afterload [Caulk 2016]. The Authors also included in their model the dependence of contraction frequency on transmural pressure and wall shear stress. A mechanobiological oscillatory model for the lymphatic contraction has been proposed by Kunert et al. [Kunert 2015]. Their contribution included a dynamical model for the contractibility of the vessel wall. The resulting model was able to control lymphatic transport via mechanobiological feedback loops, given by stretch-activated contractions and flow-induced relaxations. Recently, the relevance of this work has been questioned, see [Davis 2016]. With the aim of constructing a mathematical model of the entire lymphatic system, the previously mentioned mathematical models for lymphangions, except for [Kunert 2015, Baish 2016], are based on a relatively simple time-dependent contraction dynamics. These models 1) prescribe contraction dynamics by using trigonometric functions, and 2) prescribe time delays between adjacent lymphangions. It is no doubt highly desirable to model all mechanisms associated with lymphatic contractions by resorting to basic principles from electro-fluid mechanics. In particular, one would expect that the occurrence of a lymphatic contraction should be dependent on physical quantities, such as transmural pressure and local shear forces.

There is an extensive body of literature on cardiac contractions [Quarteroni 2016a, Colli Franzone 2014]. All these works have been greatly influenced by the pioneering work of Hodgkin and Huxley [Hodgkin 1952] on action potentials in neurons. The FitzHugh-Nagumo model [Nagumo 1962] is an example of a simplified, two-parameter formulation of the original Hodgkin-Huxley model, consisting of a system of two ODEs with a fast and a slow variable. The former represents the action potential, while the latter phenomenologically summarises all the effects of all ionic currents. Many studies have been done to couple modified versions of the FitzHugh-Nagumo model to the heart contractions [Colli Franzone 2014]. However, to date no studies have attempted to model contractions of lymphangions with the previously mentioned dynamical and phenomenological set of ODEs for action potentials.

In the present Chapter, we propose a one-dimensional model for lymph flow in collecting lymphatics coupled with an Electro-Fluid-Mechanical Contraction (EFMC) model for lymphatic vessel wall contractions based on a modified FitzHugh-Nagumo model. The current work presents the first attempt to couple the electrical activity of the lymphatic wall with the dynamics of the lymphatic

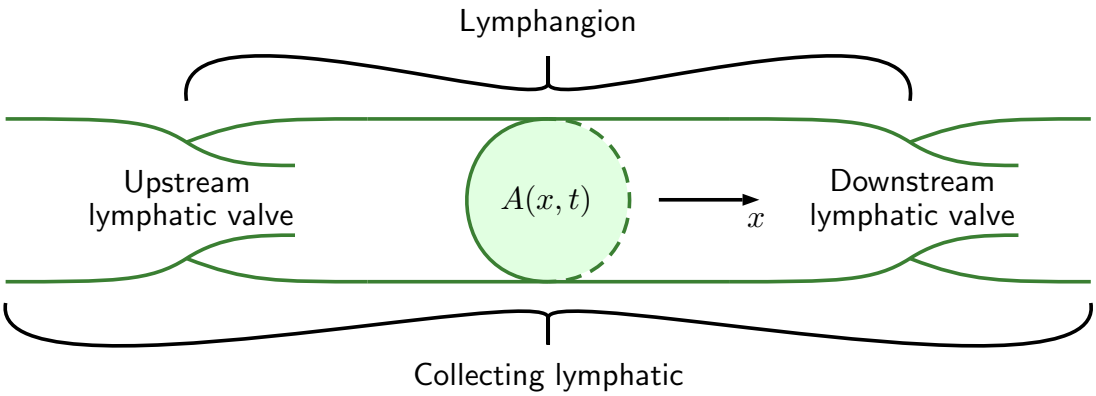

Figure 3.1: Illustration of a collecting lymphatic. A lymphangion is a lymphatic vessel delimited by upstream and downstream valves. A lymphatic vessel composed of two or more lymphangions is called a collecting lymphatic or collector. The natural lymph flow direction is from the upstream side to the downstream one and the lymphatic valves prevent backflow throughout the collecting lymphatic. The figure also shows a general cross-sectional area.

fluid modelled in a one-dimensional manner. In particular, in this work we incorporate some of the mechanobiological mechanisms which regulate the lymphatic contractions, such as (1) the positive dependency of frequency on the transmural pressure and (2) the inhibition of lymphatic contraction due to wall-shear stresses.

3.2 Methods

We aim to model the dynamics of flowing lymph inside a collecting lymphatic propelled by lymphatic contractions and pressure gradients, and the dynamics of lymphatic valves. Fig. 3.1 illustrates a collecting lymphatic, a single lymphangion and two lymphatic valves.

3.2.1 A one-dimensional model for lymph flow

Here we assume the lymph to be an incompressible Newtonian fluid. To derive the one-dimensional flow equations for a deformable lymphatic vessel, one can follow the procedure done for arteries and veins, where Reynolds' transport theorem is used to obtain the equations for the conservation of mass and momentum in a deformable tube, see [Formaggia 2009, Toro 2016]. The one-dimensional flow equations for a deformable vessel, and for a lymphatic vessel in particular, are

$$\begin{cases} \partial_t A + \partial_x q = 0\,, \\ \partial_t q + \partial_x \left(\dfrac{q^2}{A}\right) + \dfrac{A}{\rho}\partial_x p = -\dfrac{f}{\rho}\,, \end{cases} \tag{3.1}$$

where x is the space variable, t is time, $A(x,t)$ is cross-sectional luminal area of the vessel, $q(x,t) = A(x,t)u(x,t)$ is flow, $u(x,t)$ is velocity, $p(x,t)$ is pressure, ρ is lymph density, $f(x,t) = 2(\gamma+2)\pi\mu u(x,t)$ is friction force per unit length of the tube, with the parameter γ dependent on the chosen velocity profile [Alastruey 2006], and μ is the dynamic viscosity. To close the system

of equations, an additional relation between pressure $p(x,t)$ and cross-sectional area $A(x,t)$ is required and is called *tube law*. The lymphatic wall is characterized by an intimal layer of endothelial cells surrounded by a discontinuous basement membrane, a media composed of layers of smooth muscle cells intermixed with collagen and elastin, and an adventitia layer that consists of fibrous tissue [Caulk 2015, Zawieja 2008]. Elastin fibres give lymphatic vessels a compliant, elastic behaviour, while collagen prevents vessels from stretching beyond their physiological limits. The overall dynamics of elastin and collagen is reflected in highly non-linear tube laws. Here we propose the following general tube law:

$$p(x,t) = K(x,t)\,\psi\left(A(x,t);A_0(x)\right) + p_e(x,t)\,, \tag{3.2}$$

with

$$\psi(A(x,t);A_0(x)) = \left(\frac{A(x,t)}{A_0(x)}\right)^m - \left(\frac{A(x,t)}{A_0(x)}\right)^n + C\left[\left(\frac{A(x,t)}{A_0(x)}\right)^z - 1\right]\,, \tag{3.3}$$

where $p(x,t)$ is the internal pressure, $p_e(x,t)$ is the external pressure, $A_0(x)$ is the vessel cross-sectional area at zero transmural pressure (equilibrium or stress-free), $K(x,t)$ is a time-dependent coefficient, $m \geq 0$, $n \leq 0$, $z \geq 0$, and $C \geq 0$ are real numbers to be specified. The *transmural pressure* is defined as

$$p_{transm}(x,t) := p(x,t) - p_e(x,t)\,. \tag{3.4}$$

Inspired by [Macdonald 2008], we take the simplified approach to model lymphatic contractions by varying the coefficient $K(x,t)$ from a minimal value $K_{min}(x)$ to a maximum value $K_{max}(x)$ as follows

$$K(x,t) = K_{min}(x) + s(x,t)\left(K_{max}(x) - K_{min}(x)\right)\,, \tag{3.5}$$

where $s(x,t) \in [0,1]$ is the *state of contraction*. The lymphangion is contracted when $s(x,t) = 1$ and is relaxed when $s(x,t) = 0$.

The tube law can be recasted in terms of the active and passive components as follows:

$$p = f_p\left(\frac{A}{A_0}\right) + f_a\left(\frac{A}{A_0}, s\right) + p_e\,, \tag{3.6}$$

where

$$f_p\left(\frac{A}{A_0}\right) = K_{min}\,\psi\left(A;A_0\right) \tag{3.7}$$

is the passive pressure-area relationship and

$$f_a\left(\frac{A}{A_0}, s\right) = s\left(K_{max} - K_{min}\right)\psi\left(A;A_0\right) \tag{3.8}$$

is the active tension contribution. The passive pressure-area relationship mirrors the passive relationship proposed by others [Bertram 2011, Jamalian 2016]. The active tension contribution does not rely on a physiologically based model of muscle contractions, but rather emulates the contraction phenomena in terms of pressure-area curves.

Here we model lymphatic vessels from the mesentery of rats, whose parameters are found in Table 3.1. The parameters of the tube law and the minimum coefficient K_{min} were tuned to fit the experimental measurements shown in Bertram et al. [Bertram 2014a] and performed by Davis et

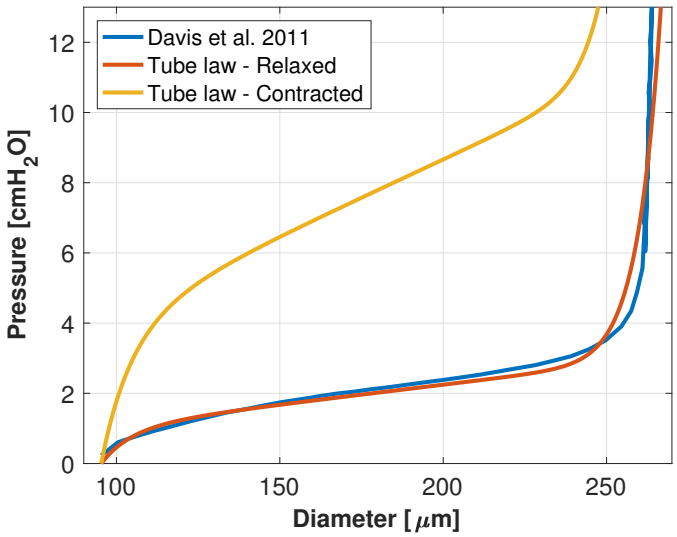

Figure 3.2: Pressure-diameter relation (tube law). Here we show the tube law used for the lymphatic wall. The parameters were tuned to fit the experimental measurements of Davis et al. [Davis 2011] and are found in Table 3.1. The figure also shows the tube laws at relaxed and contracted states. The external pressure was set to zero here.

al. [Davis 2011], while the maximum coefficient K_{max} was estimated following [Caulk 2016] and [Scallan 2012]. As can be seen in Fig. 3.2, the relationship between pressure and diameter is highly non-linear.

The Wall Shear Stress (WSS) is fundamental in the auto-regulatory homeostatic mechanisms of lymphatic contractions. Following [Alastruey 2006], the WSS in our formulation is

$$\tau(x,t) = u(x,t)\mu\frac{\gamma+2}{r(x,t)}\,, \tag{3.9}$$

where $r(x,t)$ is the inner radius of the lymphatic vessel.

Conservative formulation of the one-dimensional lymph flow equations

It is possible to write the lymph flow equations in conservative form as follows:

$$\partial_t \mathbf{Q}(x,t) + \partial_x \mathbf{F}(\mathbf{Q}(x,t),x,t) = \mathbf{S}(\mathbf{Q}(x,t),x,t)\,, \tag{3.10}$$

Parameter	Description	Value	Units	Reference
	Unknowns			
A	Lymphatic cross-sectional luminal (inner) area	$A(x,t)$	μm^2	-
q	Lymphatic flow	$q(x,t)$	$\mu L\ min^{-1}$	-
v	Excitation variable	$v(t)$	-	-
w	Recovery variable	$w(t)$	-	-
s	State of contraction ($0 \leq s \leq 1$)	$s(t)$	-	-
I	Stimulus	$I(t)$	-	-
ξ	State of the lymphatic valve ($0 \leq \xi \leq 1$)	$\xi(t)$	-	-
q_v	Flow across the lymphatic valve	$q_v(t)$	$\mu L\ min^{-1}$	-
	Material parameters			
γ	Parameter for velocity profile	2	–	Alastruey 2006 [Alastruey 2006]
μ	Lymph dynamic viscosity	1	cP	Bertram et al. 2011 [Bertram 2011]
ρ	Lymph density	998	$kg\ m^{-3}$	Macdonald et al. 2008 [Macdonald 2008]
K_{max}	Maximum coefficient	405	Pa	Estimated
K_{min}	Minimum coefficient	105	Pa	Fitted from Bertram et al. 2014 [Bertram 2014a]
r_0	Inner radius at zero transmural pressure	47.7	μm	Bertram et al. 2014 [Bertram 2014a]
A_0	Cross-sectional area at zero transmural pressure	πr_0^2	μm^2	-
L	Lymphangion length	3.0	mm	Jamalian et al. 2016 [Jamalian 2016]
p_e	External pressure	2	cmH_2O	Jamalian et al. 2016 [Jamalian 2016]
	Tube law			
m	Parameter	0.5	-	Fitted from Bertram et al. 2014 [Bertram 2014a]
n	Parameter	-5.0	-	Fitted from Bertram et al. 2014 [Bertram 2014a]
z	Parameter	19.0	-	Fitted from Bertram et al. 2014 [Bertram 2014a]
C	Parameter	1.0e-16	-	Fitted from Bertram et al. 2014 [Bertram 2014a]
	Electro-Fluid-Mechanical Contraction (EFMC) model			
$t_{excited}$	Required time to perform an action potential	≈ 2	s	Estimated
$t_{activation}$	Time required to activate an action potential	Eq. (3.38)	s	-
f_{min}	Minimum frequency at circumferential stretch $\bar{\lambda_\theta} = 1$	3.0	min^{-1}	Gashev et al. 2004 [Gashev 2004]
f_{Ca}	Maximum frequency at circumferential stretch $\bar{\lambda_\theta} = \lambda_{Ca}$	20.0	min^{-1}	Gashev et al. 2004 [Gashev 2004]
R_I	Radius of the activation region	0.1	-	Estimated
n_{Ca}	Stretch-activation parameter	20	-	Estimated
λ_{Ca}	Circumferential stretch at which the contraction frequency is f_{Ca}	2.784	-	Estimated
$k_{Ca}^{(1)}$	Baseline increasing rate of stimulus I	Eq. (3.41)	s^{-1}	-
$k_{Ca}^{(2)}$	Stretch-activated increasing rate of stimulus I	Eq. (3.41)	s^{-1}	-
k_{rel}	Decreasing rate of the stimulus I	10	s^{-1}	Estimated
a_1	Parameter	100	s^{-1}	Estimated
a_2	Parameter	0.5	-	Estimated
a_3	Parameter	25.0	-	Estimated
b_1	Parameter	3.0	s^{-1}	Estimated
b_2	Parameter	0.0	s^{-1}	Assumed
c_1	Increasing rate of contraction state s	10	s^{-1}	Estimated
c_2	Decreasing rate of contraction state s	3	s^{-1}	Estimated
$\tilde{I}$	Approximated stimulus required to trigger an action potential	Eq. (3.42)	-	-
k_{NO}	Contraction inhibition parameter ($0 \leq k_{NO} \leq 1$)	0.8	-	Estimated
τ_{NO}	Reference wall shear stress	6.0	$dyne\ cm^{-2}$	Estimated
n_{NO}	Wall shear stress inhibition parameter	1.2	-	Estimated
	Valve model			
Δp_{open}	Valve opening threshold pressure difference	0	cmH_2O	Assumed
Δp_{close}	Valve closure threshold pressure difference	0	cmH_2O	Assumed
K_{vo}	Rate coefficient valve opening	1.0	$Pa^{-1}\ s^{-1}$	Estimated
K_{vo}	Rate coefficient valve closure	1.0	$Pa^{-1}\ s^{-1}$	Estimated
B	Bernoulli resistance	Eq. (3.48)	$cmH_2O\ s^2\ \mu L^{-2}$	-
L	Lymphatic inertia	Eq. (3.48)	$cmH_2O\ s^2\ \mu L^{-1}$	-
R	Viscous resistance to flow	Eq. (3.48)	$cmH_2O\ s\ \mu L^{-1}$	-
M_{st}	Maximum valve opening ($0 \leq M_{st} \leq 1$)	1.0	-	Mynard et al. [Mynard 2012]
M_{rg}	Minimum valve closure ($0 \leq M_{rg} \leq 1$)	0.0	-	Mynard et al. [Mynard 2012]
L_{eff}	Effective length	0.5	mm	Estimated

Table 3.1: Parameters used for the one-dimensional EFMC model for lymph flow. We adopted the geometrical structure of collecting lymphatics from rat mesentery. Since the parameters of the mathematical model for the electrical activity were not directly available, we fitted the EFMC model parameter to qualitatively reproduce the experimental measurement shown in [Telinius 2015].

where

$$\mathbf{Q}(x,t) = \begin{bmatrix} A(x,t) \\ A(x,t)\,u(x,t) \end{bmatrix}, \tag{3.11}$$

$$\mathbf{F}(\mathbf{Q},x,t) = \begin{bmatrix} Au \\ Au^2 - \dfrac{K}{\rho} A_0 \partial_{A_0} \Psi \end{bmatrix}, \tag{3.12}$$

$$\mathbf{S}(\mathbf{Q},x,t) = \begin{bmatrix} 0 \\ -\dfrac{1}{\rho}\left(f + A\partial_x p_e + \Psi \partial_x K + K \partial_x A_0 \partial_{A_0} \Psi \right) \end{bmatrix}, \tag{3.13}$$

with

$$\begin{aligned}\Psi &= \int_A \psi(A;A_0)\mathrm{d}A \\ &= A_0\left(\frac{1}{m+1}\left(\frac{A}{A_0}\right)^{m+1} - \frac{1}{n+1}\left(\frac{A}{A_0}\right)^{n+1} + C\frac{1}{z+1}\left(\frac{A}{A_0}\right)^{z+1}\right),\end{aligned} \tag{3.14}$$

and

$$\partial_{A_0}\Psi = -\left(\frac{m}{m+1}\left(\frac{A}{A_0}\right)^{m+1} - \frac{n}{n+1}\left(\frac{A}{A_0}\right)^{n+1} + C\frac{z}{z+1}\left(\frac{A}{A_0}\right)^{z+1}\right). \tag{3.15}$$

$\mathbf{Q}$ is the vector of the *conserved variables*, $\mathbf{F}$ is the *physical flux* and $\mathbf{S}$ is the *source term*. The constants arising from the integrals (3.14) and (3.15) are set to zero for consistency with (3.1) and (3.2), see [Toro 2016].

The present formulation allows for a space-time coefficient $K(x,t)$ in the equations. This enables us to simulate travelling contraction-waves through the lymphatic wall by prescribing a space-time varying contraction state $s(x,t)$. However, in the present work, we consider the simpler case in which the contraction state is constant throughout the lymphangion, namely $s = s(t)$, and we also neglect the interaction between adjacent lymphangions. Then, instead of prescribing a trigonometric function for s, here we propose a set of governing ODEs given in Section 3.2.2. We also assume parameters $K_{min}(x)$, $K_{max}(x)$ and $p_e(x)$ to be constant. As a result, the source term simplifies in

$$\mathbf{S}(\mathbf{Q},x,t) = \mathbf{S}(\mathbf{Q}) = \begin{bmatrix} 0 \\ -2(\gamma+2)\pi\frac{\mu}{\rho}u \end{bmatrix}. \tag{3.16}$$

The general case of variable material properties poses mathematical [Toro 2013] and numerical challenges, and requires the use of well-balanced schemes [Müller 2013a].

Mathematical analysis of the one-dimensional lymph flow equations

Here we study the mathematical properties of (3.10) assuming constant parameters along the lymphatic vessel. The equations in (3.10) are a generalization of the one-dimensional blood flow equations [Toro 2016]. As a matter of fact, the main difference is an additional term in the tube law (3.3). For this reason, here we summarize the main mathematical structure of the lymph flow equations without proofs. System (3.10) can be written in quasi-linear form as

$$\partial_t\mathbf{Q} + \mathbf{A}(\mathbf{Q},t)\partial_x\mathbf{Q} = \mathbf{S}(\mathbf{Q}), \tag{3.17}$$

where

$$\mathbf{A}(\mathbf{Q},t) = \begin{bmatrix} 0 & 1 \\ \frac{A}{\rho}K\partial_A\psi - u^2 & 2u \end{bmatrix}, \quad \mathbf{S}(\mathbf{Q}) = \begin{bmatrix} 0 \\ -\frac{f}{\rho} \end{bmatrix}. \tag{3.18}$$

The eigenvalues of matrix $\mathbf{A}$ are

$$\lambda_1 = u - c, \quad \lambda_2 = u + c, \tag{3.19}$$

where c is the *wave speed*

$$c = \sqrt{\frac{A}{\rho}K\partial_A\psi} = \sqrt{\frac{K}{\rho}\left[m\left(\frac{A}{A_0}\right)^m - n\left(\frac{A}{A_0}\right)^n + Cz\left(\frac{A}{A_0}\right)^z\right]}. \tag{3.20}$$

We assume parameters $m \geq 0$, $n \leq 0$, $z \geq 0$, and $C \geq 0$ for the tube law. Thus, the wave speed c is always real. The wave speed increases actively during contraction as it depends on the coefficient K. This means that during lymphatic contraction, the lymphatic wall becomes stiffer and waves propagate at a faster rate. The eigenvectors of $\mathbf{A}$ are

$$\mathbf{R}_1 = \gamma_1 \begin{bmatrix} 1 \\ u-c \end{bmatrix}, \quad \mathbf{R}_2 = \gamma_2 \begin{bmatrix} 1 \\ u+c \end{bmatrix}, \tag{3.21}$$

where γ_1 and γ_2 are arbitrary scaling factors. It can be shown that system (3.10) is hyperbolic, as the eigenvalues are real and distinct and the eigenvectors $\mathbf{R}_1$ and $\mathbf{R}_2$ are linearly independent. Following proofs in [Toro 2016] and references therein, the λ_1 and λ_2 characteristic fields are genuinely non-linear outside the locus of the following function

$$G\left(\frac{A}{A_0}\right) = m(m+2)\left(\frac{A}{A_0}\right)^m - n(n+2)\left(\frac{A}{A_0}\right)^n + Cz(z+2)\left(\frac{A}{A_0}\right)^z. \tag{3.22}$$

With the choice of parameters m, n, z and C in Table 3.1, there exist at least one solution of $G\left(\frac{A}{A_0}\right) = 0$. This means that the two characteristic fields are neither genuinely non-linear nor linearly degenerate. The consequences of this are unclear to the authors, and might require further investigations. See [LeFloch 2002] for details. The Generalized Riemann Invariants (GRIs) for λ_1 and λ_2 characteristic fields are respectively

$$\left.\begin{aligned} \lambda_1 - \text{GRI}: \quad & u + \int \frac{c(A)}{A} \mathrm{d}A = constant\,, \\ \lambda_2 - \text{GRI}: \quad & u - \int \frac{c(A)}{A} \mathrm{d}A = constant\,. \end{aligned}\right\} \tag{3.23}$$

In the present work, the generalized Riemann invariants are used to couple valves with lymphangions and to impose the pressure at the terminal interfaces of the collector.

3.2.2 The Electro-Fluid-Mechanical Contraction (EFMC) model

Here we propose an Electro-Fluid-Mechanical Contraction (EFMC) model for lymphatics, based on the FitzHugh-Nagumo model for action potentials. Here we assumed that lymphatic smooth muscle cells act as pacemaker cells [Zawieja 2009] and model the ion dynamics through the FitzHugh-Nagumo model [Nagumo 1962].

The modelling system of ODEs is

$$\frac{d}{dt}\mathbf{Y} = \mathbf{L}(\mathbf{Y})\,, \tag{3.24}$$

where

$$\mathbf{Y}(t) = \begin{bmatrix} v(t) \\ w(t) \\ I(t) \\ s(t) \end{bmatrix}, \quad \mathbf{L}(\mathbf{Y}) = \begin{bmatrix} a_1\left[v\left(v-a_2\right)\left(1-a_3 v\right) - w + vI\right] \\ b_1 v(1-v)^2 - b_2 w \\ f_I(\bar{\lambda_\theta}, \bar{\tau}, v, w, I) \\ f_s(v,s) \end{bmatrix}, \tag{3.25}$$

and

$$f_I(\bar{\lambda_\theta}, \bar{\tau}, v, w, I) = \begin{cases} \left(k_{Ca}^{(1)} + k_{Ca}^{(2)}\left(\dfrac{\bar{\lambda_\theta}}{\lambda_{Ca}}\right)^{n_{Ca}}\right) f_{NO}(\bar{\tau})\,, & \sqrt{v^2+w^2} \leq R_I\,, \\ -Ik_{rel}\,, & \sqrt{v^2+w^2} > R_I\,, \end{cases} \tag{3.26}$$

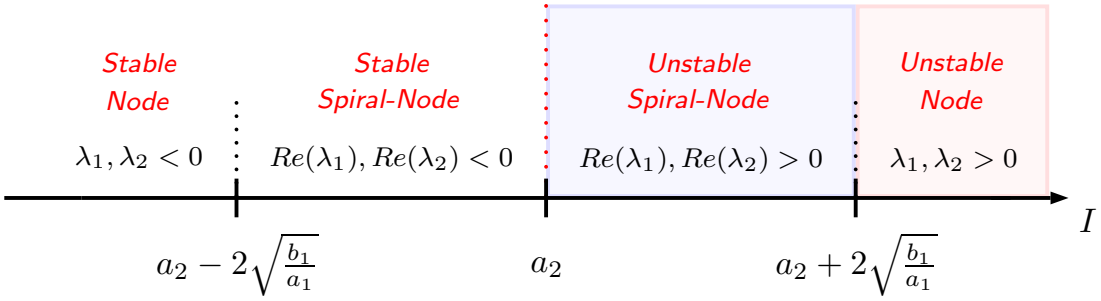

Figure 3.3: Stability analysis of the stationary point $(0,0)$ of the modified FitzHugh-Nagumo model. The nature of the stationary point depends on the stimulus I. For $I < a_2 - 2\sqrt{\frac{b_1}{a_1}}$ and $I > a_2 + 2\sqrt{\frac{b_1}{a_1}}$, the eigenvalues of the modified FHN model are real while for $a_2 - 2\sqrt{\frac{b_1}{a_1}} < I < a_2 + 2\sqrt{\frac{b_1}{a_1}}$, the eigenvalues are imaginary. Action potentials can be periodically triggered when $I > a_2$.

$$f_{NO}(\bar{\tau}) = 1 - k_{NO}\left(\frac{2}{1+exp\left(-\left|\frac{\bar{\tau}}{\tau_{NO}}\right|^{n_{NO}}\right)} - 1\right), \tag{3.27}$$

and

$$f_s(v,s) = \begin{cases} +c_1 v(1-s), & v > 0, \\ -c_2 s, & v \leq 0. \end{cases} \tag{3.28}$$

The unknowns of the above system are: the *excitation variable* $v(t)$ (membrane potential), the *recovery variable* $w(t)$, the *stimulus* $I(t)$, and the *contraction state* $s(t)$ introduced in Eq. (3.5). The first two equations in (3.24) and (3.25) are based on the FitzHugh-Nagumo (FHN) model. In the classical formulation of the FHN model, the stimulus I is constant. In the present work, I varies in time and multiplies the excitation variable v. The second equation in (3.24) has the additional factor $(1-v)^2$ which increases the rate at which the recovery variable returns to the equilibrium state, reducing the refractory period.

Lymphangions have the capability to change the contraction frequency depending on local fluid dynamic quantities, such as transmural pressure and wall shear stress [Munn 2015]. Such capability is phenomenologically modelled by a time evolution of I which is controlled by the function f_I. Three mechanisms are here taken into account: (1) environmental calcium influx, (2) stretch-activated calcium influx, and (3) contraction inhibitions induced by WSS. The environmental baseline influx is regulated by the parameter $k_{Ca}^{(1)}$. The stretch-activated calcium influx is regulated by the parameters $k_{Ca}^{(2)}$, λ_{Ca} and n_{Ca}. The contraction inhibitions induced by WSS are regulated by the function f_{NO}, which depends on parameters k_{NO}, τ_{NO} and n_{NO}. The function f_{NO} is bounded by $1-k_{NO}$ and 1, namely

$$\lim_{|\tau|\to+\infty} f_{NO}(\tau) = 1 - k_{NO} \leq f_{NO} \leq 1 = f_{NO}(0). \tag{3.29}$$

The contraction state s is controlled by the function f_s, which ensures that s lies between 0 and 1. Following [Telinius 2015], we assume: (1) that the contraction state s increases to 1 during the

depolarization phase and (2) decreases to 0 during the repolarization phase. Maximum tension is then attained at the end of the plateau of the action potential of the FHN model [Nagumo 1962]. The rate of change of s is controlled by parameters c_1 and c_2. Functions f_I and f_{NO} are evaluated at the space-averaged circumferential stretch of the vessel [Caulk 2016] and at the space-averaged WSS, respectively, at the current time

$$\bar{\lambda_\theta}(t) = \frac{1}{L}\int_0^L \frac{r(x,t)}{r_0}\mathrm{d}x\,, \quad \bar{\tau}(t) = \frac{1}{L}\int_0^L \tau(x,t)\mathrm{d}x\,, \tag{3.30}$$

where L is the length of the lymphangion.

Concerning the choice of parameters for the EFMC model, Table 3.1 gives values used in the present chapter. Most of these parameters could not be obtained by fitting the experiments and therefore we have estimated such values so as to reproduce the shape of the action potential shown in [Telinius 2015].

Mathematical analysis of the modified FitzHugh-Nagumo model

Here we analyse the modified FitzHugh-Nagumo model on which the EFMC model is based. First, we find the stationary state solution, and then we study its nature depending on the stimulus I. The stationary points are found by solving the following system

$$F_{FHN}(v,w) = \begin{bmatrix} a_1\left[v\left(v-a_2\right)\left(1-a_3 v\right) - w + vI\right] \\ b_1 v(1-v)^2 - b_2 w \end{bmatrix} = \begin{bmatrix} 0 \\ 0 \end{bmatrix}\,. \tag{3.31}$$

Assuming $b_2 = 0$, there are two stationary points: $v = w = 0$ and $v = 1$, $w = (1-a_2)(1-a_3) - I$. In our setting, v and w will always be far from $v = 1$, $w = (1-a_2)(1-a_3) - I$. Therefore, we study the case in which $v = w = 0$. The case in which $b_2 \neq 0$ leads to multiple stationary points and is here neglected. To study the nature of the stationary point, one has to evaluate the Jacobian of F_{FHN} at the stationary state and study the sign of its eigenvalues. The resulting eigenvalues are

$$\lambda_{1,2} = \frac{-a_1(a_2 - I) \pm \sqrt{a_1^2(a_2-I)^2 - 4a_1 b_1}}{2}\,. \tag{3.32}$$

One can show that: when $I < a_2$, the stationary solution is stable, and therefore action potentials are not automatically triggered; when $I > a_2$ the stationary solution is unstable, and therefore action potentials can be triggered (see Fig. 3.3).

For a time-varying stimulus I, we assume that the needed stimulus $\tilde{I}$ to trigger an action potential lies between a minimum $\tilde{I}_{min}$ and a maximum value $\tilde{I}_{max}$, defined as follows:

$$\tilde{I}_{min} := a_2\,, \quad \tilde{I}_{max} := a_2 + 2\sqrt{\frac{b_1}{a_1}}\,. \tag{3.33}$$

These two values will be useful to estimate the frequency of contractions of the EFMC model.

Qualitative analysis of the EFMC model

As shown in Fig. 3.4, when the excitation variable v and the recovery variable w are near the stationary state ($\sqrt{v^2+w^2} < R_I$), the stimulus I increases as given by (3.26). When a certain value

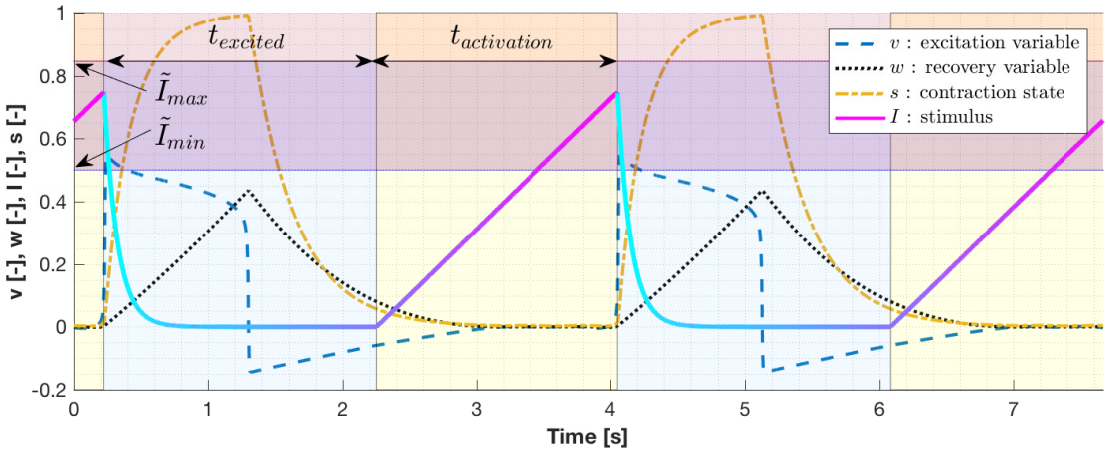

Figure 3.4: Illustration of the EFMC model in the time domain of two representative lymphatic cycles. Results show the excitation variable, recovery variable, contraction state and the stimulus for two reference lymphatic cycles. Minimum and maximum triggering values $\tilde{I}_{min}$ and $\tilde{I}_{max}$ are also shown. The horizontal blue and red shaded areas illustrate the *unstable spiral-node* and the *unstable node* regions, respectively. The *excited* and *activation* regions can be determined by the different shaded colors (blue and yellow). Here we solved the system of ODEs (3.24) with initial condition $v(0) = 0.001$, $w(0) = I(0) = s(0) = 0$. The parameters of the EFMC model were taken from Table 3.1, but here we set $f_{min} = 5$ min^{-1}, and we assumed $\bar{\alpha} = 2.8165$ and $\bar{\tau} = 0$. The colour gradient of the stimulus I is the same as in Fig. 3.5.

$\tilde{I}$ is reached (in this case $\tilde{I}_{min} < \tilde{I} < \tilde{I}_{max}$), an action potential is triggered: variables v and w perform a cycle, increase in absolute value and move far from the stationary state ($\sqrt{v^2 + w^2} > R_I$) and consequently the stimulus I decreases exponentially to zero. The state of contraction s increases until $v > 0$, and then decreases to zero, see Eq. (3.28). When the action potential ends, variables v and w return to the equilibrium point. From there on, the stimulus I restarts to increase and possibly triggers a new contraction.

As shown in Fig. 3.5, the circle of radius R_I centred at $v = w = 0$ divides the phase space into two regions. The space within the circle of radius R_I is called *activation region*, while the one outside is called *excited region*. In the excited region the numerical solution quickly performs a cycle and the stimulus I decreases exponentially to zero. In the activation region, the solution tends to the equilibrium state and the stimulus I increases. The time required for the solution to perform a cycle within the excited region can be numerically quantified and is denoted by $t_{excited}$. The time required to activate an action potential is denoted by $t_{activation}$.

Analysis of the EFMC frequency

Lymphangions contract differently according to the location of the vessel, the stretch of the lymphatic wall and wall shear stress feedback [Gashev 2004]. Here we aim to analyse the frequency of contraction of the EFMC model and to estimate parameters $k_{Ca}^{(1)}$ and $k_{Ca}^{(2)}$ in order to prescribe a baseline frequency f_{min} and a frequency f_{Ca} at circumferential stretch $\bar{\lambda}_\theta = \lambda_{Ca}$. The time t_{total} between two cycles can be written as follows:

$$t_{total} = t_{excited} + t_{activation} \,, \tag{3.34}$$

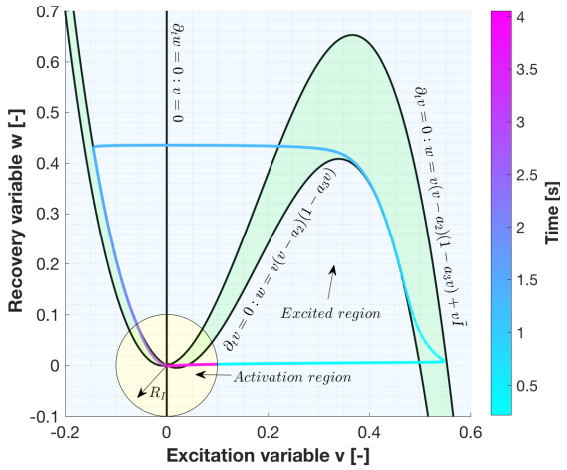

Figure 3.5: Illustration of the EFMC model in phase space of a representative lymphatic cycle. The circle of radius R_I centred in the stationary point $(0,0)$ divides the phase space into two regions: the *activation* region (yellow) and the *excited* region (blue). Three nullclines are shown: the nullcline for the recovery variable $\partial_t w = 0$, and two representative nullclines with $I = 0$ and $I = \tilde{I}$ for the excitation variable $\partial_t v = 0$. As soon as a contraction occurs, the stimulus I decreases and the third nullcline tends to the second one. Results in the time domain can be seen in Fig. 3.4.

and the related frequency is

$$f = \frac{1}{t_{total}} = \frac{1}{t_{excited} + t_{activation}} \,. \tag{3.35}$$

The excited time $t_{excited}$ can be assumed to be constant and can be evaluated numerically from the FHN model. The activation time, on the other hand, depends strongly on the rate of increase of I given by (3.26). We now estimate the activation time, namely the time required for the stimulus I to attain a certain triggering value $\tilde{I}$. Near the stationary solution $v = w = 0$, it is reasonable to assume $\sqrt{v^2 + w^2} < R_I$. Let us solve the following initial value problem

$$\left.\begin{aligned} &\text{ODE:} && \frac{d}{dt} I(t) = \left(k_{Ca}^{(1)} + k_{Ca}^{(2)} \left(\frac{\bar{\lambda_\theta}(t)}{\lambda_{Ca}} \right)^{n_{Ca}} \right) f_{NO}\big(\bar{\tau}(t)\big) \,, \quad t \geq t_{excited} \,, \\ &\text{IC:} && I(t_{excited}) = 0 \,. \end{aligned}\right\} \tag{3.36}$$

We assume that during the activation time, $\bar{\lambda_\theta}$ and $\bar{\tau}$ are constant in time because the lymphangion is already at the end of the diastolic phase. Thus, the above initial value problem can be solved exactly as

$$I(t) = t \left(k_{Ca}^{(1)} + k_{Ca}^{(2)} \left(\frac{\bar{\lambda_\theta}}{\lambda_{Ca}} \right)^{n_{Ca}} \right) f_{NO}(\bar{\tau}) \,. \tag{3.37}$$

Consequently, under the previous assumption, the activation time $t_{activation}$ required to attain a triggering value $\tilde{I}$ is

$$t_{activation} = \frac{\tilde{I}}{\left(k_{Ca}^{(1)} + k_{Ca}^{(2)} \left(\frac{\bar{\lambda_\theta}}{\lambda_{Ca}} \right)^{n_{Ca}} \right) f_{NO}(\bar{\tau})} \,. \tag{3.38}$$

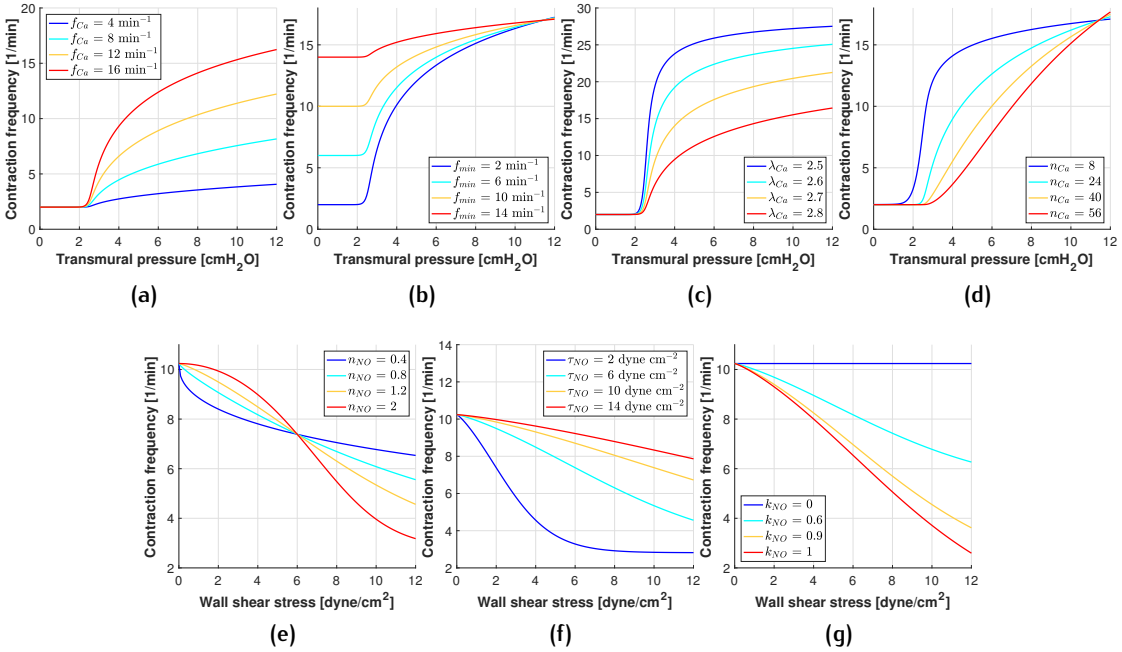

Figure 3.6: Effects of EFMC model parameters on the pressure-frequency and WSS-frequency relationships. In the top row, we show theoretical results for transmural pressure against frequency varying f_{Ca}, f_{min}, λ_{Ca} and n_{Ca}. In the bottom row, we show theoretical results for WSS againts the frequency varying n_{NO}, τ_{NO} and k_{NO}. Results are based on expression (3.43) and assuming a baseline value of $\bar{\lambda_\theta} = 2.6458$. The parameters were taken from Table 3.1.

The maximum activation time (when $\left(\bar{\lambda_\theta}/\lambda_{Ca}\right)^{n_{Ca}} \approx 0$) and the activation time at $\bar{\lambda_\theta} = \lambda_{Ca}$, both at zero WSS ($\bar{\tau} = 0$), are

$$t^{max}_{activation} = \frac{\tilde{I}}{k^{(1)}_{Ca}}\,, \quad t^{Ca}_{activation} = \frac{\tilde{I}}{k^{(1)}_{Ca} + k^{(2)}_{Ca}}\,. \tag{3.39}$$

The maximum activation time, corresponding to the minimum frequency, depends on parameter $k^{(1)}_{Ca}$. In our model, the parameter $k^{(1)}_{Ca}$ phenomenologically represents the environmental calcium influxes. Indeed, in the particular case in which there is no environmental calcium influxes ($k^{(1)}_{Ca} = 0$), the activation time becomes infinite, which means that the lymphangion does not autonomously contract. Parameter $k^{(2)}_{Ca}$, on the other hand, phenomenologically regulates the stretch-induced calcium influxes.

Assuming the frequencies f_{min} and f_{Ca}, corresponding to $t^{max}_{activation}$ and $t^{Ca}_{activation}$ respectively, to be known, we have:

$$\frac{1}{f_{min}} = t_{excited} + t^{max}_{activation}\,, \quad \frac{1}{f_{Ca}} = t_{excited} + t^{Ca}_{activation}\,. \tag{3.40}$$

Using (3.39) and (3.40), we can explicitly find parameters $k^{(1)}_{Ca}$ and $k^{(2)}_{Ca}$:

$$k^{(1)}_{Ca} = \frac{\tilde{I}}{\dfrac{1}{f_{min}} - t_{excited}}\,, \quad k^{(2)}_{Ca} = \frac{\tilde{I}}{\dfrac{1}{f_{Ca}} - t_{excited}} - \frac{\tilde{I}}{\dfrac{1}{f_{min}} - t_{excited}}\,. \tag{3.41}$$

Here we assume the triggering value $\tilde{I}$ to be the mean value of I_{max} and I_{min} defined in Eq. (3.33), namely

$$\tilde{I}_{mean} = \frac{\tilde{I}_{max} + \tilde{I}_{min}}{2} = a_2 + \sqrt{\frac{b_1}{a_1}} \,. \tag{3.42}$$

Numerical results confirmed that this is a good choice, even though $\tilde{I}_{min}$ and $\tilde{I}_{max}$ can be used as triggering values too.

Substituting $k_{Ca}^{(1)}$ and $k_{Ca}^{(2)}$ and the activation time $t_{activation}$ defined in (3.38) into (3.35), one obtains a frequency function as

$$f\left(\bar{\lambda_\theta}, \bar{\tau}, \tilde{I}\right) = \frac{1}{t_{excited} + t_{activation}\left(\bar{\lambda_\theta}, \bar{\tau}, \tilde{I}\right)} \,. \tag{3.43}$$

Then, one can easily prove the following inequalities

$$f\left(\bar{\lambda_\theta}, 0, \tilde{I}\right) > f\left(\bar{\lambda_\theta}, \bar{\tau}_1, \tilde{I}\right) > f\left(\bar{\lambda_\theta}, \bar{\tau}_2, \tilde{I}\right) \,, \quad |\bar{\tau}_1| < |\bar{\tau}_2| \,, \tag{3.44}$$

and

$$f\left(\bar{\lambda}_{\theta 1}, \bar{\tau}, \tilde{I}\right) < f\left(\bar{\lambda}_{\theta 2}, \bar{\tau}, \tilde{I}\right) \,, \quad \bar{\lambda}_{\theta 1} < \bar{\lambda}_{\theta 2} \,. \tag{3.45}$$

The first property (3.44) says that the frequency decreases as WSS increases, and maximum contraction frequency are attained at zero WSS. The second property (3.45) says that the frequency increases as the circumferential stretch increases.

The influence of the EFMC parameters on frequency-pressure and frequency-WSS relationships is shown in Fig. 3.6. At the transmural pressure $p_{Ca} \approx 11$ cmH_2O corresponding to $\bar{\lambda_\theta} = 2.6458$, the frequency attains value f_{Ca}. From the Fig. 3.6, we see that an increment of λ_{Ca} lowers the frequency-pressure curve and shifts rightward the transmural pressure at which f_{Ca} is attained. Parameter n_{Ca} changes the shape of the pressure-frequency curve, while n_{NO} and τ_{NO} affect the WSS-frequency curve. Fig. 3.6 shows that it is possible to emulate pressure-frequency and pressure-WSS curves from experimental measurements of a specific lymphangion by adjusting the EFMC parameters.

3.2.3 A lumped-parameter model for lymphatic valves

To model valves in lymphatic vessels, we adopt the work of Mynard et al. [Mynard 2012], an improvement of [Sun 1995]. Such model has already been applied to the venous system [Toro 2015b]. The time variation of the flow across the valve $q_v(t)$ is modelled as

$$\frac{d}{dt} q_v = \frac{1}{L(\xi)} \left(\Delta p(t) - R(\xi)\, q_v - B(\xi)\, q_v |q_v|\right) \,, \tag{3.46}$$

where

$$\Delta p(t) = p_u(t) - p_d(t) \,. \tag{3.47}$$

Here p_u and p_d are the upstream and downstream pressures, respectively. The above formula can be regarded as the lumped-version of a lymphatic vessel of a given length. Coefficients B, L and R are the Bernoulli resistance, the lymphatic inertia and the viscous resistance to flow, given respectively as

$$B(\xi) = \frac{\rho}{2A_{eff}^2(\xi)} \,, \quad L(\xi) = \rho \frac{L_{eff}}{A_{eff}(\xi)} \,, \quad R(\xi) = \frac{2(\gamma+2)\pi\mu}{A_{eff}^2(\xi)} L_{eff} \,, \tag{3.48}$$

where L_{eff} is the effective length and A_{eff} is the effective area, which varies from a minimum value to a maximum value as

$$A_{eff}(\xi) = A_{eff,min} + \xi(t)\left(A_{eff,max} - A_{eff,min}\right) , \tag{3.49}$$

with $\xi \in [0,1]$. Compared to the work of Mynard et al. [Mynard 2012], we have added the Poiseuille-type viscous losses insofar as the Reynolds number for lymphatics is low [Rahbar 2011] and therefore this term plays a dominant role. Although the Bernoulli resistance might not contribute significantly for lymphatic flow, in the current work we chose to keep it to maintain a general framework of both high and low Reynolds numbers. The minimum and the maximum effective areas are evaluated as follow

$$A_{eff,min} = M_{rg} A_0 , \quad A_{eff,max} = M_{st} A_0 , \tag{3.50}$$

where M_{rg} is a parameter that controls the minimum closure, while M_{st} controls the maximum opening. A_0 is taken as the mean value between the cross-sectional areas at equilibrium of the adjacent lymphangions. The *valve state* $\xi(t)$ is governed by the following ODE

$$\frac{d}{dt}\xi = f_\xi(\xi,t) = \begin{cases} K_{vo}(1-\xi)\left(\Delta p(t) - \Delta p_{open}\right) , & \Delta p(t) > \Delta p_{open} , \\ K_{vc}\,\xi\left(\Delta p(t) - \Delta p_{close}\right) , & \Delta p(t) < \Delta p_{close} , \end{cases} \tag{3.51}$$

where K_{vo} and K_{vc} are the valve opening/closure rates, and Δp_{open} and Δp_{close} are the opening/closure threshold pressures. For further details, see also [Mynard 2012].

Here we simplify the valve dynamics by assuming both the opening and closure thresholds to be zero, although it is widely accepted that lymphatic valves are biased to stay open [Davis 2011]. The resulting system of ODEs is

$$\frac{d}{dt}\mathbf{Y} = \mathbf{L}(\mathbf{Y},t) , \tag{3.52}$$

where

$$\mathbf{Y}(t) = \begin{bmatrix} q_v(t) \\ \xi(t) \end{bmatrix} , \quad \mathbf{L}(\mathbf{Y},t) = \begin{bmatrix} \frac{1}{L(\xi)}\left(\Delta p(t) - R(\xi)\,q_v - B(\xi)\,q_v|q_v|\right) \\ f_\xi(\xi,t) \end{bmatrix} . \tag{3.53}$$

3.2.4 Numerical methods

Here we briefly describe the finite volume schemes used for the one-dimensional lymph flow equations, explain how lymphatic valves and lymphangions are coupled, and illustrate the treatment of the boundary conditions at the terminal interfaces of the lymphangion. Then, we summarize the numerical methods used for the valves and the EFMC models.

A finite volume method for the one-dimensional model

Consider the system of m hyperbolic balance laws

$$\partial_t \mathbf{Q} + \partial_x \mathbf{F}(\mathbf{Q}) = \mathbf{S}(\mathbf{Q}) . \tag{3.54}$$

By integrating (3.54) over the control volume $V = [x_{i-\frac{1}{2}}, x_{i+\frac{1}{2}}] \times [t^n, t^{n+1}]$ we obtain the exact formula

$$\mathbf{Q}_i^{n+1} = \mathbf{Q}_i^n - \frac{\Delta t}{\Delta x}\left(\mathbf{F}_{i+\frac{1}{2}} - \mathbf{F}_{i-\frac{1}{2}}\right) + \Delta t \mathbf{S}_i , \tag{3.55}$$

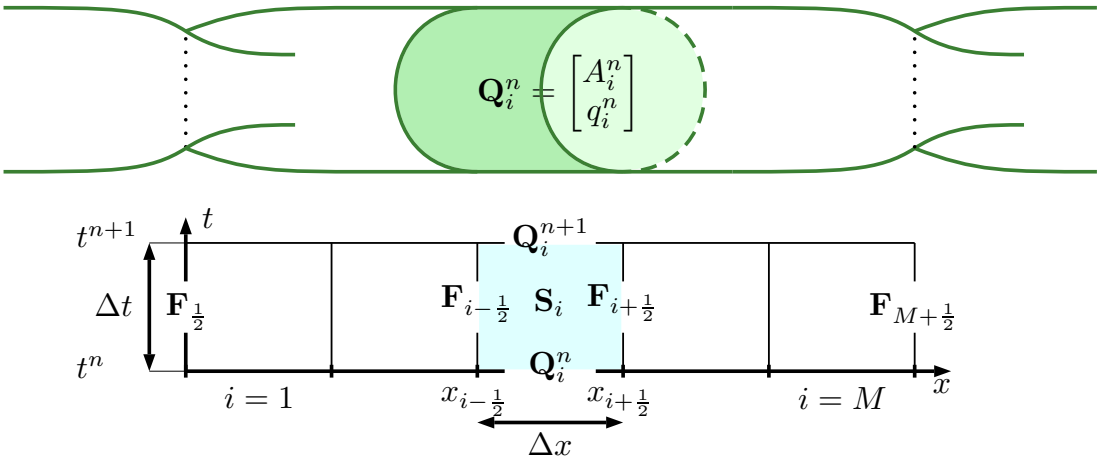

Figure 3.7: Framework for a finite volume scheme. Top: illustratation of a computational volume for a lymphangion. Bottom: illustratation of the space-time control volume.

with definitions

$$\mathbf{Q}_i^n = \frac{1}{\Delta x}\int_{x_{i-\frac{1}{2}}}^{x_{i+\frac{1}{2}}} \mathbf{Q}(x,t^n)\mathrm{d}x\,, \tag{3.56}$$

$$\left.\begin{aligned} \mathbf{F}_{i+\frac{1}{2}} &= \frac{1}{\Delta t}\int_{t^n}^{t^{n+1}} \mathbf{F}(\mathbf{Q}(x_{i+\frac{1}{2}},t))\mathrm{d}t\,, \\ \mathbf{S}_i &= \frac{1}{\Delta t \Delta x}\int_{t^n}^{t^{n+1}}\int_{x_{i-\frac{1}{2}}}^{x_{i+\frac{1}{2}}} \mathbf{S}(\mathbf{Q}(x,t))\mathrm{d}x\mathrm{d}t\,. \end{aligned}\right\} \tag{3.57}$$

Eq. (3.56) gives the spatial-integral average at time $t=t^n$ of the conserved variable $\mathbf{Q}$ while Eqs. (3.57) give the time-integral average at interface $x=x_{i+\frac{1}{2}}$ of the physical flux $\mathbf{F}$ and the volume-integral average in V of the source term $\mathbf{S}$. Spatial mesh size and time step are $\Delta x = x_{i+\frac{1}{2}} - x_{i-\frac{1}{2}}$ and $\Delta t = t^{n+1} - t^n$ respectively. Finite volume methods for (3.54) depart from (3.55) to (3.57), where integrals are approximated, and then formula (3.55) becomes a *finite volume method*, where the approximated integrals in (3.57) are called *numerical flux* and *numerical source*, respectively. Here index i runs from 1 to M, where the cell $i=1$ is the leftmost cell with $x_{\frac{1}{2}}$ being the first interface, and the cell $i=M$ is the rightmost cell with $x_{M+\frac{1}{2}}$ being the last interface. See Fig. 3.7 for an illustration of the finite volume framework. To compute the time step Δt, the Courant-Friedrichs-Lewy condition is applied for each lymphangion

$$\Delta t^j = CFL\frac{\Delta x^j}{\max\limits_{i=1,\dots,M^j}\left(|u_i^j| + c_i^j\right)}\,, \tag{3.58}$$

with $CFL=0.9$. Superindex j indicates the j-th lymphangion. Then, the time step Δt to be used is the minimum of all the time steps, namely $\Delta t = \min\limits_j\left(\Delta t^j\right)$.

In the present chapter we used the SLIC method to evaluate the numerical fluxes within the domain $(\mathbf{F}_{\frac{3}{2}},\dots,\mathbf{F}_{M-\frac{1}{2}})$ [Toro 2000]. This method is second-order accurate in space and time and is

$$q_v + A_u^* \left(-u_u + \int_{A_u}^{A_u^*} \frac{c(\tau)}{\tau} \mathrm{d}\tau \right) = 0 \qquad q_v + A_d^* \left(-u_d - \int_{A_d}^{A_d^*} \frac{c(\tau)}{\tau} \mathrm{d}\tau \right) = 0$$

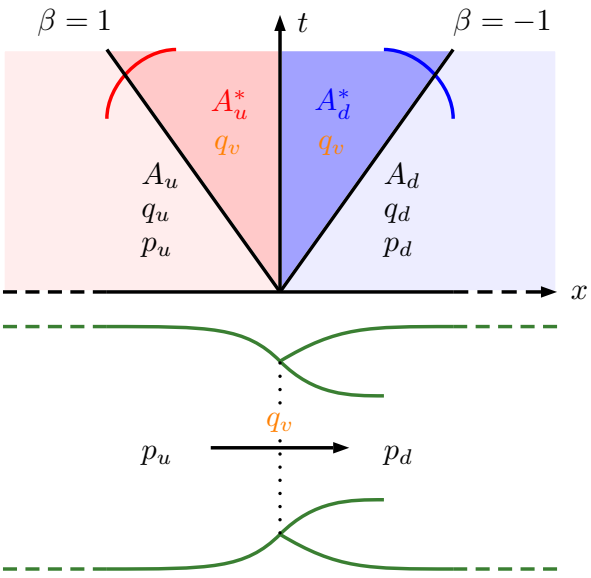

Figure 3.8: Illustration of the coupling method between two lymphangions and one valve. Riemann invariants are used to couple the flow through the valve and the two lymphangions.

based on the MUSCL-Hancock scheme where the Godunov upwind flux is replaced by the FORCE flux, see Section 14.5.3 of [Toro 2009] and references therein. The numerical source was approximated using a second order in space and time method, see Chapter 19 of [Toro 2009]. For the numerical fluxes at the boundaries ($\mathbf{F}_{\frac{1}{2}}$ and $\mathbf{F}_{M+\frac{1}{2}}$) we used a first-order Godunov-type method based on the solution of a classical Riemann problem at the interface.

Coupling between valves and lymphangions

Here we aim to couple valves and lymphangions. For each lymphangion, we need to calculate the numerical flux at the interface in which the valve is located, which can be either $\mathbf{F}_{\frac{1}{2}}$ or $\mathbf{F}_{M+\frac{1}{2}}$ according to Fig. 3.7. There are three possible modelling configurations for a lymphatic valve. It can be the leftmost or rightmost valve of a collector, or it can be interposed between two lymphangions. In every case, the flow across the lymphatic valve is calculated from (3.52), where the pressure difference Δp in (3.46) is evaluated at the current time t^n using either the two lymphangions, or one of the lymphangions and a prescribed time-varying pressure. Specifically, at $t = t^n$ the pressure difference $\Delta p(t^n)$ is

$$\Delta p(t^n) = p_u(t^n) - p_d(t^n)\,, \tag{3.59}$$

where values $p_u(t^n)$ and $p_d(t^n)$ are

$$p_u(t^n) := \begin{cases} p_M^n\,, & \text{lymphatic pressure at } i = M,\ t = t^n, \\ P_{in}(t^n)\,, & \text{prescribed upstream pressure at } t = t^n, \end{cases} \tag{3.60}$$

and

$$p_d(t^n) := \begin{cases} p_1^n\,, & \text{lymphatic pressure at } i = 1,\ t = t^n, \\ P_{out}(t^n)\,, & \text{prescribed downstream pressure at } t = t^n, \end{cases} \tag{3.61}$$

where pressures p_M^n and p_1^n refers to the upstream and downstream lymphangions, respectively, and P_{in} and P_{out} are prescribed functions of time. The three possible configurations are summarized here

$$\Delta p(t^n) := \begin{cases} P_{in}(t^n) - p_1^n\,, & \text{leftmost valve,} \\ p_M^n - p_1^n\,, & \text{valve between two lymphangions,} \\ p_M^n - P_{out}(t^n)\,, & \text{rightmost valve.} \end{cases} \tag{3.62}$$

Once we numerically solve system (3.52), the flow across the valve at the future time q_v^{n+1} is determined.

In the present chapter, to find A^* and calculate the numerical flux at the boundary we follow the numerical methodology proposed by Alastruey et al. [Alastruey 2008]. This method has already been used in [Müller 2014, Contarino 2016]. To find A^*, we solve the following non-linear algebraic equation based on the Riemann invariant

$$\mathscr{F}(A^*) := q_v^{n+1} + A^* \left(-u^n + \beta \int_{A^n}^{A^*} \frac{c(\tau)}{\tau} \mathrm{d}\tau \right) = 0\,, \tag{3.63}$$

using the Newton-Raphson iterative method. A^n and u^n are the cross-sectional area and the velocity at the cell adjacent to the boundary at current time $t = t^n$, q_v^{n+1} is the known flow rate across the valve and

$$\beta = \begin{cases} -1 & \text{downstream lymphangion}\,, \\ 1 & \text{upstream lymphangion}\,. \end{cases} \tag{3.64}$$

Then the numerical flux at the boundary is

$$\mathbf{F}_{\frac{1}{2} \text{ or } M+\frac{1}{2}} = \mathbf{F}(\mathbf{Q}^*)\,, \tag{3.65}$$

where

$$\mathbf{Q}^* = \begin{bmatrix} A^* \\ q_v^{n+1} \end{bmatrix}\,. \tag{3.66}$$

As shown in Fig. 3.8, when a valve is interposed between two lymphangions, then the non-linear problem (3.63) has to be solved twice: one for the upstream lymphangion ($\beta = 1$) and one for the downstream lymphangion ($\beta = -1$).

Imposed pressure at boundaries

The numerical procedure to impose a pressure in one of the extremities of a lymphatic vessel is similar to the coupling method for valves and lymphangions. Consider a time-varying pressure $p_I(t)$

at a terminal interface. From pressure $p_I(t)$, cross-sectional area $A_I(t)$ can be calculated by using the inverse of the tube law (3.2). The flow rate q^* can be found by applying the Riemann invariants as described in 3.2.4, and in this case it can be explicitly calculated as

$$q^* = A_I(t^n)\left(u^n - \beta\int_{A^n}^{A_I(t^n)} \frac{c(\tau)}{\tau}\mathrm{d}\tau\right), \tag{3.67}$$

where A^n, u^n and β are the cross-sectional area and the velocity at the cell adjacent to the boundary at current time $t = t^n$ and β is given by Eq. (3.64). As before, the numerical flux at the boundary is given by (3.65) with

$$\mathbf{Q}^* = \begin{bmatrix} A_I(t^n) \\ q^* \end{bmatrix}. \tag{3.68}$$

Numerical method for the systems of ODEs

The systems of ODEs (3.52) and (3.24) were numerically solved with a second-order implicit Runge-Kutta method using the Lobatto IIIC method. The Butcher tableau is

0	1/2	-1/2
1	1/2	1/2
	1/2	1/2

In the next section, we present the coupling of the systems of PDEs and ODEs, through an algorithm description.

Complete algorithm

Here we provide the complete algorithm to update the solution from time t^n to time $t^{n+1} = t^n + \Delta t$. When not specified, the initial conditions are: $p(x,0) = P_{in}(0)$, $u(x,0) = 0$, $v(0) = 0.1$, $w(0) = s(0) = I(0) = 0$ and $q_v(0) = \xi(0) = 0$.

1. Assume data for all variables at $t = t^n$.
2. Calculate the time step Δt as explained in Section 3.2.4.
3. Evolve the valve flow q and valve state ξ of each lymphatic valve from time t^n to t^{n+1} by applying a second-order implicit Runge-Kutta method to the system of ODEs (3.52) and assuming the pressure difference Δp at time t^n.
4. Calculate the numerical fluxes at the boundaries $\mathbf{F}_{\frac{1}{2}}$ and $\mathbf{F}_{M+\frac{1}{2}}$ of each lymphangion, as described in Sections 3.2.4 and 3.2.4, using the lymphatic valve flow rates at time t^{n+1}.
5. Using the contraction state s at the current time t^n, calculate the numerical fluxes $\mathbf{F}_{i+\frac{1}{2}}$ within each domain of the lymphangions using the SLIC method (Section 14.5.3 of [Toro 2009]).
6. Using the contraction state s at the current time t^n, calculate the numerical sources $\mathbf{S}_i$ within each domain of the lymphangions using a second-order method in space and time (Chapter 19 of [Toro 2009]).

7. Update the conserved variables $\mathbf{Q}$ of the PDEs of each lymphangion from time t^n to t^{n+1} according with finite volume formula (3.55).
8. Evolve the variables of the EFMC model of each lymphangion from time t^n to t^{n+1} by applying a second-order implicit Runge-Kutta method to the system of ODEs (3.24) and using the space-time averaged cross-sectional area and WSS at time t^{n+1}.

The EFMC model and the system of PDEs are coupled through the contraction state s. The variable s gives the actual value of the coefficient $K(t)$ in Eq. (3.5) to be used to calculate the physical flux in Eq. (3.12). Observe that even though we use second-order methods for every model, the accuracy of the global algorithm is formally of order one. This is caused by the coupling methods. As a matter of fact, we couple the set of ODEs and PDEs using only a first-order method. There are more sophisticated high-order coupling methods in the literature, see for instance [Borsche 2016].

3.2.5 Sensitivity Analysis

The method is divided into a local and global analysis. In the local analysis we calculated N local sensitivity matrices $S^k_{i,j}$, for $k = 1,\dots,N$, as follows: starting from the reference value in Table 3.1, we randomly varied each parameter from 70% to 130% and obtained a new set of parameters. Here, the baseline value for k_{NO} was set to 0.5. With this varied set of parameters, we calculated the local sensitivity matrix as follows

$$S^k_{i,j} = \left| \frac{x_i}{P_j(\mathbf{X})} \right| \frac{\partial P_j(\mathbf{X})}{\partial x_i} \times 100\,, \tag{3.69}$$

where $\mathbf{X} = (x_1, x_2, \dots, x_m)$ is the vector of the varied model parameters, $\mathbf{P} = (P_1, P_2, \dots, P_n)$ is the vector of the lymphatic indices and $\mathbf{S}^k = \left(S^k_{i,j}\right)_{i,j}$ is local sensitivity matrix. The value $S^k_{i,j}$ represents the non-dimensional relative change in P_j to the relative change in parameter x_j, expressed as a percentage. If the model parameter x_i does not influence index P_j, then $S^k_{i,j}$ will be almost zero. Viceversa, if there is a significant influence of x_i on P_j, then the absolute value of $S^k_{i,j}$ will be greater than zero. For instance, if 1% change in x_i leads to 1% change in P_j, then $S^k_{i,j}$ is 100%. A positive sign of $S^k_{i,j}$ indicates that an increase of parameter x_i induces an increase of index P_j. Viceversa, a negative sign of $S^k_{i,j}$ indicates that an increase of parameter x_i induces a decrease of index P_j.

Subsequently, in the global analysis we performed a statistical analysis of $S^k_{i,j}$ by calculating its mean $\bar{S}_{i,j}$ and its standard deviation $\sigma_{i,j}$. A large standard deviation $\sigma_{i,j}$ indicates a strong correlation of the studied parameter with the remaining parameters in determining the sensitivity index. To calculate $\bar{S}_{i,j}$ and $\sigma_{i,j}$, we removed possible outliers by discarding the data below the 3rd percentile and above the 97th percentile.

The partial derivative in Eq. (3.69) was approximated using a second-order finite difference method based on a percentage change of the parameter as follows:

$$S^k_{i,j} \approx \frac{\operatorname{sgn}(x_i)}{\left|P_j(\mathbf{X})\right|} \frac{P_j\left(\mathbf{X}^{i,\varepsilon_+}\right) - P_j\left(\mathbf{X}^{i,\varepsilon_-}\right)}{2\varepsilon} \times 100\,, \tag{3.70}$$

where $\mathbf{X}^{i,\varepsilon_\pm} = (x_1, \dots, x_i(1 \pm \varepsilon), \dots, x_m)$. The parameter ε was chosen as $\varepsilon = 0.05$. Compared to [van Griensven 2006], we did not constructed a stratified sampling space, but rather a simple random variation in the considered range.

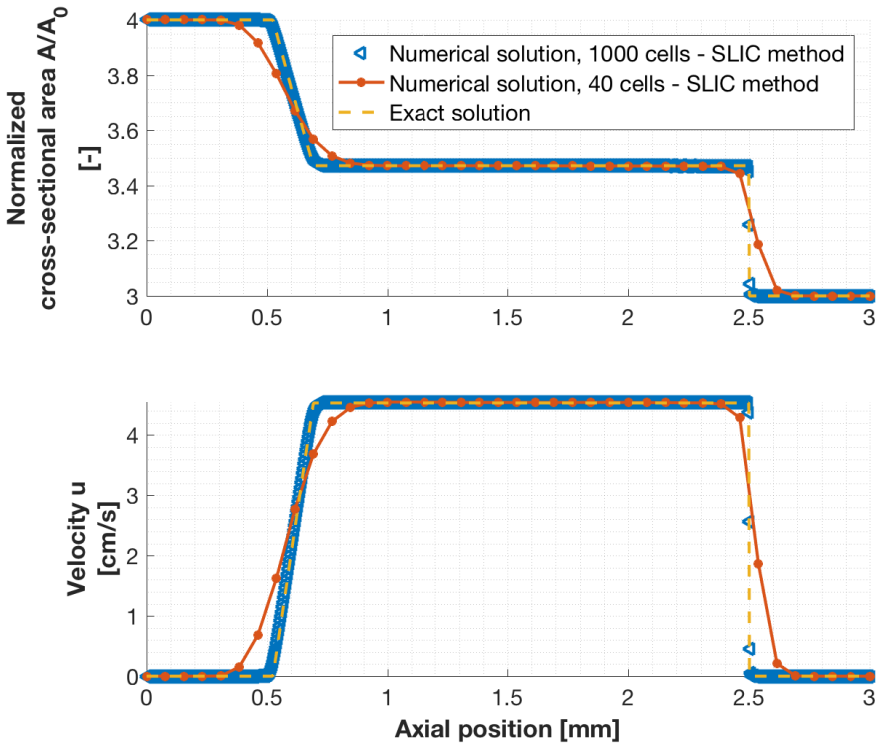

Figure 3.9: Riemann problem for a single lymphangion without contractions. Top and bottom frames show the following: normalised cross-sectional area and velocity at a fixed prescribed time. We compare the numerical results with the exact solution. The initial conditions are given in Section 3.3.1 and the output time is $t_{output} = 0.003\ s$. Here we used $M = 40$ and $M = 1000$ computational cells to discretize the lymphangion.

3.3 Results

In this section, we assemble all components of the model and show three selected test problems. Table 3.1 gives parameters used in the numerical simulations. The numerical methods to solve the coupled system of PDEs and ODEs are described in Section 3.2.4.

3.3.1 Test problem with piecewise initial condition: a Riemann problem

Here we consider a Riemann problem for the set of PDEs for a single lymphangion without valves. The Riemann problem is a particular Cauchy problem where the initial conditions are piecewise constant with a single discontinuity. The exact solution in subcritical regime is available for this PDE system but is not reported here. For the exact solution of the Riemann problem for arteries and veins see [Toro 2011, Toro 2013, Spiller 2017]. Here, the chosen initial condition for A and u is

$$A(x,0) = \begin{cases} A_L = 4A_0\ , & x < \frac{L}{2}\ , \\ A_R = 3A_0\ , & x > \frac{L}{2}\ , \end{cases} \tag{3.71}$$

where L is the lymphangion length and A_0 is the cross-sectional area at equilibrium, and $u(x,0)=0$. We assumed no contractions, dynamic viscosity $\mu=0$ and transmissive boundary conditions. Fig. 3.9 shows the numerical results using $M=40$ and $M=1000$ cells and the exact solution at the output time $t_{output}=0.003\ s$. The numerical solution with $M=40$ is comparable with the exact solution, which is composed of a left rarefaction and a right shock. The numerical solution with $M=1000$ confirms that the numerical solution converges to the exact solution. This result is typical of a 2×2 non-linear system of hyperbolic differential equations and is comparable with the Riemann problem for the Euler equations, shallow water equations and the blood flow equations [Toro 2009].

3.3.2 Representative test problems for lymphatic vessels

Here we show results for three representative test problems. In the first test, we show a numerical example of a lymphatic cycle. The second test highlights the frequency-transmural pressure relationship. The third test shows the negative chronotropic effect given by the WSS.

Test 1: representative case of a single lymphangion

Here we show a representative test of a single lymphangion, see top of Fig. 3.10, where the EFMC model, the valve model and the one-dimensional model for lymph flow are coupled. As shown in Fig. 3.10, as soon as the stimulus I goes beyond the unstable spiral-node region and falls into the unstable node region, an action potential occurs. The fast depolarization at 0.5 s is followed by a plateau period of $\approx$ 1.2 s, during which the following phenomena occur in sequence: 1) stimulus I exponentially decreases to zero; 2) the contraction state s increases and reaches its maximum value at the end of the plateau; 3) the internal pressure increases and induces 4) the closure of the upstream valve with a short transient period of backflow caused by the valve closure; 5) the downstream valve opens; 6) the downstream transvalve flow rate increases; 7) the diameter of the lymphangion decreases. After the hyperpolarization at $\approx$ 1.6 s and during the repolarization phase of $\approx$ 1.4 s, the contraction state exponentially decreases to zero. This causes the following chain of events: 1) the internal pressure decreases below the downstream pressure P_{out}; 2) the downstream valve closes; 3) there is a short period of reflux from the downstream valve determined by the valve closure which causes 4) the diameter to increase somewhat at $\approx$ 1.5 s; 5) the internal pressure decreases below the upstream pressure P_{in}; 6) the upstream valve opens; 7) the transvalve flow from the upstream valve increases; 8) the diameter of the lymphangion increases. From here on, the stimulus starts to increase until the next action potential is triggered.

Diameter decreases almost uniformly throughout the lymphangion, as shown in the space-time representation in Fig. 3.11. During the systolic phase, flow rate reaches its maximum at the downstream side, while it reaches its minimum at the upstream one. The red and blue lines in the flow rate are similar to the valve flow rates shown in Fig. 3.10. The diameter is practically independent of the space variable. This is due to the approximation $K=K(t)$ throughout the domain. The results shown in Fig. 3.11 highlight that the mathematical model gives quantitative information throughout the domain of the lymphangion.

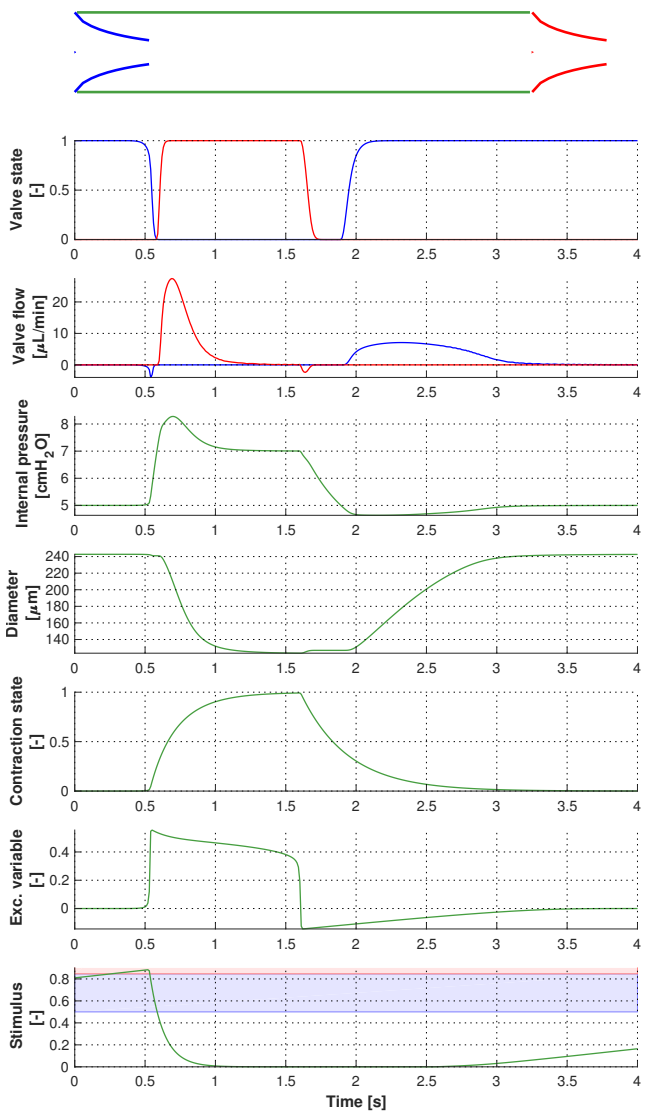

Figure 3.10: Test 1: representative case of a single lymphangion. From the top to the bottom frames we show the following: illustration of the lymphangion, time-varying valve states (open $\xi = 1$ and closed $\xi = 0$), flow rates across the valves, internal pressure, diameter, contraction state, excitation variable and stimulus. Pressure and diameter were calculated at the centre of the lymphangion. The colors shown from the second to the last panels refer the colour configuration shown in the top panel. In the bottom panel, blue and red shaded areas illustrate the *unstable spiral-node* and the *unstable node* regions, respectively. In this test, we used $M = 100$ computational cells to discretize the lymphangion. Boundary pressures: $P_{in} = 5$ cmH$_2$O and $P_{out} = 7$ cmH$_2$O. Results are shown over a representative lymphatic cycle.

Test 2: contraction frequency increases as the intraluminal pressure increases

The test shown here was inspired by the experiments performed in several works [Davis 2011, Davis 2012, Scallan 2012] where time-varying pressures were imposed at the boundaries of the

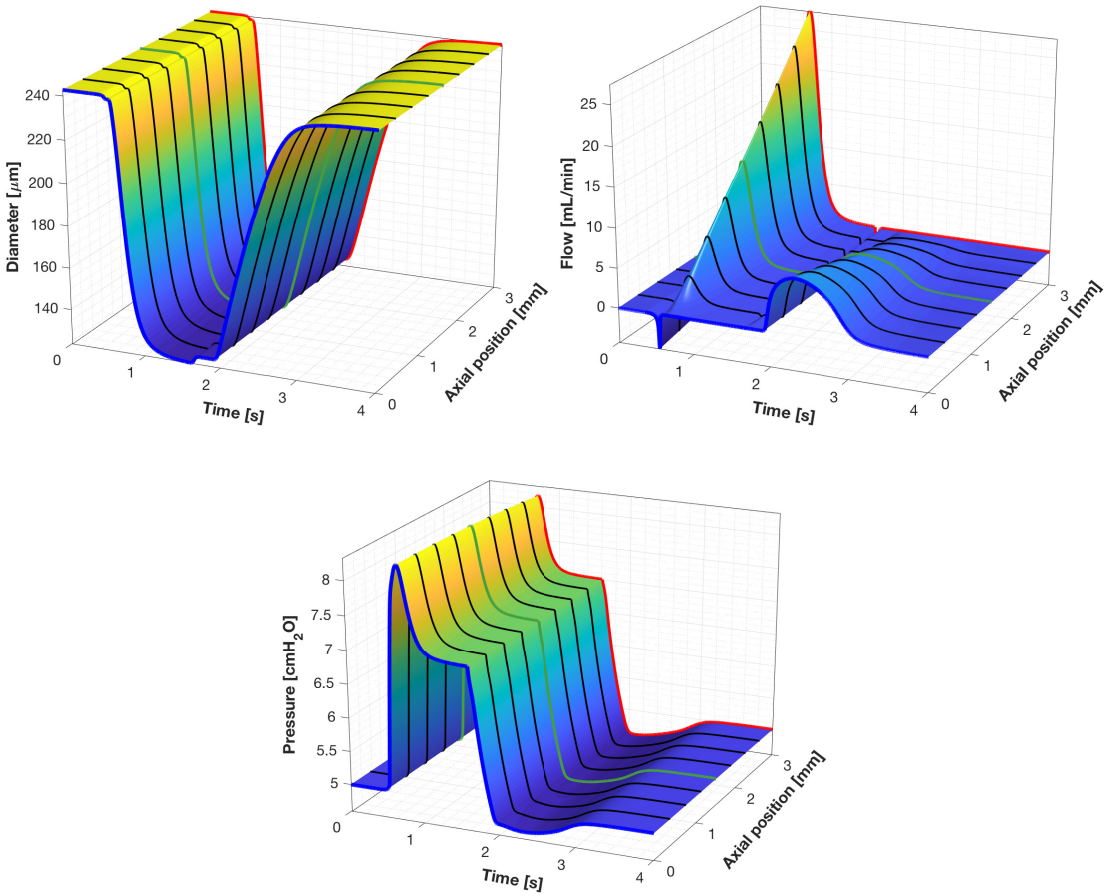

Figure 3.11: Test 1: representative case of a single lymphangion (space-time). Here we show numerical results in space and time for diameter, flow and pressure. We applied the boundary conditions explained in 3.2.4. Blue and red lines represent the numerical solutions close to the upstream and downstream valves, respectively. The green line depicts the numerical solution at the centre of the lymphangion. In this test, we used $M = 501$ computational cells to discretize the lymphangion. Boundary pressures: $P_{in} = 5$ cmH_2O and $P_{out} = 7$ cmH_2O. Results are shown over a representative lymphatic cycle.

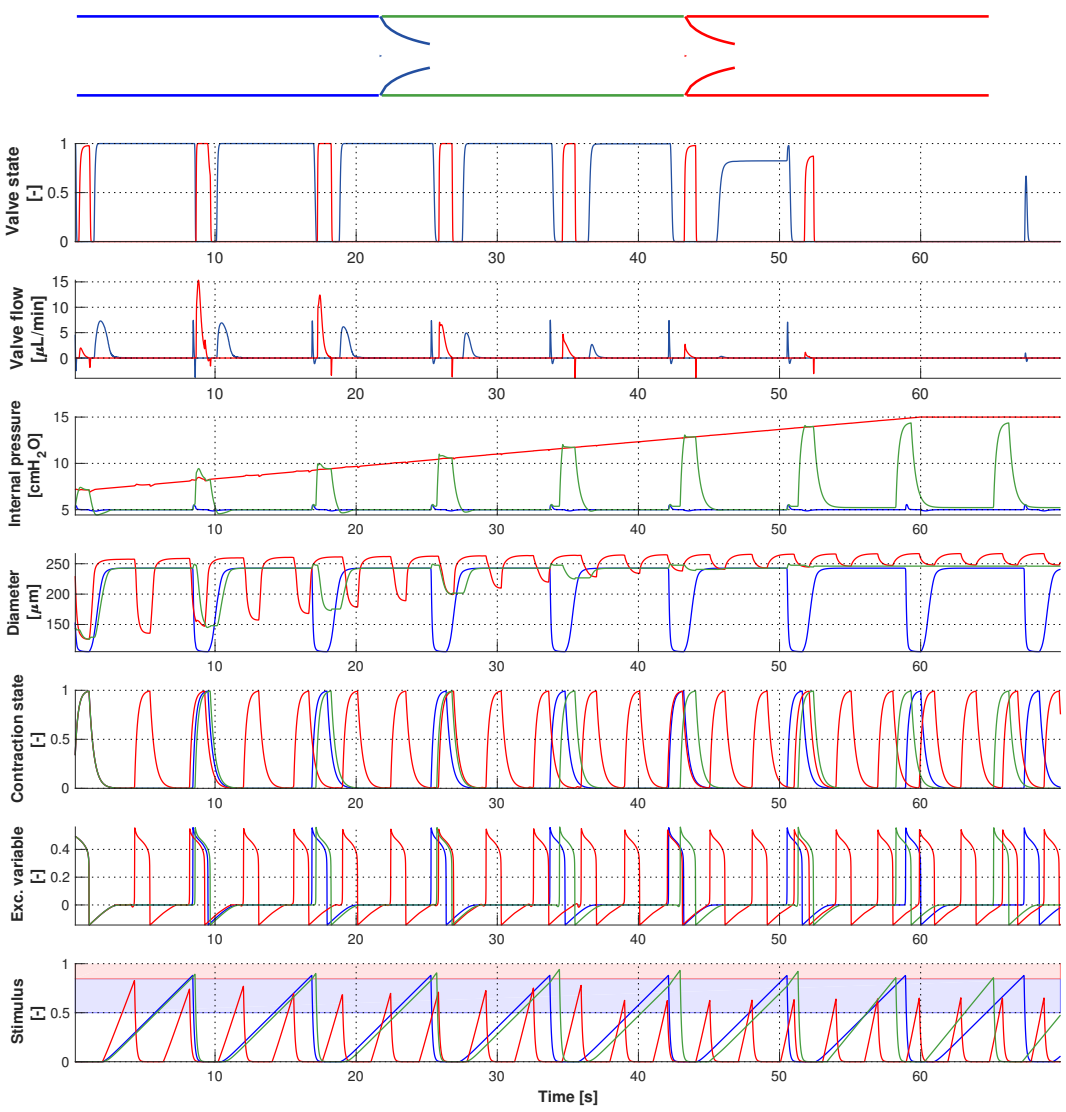

Figure 3.12: Test 2: contraction frequency increases as the intraluminal pressure increases. Time-varying boundary pressures can be found in Eq. (3.72). See caption of Fig. 3.10 for explanation of traces. The lymphangion (green lines) tries to overcome the time-varying downstream pressure. The frequency of contraction of the downstream part-lymphangion (red lines) increases with the increase of the imposed boundary pressure. At a certain output pressure ($\approx$ 14 cmH_2O), the lymphangion cannot open the downstream valve, forcing the flow through the valves to become zero.

collector. More specifically, this test emulates the *ramp-wise* P_{out} *elevation* shown in [Davis 2012]. We simulated a collector composed of one complete lymphangion and two part-lymphangions with

an overall number of two valves, and we imposed the following time-varying pressures

$$P_{out}(t) = \begin{cases} \frac{p_2 - p_1}{t_1}(t - t_1) + p_2 \ , & t < t_1 \ , \\ p_2 \ , & t_1 < t < t_{output} \ , \end{cases} \tag{3.72}$$

$$P_{in}(t) = p_{in} \ , \tag{3.73}$$

where $p_1 = 7$ cmH$_2$O, $p_2 = 15$ cmH$_2$O, $p_{in} = 5$ cmH$_2$O, $t_1 = 60$ s, $t_{output} = t_1 + 10$ s. Applying the boundary conditions explained in 3.2.4, the inlet pressure P_{in} was imposed at the leftmost interface of the upstream part-lymphangion, while the output pressure was imposed at the rightmost interface of the downstream part-lymphangion. Only an adverse transaxial-pressure difference is taken into account.

Even though the upstream and downstream part-lymphangions contract, their pressures are controlled, as shown in Fig. 3.12. The downstream pressure (red line) follows the behaviour of the imposed output pressure P_{out}, while the upstream pressure (blue line) is almost constantly P_{in}. The lymphangion responds to these changes in boundary pressures (green line). Initially, both valves close and open, but when the downstream pressure P_{out} reaches a certain value (≈ 14 cmH$_2$O), the lymphangion cannot open the downstream valve anymore. In the space-time representation, our model predicts sudden diameter changes at valve locations (result not shown), which is motivated by our simplified valve dynamics.

Since the pressure of the downstream part-lymphangion increases during the numerical simulation, its frequency of contraction rises as well. The contraction frequency of the lymphangion is not affected by the increase in the frequency of the downstream part-lymphangion. This comes from having neglected the interaction between adjacent lymphatic vessels in the EFMC model. In reality, the electrical signal in the lymphatic wall would travel through gap-junctional communications. The only interaction which would alter the frequency of contractions in the current mathematical model comes from changes in the intraluminal pressure and WSS. Therefore, this computational result highlights that the current EFMC model can only model cases in which lymphangions are electrically decoupled.

In our computational model, lymphatic valves prevent retrograde flow at any transvalve-pressure difference, apart from a short transient period determined by the valve closure. This is particularly evident at ≈ 50 s, where the lymphangion cannot entirely eject the lymphatic fluid into the downstream part-lymphangion and the diameter increases as the upstream part-lymphangion contracts. These coupled events induce the frequency of contraction of the lymphangion to increase somewhat, shortening the preceding diastole of the very last contraction.

This numerical result shows that: 1) the frequency of contractions depends on the intraluminal pressure and 2) the lymphangion tries to overcome the downstream time-varying pressure by increasing the end-systolic pressure, but this is possible up to a certain threshold. These findings confirm that the mathematical model partially mimics experimentally observed behaviours [Davis 2012].

Test 3: contraction frequency decreases with increasing WSS

The test proposed here simulates a collector composed of a one complete lymphangion and two part-lymphangions and highlights the effect of the WSS on the frequency of contractions. As done for the test 2, we imposed the following time-varying pressures at the terminal interfaces of the

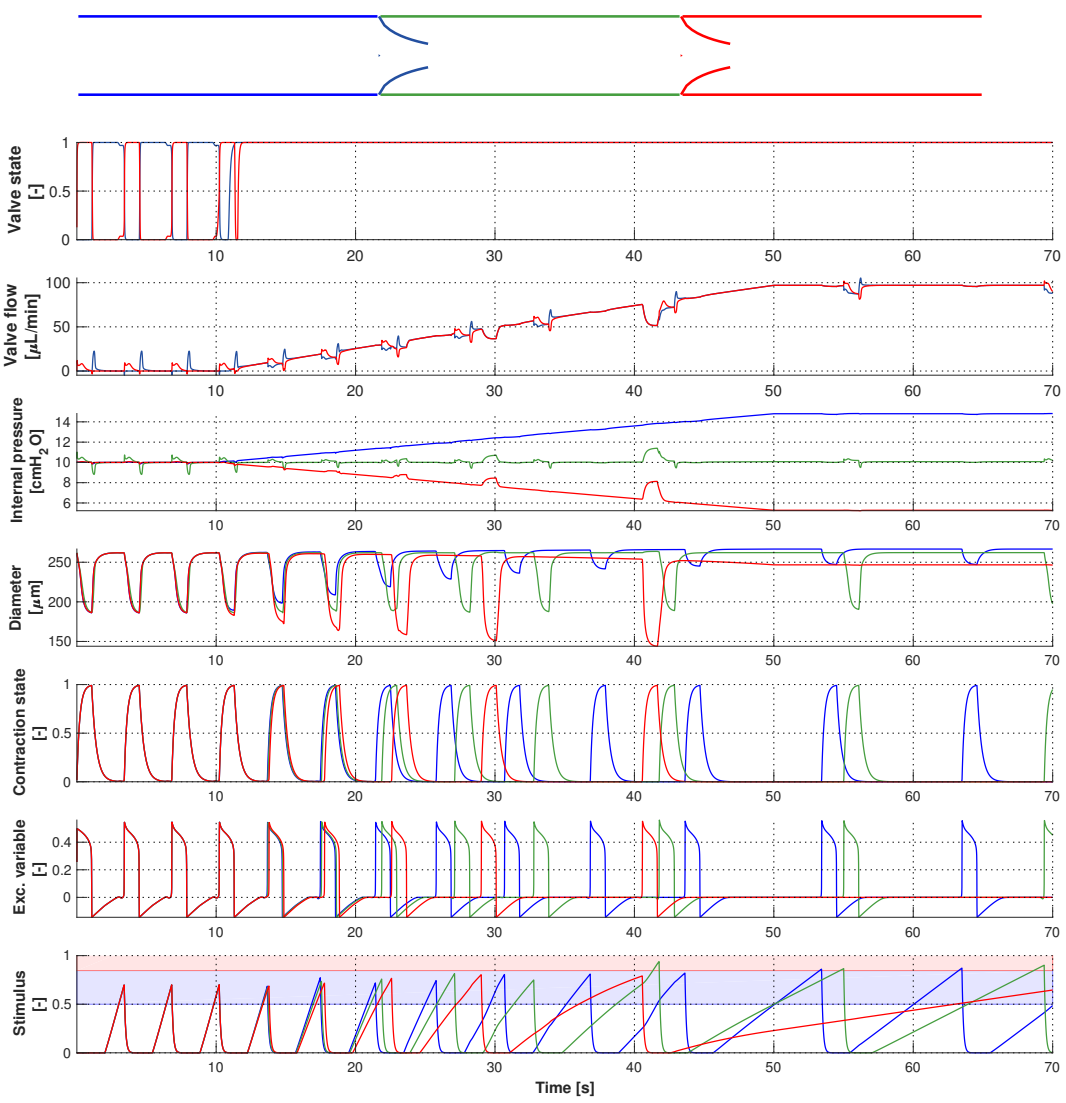

Figure 3.13: **Test 3: contraction frequency decreases with increasing WSS.** Time-varying boundary pressures can be found in Eq. (3.74). See caption of Fig. 3.10 for explanation of traces. When a favourable pressure gradient occurs, flow increases for all lymphatic vessels, reducing the rate at which the stimulus I increases and decreasing the frequency of contractions, even in the upstream part-lymphangion where the transmural pressure increases. For this test, we set $\tau_{NO} = 3$ dyne cm^{-2} and $k_{NO} = 0.9$.

collector

$$P_{out}(t) = \begin{cases} p_1 \,, & t < t_1 \,, \\ \frac{p_2^{out} - p_1}{t_2 - t_1}(t - t_2) + p_2^{out} \,, & t_1 < t < t_2 \,, \\ p_2^{out} \,, & t_2 < t < t_{output} \,, \end{cases} \tag{3.74}$$

$$P_{in}(t) = \begin{cases} p_1 \,, & t < t_1 \,, \\ \frac{p_2^{in} - p_1}{t_2 - t_1}(t - t_2) + p_2^{in} \,, & t_1 < t < t_2 \,, \\ p_2^{in} \,, & t_2 < t < t_{output} \,, \end{cases} \tag{3.75}$$

where $p_1 = 10$ cmH$_2$O, $p_2^{out} = 5$ cmH$_2$O, $p_2^{in} = 15$ cmH$_2$O, $t_1 = 10$ s, $t_2 = t_1 + 40$ s and $t_{out\,put} = t_2 + 20$ s. This test emulates the experimental setup of Gashev et al. [Gashev 2002]: we imposed a range of transaxial pressure differences maintaining an almost constant average transmural pressure of the lymphangion.

Initially, all lymphatic vessels contract at the same frequency and share the same internal pressure ≈ 10 cmH$_2$O (see Fig. 3.13). When the upstream pressure P_{in} rises and the downstream pressure P_{out} decreases, the lymphatic valves open, the transvalve flows increase while the transmural pressure of the lymphangion does not change greatly. The increment on the WSS gives a negative chronotropic effect on all lymphatic vessels, decreasing the frequencies of contractions. The lymphangion contracts at slower rates as lymph flow increases. Since the upstream part-lymphangion has a greater internal pressure (≈ 15 cmH$_2$O at the centre), its rate of contraction is greater than the remaining vessels. The downstream part-lymphangion has a lower contraction frequency since its internal pressure is lower. These variations come from changes in the rate of increase in time of stimulus I within the activation region. For instance, the downstream part-lymphangion (red lines) has substantial changes on the dynamics of stimulus I after 27 s and 41 s, leading the contraction frequency to decrease to almost ≈ 2 min^{-1}. This result confirms that the mathematical model emulates the experimentally observed effect of the WSS on the frequency of contraction [Gashev 2002].

3.3.3 Pressure versus normalised cross-sectional area (PA) plots for a single lymphangion

The aim of this exercise is to show that the numerical results of the mathematical model mimic the experimental measurements of the pressure-volume relationship [Davis 2012]. As shown in Fig. 3.14, the computational results show a qualitatively good agreement with [Davis 2012, Scallan 2012]. As the downstream pressure P_{out} increases, the PA plots shrink and the systolic pressure increases. The systolic pressure can increase up to a certain level, depending on the baseline pressure. In the current case the maximum systolic transmural pressure is ≈ 11 cmH$_2$O and decreases as P_{in} decreases. For instance, for $A/A_0 = 4$ and $P_{in} \approx 4$ cmH$_2$O, the maximum systolic reachable transmural pressure is ≈ 8 cmH$_2$O.

3.3.4 Analysis of lymphatic indices by varying P_{in} and P_{out}

The aim of this study is to quantify lymphatic indices shown in Table 3.2 for several combinations of P_{in} and P_{out}, both in the range 1 to 14 cmH$_2$O. To describe the computational results shown in Fig. 3.15, we divide the P_{in}-P_{out} space into two regions: 1) the adverse transaxial-pressure difference $\Delta P = P_{in} - P_{out} < 0$ region (lower triangle) and 2) the favourable transaxial-pressure difference $\Delta P = P_{in} - P_{out} > 0$ region (upper triangle).

Adverse pressure difference $\Delta P = P_{in} - P_{out} < 0$. Here the upstream and downstream valves open and close during the lymphatic cycle. The frequency increases as P_{in} rises, and this is in agreement with Fig. 3.6. This comes from muscle-stretch feedback from the EFMC model in Eq. (3.26). The frequency does not increase when P_{out} rises. This might be surprising because it is well-known that contraction-waves propagate between lymphangions through gap-junctional communications [Zawieja 1993]. However, for the sake of simplicity, the gap-junctional communications

	Index	Formula	Description	Units
ESD	End-Systolic Diameter	-	Diameter at the end of lymphatic contraction	μm
EDD	End-Diastolic Diameter	-	Diameter at the beginning of filling	μm
ESP	End-Systolic Pressure	-	Pressure at the end of lymphatic contraction	cmH_2O
EDP	End-Diastolic Pressure	-	Pressure at the beginning of filling	cmH_2O
ESV	End-Systolic Volume	$\pi L\left(\frac{ESD}{2}\right)^2$	Volume at the end of lymphatic contraction	nL
EDV	End-Diastolic Volume	$\pi L\left(\frac{EDD}{2}\right)^2$	Volume at the beginning of filling	nL
FREQ	Frequency	-	Frequency of lymphatic contractions	min^{-1}
EF	Ejection Fraction	$1-\frac{EDV}{ESV}$	Fractional amount of ejected lymph	-
SV	Stroke Volume	EDV − ESV	Ejected volume amount	nL
FPF	Fractional Pump Flow	EF × FREQ	Fractional change in lymphatic volume per minute	min^{-1}
CPF	Calculated Pump Flow	SV × FREQ	Flow produced by lymphatic contraction	$\mu L\ h^{-1}$
PD	Pulse Diameter	EDD − ESD	Difference between end-diastolic and end-systolic diameter	μm
SW	Stroke Work	$\int P\mathrm{d}V$	Area inside the pressure-volume loop	nL cmH_2O
PP	Pulse Pressure	ESP − EDP	Pressure amplitude generated by a lymphatic contraction	cmH_2O
WSS	Time-averaged Wall Shear Stress	$\frac{1}{t_2-t_1}\int_{t_1}^{t_2}\tau\left(\frac{L}{2},t\right)\mathrm{d}t$	Averaged WSS during a lymphatic cycle	dyne cm^{-2}
q_{mean}	Time-averaged Flow	$\frac{1}{t_2-t_1}\int_{t_1}^{t_2}q\left(\frac{L}{2},t\right)\mathrm{d}t$	Averaged flow during a lymphatic cycle	$\mu L\ h^{-1}$

Table 3.2: Lymphatic indices. t_1 and t_2 correspond to the initial and ending time of the lymphatic cycle and L is the lymphangion length. Diameter, pressure and flow were calculated at the centre of the lymphangion.

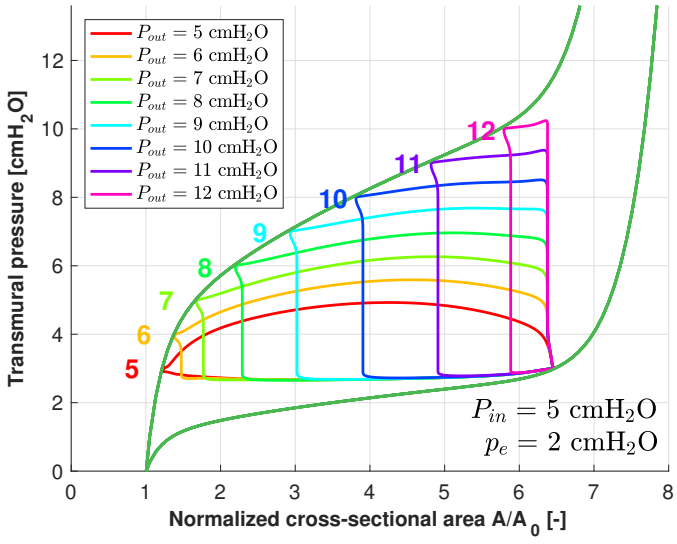

Figure 3.14: Transmural pressure against normalised cross-sectional area (PA) plots during lymphatic contractions. Here we simulated a single lymphangion with different downstream pressures P_{out} from 5 to 12 cmH$_2$O, while keeping fixed the upstream pressure P_{in} to 5 cmH$_2$O. The figure also shows the tube laws at relaxed and contracted states. Pressures and diameters were calculated at the centre of the lymphangion. In this test, we used $M = 20$ computational cells to discretize the lymphangion.

between lymphangions have not been modelled in this chapter. EF tends to decrease as P_{out} increases, while increases when P_{in} increases. FPF combines both frequency and EF: it increases when P_{in} rises, and it decreases when P_{out} increases. The maximum of FPF is when $P_{in} \approx P_{out} \approx 8$ cmH$_2$O. For larger pressures, FPF decreases. The results for FPF are not comparable with those shown by Davis et al. [Davis 2012], as in our results the frequency remains constant when P_{out} rises. The SV and PD follow the same behaviour of EF. ESD increases only when P_{out} rises, and it remains constant when P_{in} increases. On the contrary, EDD remains constant when P_{out} increases, and this is in agreement with [Davis 2012]. SW is maximum for $P_{out} \approx 8.5$ cmH$_2$O and $P_{in} \approx 5$ cmH$_2$O, and it tends to decrease elsewhere. Mean flow and CPF are comparable almost everywhere.

Favourable pressure difference $\Delta P = P_{in} - P_{out} > 0$. Here the upstream and downstream valves remain open for most of the time during the lymphatic cycle (results not shown). Averaged flow exhibits a highly non-linear behaviour when ΔP changes sign. Lymph flow is generated only by muscle contractions when ΔP is negative, with values < 1 μL min^{-1}. However, for positive sign of ΔP, lymph flow is dominated by pressure forces with permanently opened valves, with values over hundreds of μL min^{-1}. Mean flow increases as P_{in} rises, and it decreases as P_{out} increases. Subsequently, the WSS rises when P_{in} increases, and this gives a negative chronotropic effect on the frequency; this comes from the function f_{NO} in (3.26). CPF differs from the mean flow insofar as the CPF only takes into account the flow given by contractions. ESD and EDD increase when P_{in} and P_{out} rise. EF, SV and PD share a similar behaviour and reach their maximum values at $P_{in} = P_{out} \approx 6$ cmH$_2$O.

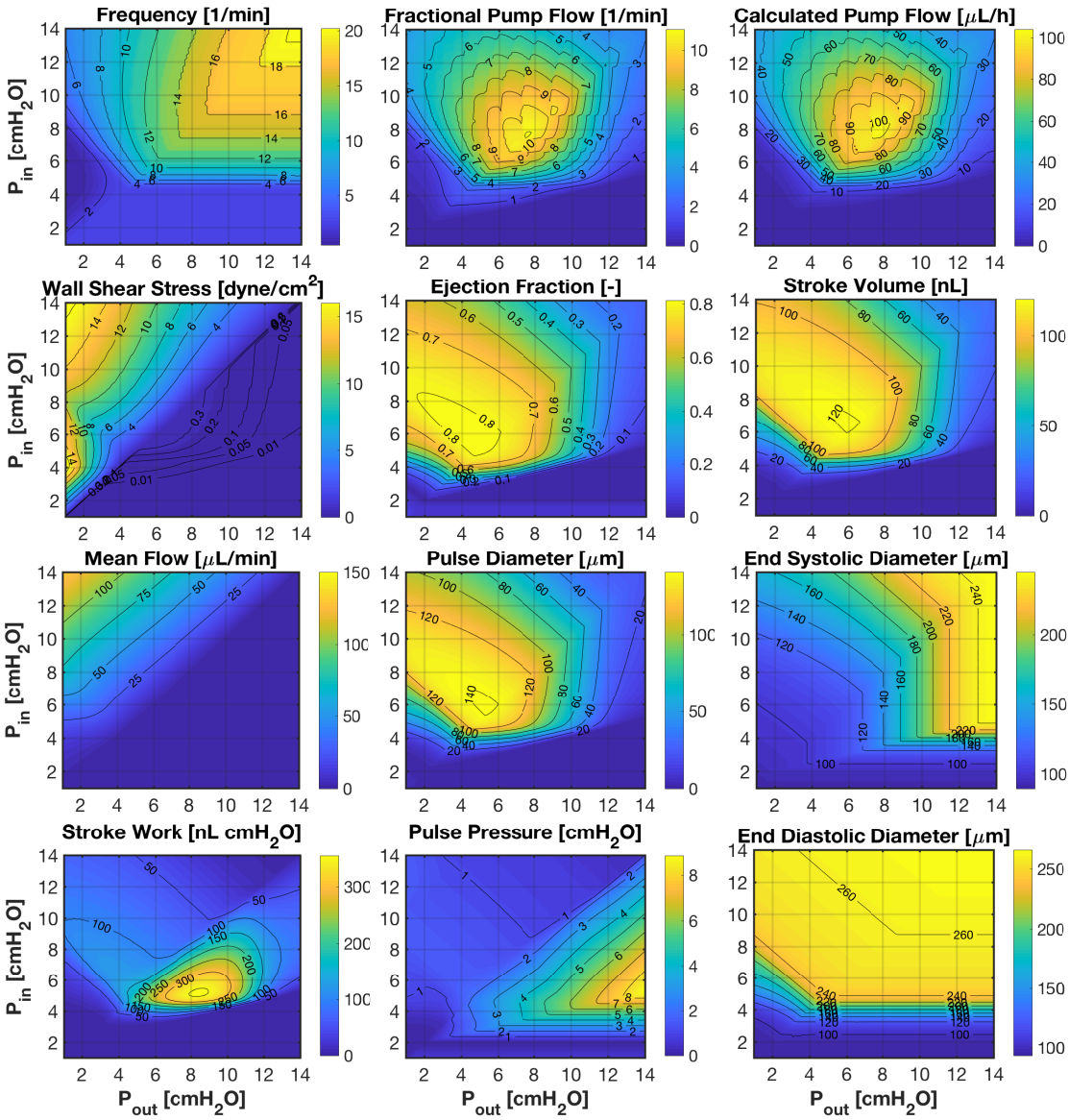

Figure 3.15: Counterplots of lymphatic indices in the $P_{in} - P_{out}$ plane. The indices shown are: frequency of contraction, FPF, CPF, WSS, EF, SV, mean flow, PD, ESD, SW, PP and EDD. See table 3.2 for the definition of the indices. We constructed a grid of points (P_{out}, P_{in}) with all possible combinations of $P_{in} = (1, 1.1, \ldots, 13.9, 14)$ and $P_{out} = (1, 1.1, \ldots, 13.9, 14)$. For each combination of P_{in} and P_{out}, we simulated a single lymphangion with two terminal valves, $t_{output} = 160\ s$ and $M = 20$ computational cells to discretize the lymphangion. The indices were calculated based on last cycle or the last two cycles, as appropriate, and using the values at the centre of the lymphangion. The total number of simulations was $131 \times 131 = 17161$. We applied the boundary conditions as explained in 3.2.4.

$P_{in} = 5$ - $P_{out} = 6$	Output parameter $\mathbf{P}(\mathbf{X})$	Frequency [min^{-1}]	EF [-]	SV [nL]	FPF [min^{-1}]	CPF [$\mu L\ h^{-1}$]	WSS [dyne cm^{-2}]	ESD [μm]	EDD [μm]	ESP [cmH_2O]	EDP [cmH_2O]	Mean Pressure [cmH_2O]	Mean Flow [$\mu L\ h^{-1}$]
Input parameter $\mathbf{X}$	$\bar{\mathbf{S}}$ [%]	10.14 ± 8.29	0.75 ± 0.04	92.79 ± 27.75	7.26 ± 5.91	55.46 ± 47.08	-0.26 ± 0.19	115.93 ± 16.28	229.09 ± 32.52	7.38 ± 0.36	5.01 ± 0.10	5.18 ± 0.15	43.55 ± 33.23
r_0 [μm]	47.19 ± 8.25	4.4 ± 7.0	-	335.0 ± 95.4	5.4 ± 7.9	295.5 ± 207.2	57.2 ± 36.0	130.4 ± 18.9	129.1 ± 18.1	-2.1 ± 5.2	8.9 ± 3.6	-	266.3 ± 186.9
a_1 [s^{-1}]	100.60 ± 17.71	3.3 ± 3.7	-	-	3.0 ± 3.5	5.0 ± 6.2	-1.8 ± 2.2	-	-	-	-	-	4.6 ± 6.1
a_2 [-]	0.50 ± 0.08	-76.7 ± 94.8	9.3 ± 13.3	16.9 ± 23.4	-63.3 ± 91.8	-100.6 ± 143.9	30.5 ± 60.2	-19.0 ± 27.0	-	2.8 ± 5.3	-	7.1 ± 3.5	-96.2 ± 138.4
a_3 [-]	24.94 ± 4.31	-20.7 ± 29.7	1.9 ± 2.7	3.8 ± 4.9	-17.6 ± 29.3	-27.6 ± 45.2	8.9 ± 19.1	-3.9 ± 5.5	-	-	-	1.6 ± 0.8	-26.6 ± 44.1
b_1 [s^{-1}]	3.01 ± 0.51	24.1 ± 35.0	-2.1 ± 3.1	-4.1 ± 5.7	20.3 ± 33.3	30.7 ± 50.4	-10.3 ± 21.0	4.0 ± 6.1	-	-	-	-1.5 ± 0.7	29.4 ± 48.3
c_1 [s^{-1}]	9.97 ± 1.71	-	2.1 ± 3.1	3.6 ± 5.4	1.3 ± 2.0	2.2 ± 3.5	-3.3 ± 4.3	-4.4 ± 6.4	-	1.7 ± 3.8	-	-	2.5 ± 4.1
c_2 [s^{-1}]	3.02 ± 0.52	10.4 ± 16.2	-	-	10.3 ± 16.0	18.6 ± 28.9	-6.8 ± 11.0	-	-	-	-5.2 ± 1.3	-	18.0 ± 27.6
R_I [s^{-1}]	0.10 ± 0.02	1.8 ± 1.5	-	-	1.8 ± 1.4	3.0 ± 2.6	-1.2 ± 1.2	-	-	-	-	-	3.0 ± 2.8
k_{rel} [s^{-1}]	10.07 ± 1.71	-	-	-	-	-	-	-	-	-	-	-	-
n_{Ca} [-]	9.99 ± 1.71	-31.1 ± 23.1	-	-	-30.2 ± 22.8	-49.9 ± 41.5	19.1 ± 15.0	-	-	-	-	-1.1 ± 0.9	-47.5 ± 39.4
λ_{Ca} [-]	2.76 ± 0.5	-437.4 ± 360.4	-	1.8 ± 4.2	-427.6 ± 353.8	-710.8 ± 620.2	279.8 ± 237.0	-	-	-19.0± 80.8	-	-16.8 ±10.4	-677.8 ± 587.6
k_{NO} [-]	0.49 ± 0.08	-	-	-	-	-	-	-	-	-	-	-	-
τ_{NO} [dyne cm^{-2}]	6.02 ± 1.03	-	-	-	-	-	-	-	-	-	-	-	-
n_{NO} [-]	1.20 ± 0.20	-	-	-	-	-	-	-	-	-	-	-	-
K_{vo} [$Pa^{-1}\ s^{-1}$]	1.00 ± 0.17	-	-	-	-	-	-	-	-	-	0.6 ± 0.5	-	-
K_{vc} [$Pa^{-1}\ s^{-1}$]	1.00 ± 0.18	-	-	-	-	-	-3.8 ± 2.4	-	-	-	-	-	6.2 ± 4.9
L_{eff} [μm]	495.54 ± 88.21	-1.9 ± 2.9	-	-	-2.3 ± 3.3	-3.6 ± 5.0	-1.6 ± 2.3	-	-	1.1 ± 2.6	-3.4 ± 1.6	-	2.4 ± 4.6
ρ [kg m^{-3}]	1010.53 ± 176.40	-	-	-	-	-	-	-	-	-	-	-	-0.5 ± 1.2
μ [cP]	1.00 ± 0.17	-2.2 ± 3.2	-	-	-2.7 ± 3.7	-4.2 ± 5.9	-56.3 ± 35.7	-	-	1.2 ± 2.8	-4.4 ± 1.8	-	2.7 ± 4.8
γ [-]	1.99 ± 0.35	-1.1 ± 1.7	-	-	-1.4 ± 2.0	-2.1 ± 3.0	-28.0 ± 17.9	-	-	0.5 ± 1.3	-2.2 ± 0.9	-	1.5 ± 3.1
K_{max} [Pa]	401.19 ± 69.55	-4.4 ± 6.6	27.2 ± 14.8	44.9 ± 24.1	15.7 ± 11.8	25.6 ± 19.5	-37.2 ± 23.7	-55.2 ± 25.6	-	3.8 ± 8.6	-	-	25.6 ± 19.4
K_{min} [Pa]	105.33 ± 17.95	-122.5 ± 108.7	-22.9 ± 19.3	-137.0 ± 88.6	-133.1 ± 109.9	-297.3 ± 223.5	89.5 ± 71.0	-	-42.5 ± 29.1	-1.3 ± 3.6	8.7 ± 3.1	-4.5 ± 3.7	-286.3 ± 213.7

Table 3.3: Sensitivity analysis of the one-dimensional lymph flow equations coupled to the EFMC model and valve dynamics. Adverse pressure difference case. The first column from the left shows parameters $\mathbf{X}$ of the model while the second column shows their means ± SDs. The first row from the top shows the studied indices $\mathbf{P}$ while the second row shows the resulting means ± SDs. Symbol "−" indicates that the absolute value of the sensitivity index $\bar{S}_{i,j}$ was less than 0.5 and therefore parameter x_i did not influence index P_j. Likewise, green-coloured parameters show an influence between 25 and 50, blue-coloured parameters show an influence between 50 and 100, and red-coloured parameters show an influence greater than 100. Results are shown using as mean ± SD. We calculated $N = 500$ local sensitivity matrices. We simulated a single lymphangion with two terminal valves, $t_{output} = 60\ s$ and $M = 20$ computational cells to discretize the lymphangion. Here we used $P_{in} = 5$ cmH_2O and $P_{out} = 6$ cmH_2O. The indices were calculated based on last cycle or the last two cycles, as appropriate, and using the values at the centre of the lymphangion. Definitions and technical details can be found in Section 3.2.5

P_{in} = 4 - P_{out} = 2	Output parameter $\mathbf{P}(\mathbf{X})$	Frequency [min^{-1}]	EF [-]	SV [nL]	FPF [min^{-1}]	CPF [$\mu L\ h^{-1}$]	WSS [dyne cm^{-2}]	ESD [μm]	EDD [μm]	ESP [cmH_2O]	EDP [cmH_2O]	Mean Pressure [cmH_2O]	Mean Flow [$\mu L\ h^{-1}$]
Input parameter $\mathbf{X}$	$\bar{\mathbf{S}}$ [%]	8.25 ± 12.10	0.29 ± 0.10	9.86 ± 5.33	2.16 ± 3.10	3.92 ± 5.63	-10.85 ± 1.48	97.34 ± 12.55	116.99 ± 16.64	3.48 ± 0.16	3.15 ± 0.05	3.16 ± 0.03	614.40 ± 314.22
r_0 [μm]	47.33 ± 7.83	-24.5 ± 7.6	0.6 ± 1.5	358.0 ± 194.0	-34.7 ± 14.3	284.7 ± 160.1	-80.3 ± 12.8	97.8 ± 12.6	106.8 ± 15.5	-	0.5 ± 0.2	-	485.9 ± 251.2
a_1 [s^{-1}]	98.38 ± 17.08	1.6 ± 6.1	-	-	2.3 ± 8.6	2.7 ± 10.1	-	-	-	-	-	-	-
a_2 [-]	0.50 ± 0.09	-33.0 ± 19.2	6.7 ± 7.7	7.6 ± 8.9	-40.4 ± 31.8	-46.8 ± 41.4	-1.2 ± 1.0	-1.1 ± 1.3	-	-	-0.5 ± 0.6	-0.5 ± 0.3	-4.2 ± 2.8
a_3 [-]	24.81 ± 4.41	-7.1 ± 3.6	1.5 ± 1.7	1.7 ± 2.1	-8.4 ± 6.8	-9.7 ± 9.1	-	-	-	-	-	-	-1.2 ± 0.7
b_1 [s^{-1}]	2.99 ± 0.54	18.1 ± 12.3	-1.4 ± 1.6	-1.6 ± 2.0	24.1 ± 18.5	28.4 ± 25.3	-	-	-	-	-	-	0.7 ± 0.6
c_1 [s^{-1}]	10.04 ± 1.74	-	1.7 ± 2.1	2.0 ± 2.5	2.0 ± 4.0	2.2 ± 4.7	-	-	-	-	-	-	-
c_2 [s^{-1}]	3.03 ± 0.51	-8.6 ± 13.0	-	-	-11.4 ± 17.1	-12.9 ± 19.7	-	-	-	-	-	-	1.3 ± 0.9
R_f [s^{-1}]	0.10 ± 0.02	1.5 ± 2.3	-	-	2.1 ± 3.0	2.4 ± 3.7	-	-	-	-	-	-	-
k_{rel} [s^{-1}]	9.97 ± 1.72	-	-	-	-	-	-	-	-	-	-	-	-
n_{Ca} [-]	10.00 ± 1.68	-	-	-	-	-	-	-	-	-	-	-	-
λ_{Ca} [-]	2.78 ± 0.48	-	-	-	-	-	-	-	-	-	-	-	-
k_{NO} [-]	0.49 ± 0.09	-50.1 ± 11.7	-	-	-73.6 ± 25.6	-90.5 ± 51.6	-	-	-	-	-	-	1.3 ± 0.9
t_{NO} [dyne cm^{-2}]	5.97 ± 1.05	29.4 ± 7.9	-	-	43.1 ± 17.4	51.0 ± 30.6	-	-	-	-	-	-	-0.7 ± 0.5
n_{NO} [-]	1.20 ± 0.20	-16.2 ± 5.3	-	-	-23.3 ± 9.8	-28.1 ± 17.4	-	-	-	-	-	-	-
K_{vo} [$Pa^{-1}\ s^{-1}$]	1.00 ± 0.18	-	-	-	-	-	-	-	-	-	-	-	-
K_{vc} [$Pa^{-1}\ s^{-1}$]	1.01 ± 0.18	-	-	-	-	-	-	-	-	-	-	-	-
L_{eff} [μm]	498.50 ± 83.98	11.8 ± 4.5	-34.6 ± 11.2	-68.1 ± 45.7	-12.9 ± 9.0	-39.0 ± 28.9	27.7 ± 4.4	-	-6.7 ± 3.8	-4.2 ± 0.4	-0.7 ± 0.2	-4.4 ± 0.4	-61.9 ± 33.9
ρ [$kg\ m^{-3}$]	991.91 ± 175.32	0.7 ± 2.5	-	0.5 ± 1.5	1.2 ± 3.8	1.4 ± 4.5	1.4 ± 0.3	-	-	-	-	-	-1.7 ± 0.8
μ [cP]	1.00 ± 0.17	-2.0 ± 2.8	-	-0.8 ± 2.0	-3.3 ± 4.3	-4.2 ± 5.4	-2.7 ± 0.5	-	-	-	-	-	-119.6 ± 61.9
γ [-]	2.03 ± 0.34	-1.1 ± 2.4	-	-	-1.8 ± 3.7	-2.0 ± 4.4	-1.4 ± 0.3	-	-	-	-	-	-59.6 ± 30.9
K_{max} [Pa]	400.55 ± 68.66	-	20.2 ± 4.5	22.8 ± 7.1	19.1 ± 6.5	20.8 ± 8.1	-	-3.2 ± 0.7	-	-	-1.2 ± 0.3	-	-0.9 ± 0.5
K_{min} [Pa]	105.59 ± 18.61	-9.3 ± 6.4	-296.8 ± 47.6	-562.3 ± 282.2	-292.4 ± 62.3	-537.9 ± 287.4	-51.7 ± 19.8	-	-55.6 ± 21.4	-3.3 ± 4.2	-	-3.4 ± 4.2	-99.9 ± 56.9

Table 3.4: Sensitivity analysis of the one-dimensional lymph flow equations coupled to the EFMC model and valve dynamics. Favourable pressure difference case. See caption of Table 3.3 for explanations. Here we used P_{in} = 4 cmH_2O and P_{out} = 2 cmH_2O.

3.3.5 Sensitivity analyses of the mathematical model

The mathematical model for lymphatic collectors proposed here depends on several parameters which strongly influence the indices shown in Section 3.3.4. To investigate the influence of each parameter on the indices, we performed two sensitivity analyses based on [van Griensven 2006]. The methodology is described in the Section 3.2.5. Based on the results shown in Section 3.3.4, we performed two sensitivity analyses: one for an adverse pressure difference $\Delta P = P_{in} - P_{out} < 0$ (Table 3.3) and one for a favourable pressure difference $\Delta P = P_{in} - P_{out} > 0$ (Table 3.4).

Adverse pressure difference $\Delta P = P_{in} - P_{out} < 0$. The radius at equilibrium r_0 positively influences indices SV, CPF, ESD, EDD, WSS and mean flow. Among the parameters of the EFMC model, a_2 is the most influential one, followed by a_3 and b_1. Indeed, a_2 is the threshold to change the nature of the stationary point described in Section 3.2.2 from stable to unstable. Parameters R_I and k_{rel} do not significantly influence the studied output parameters. The frequency, and thus FPF and CPF, is strongly influenced by λ_{Ca} and n_{Ca}, and this is in agreement with Frames 3.6c and 3.6d, respectively, of Fig. 3.6. Parameters k_{NO}, τ_{NO}, n_{NO}, which are related to WSS and flows, do not affect the lymphatic indices since $\Delta P < 0$. The parameter of the valve model K_{vo}, K_{vc} and L_{eff} do not affect the indices. μ and γ only affect the WSS, while the density ρ does not affect the indices. The maximum and minimum coefficients K_{max} and K_{min} affect the ESD and EDD, respectively, and also influence most of the parameters, such as the frequency, EF, SV, FPF, CPF and mean flow.

Favourable pressure difference $\Delta P = P_{in} - P_{out} > 0$. Compared to the adverse pressure difference case, there are significant changes. The most influential parameters are: r_0, a_2, b_1 and K_{min}. The effects of parameters k_{NO}, τ_{NO} and n_{NO} are more evident than in the case of an adverse pressure difference. An increase of parameter k_{NO} decreases the frequency, indeed the greater this parameter, the greater the influence of the contraction inhibition given by the WSS. On the contrary, an increment of parameter τ_{NO} increases the frequency. Results for k_{NO} and τ_{NO} are in agreement with Frames 3.6g and 3.6f, respectively, of Fig. 3.6. An increase of parameters L_{eff}, ρ, μ and γ causes the mean flow to decrease. Between the K_{min} and K_{max}, the most influential one is K_{min}, as it affects the frequency, SV, FPF and CPF.

3.3.6 A quantitative study on the effect of stenotic and regurgitant lymphatic valves

The mathematical model for collectors proposed in the present chapter includes a well-established model for valves proposed by Mynard et al. [Mynard 2012]. It has already been used for the heart valve modelling [Mynard 2015], as well as for the venous valves [Toro 2015b]. More interestingly, the model allows for a quantitative study of the effect of stenotic and regurgitant valves. For instance, the model was already used to study the impact on brain haemodynamics of bilateral stenotic and regurgitant valves of the internal jugular veins [Toro 2015b, Cristini 2014]. In the lymphatic system, stenotic and regurgitant valves have not been reported. This is probably due to the different load regimes that lymphatic valves experience. As suggested by [Sabine 2015], mutations in FOXC2 is associated with valve incompetence and possibly leads to backflow. In this section, we speculate what would be the consequences on regurgitant valves leading to backflow or stenotic valves leading to obstructions in the collecting lymphatic.

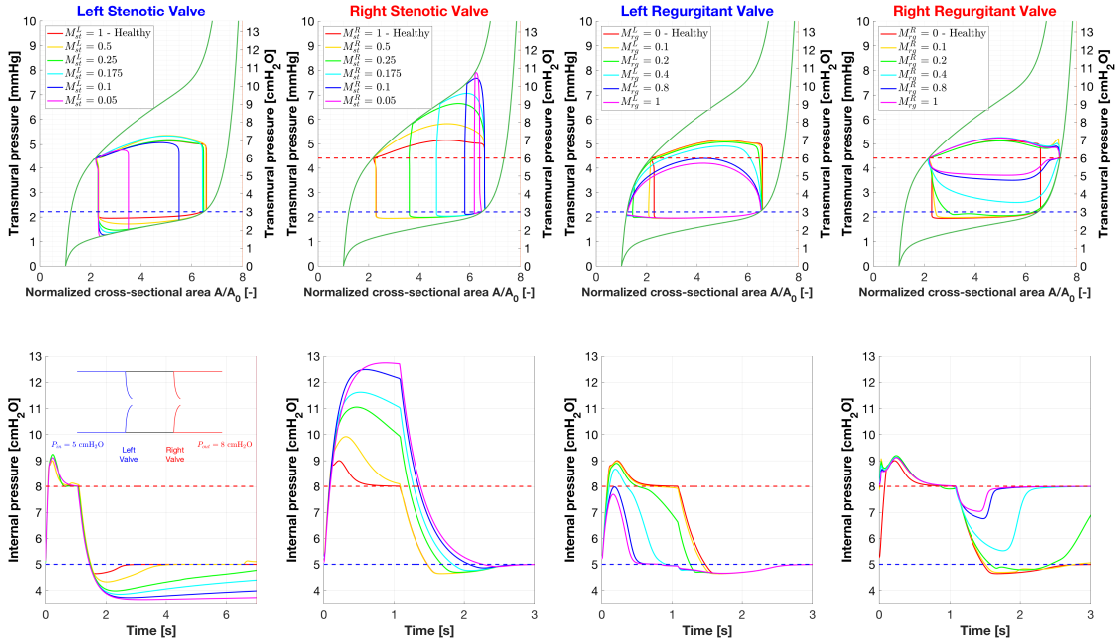

Figure 3.16: Effect of stenotic and regurgitant lymphatic valves. From the top to the bottom lines we show: PA loops and lymphatic pressure at the centre of the lymphangion. The first two columns show results for the left and right stenotic valves, while the remaining two columns show results for the left and right regurgitant valves. Parameters $M_{st}^{L/R}$ and $M_{rg}^{L/R}$ were varied from 0 to 1. Here we set the boundary pressures $P_{in} = 5$ cmH_2O and $P_{out} = 8$ cmH_2O.

We modelled a single collector with one complete lymphangion and two incomplete lymphangions, with an overall number of two valves. Here we used $M = 20$ computational cells to discretize the one-dimensional lymph vessel. We simulated a collector cannulated at each end, that is, we imposed a fixed pressure at the leftmost and rightmost interfaces of the collector, as described in 3.2.4. The imposed pressures were $P_{in} = 5$ cmH$_2$O and $P_{out} = 8$ cmH$_2O$.

We consider four possible situations: a left stenotic valve, a right stenotic valve, a left regurgitant valve and a right regurgitant valve. The numerical results of the middle lymphangion are shown in Fig. 3.16.

A **left stenotic valve** diminishes the inflow from the upstream valve. This results in the following: the greater the severity of the left stenosis, the greater the time required to fill the middle lymphangion after a contraction. For the tests considered here, contractions occur at a frequency of ≈ 7 min^{-1}, which means approximately every ≈ 8.6 s. For a severe left stenosis ($M_{st}^{L} = 0.05$), the time required to fill the lymphangion is ≈ 23 s. A severe reduction of the EDD can happen when the lymphangion does not have enough time to fill itself, and this may happen when the contraction period is less than 8.6 s. To verify this hypothesis, we performed additional simulations with a left stenotic valve, varying the frequency and for different severities of the stenosis. We set $f_{min} = f_{Ca}$ from 4 to 24 min^{-1} and calculated the resulting frequency, CPF and the efficiency, defined as the ratio between the CPF in the stenotic case and the CPF in the healthy case. The numerical results are shown in Fig. 3.17. For a mildly stenosis ($M_{st}^{L} > 0.1$) and low frequencies, the CPF does not

suffer any changes, but as soon as the frequency increases (e.g. above approximately 8 min^{-1} for $M_{st}^L = 0.25$), the CPF decreases depending on the severity of the stenoses. At the frequency of $f = 21$ min^{-1} and $M_{st}^L = 0.25$, the CPF reduces from ≈ 56.4 μL h^{-1} to ≈ 19.7 μL h^{-1}, that is it reduces of the 65 %. For even more severe left stenoses ($M_{st}^L < 0.25$), the CPF drastically decreases and the lymphangion becomes unable to eject the lymph forward. At the frequency of $f = 21$ min^{-1} and $M_{st}^L = 0.05$, the CPF reduces of the 96 %, namely it reduces to ≈ 1.9 μL h^{-1}. This comes from a decrease of the EDD for high frequencies. The PA loops for different frequencies and a severe left stenosis are also shown. The higher the frequencies, the greater the shrinkage of the PA loops. Overall, a left stenosis causes a decrease of the CPF for high frequencies of contractions.

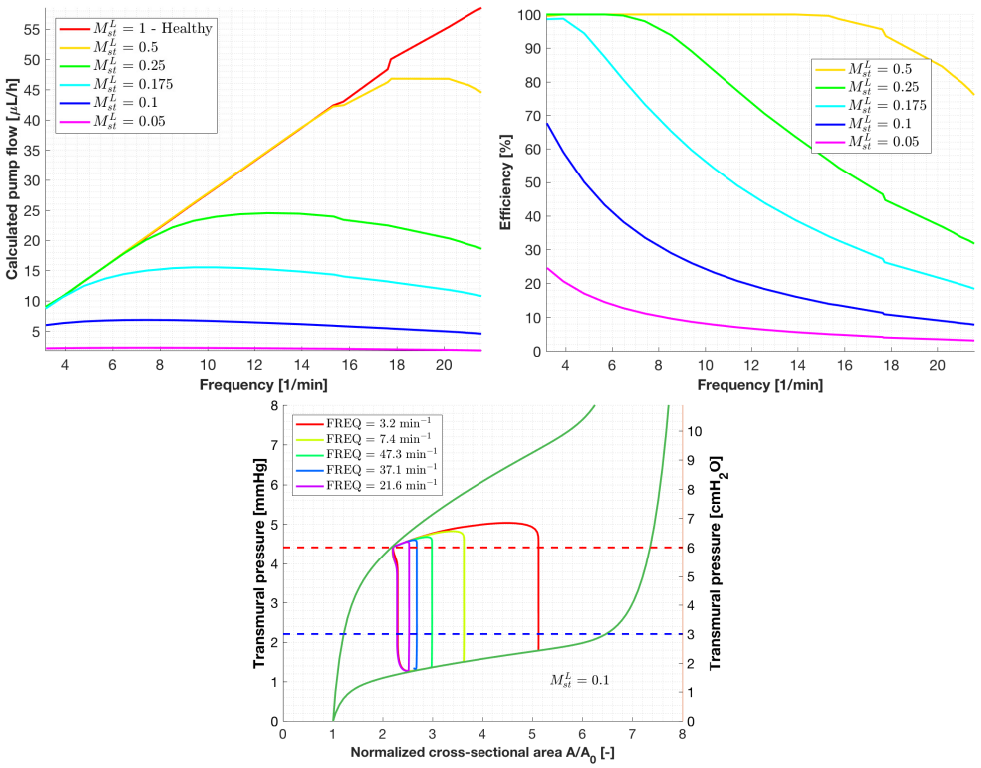

Figure 3.17: High frequencies of contractions with a left stenotic valve diminish the CPF. We simulated one collector with one complete lymphangion and two incomplete lymphangions with an overall number of two valves. We imposed boundary pressures at the ending interfaces $P_{in} = 5$ cmH_2O and $P_{out} = 8$ cmH_2O. The left valve is assumed stenotic. Results for the middle lymphangion are shown. Here we show frequency against CPF (top frame) and Efficiency (centre frame) for different severity of the stenosis, and pressure against normalised area (bottom frame) for different frequencies and with a severe stenosis. The efficiency is defined here as the ratio between the CPF in the stenotic case and the CPF in the healthy case. The higher the frequency, the greater the negative effect on the CPF caused by a severe left stenotic valve.

A **right stenotic valve** drastically increases the ESP and the ESD. This comes from the difficulties for the lymph to be pushed downstream through a stenotic passage. As a matter of fact, the outflow greatly decreases (result not shown).

		Stenotic valve				Regurgitant valve				Healthy valves
		Left		Right		Left		Right		
		$M^L_{st}=0.5$	$M^L_{st}=0.1$	$M^R_{st}=0.5$	$M^R_{st}=0.1$	$M^L_{rg}=0.1$	$M^L_{rg}=0.8$	$M^R_{rg}=0.1$	$M^R_{rg}=0.8$	$M_{st}=1\ M_{rg}=0$
Frequency	[min^{-1}]	6.97 ≈	2.64 ↓	6.98 ≈	7.06 ≈	6.98 ≈	6.96 ≈	10.19 ↑	15.48 ↑	6.98
SW	[nL cmH_2O]	400.28 ≈	310.05 ↓	449.58 ↑	131.83 ↓	393.75 ≈	320.65 ↓	403.55 ≈	204.84 ↓	384.98
EF	[-]	0.67 ≈	0.49 ↓	0.65 ≈	0.09 ↓	0.69 ≈	0.81 ↑	0.69 ≈	0.70 ≈	0.66
SV	[nL]	95.40 ≈	45.93 ↓	90.47 ≈	12.92 ↓	96.04 ≈	112.77 ↑	104.50 ≈	110.59 ↑	91.88
FPF	[min^{-1}]	4.66 ≈	1.30 ↓	4.55 ≈	0.66 ↓	4.83 ≈	5.66 ↑	7.03 ↑	10.87 ↑	4.62
CPF	[$\mu L\ h^{-1}$]	39.87 ≈	7.27 ↓	37.87 ≈	5.47 ↓	40.20 ≈	47.12 ↑	63.92 ↑	102.74 ↑	38.46
Mean Flow	[$\mu L\ h^{-1}$]	39.12 ≈	10.55 ↓	39.30 ≈	7.82 ↓	34.57 ≈	0.49 ↓	44.91 ≈	0.19 ↓	39.43
WSS	[mdyne cm^{-2}]	157.76 ≈	49.71 ↓	158.58 ≈	16.17 ↓	132.23 ↓	-6.13 ↓	178.83 ≈	4.21 ↓	160.03
Peak Velocity	[mm s^{-1}]	4.83 ≈	4.56 ≈	2.66 ↓	1.32 ↓	4.45 ≈	2.71 ↓	4.79 ≈	4.00 ↓	4.83
ESD	[μm]	141.43 ≈	141.83 ≈	143.22 ≈	231.14 ↑	134.72 ≈	105.12 ↓	141.40 ≈	141.11 ≈	141.12
EDD	[μm]	245.94 ≈	199.02 ↓	242.71 ≈	242.71 ≈	242.71 ≈	242.71 ≈	253.66 ≈	258.55 ≈	242.71
ESP	[cmH_2O]	9.01 ≈	8.92 ≈	9.94 ≈	12.74 ↑	8.99 ≈	8.27 ≈	9.05 ≈	9.20 ≈	9.02
EDP	[cmH_2O]	5.19 ≈	4.23 ↓	5.00 ≈	5.00 ≈	5.00 ≈	5.00 ≈	6.31 ↑	8.00 ↑	5.00

Table 3.5: Analysis of the effect of lymphatic valve deficits. Here we compare indexes for healthy and defective valves. In the first column, we show indexes, while in the second and third we show results for the stenotic and regurgitant valve, respectively. In the last column results for healthy valves are shown. A green-coloured result indicates a normalised, percentage change in absolute compared to the healthy case value between 15 and 50 %. Likewise, a blue-coloured result indicates a change between 50 and 100 % and a red-coloured result indicates a change above 100 %. The arrows indicate a positive or a negative change.

The mathematical results suggest that a stenotic valve causes an increase of the systolic peaks in the upstream lymphangions and maintains almost unchanged the downstream pressures. Moreover, it causes a reduction of the CPF for high frequencies of contractions in the downstream lymphangions. These results suggest a great reduction of the CPF may occur when the collecting lymphatics are blocked where the frequency of lymphatic contraction is high.

A **left regurgitant valve** has a significant impact on the effective pump flow, namely the real amount of flow ejected from the lymphangion. As the severity of the left regurgitant valve increases, backflows increase. This means that during contractions, the lymph is ejected backwards into the upstream lymphangion, and not forward into the downstream one. Moreover, the ESD diameter decreases and for a severe left regurgitant valve the downstream valve stays closed most of the time (result not shown) insofar as the ESP decreases.

To conclude, a **right regurgitant valve** increases the leakage from the downstream valve, even for small values of M^R_{st}. This results in increasing the EDP from 5 cmH_2O to 8 cmH_2O, which corresponds to the downstream boundary pressures P_{out}. For severe right regurgitant valves, the upstream valve does not open during the lymphatic cycle (results not shown).

The effects of regurgitant and stenotic valves are summarised in the indexes shown in Table 3.5. For a left stenotic case, there are almost no variations in any of the indexes. As discussed before, problems arise for high frequencies of contractions. For a right stenotic valve, EF, SV, FPF and CPF decrease almost fourfold, while the ESP increases. The cases of regurgitant valves show interesting properties on some of the indexes. As a matter of fact, EF, SV, FPF and CPF indexes do not indicate any reduction in the pumping performance. Instead, based on the results in Table 3.5, it seems that the pumping action of the lymphangion has undergone improvements with the incompetence of the valves. For instance, with a left regurgitant valve case, EF, SV, FPF and CPF increase. The same happens for the right regurgitant valve case for indexes SV, FPF and CPF, though FPF and CPF might have increased because the frequency was increased. This is obviously misleading: since a significant amount of lymph is flowing retrograde due to the deficit, the effective time-averaged flow

is approximately zero. Thus, we would expect CPF to be zero. As it was pointed out by Scallan et al. [Scallan 2016], indexes EF, SV, FPF and CPF are usually assumed to represent forward lymph flow and fail to account passive flow or non-ideal valves.

3.4 Discussion

The main contribution of this chapter is the construction of a one-dimensional model for lymph flow in deformable lymphatic vessels coupled to a model for muscle contraction with fluid-mechanically dependent frequency, and the numerical implementation of the full model involving the deployment of modern numerical methods for solving the coupled systems of equations.

3.4.1 Comparison between zero and one-dimensional models

Most of the computational results shown here are qualitatively comparable to those from 0D models for lymph flow. For instance, the simulation of a lymphatic cycle shown in Fig. 3.10 resembles the results shown in Fig. 10 of Bertram et al. [Bertram 2014a]. This is indeed not surprising as 0D models are special cases of 1D models; the latter, however, exhibit the additional ability of accurately capturing wave propagation and transport features, which are badly smeared by zero-dimensional models, as demonstrated in [Borsche 2016]. Under resting conditions and average values, 0D models are an optimal choice in terms of resolution, simplicity and computational times. However, such models would be of limited accuracy for spatial resolution of flow quantities and especially under postural changes as the non-linear terms could play a significant role. In this regard, pathological cases and abnormal pressure wave propagation can be studied through the one-dimensional approach at a higher but still acceptable computational cost.

3.4.2 Characterization of the lymphatic wall electrical activity

There are so far just a few works on computational modelling of the lymphatic electrical activity [Baish 2016, Kunert 2015] in the open literature. Here, building upon existing works, we propose a model for the electrical activity of the lymphatic wall, based on the FitzHugh-Nagumo model, coupled to the vessel wall mechanics. As shown in Fig. 3.6, the action potential of the EFMC model is divided into four phases: (1) fast depolarization, (2) plateau period, (3) hyperpolarization and (4) repolarization. The profile of the action potential, for the rat in the present case, resembles well that described by Telinius et al. [Telinius 2015] for human mesenteric vessels. There are however some differences, namely: (1) the plateau duration here is $1.2\ s$ compared to $1.7 \pm 0.2\ s$ and (2) there are no spikes preceding and following the plateau phase. The overall agreement is encouraging even though the works are for different species. The shape of the pressure variation during a lymphatic contraction mimics the pressure measurements by Davis et al. [Davis 2012], where a fast increase of the internal pressure is followed by an exponential-like pressure decay. Compare the internal pressure of the lymphangion of Fig. 3.12 at $t \approx 60\ s$ with Fig. 6 of Davis et al. [Davis 2012].

3.4.3 Frequency of contractions of the EFMC depend on local fluid dynamics

Lymphatic contractions are a complex phenomenon. The activation of an action potential and the subsequent lymphatic contraction depend on local fluid dynamic quantities, such as transmural pressure and wall shear stress [Munn 2015]. The dynamics of frequencies in bovine mesenteric vessels were described by McHale and Roddie [McHale 1975] by varying the intraluminal pressure. The authors showed that the frequency of contractions increases as the circumferential stretch increases. Gashev et al. [Gashev 2002] studied rat mesenteric lymphatics in response to imposed flow and showed that the frequency dropped from 9.0 ± 1.6 min^{-1} to 3.1 ± 1.4 min^{-1} when flow changed from zero to a positive value given by a transaxial-pressure difference of 7 cmH_2O. Both features are incorporated by our computational model. The frequency of contraction in the EFMC model strongly depends on both circumferential stress and wall shear stress, as illustrated in Figs. 3.12, 3.13 and 3.14, and the frequency-pressure and frequency-WSS curves can be modified so as to fit experimental measurements and regional variability, as demonstrated in Fig. 3.6.

3.4.4 The advantage of the EFMC model in networks of collecting lymphatics

The occurrence of lymphatic contractions in a network of lymphangions is challenging to model. Jamalian et al. [Jamalian 2016] studied the effect on the time-averaged flow of the temporal coordination of contractions in different vessels in a branched network. Bertram et al. [Bertram 2017] proposed a formula of the transmural pressure-frequency dependence through experimental measurements, for a single lymphangion. However, for a network of lymphangions, the following problem arises: how can we prescribe refractory periods and time delays, including both transmural pressure and wall-shear-stress regulatory mechanisms? The EFMC model of this chapter represents an attempt to solve this problem. The governing laws of the EFMC model naturally trigger action potentials by local fluid dynamic quantities and provide the contraction state s. This gives each lymphangion the autonomous capability to trigger a lymphatic contraction, which is desirable for a network of lymphangions.

3.4.5 Extension of the Mynard's valve model to the lymphatic framework

Lymphatic valves perform an important function for lymphatic homeostasis, as their primary role is to prevent backflow. The forward flow resistance associated with an open valve state has been the subject of studies, as it is extremely complicated to acquire measurements on these microvessels at low-pressure differences [Bertram 2014a]. The computational model proposed here builds on the previous work of Mynard et al. [Mynard 2012], is based on a lumped parameter model of a deformable vessel and provides the resistance value for flow dynamics. Our valve model depends on the geometrical parameters of the vessel and on the fluid dynamic properties, including the dynamic viscosity, the length of the lymphatic valve and the cross-sectional area of the lymphangion, and has the ability to model flow at both high and low Reynolds numbers. The flow resistance predicted by our mathematical model agrees with reported literature values. At maximal valve opening ($\xi = 1$), the flow resistance is $R = 2.4594 \times 10^6\ g\ cm^{-4}\ s^{-1}$, which is comparable with $2 \times 10^6\ g\ cm^{-4}\ s^{-1}$ used in run 2 of Bertram et al. [Bertram 2014a] and is 4-fold greater than $0.6 \times 10^6\ g\ cm^{-4}\ s^{-1}$, estimated through experimental measurements by [Bertram 2014a]. Using the geometrical parameters of [Wilson 2015] (valve length to $L_{eff} = 240\ \mu m$ and radius at equilibrium to $r_0 = 50$

μm), the resistance value is $R = 0.98 \times 10^6\ g\ cm^{-4}\ s^{-1}$, which closely agrees with $0.95 \times 10^6\ g\ cm^{-4}\ s^{-1}$ predicted by Wilson et al. [Wilson 2015]. This agreement gives us a degree of confidence on the results obtained through the valve model and suggests that valves in larger vessels, such as in human lymphatic vessels, can be modeled by our modelling framework.

3.4.6 A theoretical study of lymphatic valve impairments

The mathematical model for valve dynamics gives the possibility to study the effect of two pathological cases: stenotic and regurgitant valves. As calcification, a fundamental factor of stenotic and regurgitant valves development, has not been reported in the literature, the computational results shown here are only speculative. However, as suggested by [Sabine 2015], mutations in FOXC2 is associated with valve incompetence and possibly leads to backflow. In this regard, modelling of regurgitant valves can give some insightful results. As expected, our computations showed that a regurgitant valve was unable to prevent backflow at any transvalvular pressure gradients, leading to an entirely inefficient lymphatic pump with an adverse pressure gradient. In a stenotic valve, we noticed an unexpected, strong relationship between the frequency of contraction and the ejected lymph flow; see Fig. 3.17. For a mildly stenotic valve, the efficiency of the downstream lymphangion decreased as the contraction rate increased. This suggests that a blockage in a lymphatic district may have a high flow impact in locations with a high frequency of contraction.

3.5 Limitations and future development

Regarding limitations of the present model, there are several issues that need to be addressed. Lymphatic contraction modelling poses several challenges. Muscle contractions add tensile stress and result from internally generated forces, initiated at the cellular level, which depend on calcium dynamics as well as the length-tension relationship. Previous contraction models [Caulk 2016, Bertram 2016b] could not be used in our one-dimensional setting because the resulting systems of equations turned out to be mixed elliptic-hyperbolic and thus ill-posed. Our current model is based on the previous work of MacDonald et al. [Macdonald 2008], is hyperbolic and mimics the contraction phenomena in terms of pressure-diameter curves. Although the computational results shown in the current work are encouraging, they need to be considered with caution. The model has several drawbacks, as seen from the active component in Eq. (3.8): 1) it neglects the length-tension relationship; 2) the tensile active stress increases as the circumferential stress increases; 3) the estimation of the range of variation of coefficients K_{min} and K_{max} comes only through the external manifestation of the pressure-diameter relationship. Our work could be improved by implementing the contraction model based on the work of others but in a hyperbolic setting [Caulk 2016, Bertram 2016b].

The mathematical model for the excitability of the lymphatic wall is based on the FitzHugh-Nagumo model, which might not adequately represent the lymphatic electrical dynamics. We assumed that the lymphatic wall exhibits an electrical behaviour similar to that of cardiac cells. In addition, we assumed lymphatic contractions to be homogeneous throughout the lymphangion. Experimental observations have shown that contractions propagate at a certain speed ($4 \sim 8\ mm\ s^{-1}$) [Ohhashi 1980], and there can be dephasing between parts of the same lymphangion. Therefore, we might not have taken full advantage of the one-dimensional model to describe lymphatic

contractions; the spatial variation contained in the PDEs is not operational. Moreover, adjacent lymphangions do not communicate through a lymphatic valve, in our model. This caused unrealistic behaviours in the computational results, where adjacent lymphangions are regarded as electrically decoupled, see Fig. 3.12. There are approaches to overcome this problem, used in other contexts, such as for example adding an ad hoc diffusion term in the FitzHugh-Nagumo [Colli Franzone 2014].

Another important characteristic of lymphatic valves is that they display hysteresis and are biased to stay open even when facing small negative pressure drop. The opening and closure thresholds are assumed to be zero for lymphatic valves in the current work, but experimental measurements have shown that the thresholds depend on transmural pressure. Our assumption might affect the computational results. For instance, the indices shown in Section 3.3.4 might display a higher non-linear behaviour for different combinations of upstream and downstream pressures. Also, the behaviour of the pressure-ramp test shown in Fig. 3.12 might not be comprised in the behaviours described by Bertram et al. [Bertram 2017]. However, one of our primary goal of this work was to propose in the lymphatic framework a preliminary extension of the valve model [Mynard 2012], leaving room for possible future improvements, such as the incorporation of the formula for the valve threshold proposed by Bertram et al. [Bertram 2014b].

3.6 Conclusion

In this chapter, we have proposed a one-dimensional model for collecting lymphatics coupled to a novel Electro-Fluid-Mechanical Contraction (EFMC) model for dynamical contractions based on a modified FitzHugh-Nagumo model for action potentials, and to a lumped parameter model for valve dynamics. The full model has been implemented in a practical computational setup. By using the computational model, we quantified several lymphatic indices for a wide range of upstream and downstream pressure combinations. Our theoretical analysis, together with numerical experiments, showed that the contraction frequency strongly depends on both circumferential stretch and wall shear stress. Inspired by reported experiments on cannulated collectors, we carried out numerical computations, the results of which showed good agreement with the observed experimental trend.

The modelling framework proposed here has some distinctive advantages, such as the ability to model flow in deformable vessels at both high and low Reynolds numbers, and in the longer term, could provide the basis for more general models that include networks of arteries, veins, lymphatics, lymph nodes and other relevant fluid districts. Furthermore, the current mathematical model of collecting lymphatics can be coupled to multi-scale, closed-loop mathematical model of the cardiovascular system and can give quantitative information in healthy and pathological cases. The success of the proposed research directions is strongly limited by the existence of many parameters in models which are difficult to measure or estimate.

Chapter 4

Working principles of the glymphatic system: A hypothesis based on a holistic multi-scale mathematical model of the murine extracellular fluid systems

4.1 Introduction

Recent advances in medical science regarding the dynamics of brain fluids and solutes has created a lot of excitement, particularly regarding the potential for explaining the development of neurological disorders. Neurotoxic materials are constantly cleared from the brain parenchyma through the so-called glymphatic system [Iliff 2012]. The glymphatic system is defined as the intraparenchymal cerebrospinal fluid (CSF) movement from para-arterial CSF spaces to para-venous CSF spaces. Intracranial solutes and waste products are carried by the continuous water movement of the interstitial fluid (ISF) towards para-venous CSF spaces and are drained into the venous system through arachnoid villi or the lymphatic system [Louveau 2017]. The ISF-CSF water movement through glial cells is regulated by aquaporin-4 (AQP4) channels which are highly expressed at the astrocytic endfeet membranes [Nakada 2017]. Thanks to the AQP4 channels and the pseudolymphatic function of waste removal, this system of ISF-CSF movement and clearance of solutes has been termed "glymphatic system".

Dysfunctions of the glymphatic system can result in possible accumulation of neurotoxins in the brain and have been implicated in many disease states, including Alzheimer's disease [Iliff 2012, Iliff 2014], migraine [Schain 2017], and Idiopathic Intracranial Hypertension [Bezerra 2018]. There have been several discussions on the possible mechanisms and forces by which the glymphatic system works. It has been shown through a mathematical model that arterial pulsation is an unlikely origin of the driving force through astrocyte networks [Asgari 2016]. Three possible mechanisms have been suggested: 1) diffusion, a size-dependent random molecular walk, 2) advection or bulk

flow, a molecular size-independent force produced by chemical or hydrostatic or electrical gradient, or 3) convection, defined as a combination of diffusion and advection [Plog 2018]. Also, Smith et al. [Smith 2017] showed that the glymphatic system is unlikely driven by bulk flow. Their results suggest that water movement in the cranial subarachnoid space is driven by convection, while that within the parenchyma is driven by diffusion. However, to date to the Authors' knowledge, there is no satisfactory explanation of the mechanisms which drive the glymphatic system.

It is not surprising that the working principles of the glymphatic system have not yet been elucidated, as there are still uncertainties regarding how CSF and ISF interact and are produced. The classical understanding of the CSF dynamics is that CSF is produced by the choroids plexus in the ventricles, moves into the cerebral subarachnoid space and is drained into arachnoid villi [Brinker 2014]. However, this old concept of CSF production and drainage has been questioned for a long time. Cserr proposed in 1988 [Cserr 1988] a model of the ISF-CSF dynamics which has not yet been entirely accepted by the scientific community. The author proposed that ISF is secreted in the blood-brain barrier and drains into CSF space. These principles have been further studied and summarized in the *Bulat-Klarica-Orešković* hypothesis [Orešković 2017, Linninger 2017]. The Authors proposed that the CSF dynamics is regulated by Starling forces, and their theory explains why the injection of mannitol can increase or reduce the CSF volume [Linninger 2016].

Building on the previous mathematical models of the entire human vasculature system [Müller 2013b, Müller 2014, Mynard 2015, Strocchi 2017, Liang 2009a] and of the murine circulation [Aslanidou 2015, Cuomo 2015], in this chapter we build for the first time a mathematical model of all the main the murine fluid systems with a particular emphasis on the cerebral fluids. This mathematical model includes the dynamics of the heart, major arteries and veins, microcirculation, lungs, cerebrospinal fluid, intracranial Starling forces, Starling resistors, venous valves, Monro-Kellie hypothesis and brain lymphatics. The mathematical model is validated against literature values and MR-flow measurements. Furthermore, the model is validated against *in-vivo* intracranial pressures taken in healthy mice and in mice with impairment of the intracranial venous drainage. Following [Linninger 2016], we assumed the hypothesis of *Bulat-Klarica-Orešković* [Orešković 2017] and modelled the ISF production/absorption by Starling forces through the blood-brain barrier, together with the CSF production by the choroid plexus and by the ISF compartment, and the CSF absorption through arachnoid villi and lymphatics. Our mathematical model has the advantage of taking into account most of the fluid phenomena, from the heart dynamics to the CSF and ISF production, in a closed circuit. This globality of interactive phenomena gives us the capability to study the interaction of all relevant fluid systems, in both healthy and pathological cases. Through a systematic use of the computational model in healthy and pathological cases, in this chapter, we propose a hypothesis of the possible working principles of the glymphatic system.

4.2 Methods

Our multi-scale mathematical model of the murine fluid system is composed of a network of major arteries, see Figs. 4.1, 4.2, major veins, see Figs. 4.3, 4.4, and lumped parameter models for the heart, pulmonary circulation, arterioles, capillaries, venules, cerebrospinal fluid, brain interstitial fluid and lymphatics. In the following sections, we describe the mathematical models used for each one of these compartments.

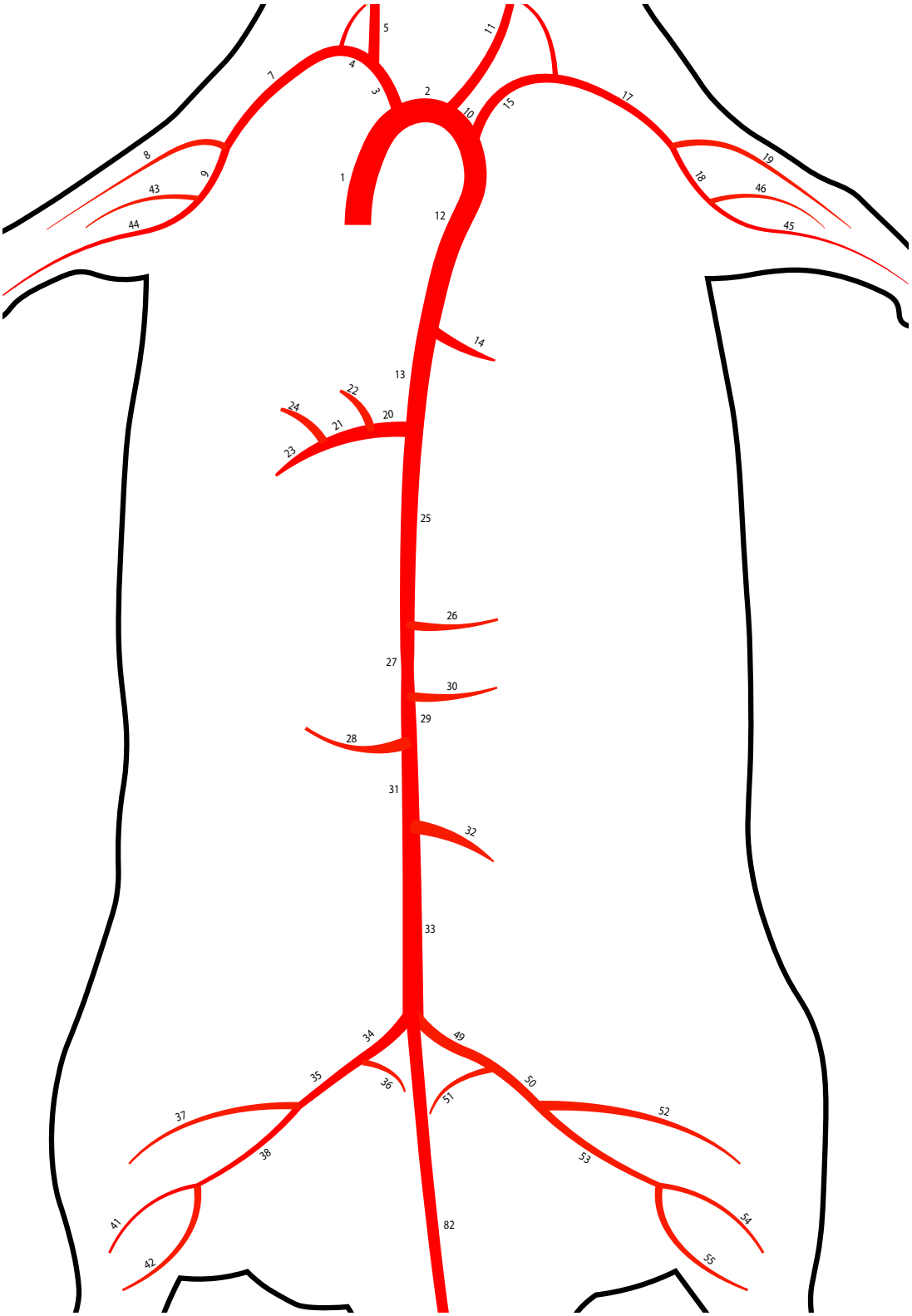

Figure 4.1: Modelling network of the murine arterial tree. Numbers refer to table 4.1, where geometrical and mechanical parameters for each vessel are reported.

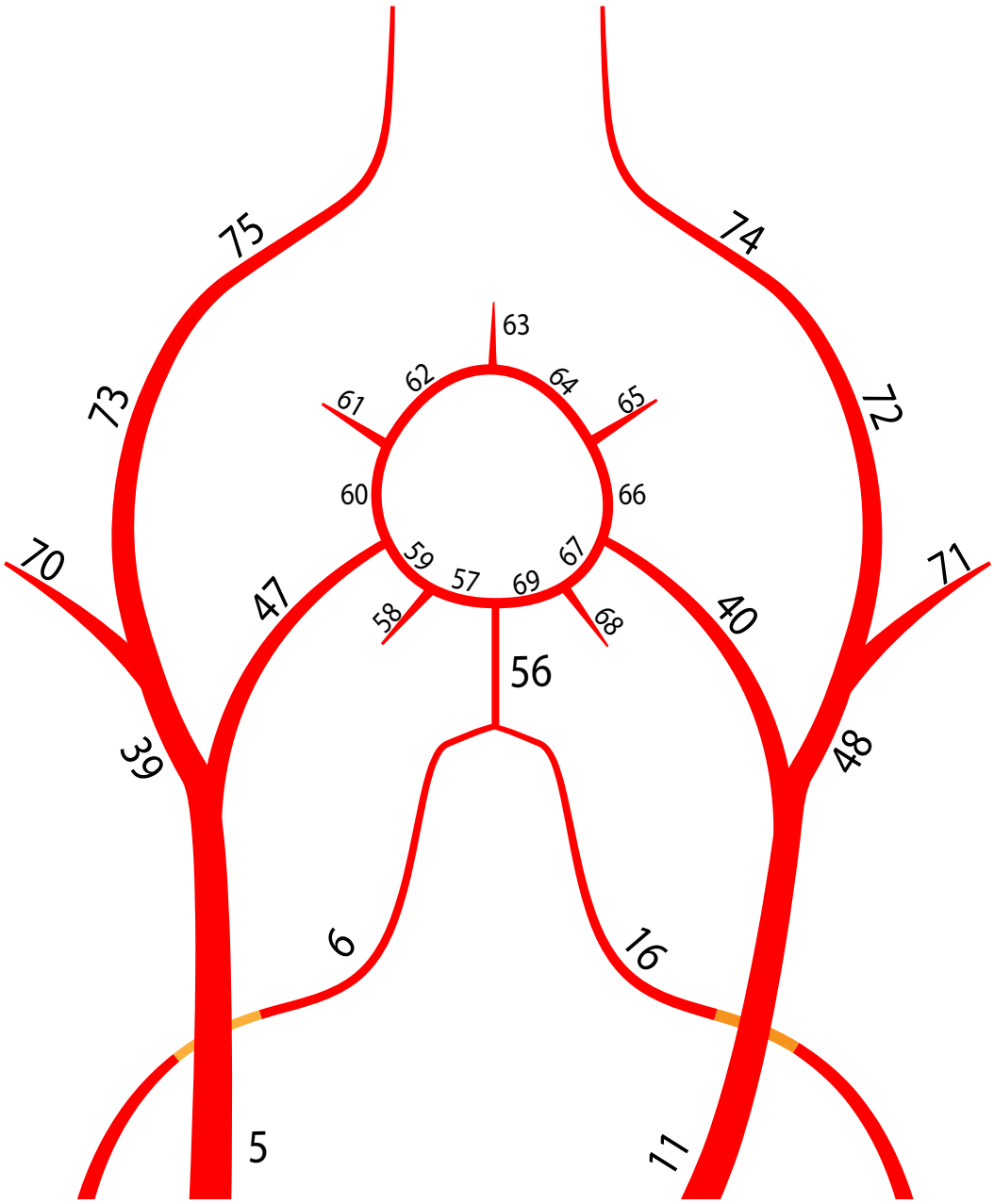

Figure 4.2: Modelling network of the murine arterial tree (head and neck). Numbers refer to table 4.1, where geometrical and mechanical parameters for each vessel are reported.

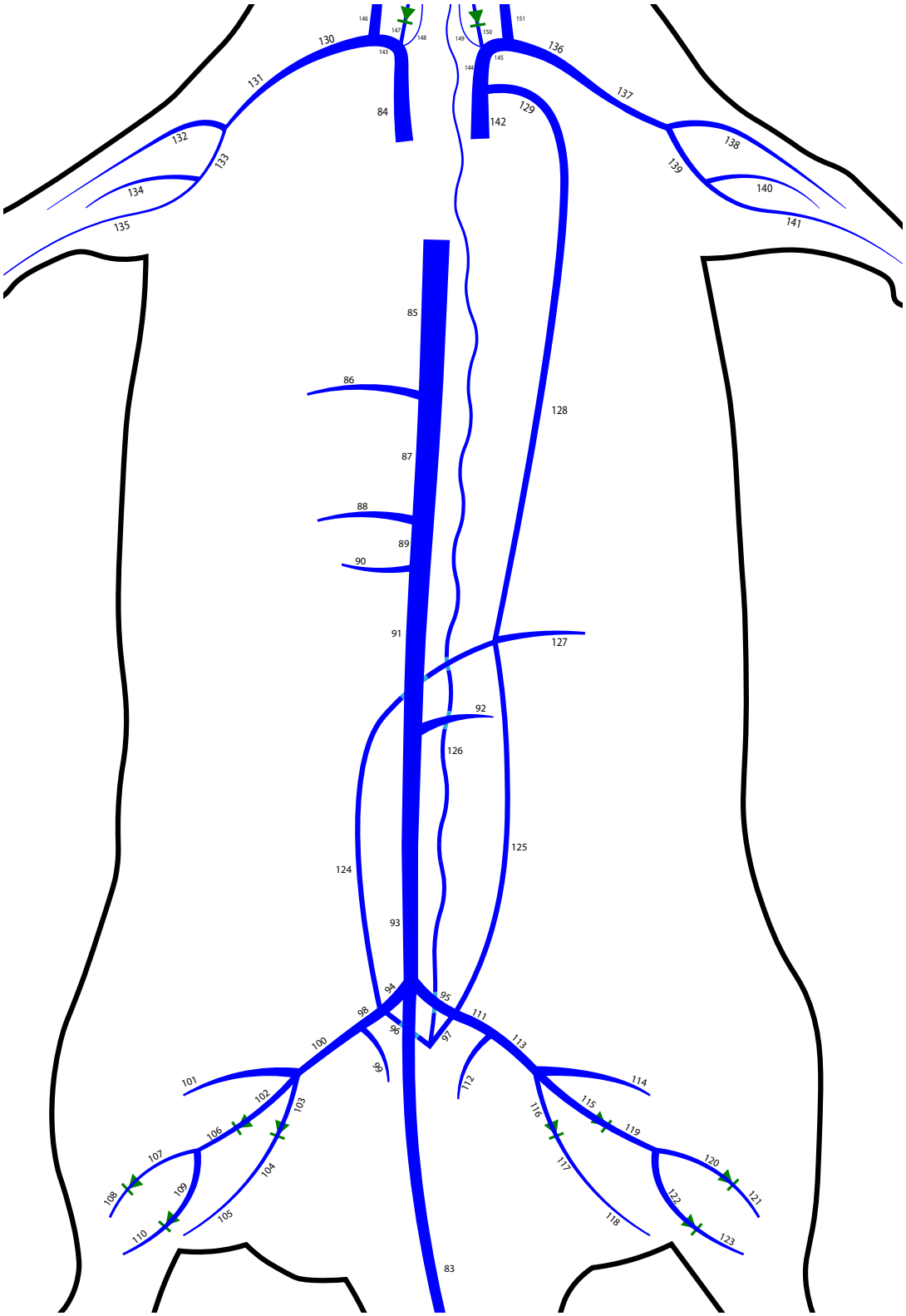

Figure 4.3: Modelling network of the murine venous tree. Numbers refer to table 4.1, where geometrical and mechanical parameters for each vessel are reported. The green triangle shows location of venous valves.

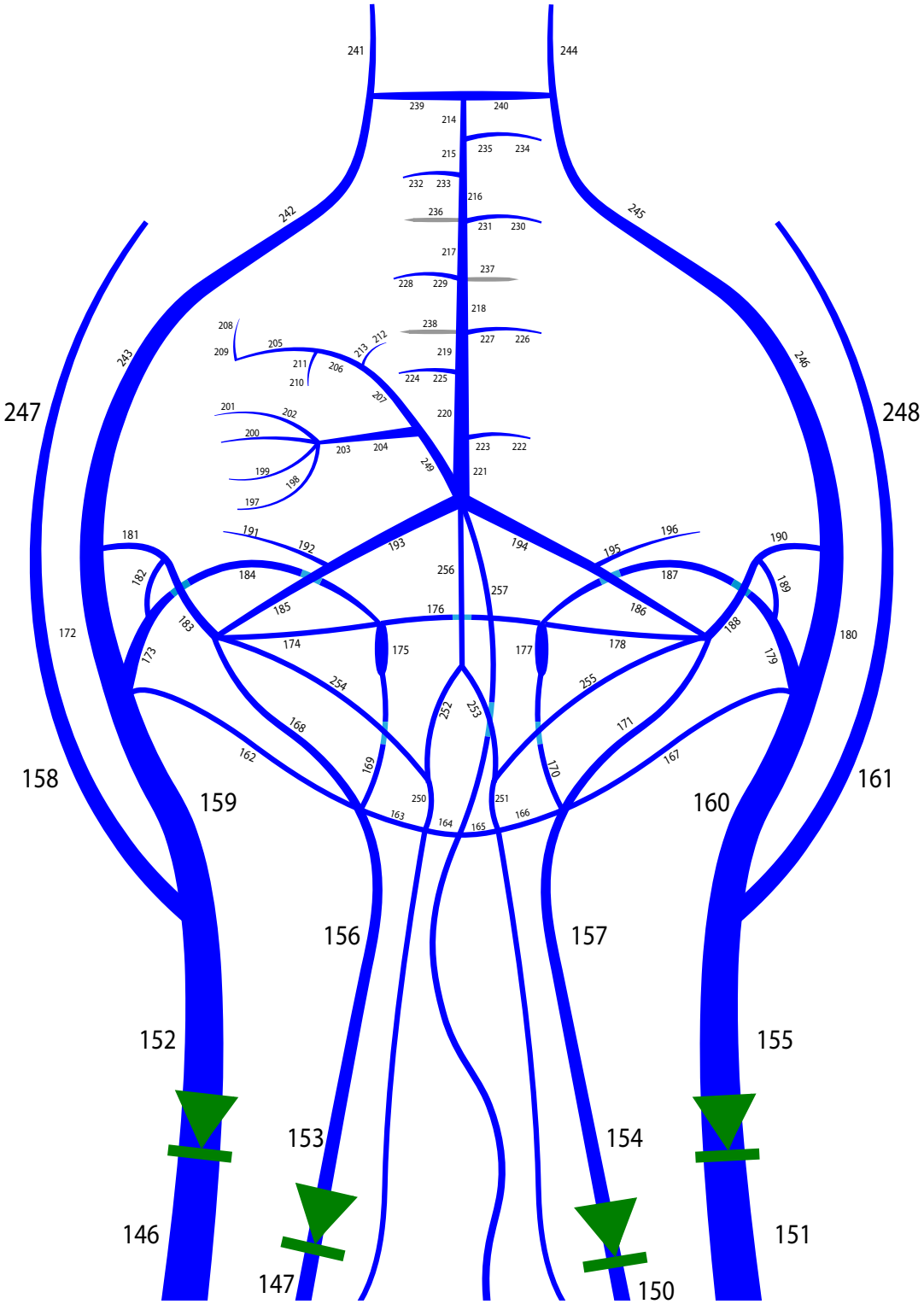

Figure 4.4: Modelling network of the murine venous tree (head and neck). Numbers refer to table 4.1, where geometrical and mechanical parameters for each vessel are reported. The green triangle shows location of venous valves.

4.2.1 One-dimensional blood flow equations

The one-dimensional blood flow equations for a compliant vessel are the following

$$\begin{cases} \partial_t A + \partial_x q = 0\,, \\ \partial_t q + \partial_x \left(\dfrac{q^2}{A}\right) + \dfrac{A}{\rho}\partial_x p = -f\,, \end{cases} \tag{4.1}$$

where x is the space variable, t is time, $A(x,t)$ is the cross-sectional area of the vessel, $q(x,t) = A(x,t)u(x,t)$ is the flow, $u(x,t)$ is the velocity, $p(x,t)$ is the pressure, ρ is the blood density, $f(x,t) = f_{friction}(x,t) + f_{stenosis}(x,t)$, with $f_{friction}(x,t) = \frac{2(\gamma+2)\pi\mu}{\rho}u(x,t)$ being the friction force, with the parameter γ dependent on the chosen velocity profile [Alastruey 2006], μ is the dynamic viscosity, and $f_{stenosis}$ accounts for additional energy loss due to strictures/stenosis and will be discussed later within this section.

Tube law for arteries and veins

In system (4.1), there are two governing partial differential equations and three unknowns, namely $A(x,t)$, $q(x,t)$ and $p(x,t)$. For this reason, an extra relation is required to close the system, the *tube law*, which relates pressure $p(x,t)$ and cross-sectional area $A(x,t)$. A purely elastic tube law reads

$$p(x,t) = K(x)\psi(A(x,t);A_0(x)) + p_e(x,t)\,, \tag{4.2}$$

with

$$\psi(A(x,t);A_0(x)) = \left[\left(\frac{A(x,t)}{A_0(x)}\right)^m - \left(\frac{A(x,t)}{A_0(x)}\right)^n\right], \tag{4.3}$$

where $p_e(x,t)$ is the external pressure, $A_0(x)$ is vessel cross-sectional area at equilibrium and might be modified in the presence of strictures (see 4.2.1 for details), $K(x)$ is the bending stiffness of the vessel wall, $m \geq 0$ and $n \leq 0$ are real numbers to be specified. For hyperbolicity m and n must satisfy additional constraints, see [Toro 2013]. For more information about the mathematical structure of the equations, see [Formaggia 2009, Toro 2013]. Relation (4.2) models a purely elastic behavior of the vessel wall. Other tube laws may also account for visco-elasticity, elastin and collagen, see [Matthys 2007a, Blanco 2014, Montecinos 2014a]. Practical choices for the parameters m, n and K are

$$K(x) = \begin{cases} K_a = \dfrac{E(x)}{1-\nu^2}\left(\dfrac{h_0(x)}{r_0(x)}\right), & m = \dfrac{1}{2}\,, \quad n = 0 \quad \text{for arteries / dural sinuses,} \\ K_v = \dfrac{E(x)}{12(1-\nu^2)}\left(\dfrac{h_0(x)}{r_0(x)}\right)^3, & m \approx 10\,, \quad n = -3/2 \quad \text{for veins,} \end{cases} \tag{4.4}$$

where ν, h_0, r_0 are the Poisson ratio (set to $\nu = 0.5$), the wall-thickness at equilibrium and the cross-sectional radius at equilibrium.

Since h_0 and the E are unknown for most of the murine vessels, we followed [Müller 2013b] and estimated parameter K based on the wave speed at equilibrium $c_0 = \sqrt{\frac{K}{\rho}(m-n)}$. The wave speed was estimated based on the formula proposed by [Aslanidou 2015] for arteries, while for veins we used the formula proposed by [Müller 2013b] with $c_0^{max} = 3$ m/s and $c_0^{min} = 1$ m/s. For dural sinuses, we set $c_0 = 3$ m/s.

Incorporation of blood rheological properties

Secomb and Pries [Secomb 2013] studied the rheological properties of blood and showed that there is highly non-linear dependence between the apparent blood viscosity with the vessel diameter. For blood vessels smaller than 300 μm in diameter, the apparent blood viscosity decreases. This phenomenon is called the Fåhræus-Lindqvist effect. This decrement continuous up to ≈ 10 μm, and inverts for smaller values at which the apparent blood viscosity increases. Following the work of Aslanidou et al. [Aslanidou 2015] we incorporated the rheological properties of blood viscosity proposed by [Secomb 2013]

$$\mu_{rel} = \left[1 + (\mu^*_{0.45} - 1)\frac{(1-H_d)^C - 1}{(1-0.45)^C - 1}\left(\frac{d}{d-1.1}\right)^2\right]\left(\frac{d}{d-1.1}\right)^2 , \tag{4.5}$$

with

$$C = \left(0.8 + e^{-0.075d}\right)\left(-1 + \frac{1}{1+10^{-11}d^{12}}\right) + 1 + \frac{1}{1+10^{-11}d^{12}} , \tag{4.6}$$

$$\mu^*_{0.45} = 6e^{-0.085d} + 3.2 - 2.44e^{-0.06d^{0.645}} , \tag{4.7}$$

where μ_{rel} is the relative viscosity, H_d is the discharge hematocrit, C describe the dependence of viscosity on hematocrit, d is the diameter of the vessel and is here approximated as $d \approx d_0$. The dynamic viscosity can be calculated from the relative viscosity and the plasma viscosity as $\mu = \mu_{rel}\mu_{plasma}$.

Energy loss due to strictures/stenosis

Strictures in blood vessel cause additional energy loss in the momentum equation. Based on [Seeley 1976] and [Müller 2015b], this is accounted in the one-dimensional momentum equation by the additional term $f_{friction}$ which has the following form

$$f_{stenosis}(x,t) = A(x,t)\,u(x,t)^2\,\frac{1}{L_s}\left(\frac{K_v}{Re_0(x,t)} + \frac{K_t}{2}\left(\frac{S_0}{S_1} - 1\right)^2\right)\left(\frac{S_1}{S_0}\right)^2 , \tag{4.8}$$

where L_s is the length of the stenosis, S_0/S_1 is the unobstructed/obstructed cross-sectional area, d_0/d_1 is the unobstructed/obstructed cross-sectional diameter and $Re_0(x,t) = \frac{\rho d_0}{\mu}u(x,t)$ is the Reynolds number in the unobstructed section. $K_t = 1.52$ is related to turbulent effects, K_v represents the viscous losses and has the following form:

$$K_v = 32\frac{L_a}{d_0}\left(\frac{S_0}{S_1}\right) , \tag{4.9}$$

with

$$L_a = 0.83L_s + 1.64d_1 . \tag{4.10}$$

An obstruction of percentage degree $0 \leq p_{ob} < 100$ defines the unobstructed and obstructed cross-sectional areas as

$$S_0 = \bar{A}_0 , \tag{4.11}$$

$$S_1 = \bar{A}_0\left(1 - \frac{p_{ob}}{100}\right) , \tag{4.12}$$

where $\bar{A}_0$ is the input cross-sectional area at equilibrium of Table 4.1. The cross-sectional area at equilibrium for the stenotic vessel is set to $A_0 = S_1$: it remains unaltered from the starting value $\bar{A}_0$ when $p_{ob} = 0$, or decreases to $A_0 = \bar{A}_0 \left(1 - \frac{p_{ob}}{100}\right)$ when $p_{ob} > 0$.

Conservative formulation of the one-dimensional equations

It is possible to write the blood flow equations in conservative form as follows:

$$\partial_t \mathbf{Q} + \partial_x \mathbf{F}(\mathbf{Q}, x) = \mathbf{S}(\mathbf{Q}, x) \,, \tag{4.13}$$

where

$$\mathbf{Q} = \begin{bmatrix} A \\ Au \end{bmatrix} \,, \quad \mathbf{F}(\mathbf{Q}, x) = \begin{bmatrix} Au \\ Au^2 - \frac{K}{\rho} A_0 \partial_{A_0} \Psi \end{bmatrix} \,, \tag{4.14}$$

$$\mathbf{S}(\mathbf{Q}, x) = \begin{bmatrix} 0 \\ -f_{friction} - f_{stenosis} - \frac{1}{\rho} \left(A \partial_x p_e + \Psi \partial_x K + K \partial_x A_0 \partial_{A_0} \Psi \right) \end{bmatrix} \,, \tag{4.15}$$

with

$$\Psi = \Psi(A; A_0) = \int_A \psi(A; A_0) \mathrm{d}A = A_0 \left(\frac{1}{m+1} \left(\frac{A}{A_0} \right)^{m+1} - \frac{1}{n+1} \left(\frac{A}{A_0} \right)^{n+1} \right) \,, \tag{4.16}$$

and

$$\partial_{A_0} \Psi = \partial_{A_0} \Psi(A; A_0) = \partial_{A_0} \int_A \psi(A; A_0) \mathrm{d}A = - \left(\frac{m}{m+1} \left(\frac{A}{A_0} \right)^{m+1} - \frac{n}{n+1} \left(\frac{A}{A_0} \right)^{n+1} \right) . \tag{4.17}$$

The constants arising from the integrals (4.16) and (4.17) are set to zero for consistency with (4.1) and (4.2), see [Elad 1991, Brook 1999, Toro 2016].

We also assume parameters $K(x)$ and $p_e(x)$ to be constant. As a result, the source term simplifies to

$$\mathbf{S}(\mathbf{Q}, x, t) = \mathbf{S}(\mathbf{Q}) = \begin{bmatrix} 0 \\ -f_{friction} - f_{stenosis} \end{bmatrix} . \tag{4.18}$$

The general case of variable material properties poses mathematical [Toro 2013] and numerical challenges, and requires the use of well-balanced schemes [Müller 2013a]. For a complete view of the mathematical analysis and derivation of the one-dimensional blood flow equations, refer to [Toro 2013, Formaggia 2009, Toro 2016].

4.2.2 Zero-dimensional mathematical models

Based on [Müller 2014, Linninger 2017], we model heart dynamics, microcirculation, cerebrospinal fluid compartments and lymphatic system through a set of Ordinary Differential Equations (ODEs) based on mass and momentum conservation.

A compartment of volume V is governed by the following ODE:

$$\frac{d}{dt} V(t) = \sum_{in} q_{in}(t) - \sum_{out} q_{out}(t) \,, \tag{4.19}$$

where q_{in} and q_{out} are inflow and outflow, respectively. We associate to each compartment a pressure-volume relationship

$$P(V) = \begin{cases} \frac{V-V_0}{C} + P_{ext} \ , & \text{microcirculation, CSF, ISF, lymphatics} \\ (E_a e(t) + E_b)(V - V_0) + P(V) S \frac{d}{dt} V + P_{ext} \ , & \text{heart chambers} \\ P_0 e^{\frac{V-V_0}{\phi}} \ , & \text{pericardium, brain} \\ \phi E_0 e^{\frac{V}{\phi}} + S \frac{d}{dt} V + P_{ext} \ . & \text{lung microcirculation} \end{cases} \tag{4.20}$$

V_0 is dead volume; C is compliance; E_a and E_b are the elastances of the heart model; $e(t)$ is a prescribed normalized function and differs for ventricles and atria; S is the viscoelasticity coefficient; P_0 is the pressure at $V = V_0$; ϕ is a parameter related to the compliance of the compartment; E_0 is the elastance of the lung microcirculation. For atria we use

$$e(t) = \begin{cases} \frac{1}{2}\left(1 + \cos\left(\pi \frac{t + T - t_{ar}}{T_{arp}}\right)\right) & 0 \le t \le t_{ar} + T_{arp} - T \ , \\ 0 & t_{ar} + T_{arp} - T < t \le t_{ac} \ , \\ \frac{1}{2}\left(1 - \cos\left(\pi \frac{t - t_{ac}}{T_{acp}}\right)\right) & t_{ac} < t \le t_{ac} + T_{acp} \ , \\ \frac{1}{2}\left(1 + \cos\left(\pi \frac{t - t_{ar}}{T_{arp}}\right)\right) & t_{ac} + T_{acp} < t \le T \ , \end{cases} \tag{4.21}$$

while for ventricles, we use

$$e(t) = \begin{cases} \frac{1}{2}\left(1 - \cos\left(\pi \frac{t}{T_{vcp}}\right)\right) & 0 \le t \le T_{vcp} \ , \\ \frac{1}{2}\left(1 + \cos\left(\pi \frac{t - T_{vcp}}{T_{vrp}}\right)\right) & T_{vcp} \le t \le T_{vcp} + T_{vrp} \ , \\ 0 & T_{vcp} + T_{vrp} < t \le T \ . \end{cases} \tag{4.22}$$

T represents the duration of the cardiac cycle; T_{acp}, T_{vcp}, T_{arp}, T_{vrp} represent the duration of atrial/ventricular contraction/relaxation, respectively; t_{ac} and t_{ar} are the times within the cardiac cycle at which atrial contraction and relaxation begin.

The pericardium volume is the sum of the heart chambers and pericardial fluid volume

$$V_{pericardium} = V_{left\ ventricle} + V_{right\ ventricle} + V_{left\ atrium} + V_{right\ ventricle} + V_{pericardial\ fluid} \ . \tag{4.23}$$

The intracranial volume is the sum of the intracranial volumes within the skull

$$V_{intracranium} = V_{intracranial\ blood} + V_{intracranial\ CSF} + V_{brain\ ISF} + V_{brain\ solid\ matrix} \ , \tag{4.24}$$

where the $V_{intracranial\ blood}$ is the sum of all intracranial vessel $V_{1D\ intracranial\ blood}$ and microcirculation volumes $V_{0D\ intracranial\ blood}$, and $V_{intracranial\ CSF}$ is the sum of all CSF volumes with the exception of the spinal subarachnoid space volume. The external pressure of the compartments are set as

follows:

$$P_{ext} = \begin{cases} P_{pericardium} + P_{intrathoracic}\,, & \text{heart chamber} \\ P_{intrathoracic}\,, & \text{lung microcirculation, intrathoracic vessels} \\ P_{intracranium}\,, & \text{intracranial: microcirculation, vessels, CSF and brain ISF} \\ 0\,, & \text{otherwise.} \end{cases} \tag{4.25}$$

The framework proposed here is based on [Liang 2009b, Linninger 2017, Müller 2014] and [Sun 1997]. Here we assumed a *relaxed version* of the Monro-Kellie doctrine. The external pressure $P_{intracranium}$ acts uniformly on every one- or zero-dimensional model within the skull (see the discussion for details).

The flow rate between two compartments, say from V_1 to V_2, is modelled in a general framework as

$$\frac{d}{dt}q(t) = \frac{1}{L}\left(P_1(t) - P_2(t) - \sigma(\pi_1 - \pi_2) - Rq(t) - B|q(t)|q(t)\right)\,, \tag{4.26}$$

where L is inertia, R is viscous resistance to flow, B is Bernoulli coefficient, σ is the reflection coefficient, $P_{1,2}$ and $\pi_{1,2}$ are the hydrostatic and oncotic pressure of compartment $V_{1,2}$. This formulation is general and has to be adapted to each specific dynamics. For instance, for the heart dynamics, the contribution of the oncotic forces is zero as $\Delta\pi = \pi_1 - \pi_2 = 0$. Analogously, the fluid exchange at the microvasculature between arterioles, venules and veins is governed only by hydrostatic forces with zero Bernoulli resistance contribution. The Starling equation for fluid filtration can be recovered the stationary solution of (4.26) assuming zero Bernoulli coefficient, and has the following form:

$$q(t) = \frac{1}{R}\left(P_1(t) - P_2(t) - \sigma(\pi_1 - \pi_2)\right)\,. \tag{4.27}$$

The resulting system of ODEs may be written as

$$\frac{d}{dt}\mathbf{Y} = \mathbf{L}\left(\mathbf{Y}, t, V_{1D\ intracranial\ blood}\right)\,, \tag{4.28}$$

where $\mathbf{Y}(t) = (V_1, V_2, \ldots, V_{n_1}, q_1, q_2, \ldots, q_{n_2})$ is the vector of unknowns.

A mathematical model of the Monro-Kellie hypothesis

The Monro-Kellie hypothesis describes the principle of homeostatic intracranial volume regulation and states that the sum of all intracranial fluid compartments (parenchyma, cerebrospinal fluid and blood) remains *strictly* constant. In the current work, we relax this doctrine. We assume that the sum of all intracranial fluid compartments is *almost* constant. This is achieved by setting a very low compliance of whole intracranial volume

$$C = \frac{dP_{intracranium}}{dV} = \frac{\phi}{P_{intracranium}}\,. \tag{4.29}$$

For instance, at the average intracranial murine pressure $P_{intracranium} \approx 3$ mmH$_2$O and $\phi \approx 1.4\ \mu L$, the intracranial compliance is $C = 0.46$ mmHg μL^{-1}. This means that the intracranial pressure approximately increases by 1 mmHg when the intracranial volume increases by 0.46 μL, which corresponds to the $\approx 0.1\%$ of the averaged intracranial murine volume [Chuang 2011].

The mathematical model of the relaxed version of the Monro-Kellie doctrine allows for the interaction of all four-fluid brain compartments. At each cardiac contraction, the following chain of events occurs: 1) during the systolic phase, the cerebral arterial inflow transiently increases the intracranial volume; 2) the external pressure of all intracranial compartments increases; 2) CSF is displaced from the cerebral subarachnoid space into the spinal subarachnoid space; 3) intracranial veins are squeezed and displace venous blood out of the brain towards to right atrium; 4) during the diastolic phase, venous blood decreases; 5) the transient reduction of the intracranial pressure causes suction of CSF from the spinal subarachnoid space back to the cerebral subarachnoid space. During each cardiac cycle, this chain of fluid-dynamical events regulates the intracranial fluid volumes.

No.	Name	Tube law	p_{ext}	r_0 [mm]	c_0 [m s^{-1}]	L [mm]	$R_{terminal}$ [mmHg mL s^{-1}]	Mothers	Daugthers	Reference
1	Ascending aorta	Artery	$P_{intrath}$	0.74	3.30	2.60	-	Left ventricle	2, 3	[Aslanidou 2015]
2	Aortic arch I	Artery	$P_{intrath}$	0.67	3.42	0.70	-	1	10, 11	[Aslanidou 2015]
3	Brachiocephalic	Artery	$P_{intrath}$	0.38	4.13	2.10	-	1	4, 5	[Aslanidou 2015]
4	Right subclavian I	Artery	-	0.27	4.62	1.90	-	3	6, 7	[Aslanidou 2015]
5	Right carotid	Artery	-	0.25	4.73	10.20	-	3	39, 47	[Aslanidou 2015]
6	Right vertebral	Artery	-	0.17	5.43	13.30	-	4	56	[Aslanidou 2015]
7	Right subclavian II	Artery	-	0.15	5.63	9.10	-	4	8, 9	[Aslanidou 2015]
8	Right radial	Artery	-	0.23	4.91	3.70	7755.99	7	Arteriole 8	[Müller 2014] + AS
9	Right ulnar I	Artery	-	0.28	4.58	1.10	-	7	43, 44	[Müller 2014] + AS
10	Aortic arch II	Artery	$P_{intrath}$	0.59	3.55	1.20	-	2	12, 15	[Aslanidou 2015]
11	Left carotid	Artery	-	0.29	4.53	13.30	-	2	40, 48	[Aslanidou 2015]
12	Thoracic aorta I	Artery	$P_{intrath}$	0.57	3.60	12.20	-	10	13, 14	[Aslanidou 2015]
13	Thoracic aorta II	Artery	$P_{intrath}$	0.54	3.66	14.50	-	12	20, 25	[Aslanidou 2015]
14	Intercoastals	Artery	$P_{intrath}$	0.26	4.71	1.60	3435.81	12	Arteriole 14	[Aslanidou 2015]
15	Left subclavian I	Artery	-	0.29	4.51	1.80	-	10	16, 17	[Aslanidou 2015]
16	Left vertebral	Artery	-	0.15	5.63	13.20	-	15	56	[Aslanidou 2015]
17	Left subclavian II	Artery	-	0.15	5.63	9.10	-	15	18, 19	[Aslanidou 2015]
18	Left ulnar I	Artery	-	0.28	4.58	1.10	-	17	45, 46	[Müller 2014] + AS
19	Left radial	Artery	-	0.23	4.91	3.70	7755.99	17	Arteriole 19	[Müller 2014] + AS
20	Celiac I	Artery	-	0.22	4.92	2.17	-	13	21, 22	[Aslanidou 2015]
21	Celiac II	Artery	-	0.21	4.99	0.93	-	20	23, 24	[Aslanidou 2015]
22	Hepatic	Artery	-	0.12	6.07	3.40	7301.10	20	Arteriole 22	[Aslanidou 2015]
23	Splenic	Artery	-	0.14	5.76	6.90	6258.09	21	Arteriole 23	[Aslanidou 2015]
24	Gastric	Artery	-	0.15	5.70	5.10	6042.29	21	Arteriole 24	[Aslanidou 2015]
25	Abdomainal aorta I	Artery	-	0.49	3.78	2.90	-	13	26, 27	[Aslanidou 2015]
26	Superior mesenteric	Artery	-	0.29	4.51	4.70	3021.15	25	Arteriole 26	[Aslanidou 2015]
27	Abdominal aorta II	Artery	-	0.44	3.93	0.80	-	25	29, 31	[Aslanidou 2015]
28	Right renal	Artery	-	0.20	5.11	2.90	4380.66	29	Arteriole 28	[Ruan 1999]
29	Abdominal aorta III	Artery	-	0.44	3.93	0.80	-	27	28, 30	[Aslanidou 2015]
30	Left renal	Artery	-	0.20	5.11	1.50	4380.66	29	Arteriole 30	[Ruan 1999]
31	Abdominal aorta IV	Artery	-	0.41	4.03	6.90	-	27	32, 33	[Aslanidou 2015]
32	Inferior mesenteric	Artery	-	0.26	4.69	0.63	3393.25	31	Arteriole 32	[Müller 2014] + AS
33	Abdominal aorta V	Artery	-	0.36	4.19	2.10	-	31	34, 49, 82	[Aslanidou 2015]
34	Right common Iliac	Artery	-	0.24	4.78	3.40	-	33	35, 36	[Aslanidou 2015]
35	Right external Iliac	Artery	-	0.22	4.92	1.01	-	34	37, 38	[Aslanidou 2015]
36	Right internal Iliac	Artery	-	0.10	6.40	4.00	170952.70	34	Arteriole 36	[Aslanidou 2015]
37	Right deep femoral	Artery	-	0.26	4.69	1.88	3393.25	35	Arteriole 37	[Müller 2014] + AS
38	Right femoral	Artery	-	0.21	4.99	3.09	-	35	41, 42	[Aslanidou 2015]
39	Right external carotid	Artery	-	0.26	4.69	0.68	-	5	70, 73	[Müller 2014] + AS
40	Left internal carotid	Artery	-	0.18	5.35	6.60	-	11	66	[Aslanidou 2015]
41	Right posterior tibial	Artery	-	0.13	5.87	4.30	132246.43	38	Arteriole 41	[Aslanidou 2015]

42	Right anterior tibial	Artery	-	0.15	5.60	3.00	114902.64	38	Arteriole 42	[Aslanidou 2015]
43	Right interosseous artery	Artery	-	0.13	5.92	1.17	13572.99	9	Arteriole 43	[Müller 2014] + AS
44	Right ulnar II	Artery	-	0.26	4.67	2.83	6686.20	9	Arteriole 44	[Müller 2014] + AS
45	Left ulnar II	Artery	-	0.26	4.67	2.83	6686.20	18	Arteriole 45	[Müller 2014] + AS
46	Left interosseous	Artery	-	0.13	5.92	1.17	13572.99	18	Arteriole 46	[Müller 2014] + AS
47	Right internal carotid	Artery	-	0.18	5.35	6.60	-	5	61, 62	[Aslanidou 2015]
48	Left external carotid	Artery	-	0.26	4.69	0.68	-	11	71, 72	[Müller 2014] + AS
49	Left common Iliac	Artery	-	0.24	4.78	3.40	-	33	50, 51	[Aslanidou 2015]
50	Left external Iliac	Artery	-	0.22	4.92	1.01	-	49	52, 53	[Aslanidou 2015]
51	Left internal Iliac	Artery	-	0.10	6.40	4.00	170952.70	49	Arteriole 51	[Aslanidou 2015]
52	Left deep femoral	Artery	-	0.26	4.69	1.88	3393.25	50	Arteriole 52	[Müller 2014] + AS
53	Left femoral	Artery	-	0.21	4.99	3.09	-	50	54, 55	[Aslanidou 2015]
54	Left posterior tibial	Artery	-	0.13	5.87	4.30	132246.43	53	Arteriole 54	[Aslanidou 2015]
55	Left anterior tibial	Artery	-	0.15	5.60	3.00	114902.64	53	Arteriole 55	[Aslanidou 2015]
56	Basilar artery	Artery	$P_{intracranium}$	0.12	6.11	4.80	-	6, 16	57, 69	[Aslanidou 2015]
57	Right posterior cerebral artery I	Artery	$P_{intracranium}$	0.09	6.69	2.56	-	56	58, 59	[Aslanidou 2015]
58	Right posterior cerebral artery II	Artery	$P_{intracranium}$	0.10	6.45	3.50	14512.51	57	Arteriole 58	[Aslanidou 2015]
59	Right posterior communicating artery	Artery	$P_{intracranium}$	0.11	6.35	2.67	-	57	60	[Aslanidou 2015]
60	Right internal carotid artery II	Artery	$P_{intracranium}$	0.13	5.87	1.50	-	59	61, 62	[Aslanidou 2015]
61	Right middle cerebral artery	Artery	$P_{intracranium}$	0.09	6.75	2.20	6096.22	47, 60	Arteriole 61	[Aslanidou 2015]
62	Right anterior cerebral artery I	Artery	$P_{intracranium}$	0.11	6.19	2.60	-	47, 60	63	[Aslanidou 2015]
63	Right anterior cerebral artery II	Artery	$P_{intracranium}$	0.11	6.19	2.10	4980.13	62, 64	Arteriole 63	[Aslanidou 2015]
64	Left anterior cerebral artery I	Artery	$P_{intracranium}$	0.11	6.19	2.60	-	66	63	[Aslanidou 2015]
65	Left middle cerebral artery	Artery	$P_{intracranium}$	0.09	6.75	2.20	6096.22	66	Arteriole 65	[Aslanidou 2015]
66	Left internal carotid artery II	Artery	$P_{intracranium}$	0.13	5.87	1.50	-	40, 67	64, 65	[Aslanidou 2015]
67	Left posterior communicating artery	Artery	$P_{intracranium}$	0.11	6.35	2.67	-	69	66	[Aslanidou 2015]
68	Left posterior cerebral artery II	Artery	$P_{intracranium}$	0.10	6.45	3.50	14512.51	69	Arteriole 68	[Aslanidou 2015]
69	Left posterior cerebral artery I	Artery	$P_{intracranium}$	0.09	6.69	2.56	-	56	67, 68	[Aslanidou 2015]
70	Right facial artery	Artery	-	0.09	6.75	3.20	15000.00	39	Arteriole 70	[Aslanidou 2015]
71	Left facial artery	Artery	-	0.09	6.75	3.20	15000.00	48	Arteriole 71	[Aslanidou 2015]
72	Left superficial temporal artery I	Artery	-	0.14	5.80	4.83	-	48	74	MRI
73	Right superficial temporal artery I	Artery	-	0.14	5.80	4.83	-	39	75	MRI
74	Left superficial temporal artery II	Artery	-	0.11	6.20	2.00	6428.57	72	Arteriole 74	MRI
75	Right superficial temporal artery II	Artery	-	0.11	6.20	2.00	6428.57	73	Arteriole 75	MRI
82	Middle caudal artery	Artery	-	0.14	5.76	28.10	6258.09	33	Arteriole 82	[Aslanidou 2015]
83	Middle caudal vein	Vein	-	0.14	2.26	28.10	-	Venules 83	93	-
84	Right cranial vena cava	Vein	$P_{intrath}$	0.60	1.16	7.00	40.42	143, 147, 148, 402	Right atrium	[Müller 2014] + AS
85	Inferior vena cava I	Vein	$P_{intrath}$	0.70	1.00	5.04	15.00	86, 87	Right atrium	[Müller 2014] + AS
86	Hepatic vein	Vein	$P_{intrath}$	0.44	1.44	2.24	-	Venules 86	85	[Müller 2014] + AS
87	Inferior vena cava II	Vein	$P_{intrath}$	0.70	1.00	0.49	-	88, 89	85	[Müller 2014] + AS
88	Left renal vein	Vein	-	0.23	1.95	1.05	-	Venules 88	87	[Müller 2014] + AS
89	Inferior vena cava III	Vein	-	0.70	1.00	0.49	-	90, 91	87	[Müller 2014] + AS
90	Right renal vein	Vein	-	0.23	1.95	1.05	-	Venules 90	89	[Müller 2014] + AS

91	Inferior vena cava IV	Vein	-	0.70	1.00	4.12	-	92, 93	89	[Müller 2014] + AS
92	Inferior mesenteric vein	Vein	-	0.41	1.51	1.98	-	Venules 92	91	[Müller 2014] + AS
93	Inferior vena cava V	Vein	-	0.70	1.00	2.64	-	83, 94, 95	91	[Müller 2014] + AS
94	Left common Iliac vein I	Vein	-	0.53	1.28	1.25	-	96, 98	93	[Müller 2014] + AS
95	Right common Iliac vein I	Vein	-	0.53	1.28	1.25	-	97, 111	93	[Müller 2014] + AS
96	Right lumbar vein	Vein	-	0.09	2.49	1.25	-	126	94, 124	[Müller 2014] + AS
97	Left lumbar vein	Vein	-	0.09	2.49	1.25	-	126	95, 125	[Müller 2014] + AS
98	Right common Iliac vein II	Vein	-	0.53	1.28	0.66	-	99, 100	94, 124	[Müller 2014] + AS
99	Right internal Iliac vein	Vein	-	0.14	2.26	1.65	-	Venules 99	98	[Müller 2014] + AS
100	Right external Iliac vein	Vein	-	0.46	1.41	4.75	-	101, 102, 103	98	[Müller 2014] + AS
101	Right deep femoral vein	Vein	-	0.32	1.71	4.15	-	Venules 101	100	[Müller 2014] + AS
102	Right femoral vein	Vein	-	0.32	1.71	8.38	-	106	100	[Müller 2014] + AS
103	Right great saphenous vein I	Vein	-	0.21	2.00	2.47	-	104	100	[Müller 2014] + AS
104	Right great saphenous vein III	Vein	-	0.20	2.03	9.89	-	105	103	[Müller 2014] + AS
105	Right great saphenous vein II	Vein	-	0.17	2.13	12.37	-	Venules right leg	104	[Müller 2014] + AS
106	Right popliteal vein	Vein	-	0.31	1.73	6.27	-	107, 109	102	[Müller 2014] + AS
107	Right posterior tibial vein I	Vein	-	0.14	2.26	5.71	-	108	106	[Müller 2014] + AS
108	Right posterior tibial vein II	Vein	-	0.14	2.26	5.71	-	Venules 108	107	[Müller 2014] + AS
109	Right anterior tibial vein I	Vein	-	0.14	2.26	5.28	-	110	106	[Müller 2014] + AS
110	Right anterior tibial vein II	Vein	-	0.14	2.26	5.94	-	Venules right leg	109	[Müller 2014] + AS
111	Left common Iliac vein II	Vein	-	0.53	1.28	0.66	-	112, 113	95, 125	[Müller 2014] + AS
112	Left internal Iliac vein	Vein	-	0.14	2.26	1.65	-	Venules 112	111	[Müller 2014] + AS
113	Left external Iliac vein	Vein	-	0.46	1.41	4.75	-	114, 115, 116	111	[Müller 2014] + AS
114	Left deep femoral vein	Vein	-	0.32	1.71	4.15	-	Venules 114	113	[Müller 2014] + AS
115	Left femoral vein	Vein	-	0.32	1.71	8.38	-	119	113	[Müller 2014] + AS
116	Left great saphenous vein I	Vein	-	0.21	2.00	2.47	-	117	113	[Müller 2014] + AS
117	Left great saphenous vein III	Vein	-	0.20	2.03	9.89	-	118	116	[Müller 2014] + AS
118	Left great saphenous vein II	Vein	-	0.17	2.13	12.37	-	Venules left leg	117	[Müller 2014] + AS
119	Left popliteal vein	Vein	-	0.31	1.73	6.27	-	120, 122	115	[Müller 2014] + AS
120	Left posterior tibial vein I	Vein	-	0.14	2.26	5.71	-	121	119	[Müller 2014] + AS
121	Left posterior tibial vein I	Vein	-	0.14	2.26	5.71	-	Venules 121	120	[Müller 2014] + AS
122	Left anterior tibial vein I	Vein	-	0.14	2.26	5.28	-	123	119	[Müller 2014] + AS
123	Left anterior tibial vein II	Vein	-	0.14	2.26	5.94	-	Venules left leg	122	[Müller 2014] + AS
124	Ascending lumbar vein	Vein	-	0.18	2.09	7.58	-	96, 98	128	[Müller 2014] + AS
125	Hemiazygos vein	Vein	-	0.26	1.87	7.58	-	97, 111	128	[Müller 2014] + AS
126	Vertebral venous plexus	Vein	-	0.15	2.22	23.41	-	257	96, 97	[Müller 2014] + AS
127	Intercostal vein	Vein	$P_{intrath}$	0.37	1.60	0.66	-	Venules 127	128	[Müller 2014] + AS
128	Azygos vein II	Vein	$P_{intrath}$	0.39	1.55	9.23	-	124, 125, 127	129	[Müller 2014] + AS
129	Azygos vein I	Vein	$P_{intrath}$	0.39	1.55	0.66	-	128	142	[Müller 2014] + AS
130	Right subclavian vein II	Vein	-	0.48	1.38	0.99	-	131	143	[Müller 2014] + AS
131	Right subclavian vein III	Vein	-	0.48	1.38	8.90	-	132, 133	130	[Müller 2014] + AS
132	Right radial vein	Vein	-	0.18	2.09	13.39	-	Venules 132	131	[Müller 2014] + AS
133	Right ulnar vein I	Vein	-	0.18	2.09	3.30	-	134, 135	131	[Müller 2014] + AS

134	Right interosseous vein	Vein	-	0.09	2.49	2.31	-	Venules 134	133	[Müller 2014] + AS
135	Right ulnar vein II	Vein	-	0.18	2.09	10.09	-	Venules 135	133	[Müller 2014] + AS
136	Left subclavian vein II	Vein	-	0.48	1.38	0.99	-	137	145	[Müller 2014] + AS
137	Left subclavian vein III	Vein	-	0.48	1.38	8.90	-	138, 139	136	[Müller 2014] + AS
138	Left radial vein	Vein	-	0.18	2.09	13.39	-	Venules 138	137	[Müller 2014] + AS
139	Left ulnar vein I	Vein	-	0.18	2.09	3.30	-	140, 141	137	[Müller 2014] + AS
140	Left interosseous vein	Vein	-	0.09	2.49	2.31	-	Venules 140	139	[Müller 2014] + AS
141	Left ulnar vein II	Vein	-	0.18	2.09	10.09	-	Venules 141	139	[Müller 2014] + AS
142	Left cranial vena cava II	Vein	$P_{intrath}$	0.60	1.16	3.00	40.42	129, 144	Right atrium	[Müller 2014] + AS
143	Right subclavian vein I	Vein	-	0.52	1.30	0.99	-	130, 146	84	[Müller 2014] + AS
144	Left cranial vena cava I	Vein	$P_{intrath}$	0.60	1.16	4.00	-	145, 149, 150, 401	142	[Müller 2014] + AS
145	Left subclavian vein I	Vein	-	0.52	1.30	0.99	-	136, 151	144	[Müller 2014] + AS
146	Right external jugular vein II	Vein	-	0.61	1.14	5.00	-	152	143	MRI
147	Right internal jugular vein III	Vein	-	0.10	2.45	1.00	-	153	84	[Müller 2014, Mancini 2015] + AS
148	Right vertebral vein	Vein	-	0.07	2.65	6.00	-	164, 250	84	[Müller 2014] + AS
149	Left vertebral vein	Vein	-	0.07	2.65	6.00	-	165, 251	144	[Müller 2014] + AS
150	Left internal jugular vein III	Vein	-	0.10	2.45	1.00	-	154	144	[Müller 2014, Mancini 2015] + AS
151	Left external jugular vein II	Vein	-	0.61	1.14	5.00	-	155	145	MRI
152	Right external jugular vein I	Vein	-	0.54	1.27	5.00	-	158, 159	146	MRI
153	Right internal jugular vein II	Vein	-	0.10	2.45	1.00	-	156	147	[Müller 2014, Mancini 2015] + AS
154	Left internal jugular vein II	Vein	-	0.10	2.45	1.00	-	157	150	[Müller 2014, Mancini 2015] + AS
155	Left external jugular vein I	Vein	-	0.54	1.27	5.00	-	160, 161	151	MRI
156	Right internal jugular vein I	Vein	-	0.10	2.45	1.00	-	162, 163, 168, 169	153	[Müller 2014, Mancini 2015] + AS
157	Left internal jugular vein I	Vein	-	0.10	2.45	1.00	-	166, 167, 170, 171	154	[Müller 2014, Mancini 2015] + AS
158	Right anterior facial vein II	Vein	-	0.33	1.70	9.00	-	247	152	MRI
159	Right posterior facial vein	Vein	-	0.45	1.43	5.07	-	172, 173	152	MRI
160	Left posterior facial vein	Vein	-	0.45	1.43	5.07	-	179, 180	155	MRI
161	Left anterior facial vein II	Vein	-	0.33	1.70	9.00	-	248	155	MRI
162	Anastomosis	Vein	-	0.05	3.00	0.50	-	172, 173	156	-
163	Right lateral anterior condylar vein	Vein	-	0.10	2.45	0.99	-	164, 250	156	[Müller 2014] + AS
164	Right anastomotic vein	Vein	-	0.10	2.45	0.66	-	257	148, 163	[Müller 2014] + AS
165	Left anastomotic vein	Vein	-	0.10	2.45	0.66	-	257	149, 166	[Müller 2014] + AS
166	Left lateral anterior condylar vein	Vein	-	0.10	2.45	0.99	-	165, 251	157	[Müller 2014] + AS
167	Anastomosis	Vein	-	0.05	3.00	0.50	-	179, 180	157	-
168	Right sigmoid sinus	Dural sinus	$P_{intracranium}$	0.10	3.00	1.65	-	185	156	[Müller 2014] + AS
169	Right inferior petrosal sinus	Dural sinus	$P_{intracranium}$	0.09	3.00	1.05	-	175	156	[Müller 2014] + AS
170	Left inferior petrosal sinus	Dural sinus	$P_{intracranium}$	0.09	3.00	1.05	-	177	157	[Müller 2014] + AS
171	Left sigmoid sinus	Dural sinus	$P_{intracranium}$	0.10	3.00	1.65	-	178, 186	157	[Müller 2014] + AS
172	Right superficial temporal vein	Vein	-	0.38	1.59	4.50	-	181, 243	159, 162	MRI
173	Right interpterygoid emissary vein II	Vein	-	0.05	3.00	0.30	-	182, 184	159, 162	-
174	Right superior petrosal sinus	Dural sinus	$P_{intracranium}$	0.10	3.00	1.88	-	185	175, 176, 184	[Müller 2014] + AS
175	Right cavernous sinus	Dural sinus	$P_{intracranium}$	0.09	3.00	0.49	-	174	169	[Müller 2014] + AS
176	Intracavernous sinus	Dural sinus	$P_{intracranium}$	0.12	3.00	0.66	-	174	177, 178, 187	[Müller 2014] + AS

177	Left cavernous sinus	Dural sinus	$P_{intracranium}$	0.09	3.00	0.49	-	176	170	[Müller 2014] + AS
178	Left superior petrosal sinus	Dural sinus	$P_{intracranium}$	0.10	3.00	1.88	-	176	171, 188, 255	[Müller 2014] + AS
179	Left interpterygoid emissary vein II	Vein	-	0.05	3.00	0.30	-	187, 189	160, 167	-
180	Left superficial temporal vein	Vein	-	0.38	1.59	4.50	-	190, 246	160, 167	MRI
181	Right petrosquamosus sinus II	Vein	-	0.38	1.59	2.50	-	183	172	MRI
182	Anastomosis	Vein	-	0.05	3.00	2.50	-	183	173	-
183	Right petrosquamosus sinus I	Vein	-	0.35	1.64	2.50	-	185	181, 182	MRI
184	Right interpterygoid emissary vein I	Vein	-	0.05	3.00	0.40	-	174	173	MRI
185	Right transverse sinus I	Dural sinus	$P_{intracranium}$	0.30	3.00	2.90	-	192, 193	168, 174, 183, 254	MRI
186	Left transverse sinus I	Dural sinus	$P_{intracranium}$	0.30	3.00	2.90	-	194, 195	171, 188, 255	MRI
187	Left interpterygoid emissary vein I	Vein	-	0.05	3.00	0.40	-	176	179	MRI
188	Left petrosquamosus sinus I	Vein	-	0.35	1.64	2.50	-	178, 186	189, 190	MRI
189	Anastomosis	Vein	-	0.05	3.00	2.50	-	188	179	-
190	Left petrosquamosus sinus II	Vein	-	0.38	1.59	2.50	-	188	180	MRI
191	Right Labbé vein	Vein	$P_{intracranium}$	0.14	2.26	1.65	-	Venules 191	Starling 191 → 192	[Müller 2014] + AS
192	Terminal cerebral vein	Vein	$P_{intracranium}$	0.14	2.26	0.33	-	Starling 191 → 192	185	[Müller 2014] + AS
193	Right transverse sinus II	Dural sinus	$P_{intracranium}$	0.30	3.00	2.90	-	221, 249	185	MRI
194	Left transverse sinus II	Dural sinus	$P_{intracranium}$	0.30	3.00	2.90	-	221, 249	186	MRI
195	Terminal cerebral vein	Vein	$P_{intracranium}$	0.14	2.26	0.33	-	Starling 194 → 195	186	[Müller 2014] + AS
196	Left Labbé vein	Vein	$P_{intracranium}$	0.14	2.26	1.65	-	Venules 196	Starling 196 → 197	[Müller 2014] + AS
197	Right basal vein of Rosenthal I	Vein	$P_{intracranium}$	0.12	2.36	0.33	-	Venules 197	198	[Müller 2014] + AS
198	Right basal vein of Rosenthal II	Vein	$P_{intracranium}$	0.12	2.36	2.31	-	197	203	[Müller 2014] + AS
199	Right internal cerebral vein	Vein	$P_{intracranium}$	0.12	2.36	1.65	-	Venules 199	203	[Müller 2014] + AS
200	Left internal cerebral vein	Vein	$P_{intracranium}$	0.12	2.36	1.65	-	Venules 200	203	[Müller 2014] + AS
201	Left basal vein of Rosenthal I	Vein	$P_{intracranium}$	0.12	2.36	0.33	-	Venules 201	202	[Müller 2014] + AS
202	Left basal vein of Rosenthal II	Vein	$P_{intracranium}$	0.12	2.36	2.31	-	201	203	[Müller 2014] + AS
203	Terminal cerebral vein	Vein	$P_{intracranium}$	0.34	1.67	0.33	-	198, 199, 200, 202	Starling 203 → 204	[Müller 2014] + AS
204	Vein of Galen	Vein	$P_{intracranium}$	0.37	1.60	0.30	-	Starling 203 → 204	249	[Müller 2014] + AS
205	Inferior sagittal sinus	Dural sinus	$P_{intracranium}$	0.15	3.00	1.21	-	209	206	[Müller 2014] + AS
206	Inferior sagittal sinus	Dural sinus	$P_{intracranium}$	0.15	3.00	1.21	-	205, 211	207	[Müller 2014] + AS
207	Inferior sagittal sinus	Dural sinus	$P_{intracranium}$	0.15	3.00	1.21	-	206, 213	249	[Müller 2014] + AS
208	Cerebral vein	Vein	$P_{intracranium}$	0.14	2.26	0.99	-	Venules 208	Starling 208 → 209	[Müller 2014] + AS
209	Terminal cerebral vein	Vein	$P_{intracranium}$	0.14	2.26	0.33	-	Starling 208 → 209	205	[Müller 2014] + AS
210	Cerebral vein	Vein	$P_{intracranium}$	0.14	2.26	0.99	-	Venules 210	Starling 210 → 211	[Müller 2014] + AS
211	Terminal cerebral vein	Vein	$P_{intracranium}$	0.14	2.26	0.33	-	Starling 210 → 211	206	[Müller 2014] + AS
212	Cerebral vein	Vein	$P_{intracranium}$	0.14	2.26	0.99	-	Venules 212	Starling 212 → 213	[Müller 2014] + AS
213	Terminal cerebral vein	Vein	$P_{intracranium}$	0.14	2.26	0.33	-	Starling 212 → 213	207	[Müller 2014] + AS
214	Superior sagittal sinus I	Dural sinus	$P_{intracranium}$	0.15	3.00	0.99	-	240	215	MRI
215	Superior sagittal sinus II	Dural sinus	$P_{intracranium}$	0.15	3.00	0.99	-	214, 235	216	MRI
216	Superior sagittal sinus III	Dural sinus	$P_{intracranium}$	0.20	3.00	0.99	-	215, 233	217	MRI
217	Superior sagittal sinus IV	Dural sinus	$P_{intracranium}$	0.20	3.00	0.99	-	216, 231, 236	218	MRI
218	Superior sagittal sinus V	Dural sinus	$P_{intracranium}$	0.20	3.00	0.66	-	217, 229, 237	219	MRI
219	Superior sagittal sinus VI	Dural sinus	$P_{intracranium}$	0.20	3.00	1.65	-	218, 227, 238	220	MRI

220	Superior sagittal sinus VII	Dural sinus	$P_{intracranium}$	0.20	3.00	0.82	-	219, 225	221	MRI
221	Superior sagittal sinus VIII	Dural sinus	$P_{intracranium}$	0.20	3.00	0.82	-	220, 223	193, 194, 256, 257	MRI
222	Cerebral vein	Vein	$P_{intracranium}$	0.14	2.26	1.65	-	Venules 222	Starling 222 → 223	[Müller 2014] + AS
223	Terminal cerebral vein	Vein	$P_{intracranium}$	0.14	2.26	0.33	-	Starling 222 → 223	221	[Müller 2014] + AS
224	Cerebral vein	Vein	$P_{intracranium}$	0.14	2.26	1.65	-	Venules 224	Starling 224 → 225	[Müller 2014] + AS
225	Terminal cerebral vein	Vein	$P_{intracranium}$	0.14	2.26	0.33	-	Starling 224 → 225	220	[Müller 2014] + AS
226	Cerebral vein	Vein	$P_{intracranium}$	0.14	2.26	1.65	-	Venules 226	Starling 226 → 227	[Müller 2014] + AS
227	Terminal cerebral vein	Vein	$P_{intracranium}$	0.14	2.26	0.33	-	Starling 226 → 227	219	[Müller 2014] + AS
228	Cerebral vein	Vein	$P_{intracranium}$	0.14	2.26	1.65	-	Venules 228	Starling 228 → 229	[Müller 2014] + AS
229	Terminal cerebral vein	Vein	$P_{intracranium}$	0.14	2.26	0.33	-	Starling 228 → 229	218	[Müller 2014] + AS
230	Cerebral vein	Vein	$P_{intracranium}$	0.14	2.26	1.65	-	Venules 230	Starling 230 → 231	[Müller 2014] + AS
231	Terminal cerebral vein	Vein	$P_{intracranium}$	0.14	2.26	0.33	-	Starling 230 → 231	217	[Müller 2014] + AS
232	Cerebral vein	Vein	$P_{intracranium}$	0.14	2.26	1.65	-	Venules 232	Starling 232 → 233	[Müller 2014] + AS
233	Terminal cerebral vein	Vein	$P_{intracranium}$	0.14	2.26	0.33	-	Starling 232 → 233	216	[Müller 2014] + AS
234	Cerebral vein	Vein	$P_{intracranium}$	0.14	2.26	1.65	-	Venules 234	Starling 234 → 235	[Müller 2014] + AS
235	Terminal cerebral vein	Vein	$P_{intracranium}$	0.14	2.26	0.33	-	Starling 234 → 235	215	[Müller 2014] + AS
236	Arachnoid villi	Vein	$P_{intracranium}$	0.14	2.26	0.33	-	Cranial SAS	217	-
237	Arachnoid villi	Vein	$P_{intracranium}$	0.14	2.26	0.33	-	Cranial SAS	218	-
238	Arachnoid villi	Vein	$P_{intracranium}$	0.14	2.26	0.33	-	Cranial SAS	219	-
239	Left rostral vein	Vein	-	0.30	1.76	2.78	-	240	242	MRI
240	Right rostral vein	Vein	-	0.30	1.76	2.78	-	244	214, 239	MRI
241	Right supraorbital	Vein	-	0.20	2.04	0.55	-	Venules 241	242	MRI
242	Right superficial temporal vein	Vein	-	0.30	1.76	5.77	-	239, 241	243	MRI
243	Right superficial temporal vein	Vein	-	0.33	1.70	5.77	-	242	172	MRI
244	Left supraorbital	Vein	-	0.20	2.04	0.55	-	Venules 244	240, 245	MRI
245	Left superficial temporal vein	Vein	-	0.30	1.76	5.77	-	244	246	MRI
246	Left superficial temporal vein	Vein	-	0.33	1.70	5.77	-	245	180	MRI
247	Right anterior facial vein I	Vein	-	0.28	1.82	9.00	-	Venules 247	158	MRI
248	Left anterior facial vein I	Vein	-	0.28	1.82	9.00	-	Venules 248	161	MRI
249	Straight sinus	Dural sinus	$P_{intracranium}$	0.23	3.00	1.32	-	204, 207	193, 194, 256, 257	[Müller 2014] + AS
250	Right suboccipital sinus	Vein	-	0.09	2.49	0.33	-	252, 254	148, 163	[Müller 2014] + AS
251	Left suboccipital sinus	Vein	-	0.09	2.49	0.33	-	253, 255	149, 166	[Müller 2014] + AS
252	Right marginal sinus	Dural sinus	$P_{intracranium}$	0.09	3.00	1.32	-	256	250	[Müller 2014] + AS
253	Left marginal sinus	Dural sinus	$P_{intracranium}$	0.09	3.00	1.32	-	256	251	[Müller 2014] + AS
254	Right mastoid emissary vein	Vein	-	0.09	2.49	2.37	-	185	250	[Müller 2014] + AS
255	Left mastoid emissary vein	Vein	-	0.09	2.49	2.37	-	178, 186	251	[Müller 2014] + AS
256	Occipital sinus	Dural sinus	$P_{intracranium}$	0.10	3.00	1.15	-	221, 249	252, 253	[Müller 2014] + AS
257	Occipital vein	Vein	-	0.12	2.36	1.65	-	221, 249	126, 164, 165	[Müller 2014] + AS
401	Left Jugular trunk	Vein	-	0.12	2.36	2.31	-	Lymphatics	144	-
402	Right Jugular trunk	Vein	-	0.12	2.36	2.31	-	Lymphatics	84	-

Table 4.1: Geometrical and mechanical parameters for the modelled venous and arterial systems. No: vessel number, tube law: identify the type of tube law according to Eq. (4.4), p_{ext}: External pressure in the tube law of Eq. (4.2), r_0: radius of the vessel at equilibrium, c_0: wave speed for $A = A_0$, L: length of the vessel, $R_{terminal}$ terminal resistance to couple one-dimensional vessels with zero-dimensional model, Mothers: inlet boundary condition (lumped model or a junction with the shown vessel numbers), Daughters: outlet boundary condition (lumped model of a junction with the shown vessel numbers), Reference: bibliographic source or MRI imaging segmented geometry. AS, allometric scaling.

Name	P_{ext}	Oncotic pressure [mmHg]	C [$10^2 \times \mu$L mmHg^{-1}]	V_0 [μL]	S [mmHg s mL^{-1}]	E_0 [mmHg s mL^{-1}]	ϕ [μL]	P_0 [mmHg]
Right atrium	$P_{intrath} + P_{pericardium}$	-	-	0.011	0.23	-	-	-
Right ventricle	$P_{intrath} + P_{pericardium}$	-	-	0.333	0.23	-	-	-
Pulmonary arteries	$P_{intrath}$	-	-	-	4.65	72.00	5.556	-
Pulmonsary capillaries	$P_{intrath}$	-	-	-	4.65	72.00	16.667	-
Pulmonary veins	$P_{intrath}$	-	-	-	4.65	72.00	55.556	-
Left atrium	$P_{intrath} + P_{pericardium}$	-	-	0.019	0.23	-	-	-
Left ventricle	$P_{intrath} + P_{pericardium}$	-	-	7.222	0.23	-	-	-
Intrathoracic ($P_{intrath} = -3.5$ mmHg)	-	-	-	-	-	-	-	-
Pericardium ($P_{pericardium}$)	-	-	-	111.111	-	-	27.778	1.0
Pericardial fluid	$P_{pericardium}$	-	-	8.333	-	-	-	-
Brain solid matrix	$P_{intracranium}$	-	-	272.222	-	-	-	-
Brain interstitial fluid (ISF)	$P_{intracranium}$	6.0	15.12	116.667	-	-	-	-
Left ventricle (CSF)	$P_{intracranium}$	6.0	343.31	2.000	-	-	-	-
Right ventricle (CSF)	$P_{intracranium}$	6.0	343.31	2.000	-	-	-	-
Third ventricle (CSF)	$P_{intracranium}$	6.0	214.57	1.250	-	-	-	-
Aqueduct of Sylvius (CSF)	$P_{intracranium}$	6.0	1.25	0.007	-	-	-	-
Fourth ventricle (CSF)	$P_{intracranium}$	6.0	119.21	0.472	-	-	-	-
Cerebral subarachnoid space (CSF)	$P_{intracranium}$	6.0	134.92	13.889	-	-	-	-
Spinal subarachnoid space (CSF)	-	6.0	290.25	18.056	-	-	-	-
Intracranium ($P_{intracranium}$)	-	-	-	421.528	-	-	0.139	10.0
Arteriole 8	-	25.0	5.04	-	-	-	-	-
Arteriole 14	-	25.0	50.04	-	-	-	-	-
Arteriole 19	-	25.0	5.04	-	-	-	-	-
Arteriole 22	-	25.0	7.56	-	-	-	-	-
Arteriole 23	-	25.0	5.04	-	-	-	-	-
Arteriole 24	-	25.0	11.88	-	-	-	-	-

Arteriole 26	–	25.0	29.16	–	–	–	–	–
Arteriole 28	–	25.0	24.48	–	–	–	–	–
Arteriole 30	–	25.0	24.48	–	–	–	–	–
Arteriole 32	–	25.0	6.41	–	–	–	–	–
Arteriole 36	–	25.0	6.55	–	–	–	–	–
Arteriole 37	–	25.0	41.40	–	–	–	–	–
Arteriole 41	–	25.0	18.00	–	–	–	–	–
Arteriole 42	–	25.0	41.40	–	–	–	–	–
Arteriole 43	–	25.0	1.55	–	–	–	–	–
Arteriole 44	–	25.0	5.04	–	–	–	–	–
Arteriole 45	–	25.0	5.04	–	–	–	–	–
Arteriole 46	–	25.0	1.55	–	–	–	–	–
Arteriole 51	–	25.0	6.55	–	–	–	–	–
Arteriole 52	–	25.0	41.40	–	–	–	–	–
Arteriole 54	–	25.0	18.00	–	–	–	–	–
Arteriole 55	–	25.0	41.40	–	–	–	–	–
Arteriole 58	$P_{intracranium}$	25.0	5.04	0.556	–	–	–	–
Arteriole 61	$P_{intracranium}$	25.0	5.04	0.556	–	–	–	–
Arteriole 63	$P_{intracranium}$	25.0	5.04	0.556	–	–	–	–
Arteriole 65	$P_{intracranium}$	25.0	5.04	0.556	–	–	–	–
Arteriole 68	$P_{intracranium}$	25.0	5.04	0.556	–	–	–	–
Arteriole 70	–	25.0	1.33	–	–	–	–	–
Arteriole 71	–	25.0	2.00	–	–	–	–	–
Arteriole 74	–	25.0	2.00	–	–	–	–	–
Arteriole 75	–	25.0	2.00	–	–	–	–	–
Arteriole 82	–	25.0	2.00	–	–	–	–	–
Capillaries 8	–	25.0	0.50	–	–	–	–	–
Capillaries 14	–	25.0	5.00	–	–	–	–	–
Capillaries 19	–	25.0	0.50	–	–	–	–	–
Capillaries 22	–	25.0	0.76	–	–	–	–	–
Capillaries 23	–	25.0	0.50	–	–	–	–	–
Capillaries 24	–	25.0	1.19	–	–	–	–	–
Capillaries 26	–	25.0	2.92	–	–	–	–	–
Capillaries 28	–	25.0	2.45	–	–	–	–	–
Capillaries 30	–	25.0	2.45	–	–	–	–	–
Capillaries 32	–	25.0	0.64	–	–	–	–	–
Capillaries 36	–	25.0	0.66	–	–	–	–	–
Capillaries 37	–	25.0	4.14	–	–	–	–	–

Capillaries 41	–	25.0	1.80	–	–	–	–	–
Capillaries 42	–	25.0	4.14	–	–	–	–	–
Capillaries 43	–	25.0	0.15	–	–	–	–	–
Capillaries 44	–	25.0	0.50	–	–	–	–	–
Capillaries 45	–	25.0	0.50	–	–	–	–	–
Capillaries 46	–	25.0	0.15	–	–	–	–	–
Capillaries 51	–	25.0	0.66	–	–	–	–	–
Capillaries 52	–	25.0	4.14	–	–	–	–	–
Capillaries 54	–	25.0	1.80	–	–	–	–	–
Capillaries 55	–	25.0	4.14	–	–	–	–	–
Capillaries 58	$P_{intracranium}$	25.0	0.50	0.056	–	–	–	–
Capillaries 61	$P_{intracranium}$	25.0	0.50	0.056	–	–	–	–
Capillaries 63	$P_{intracranium}$	25.0	0.50	0.056	–	–	–	–
Capillaries 65	$P_{intracranium}$	25.0	0.50	0.056	–	–	–	–
Capillaries 68	$P_{intracranium}$	25.0	0.50	0.056	–	–	–	–
Capillaries 70	–	25.0	0.13	–	–	–	–	–
Capillaries 71	–	25.0	0.20	–	–	–	–	–
Capillaries 74	–	25.0	0.20	–	–	–	–	–
Capillaries 75	–	25.0	0.20	–	–	–	–	–
Capillaries 82	–	25.0	0.20	–	–	–	–	–
Venules E	$P_{intracranium}$	25.0	0.65	–	–	–	–	–
Venules F	$P_{intracranium}$	25.0	0.65	–	–	–	–	–
Venules ISS	$P_{intracranium}$	25.0	7.56	–	–	–	–	–
Venules SSS	$P_{intracranium}$	25.0	7.56	–	–	–	–	–
Venules C	–	25.0	12.13	–	–	–	–	–
Venules D	–	25.0	12.13	–	–	–	–	–
Venules right leg	–	25.0	24.48	–	–	–	–	–
Venules left leg	–	25.0	24.48	–	–	–	–	–
Venules 83	–	25.0	5.58	–	–	–	–	–
Venules 86	–	25.0	189.72	–	–	–	–	–
Venules 88	–	25.0	72.00	–	–	–	–	–
Venules 90	–	25.0	72.00	–	–	–	–	–
Venules 92	–	25.0	24.48	–	–	–	–	–
Venules 99	–	25.0	38.88	–	–	–	–	–
Venules 101	–	25.0	24.48	–	–	–	–	–
Venules 108	–	25.0	5.58	–	–	–	–	–
Venules 112	–	25.0	38.88	–	–	–	–	–
Venules 114	–	25.0	24.48	–	–	–	–	–

Venules 121	-	25.0	5.58	-	-	-	-	-
Venules 127	-	25.0	11.16	-	-	-	-	-
Venules 132	-	25.0	15.48	-	-	-	-	-
Venules 134	-	25.0	4.64	-	-	-	-	-
Venules 135	-	25.0	15.48	-	-	-	-	-
Venules 138	-	25.0	15.48	-	-	-	-	-
Venules 140	-	25.0	4.64	-	-	-	-	-
Venules 141	-	25.0	15.48	-	-	-	-	-
Lymphatics	$P_{intracranium}$	-	0.18	0.008	-	-	-	-

Table 4.2: Parameters for zero-dimensional models. P_{ext}: External pressure in the tube law of Eq. (4.20), Oncotic pressure: fixed value of the oncotic pressure, C: compliance of the compartment, V_0: dead volume, S: viscoelastic coefficient, E_0 elastance, ϕ: constant volume, P_0: pressure at $V = V_0$. Parameters were derived from applying allometric scaling to [Müller 2014, Liang 2009b, Linninger 2009, Linninger 2017] and modified when necessary to fit the output of the computational model with physiological values reported in the literature.

Name	R [mmHg s μL^{-1}]	L [mmHg s^2 mL^{-1}]	B [mmHg s^2 mL^{-2}]	σ [-]	**Directionality** [-]
Heart and pulmonary circulation					
Tricuspid valve	0.465×10^{-3}	0.012	0.883	-	Unidirectional
Pulmonary valve	0.465×10^{-3}	0.030	1.379	-	Unidirectional
Pulmonary arteries → Pulmonary capillaries	4.648×10^{-3}	0.030	-	-	-
Pulmonary capillaries → Pulmonary veins	4.648×10^{-3}	0.030	-	-	-
Pulmonary veins → Left atrium	0.465×10^{-3}	0.030	-	-	-
Mitral valve	0.465×10^{-3}	0.012	0.883	-	Unidirectional
Aortic valve	0.046×10^{-3}	0.003	1.379	-	Unidirectional
Blood interstitial and cerebrospinal fluids					
Capillaries 58 → Brain interstitial fluid (ISF)	907.530	-	-	1.0	-
Capillaries 61 → Brain interstitial fluid (ISF)	907.530	-	-	1.0	-
Capillaries 63 → Brain interstitial fluid (ISF)	907.530	-	-	1.0	-
Capillaries 65 → Brain interstitial fluid (ISF)	907.530	-	-	1.0	-
Capillaries 68 → Brain interstitial fluid (ISF)	907.530	-	-	1.0	-
Capillaries 61 → Right ventricle (CSF)	30896.671	-	-	1.0	-
Capillaries 63 → Right ventricle (CSF)	26482.861	-	-	1.0	-
Capillaries 63 → Left ventricle (CSF)	26482.861	-	-	1.0	-
Capillaries 65 → Left ventricle (CSF)	30896.671	-	-	1.0	-
Capillaries 58 → Third ventricle (CSF)	18538.003	-	-	1.0	-

Capillaries 68 → Third ventricle (CSF)	18538.003	–	–	1.0	–
Capillaries 58 → Fourth ventricle (CSF)	18538.003	–	–	1.0	–
Capillaries 68 → Fourth ventricle (CSF)	18538.003	–	–	1.0	–
Brain interstitial fluid (ISF) → Left ventricle (CSF)	1.892	–	–	1.0	–
Brain interstitial fluid (ISF) → Right ventricle (CSF)	1.892	–	–	1.0	–
Brain interstitial fluid (ISF) → Third ventricle (CSF)	3.110	–	–	1.0	–
Brain interstitial fluid (ISF) → Fourth ventricle (CSF)	2.628	–	–	1.0	–
Brain interstitial fluid (ISF) → Cranial sub. space (CSF)	0.729	–	–	1.0	–
Brain interstitial fluid (ISF) → Venules E	586.263	–	–	1.0	–
Brain interstitial fluid (ISF) → Venules F	586.263	–	–	1.0	–
Brain interstitial fluid (ISF) → Venules ISS	586.263	–	–	1.0	–
Brain interstitial fluid (ISF) → Venules SSS	586.263	–	–	1.0	–
Cranial sub. space (CSF) → Arachnoid 238	232.379	–	–	–	Unidirectional
Cranial sub. space (CSF) → Arachnoid 237	232.379	–	–	–	Unidirectional
Cranial sub. space (CSF) → Arachnoid 236	232.379	–	–	–	Unidirectional
Cranial sub. space (CSF) → Lymphatics	2788.548	–	–	–	Unidirectional
Lymphatics → Left jugular trunk	4182.822	–	–	–	Unidirectional
Lymphatics → Right jugular trunk	4182.822	–	–	–	Unidirectional
Left ventricle (CSF) → Third ventricle (CSF)	0.093	0.480	–	–	–
Right ventricle (CSF) → Third ventricle (CSF)	0.093	0.480	–	–	–
Third ventricle (CSF) → Aqueduct of Sylvius (CSF)	1.859	0.480	–	–	–
Aqueduct of Sylvius (CSF) → Fourth ventricle (CSF)	0.093	0.480	–	–	–
Fourth ventricle (CSF) → Cranial sub. space (CSF)	0.093	0.480	–	–	–
Cranial sub. space (CSF) → Spinal sub. space (CSF)	0.046	0.900	–	–	–
Peripheral microcirculation					
Arteriole 08 → Capillaries 08	3.878	1.080	–	–	–
Arteriole 14 → Capillaries 14	1.718	0.540	–	–	–
Arteriole 19 → Capillaries 19	3.878	1.080	–	–	–
Arteriole 22 → Capillaries 22	3.651	0.900	–	–	–
Arteriole 23 → Capillaries 23	3.129	1.080	–	–	–
Arteriole 24 → Capillaries 24	3.021	0.720	–	–	–
Arteriole 26 → Capillaries 26	1.511	0.420	–	–	–
Arteriole 28 → Capillaries 28	2.190	0.480	–	–	–
Arteriole 30 → Capillaries 30	2.190	0.480	–	–	–
Arteriole 32 → Capillaries 32	1.697	1.200	–	–	–
Arteriole 36 → Capillaries 36	85.476	1.080	–	–	–
Arteriole 37 → Capillaries 37	1.697	0.840	–	–	–

Arteriole 41 → Capillaries 41	66.123	1.260	–	–	–
Arteriole 42 → Capillaries 42	57.451	0.840	–	–	–
Arteriole 43 → Capillaries 43	6.786	4.200	–	–	–
Arteriole 44 → Capillaries 44	3.343	1.080	–	–	–
Arteriole 45 → Capillaries 45	3.343	1.080	–	–	–
Arteriole 46 → Capillaries 46	6.786	4.200	–	–	–
Arteriole 51 → Capillaries 51	85.476	1.080	–	–	–
Arteriole 52 → Capillaries 52	1.697	0.840	–	–	–
Arteriole 54 → Capillaries 54	66.123	1.260	–	–	–
Arteriole 55 → Capillaries 55	57.451	0.840	–	–	–
Arteriole 82 → Capillaries 82	3.129	0.480	–	–	–
Capillaries 08 → Venules 132	3.878	0.174	–	–	–
Capillaries 14 → Venules 127	1.718	0.090	–	–	–
Capillaries 19 → Venules 138	3.878	0.174	–	–	–
Capillaries 22 → Venules 86	3.651	0.144	–	–	–
Capillaries 23 → Venules 86	3.129	0.180	–	–	–
Capillaries 24 → Venules 86	3.021	0.114	–	–	–
Capillaries 26 → Venules 86	1.511	0.072	–	–	–
Capillaries 28 → Venules 90	2.190	0.084	–	–	–
Capillaries 30 → Venules 88	2.190	0.084	–	–	–
Capillaries 32 → Venules 92	1.697	0.198	–	–	–
Capillaries 36 → Venules 99	85.476	0.180	–	–	–
Capillaries 37 → Venules 101	1.697	0.138	–	–	–
Capillaries 41 → Venules 108	66.123	0.210	–	–	–
Capillaries 42 → Venules right leg	57.451	0.138	–	–	–
Capillaries 43 → Venules 134	6.786	0.702	–	–	–
Capillaries 44 → Venules 135	3.343	0.174	–	–	–
Capillaries 45 → Venules 141	3.343	0.174	–	–	–
Capillaries 46 → Venules 140	6.786	0.702	–	–	–
Capillaries 51 → Venules 112	85.476	0.180	–	–	–
Capillaries 52 → Venules 114	1.697	0.138	–	–	–
Capillaries 54 → Venules 121	66.123	0.210	–	–	–
Capillaries 55 → Venules left leg	57.451	0.702	–	–	–
Capillaries 82 → Venules 83	3.129	0.084	–	–	–
Venules right leg → Vein 110	114.903	0.252	–	–	–
Venules left leg → Vein 123	114.903	0.252	–	–	–
Venules 83 → Vein 83	3.129	0.372	–	–	–
Venules 86 → Vein 86	0.630	0.078	–	–	–

Venules 88 → Vein 88	2.190	0.144	–	–	–
Venules 90 → Vein 90	2.190	0.144	–	–	–
Venules 92 → Vein 92	1.697	0.360	–	–	–
Venules 99 → Vein 99	85.476	0.324	–	–	–
Venules 101 → Vein 101	1.697	0.252	–	–	–
Venules 108 → Vein 108	66.123	0.372	–	–	–
Venules 112 → Vein 112	85.476	0.324	–	–	–
Venules 114 → Vein 114	1.697	0.252	–	–	–
Venules 121 → Vein 121	66.123	0.372	–	–	–
Venules 127 → Vein 127	1.718	0.162	–	–	–
Venules 132 → Vein 132	3.878	0.312	–	–	–
Venules 134 → Vein 134	6.786	1.254	–	–	–
Venules 135 → Vein 135	3.343	0.312	–	–	–
Venules 138 → Vein 138	3.878	0.312	–	–	–
Venules 140 → Vein 140	6.786	1.254	–	–	–
Venules 141 → Vein 141	3.343	0.312	–	–	–
Venules right leg → Vein 105	114.903	0.252	–	–	–
Venules left leg → Vein 118	114.903	0.252	–	–	–
Intracranial microcirculation					
Arteriole 58 → Capillaries 58	4.837	0.244	–	–	–
Arteriole 61 → Capillaries 61	2.032	0.102	–	–	–
Arteriole 63 → Capillaries 63	1.660	0.166	–	–	–
Arteriole 65 → Capillaries 65	2.032	0.102	–	–	–
Arteriole 68 → Capillaries 68	4.837	0.244	–	–	–
Arteriole 70 → Capillaries 70	5.000	0.119	–	–	–
Arteriole 71 → Capillaries 71	5.000	0.119	–	–	–
Arteriole 74 → Capillaries 74	2.143	1.146	–	–	–
Arteriole 75 → Capillaries 75	2.143	1.146	–	–	–
Capillaries 58 → Venules F	4.837	0.067	–	–	–
Capillaries 61 → Venules SSS	2.032	0.030	–	–	–
Capillaries 63 → Venules ISS	3.320	0.095	–	–	–
Capillaries 63 → Venules SSS	3.320	0.095	–	–	–
Capillaries 65 → Venules SSS	2.032	0.030	–	–	–
Capillaries 68 → Venules E	4.837	0.067	–	–	–
Capillaries 70 → Venules C	5.000	0.454	–	–	–
Capillaries 71 → Venules D	5.000	0.454	–	–	–
Capillaries 74 → Venules D	2.143	0.454	–	–	–

Capillaries 75 → Venules C	2.143	0.454	-	-	-
Venules E → Vein 201	14.512	1.859	-	-	-
Venules E → Vein 200	14.512	1.859	-	-	-
Venules E → Vein 196	14.512	1.861	-	-	-
Venules F → Vein 199	14.512	1.859	-	-	-
Venules F → Vein 197	14.512	1.859	-	-	-
Venules F → Vein 191	14.512	1.861	-	-	-
Venules iSS → Vein 208	9.960	1.035	-	-	-
Venules iSS → Vein 210	9.960	1.035	-	-	-
Venules iSS → Vein 212	9.960	1.035	-	-	-
Venules SSS → Vein 234	5.446	0.728	-	-	-
Venules SSS → Vein 232	5.446	0.728	-	-	-
Venules SSS → Vein 230	5.446	0.728	-	-	-
Venules SSS → Vein 228	5.446	0.728	-	-	-
Venules SSS → Vein 226	5.446	0.728	-	-	-
Venules SSS → Vein 224	5.446	0.728	-	-	-
Venules SSS → Vein 222	5.446	0.728	-	-	-
Venules C → Vein 247	1.579	0.742	-	-	-
Venules C → Vein 241	30.000	0.742	-	-	-
Venules D → Vein 248	1.579	0.742	-	-	-
Venules D → Vein 244	30.000	0.742	-	-	-
Starling resistors					
Starling 191 → 192	0.232	0.306	-	-	-
Starling 196 → 195	0.232	0.306	-	-	-
Starling 203 → 204	0.232	0.306	-	-	-
Starling 208 → 209	0.232	0.306	-	-	-
Starling 210 → 211	0.232	0.306	-	-	-
Starling 212 → 213	0.232	0.306	-	-	-
Starling 222 → 223	0.232	0.306	-	-	-
Starling 224 → 225	0.232	0.306	-	-	-
Starling 226 → 227	0.232	0.306	-	-	-
Starling 228 → 229	0.232	0.306	-	-	-
Starling 230 → 231	0.232	0.306	-	-	-
Starling 232 → 233	0.232	0.306	-	-	-
Starling 234 → 235	0.232	0.306	-	-	-

Table 4.3: Parameters for zero-dimensional flow dynamics. R: viscous resistance to flow, B: Bernoulli coefficient, σ: reflection coefficient, Directionality: the equation behaves as a valve and strictly prevents backflows if unidirectional is written. Parameters were derived from applying allometric scaling to [Müller 2014, Liang 2009b, Linninger 2009, Linninger 2017] and modified when necessary to fit the output of the computational model with physiological values reported in the literature.

Parameter	Description	Value	Units	Reference
γ	Parameter for velocity profile	2	–	[Alastruey 2006]
H_d	Hematocrit	0.45	–	[Windberger 2003]
μ	Plasma dynamic viscosity	1.20	cP	[Windberger 2003]
	Cardiac model			
E_a^{ra}	Right atrial elastance amplitude	0.216	mmHg μL^{-1}	[Müller 2013b] + AS
E_a^{rv}	Right ventricular elastance amplitude	1.980	mmHg μL^{-1}	[Müller 2013b] + AS
E_b^{ra}	Right atrial elastance baseline	0.180	mmHg μL^{-1}	[Müller 2013b] + AS
E_b^{rv}	Right ventricular elastance baseline	0.180	mmHg μL^{-1}	[Müller 2013b] + AS
E_a^{la}	Left atrial elastance amplitude	0.252	mmHg μL^{-1}	[Müller 2013b] + AS
E_b^{la}	Left atrial elastance baseline	0.324	mmHg μL^{-1}	[Müller 2013b] + AS
E_a^{lv}	Left ventricular elastance amplitude	13.212	mmHg μL^{-1}	[Müller 2013b] + AS
E_b^{lv}	Left ventricular elastance baseline	0.180	mmHg μL^{-1}	[Müller 2013b] + AS
T_{acp}^a	Duration of atrial contraction	32.275	ms	[Müller 2013b, Liang 2009b] + AS
T_{arp}^a	Duration of atrial relaxation	38.730	ms	[Müller 2013b, Liang 2009b] + AS
t_{ac}^a	Time at which atrial contraction starts	92.952	ms	[Müller 2013b, Liang 2009b] + AS
t_{ac}^a	Time at which atrial relaxation starts	125.226	ms	[Müller 2013b, Liang 2009b] + AS
T_{vcp}^a	Duration of ventricular contraction	45.185	ms	[Müller 2013b, Liang 2009b] + AS
T_{vrp}^a	Duration of ventricular relaxation	21.947	ms	[Müller 2013b, Liang 2009b] + AS
t_{vc}^a	Time at which ventricular contraction starts	0.000	ms	[Müller 2013b, Liang 2009b] + AS
t_{vc}^a	Time at which ventricular relaxation starts	38.730	ms	[Müller 2013b, Liang 2009b] + AS
	Valve model			
Δp_{open}	Valve opening threshold pressure difference	0	mmHg	[Müller 2013b]
Δp_{close}	Valve closure threshold pressure difference	0	mmHg	[Müller 2013b]
K_{vo}	Rate coefficient valve opening	7.7	Pa^{-1} s^{-1}	[Müller 2013b] + AS
K_{vo}	Rate coefficient valve closure	7.7	Pa^{-1} s^{-1}	[Müller 2013b] + AS
M_{st}	Maximum valve opening ($0 \leq M_{st} \leq 1$)	1.0	-	[Mynard 2012]
M_{rg}	Minimum valve closure ($0 \leq M_{rg} \leq 1$)	0.0	-	[Mynard 2012]

L_{eff}	Effective length:	$L_{eff} = 0.5\left(d_0^{up} + d_0^{down}\right)$	mm	Estimated
$d_0^{up,down}$	Diameter at rest of upstream/downstream vessel	-	mm	-

Table 4.4: Parameters for cardiac model, venous valve dynamics and blood rheology. AS, allometric scaling.

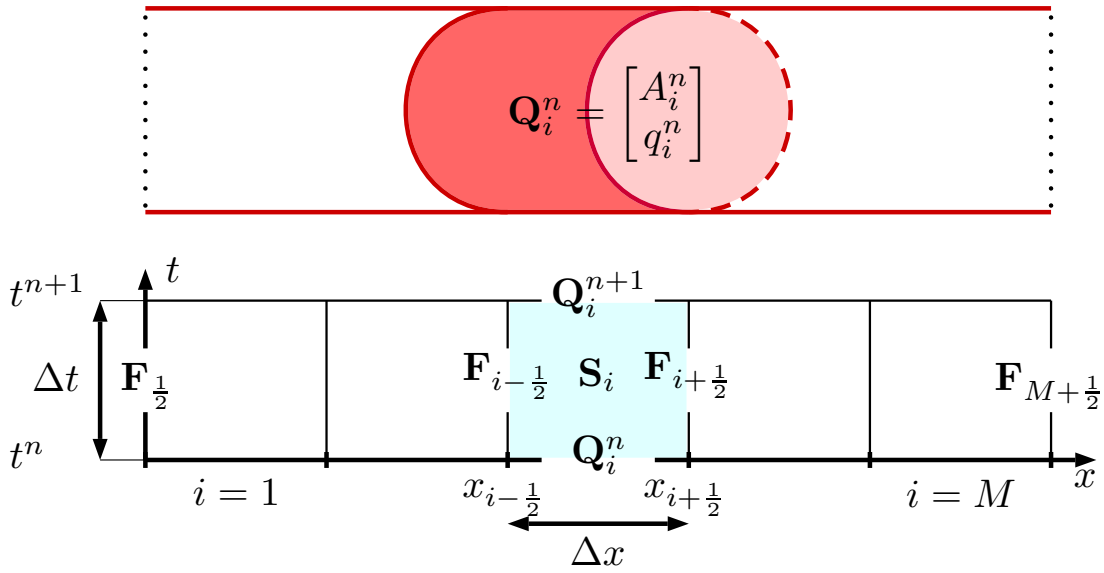

Figure 4.5: Framework for a finite volume scheme. Top: illustratation of a computational volume for a vessel. Bottom: illustratation of the space-time control volume.

4.2.3 Numerical methods for the solution of the system of equations

One- and zero-dimensional models

Consider the system of m hyperbolic balance laws

$$\partial_t \mathbf{Q} + \partial_x \mathbf{F}(\mathbf{Q}) = \mathbf{S}(\mathbf{Q}) \,. \tag{4.30}$$

By integrating (4.30) over the control volume $V = [x_{i-\frac{1}{2}}, x_{i+\frac{1}{2}}] \times [t^n, t^{n+1}]$ we obtain the exact formula

$$\mathbf{Q}_i^{n+1} = \mathbf{Q}_i^n - \frac{\Delta t}{\Delta x}\left(\mathbf{F}_{i+\frac{1}{2}} - \mathbf{F}_{i-\frac{1}{2}}\right) + \Delta t \mathbf{S}_i \,, \tag{4.31}$$

with definitions

$$\mathbf{Q}_i^n = \frac{1}{\Delta x}\int_{x_{i-\frac{1}{2}}}^{x_{i+\frac{1}{2}}} \mathbf{Q}(x, t^n)\mathrm{d}x \,, \tag{4.32}$$

$$\left.\begin{aligned} \mathbf{F}_{i+\frac{1}{2}} &= \frac{1}{\Delta t}\int_{t^n}^{t^{n+1}} \mathbf{F}(\mathbf{Q}(x_{i+\frac{1}{2}}, t))\mathrm{d}t \,, \\ \mathbf{S}_i &= \frac{1}{\Delta t \Delta x}\int_{t^n}^{t^{n+1}}\int_{x_{i-\frac{1}{2}}}^{x_{i+\frac{1}{2}}} \mathbf{S}(\mathbf{Q}(x,t))\mathrm{d}x\mathrm{d}t \,. \end{aligned}\right\} \tag{4.33}$$

Eq. (4.32) gives the spatial-integral average at time $t = t^n$ of the conserved variable $\mathbf{Q}$ while Eqs. (4.33) give the time-integral average at interface $x = x_{i+\frac{1}{2}}$ of the physical flux $\mathbf{F}$ and the volume-integral average in V of the source term $\mathbf{S}$. Spatial mesh size and time step are $\Delta x = x_{i+\frac{1}{2}} - x_{i-\frac{1}{2}}$ and $\Delta t = t^{n+1} - t^n$ respectively. Finite volume methods for (4.30) depart from (4.31) to (4.33), where integrals are approximated, and then formula (4.31) becomes a *finite volume method*, where the

approximated integrals in (4.33) are called *numerical flux* and *numerical source*, respectively. Here index i runs from 1 to M, where the cell $i=1$ is the leftmost cell with $x_{\frac{1}{2}}$ being the first interface, and the cell $i=M$ is the rightmost cell with $x_{M+\frac{1}{2}}$ being the last interface. See Fig. 4.5 for an illustration of the finite volume framework. To compute the time step Δt, the Courant-Friedrichs-Lewy condition is applied for each vessel at each time step

$$\Delta t^j = CFL \frac{\Delta x^j}{\max\limits_{i=1,\dots,M^j} \left(|u_i^j| + c_i^j \right)} , \tag{4.34}$$

with $CFL = 0.9$. Superindex j indicates the j-th vessel. Then, the time step Δt to be used is the minimum of all the time steps, namely $\Delta t = \min\limits_j \left(\Delta t^j \right)$. More advanced techniques for the choice of the time stepping have been proposed in the literature [Dumbser 2007b, Müller 2016, Dumbser 2014].

In the present chapter we used the SLIC method to evaluate the numerical fluxes within the domain $(\mathbf{F}_{\frac{3}{2}}, \dots, \mathbf{F}_{M-\frac{1}{2}})$ [Toro 2000]. This method is second-order accurate in space and time and is based on the MUSCL-Hancock scheme where the Godunov upwind flux is replaced by the FORCE flux, see Section 14.5.3 of [Toro 2009] and references therein. The numerical source was approximated using a second order in space and time method, see Chapter 19 of [Toro 2009]. For the numerical fluxes at the boundaries ($\mathbf{F}_{\frac{1}{2}}$ and $\mathbf{F}_{M+\frac{1}{2}}$), we used a first-order Godunov-type method based on the solution of a classical Riemann problem at the interface.

The system of ODEs in (4.28) were solved numerically with an implicit Euler method.

Boundary conditions

We modelled five types of boundary conditions: junctions, imposed flow, Poiseuille's law, starling mechanism and venous valves. Junctions between vessels were treated as explained in 2. Poiseuille's law $q = \frac{\Delta P}{R}$ was applied at each terminal vessel of the arterial and venous network and couples vessels to 0D models. The numerical treatment can be derived from 3.2.4 and is explained in details in [Alastruey 2008]. The flow rate through the aortic valve was imposed at the first interface of the ascending aorta and the numerical treatment can be extended from [Alastruey 2008, Strocchi 2017, Müller 2013b]. Starling resistors were implemented in the mathematical model based on [Müller 2014] by setting $P_2 = max\left(P_{intracranium}, P_2\right)$ and by setting $R = \infty$ if $P_1 < P_{intracranium}$ in Eq. (4.26). Venous valves were treated as explained in Section 3.2.4.

4.2.4 *In-vivo* magnetic resonance imaging in mice: angiography, venography and blood flow quantification

Wild-type mice (C57BL6, Jackson Laboratory) aged 10 to 12 weeks (weight 24–29 g) were imaged. All measurements were performed with a 7T small animal magnetic resonance scanner (ClinScan, Bruker BioSpin, Ettlingen, Germany) using a 30 mm diameter cylindrical birdcage radiofrequency coil and an MR-compatible physiological monitoring and gating system for mice (SA Instruments, Inc., Stony Brook, NY). Maximum gradient strength of the system was 500 mT/m and the peak slew rate achievable was 6667 mT/m/ms. Mice were anaesthetized using 1.25% isoflurane in oxygen and body temperature was maintained at 37° using thermostated circulating water. All animals were used in accordance with a protocol approved by the animal care and use committee at Department of Radiology, University of Virginia (USA).

Structural analysis of arterial and venous murine intracranial network: Angiography and venography

Structural imaging data of intracranial arteries were acquired with a high-resolution 3D isotropic Spiral Cine Phase Contrast (SCPC) technique [repetition time (TR) = 15 milliseconds, echo time (TE) = 0.63 milliseconds, field of view (FOV) = 25x25 mm, slice thickness = 0.01 mm, number of averages (NEX) = 1, flip angle (FA) = 20°, number of sagittal slices = 160, total imaging time = 15 minutes]. Structural imaging data of intracranial veins were acquired with a high-resolution 3D isotropic SCPC technique with a saturation band positioned caudal to the slices, in order to saturate the arterial signal [TR = 17 milliseconds, TE = 4.54 milliseconds, FOV = 17x26 mm, slice thickness = 0.3 mm, NEX = 2, FA = 90°, total imaging time = 13 minutes]. Diameters and lengths were quantified using semi-automatic segmentation tools provided in the OsiriX software.

Structural analysis of the murine brain ventricular system

Structural imaging data of the brain ventricular system (lateral ventricles, third ventricles, aqueduct of Sylvius and fourth ventricle) were acquired with a high-resolution 3D isotropic T2-Weighted SPACE technique [TR = 3000 milliseconds, TE = 139 milliseconds, FOV = 26x20.5 mm, slice thickness = 0.13 mm, NEX = 3, FA = 120°, number of slices = 160, total imaging time = 16 minutes]. Ventricle volumes were quantified using semi-automatic segmentation tools provided in the OsiriX software.

Flow measurements through a spiral-MRI technique

Flow measurements were performed with a 2D SCPC MRI technique [TR = 3.3 milliseconds, TE = 0.91 milliseconds, FOV = 30x30 mm, slice thickness = 0.186 mm, NEX = 2, FA = 20°, total imaging time = 10 minutes]. The 2D slice of the SCPC sequence was positioned orthogonal to the direction of flow at both the external jugular veins (EJVs) and common carotid arteries (CCAs) and at the aortic root (AR) with a VENC of 70/25 cm/s (EJVs-CCAs/AR). Flow measurements were performed in the same MRI session when TOF and 3D SCPC sequences were acquired, so that morphological and flow quantification data are mouse-specific. Blood flow quantifications were performed using SPIN (Signal Processing in NMR, Detroit, MI) by a single trained examiner. See [Janiczek 2011, Naresh 2016] for an example of flow measurements of the mouse aortic arch using a 3D/2D SCPC technique.

4.2.5 *In-vivo* intracranial pressure measurements

Mice were anaesthetized (ketamine/xylazine, i.p.) and the skin was incised to expose the skull. A 0.5 mm diameter hole was drilled in the skull above the right parietal lobe. A pressure sensor (model SPR100; Millar) was inserted perpendicularly into the cortex at a depth of 1 mm. The pressure sensor was connected to the PCU-2000 pressure control unit (Millar) and recorded for 5 min after stabilization of the signal (around a minute after insertion of the probe). The average pressure was calculated over the last 2 minutes of recording (between minute 4 and 6 of the recording). Animals were sacrificed at the conclusion of the measurement. The measurements were filtered through a low-pass Gaussian mask in a post-processing phase.

4.2.6 Allometric scaling: from humans to mice

The study of the relationship of body size to anatomy and physiology is known as allometry. Most of the parameters needed for our computational model could not be derived from literature. This motivated us to take advantage of previously existing work for humans [Müller 2013b, Mynard 2015, Blanco 2015] and use allometric scaling to derive reasonable values for the zero- and one-dimensional mathematical models. Any physiological parameter X is considered to be dependent on the body weight W through the following allometric scaling

$$X = gW^{\alpha}\,, \tag{4.35}$$

where g is an empirical constant and α is the allometric scaling power which determines the rate of growth ($\alpha > 0$) or decline ($\alpha < 0$). If one knows the physiological parameter at one body weight (X_1, W_1) the value of another body weight (X_2, W_2) can be predicted as

$$X_2 = X_1 \left(\frac{W_2}{W_1}\right)^{\alpha}\,. \tag{4.36}$$

The allometric scaling power α can be derived from a dimensional analysis of parameter X. Starting from reported values of multi-scale mathematical models of the human fluid systems [Müller 2013b, Liang 2009b, Sun 1997] and assuming a human body weight of $W_{human} = 90$ kg, we obtained most of the computational parameters for a mouse of body weight $W_{mice} = 0.025$ kg using the following allometric scaling powers: volume $\alpha_v = 0$, resistance $\alpha_R = -3/4$, inertia $\alpha_L = -3/4$, Bernoulli coefficient $\alpha_B = -4/3$, compliance $\alpha_C = 0$, time $\alpha_T = 1/4$, arterial radius $\alpha_{r_0,artery} = 3/8$, arterial length $\alpha_{L,artery} = 1/4$, venous radius $\alpha_{r_0,vein} = 5/12$, venous length $\alpha_{L,vein} = 7/24$, rate of closure/opening coefficient $\alpha_{K_{vc,vo}} = -1/4$. For instance, for a human cardiac cycle duration of $T_{human} = 1$ s, the duration of the murine cardiac cycle becomes $T_{mouse} = (0.025/90)^{1/4} = 0.1291$ s, which is in agreement with the averaged murine heart rate (464.8 beats/min vs 470–620 beats/min [Cingolani 2011]). Although the allometric scaling gave satisfactory results, we adjusted the model parameters in order to 1) adopt intracranial geometrical information derived from MRI results of a cohort of mice, 2) use the diameters and lengths of the main mouse vessels reported in the literature, 3) fit the central venous pressure to that of mice, 4) fit the heart parameters with values reported in the literature. For complete references and reviews of allometric scaling, see [Li 2000, Dawson 2014, Dawson 2005, Dawson 2001, Holt 1981].

4.3 Results

Here we show the computational results. Parameters used for the network of the one-dimensional vessels and the system of ODES are reported in Tables 4.1, 4.2 and 4.3. Other used parameters in the computational model can be found in Table 4.4. The number of cells for each vessel was chosen according to $M_{cells} = ceiling(L/\Delta)$, where L is the length of the vessel, Δ is the specified space size and is set here to be $\Delta = 1$ mm. Each simulation was run on an Intel Core i7-2600 with 4 cores (3.40 GHz clock speed). Throughout the chapter, we refer to the *intracerebral CSF compartment* as the set of lateral and third ventricles, while to the *extracerebral CSF compartment* as the set of the fourth ventricle and the cranial subarachnoid space.

Parameter	Units	Numerical prediction	Normal range	Reference
Heart dynamics				
Heart rate	beats/min	464.58	442 ± 15	[Wiesmann 2000]
Cardiac output (CO)	mL/min	9.70	8 - 16	[Cingolani 2011]
Cardiac index	mL/min/g	0.39	0.35 - 0.58	[Wiesmann 2000]
End-diastolic volume	μL	36.23	25 - 53	[Cingolani 2011]
End-systolic volume	μL	15.35	7 - 21	[Cingolani 2011]
Stroke volume	μL	20.88	17 - 36	[Cingolani 2011]
Stroke work	mmHg μL	2012.02	1200 - 2700	[Pacher 2008]
Ejection fraction	%	57.63	55 - 72	[Wiesmann 2000]
End-diastolic pressure	mmHg	3.74	1 - 6	[Cingolani 2011]
End-systolic pressure	mmHg	105.22	92 - 118	[Cingolani 2011]
Pressure rate dP/dt_{max}	mmHg/s	10038.00	8200 - 14200	[Cingolani 2011]
Pressure rate $-dP/dt_{min}$	mmHg/s	7486.69	6700 - 10500	[Cingolani 2011]
ESPVR	mmHg/μL	12.95	7 - 14	[Cingolani 2011]
EDPVR	mmHg/μL	0.13	0.04 - 0.12	[Cingolani 2011]
Peripheral blood flow results				
Mean arterial pressure (MAP)	mmHg	93.71	81 - 105	[Cingolani 2011]
Central venous pressure	mmHg	1.03	0.80 ± 0.50	[Scheuermann-Freestone 2001]
Total peripheral resistance MAP/CO	mmHg min/mL	9.66	6 - 12	[Cingolani 2011]
Blood fluid dynamics and properties: median (min - max)				
Average Reynolds number	-	1.44 (0.00 - 13.70)	-	-
Peak Reynolds number	-	4.54 (0.04 - 195.55)	-	-
Average Womersley number	-	0.33 (0.10 - 2.11)	-	-
Peak Womersley number	-	0.68 (0.21 - 4.39)	-	-
Plasma dynamic viscosity	cP	1.20	1.29 - 1.34	[Windberger 2003]
Apparent dynamic viscosity	cP	3.62 (3.04 - 3.85)	3.5	[Feintuch 2006]
Haemodynamical results of selected one-dimensional vessels				
Ascending aorta (1)	mL/min	9.69	9.31 ± 2.57	MR-flow measurements
Left common carotid artery (5)	mL/min	1.29	2.00 ± 0.89	MR-flow measurements
Right common carotid artery (11)	mL/min	1.23	1.79 ± 1.10	MR-flow measurements
Left external jugular vein (152)	mL/min	1.35	1.04 ± 0.65	MR-flow measurements
Right external jugular vein (155)	mL/min	1.20	1.11 ± 0.80	MR-flow measurements
Innominate artery (3)	%CO	21.32	16.9 14.7 ± 3.2	[Feintuch 2006] [Barakat 1997] (rabbit)
Right common carotid artery (5)	%CO	13.29	8.86	[Cuomo 2015]
Left common carotid artery (11)	%CO	12.69	10.00	[Cuomo 2015]

			10.4	[Feintuch 2006]
Right subclavian artery (7)	%CO	7.10	8.53	[Cuomo 2015]
Left subclavian artery (17)	%CO	7.10	11.43	[Cuomo 2015]
			7.1 ± 2.5	[Barakat 1997] (rabbit)
Celiac I (20)	%CO	10.12	5.33	[Cuomo 2015]
			23.3 ± 5.8	[Barakat 1997] (rabbit)
Right renal (28)	%CO	5.12	6.10	[Cuomo 2015]
			6.2 ± 2.6	[Barakat 1997] (rabbit)
Left renal (30)	%CO	5.03	2.84	[Cuomo 2015]
			5.1 ± 2.2	[Barakat 1997] (rabbit)
Right commmon Iliac artery (34)	%CO	7.12	7.12	[Cuomo 2015]
			6.0 ± 2.5	[Barakat 1997] (rabbit)
Left commmon Iliac artery (49)	%CO	7.12	6.95	[Cuomo 2015]
			6.0 ± 2.5	[Barakat 1997] (rabbit)
Middle caudal artery - tail (82)	%CO	2.57	2.54	[Cuomo 2015]
Ascending aorta (1)	m/s	0.04	0.17 ± 0.24	[Aslanidou 2015]
Descending aorta (12)	m/s	0.04	0.09 ± 0.12	[Aslanidou 2015]
Infrarenal aortic region (33)	m/s	0.04	0.06 ± 0.06	[Aslanidou 2015]
Left renal artery (30)	m/s	0.04	0.10 ± 0.04	[Aslanidou 2015]
Right renal artery (28)	m/s	0.04	0.11 ± 0.04	[Aslanidou 2015]
Descending aorta (12)	mmHg	93.57	96.5 ± 18.6	[Aslanidou 2015]
Thoracic aorta (25)	mmHg	93.27	99.6 ± 17.4	[Aslanidou 2015]
Pararenal region (31)	mmHg	93.12	107.2 ± 31.4	[Aslanidou 2015]
Peripheral microcirculation: mean (min - max)				
Arterioles	mmHg	55.20 (53.35 - 56.61)	35 - 80	-
Capillaries	mmHg	37.55 (36.62 - 38.20)	18 - 35	-
Venules	mmHg	20.07 (19.08 - 21.58)	5 - 18	-
Intracranial microcirculation: mean (min - max)				
Arterioles	mmHg	43.48 (42.19 - 44.84)	35 - 80	-
Capillaries	mmHg	30.45 (29.64 - 31.39)	18 - 35	-
Venules	mmHg	17.21 (16.47 - 18.00)	5 - 18	-
Volumes of intracranial compartments				
Intracranial volume	μL	421.39	415 ± 24	[Kovačević 2005]
Cerebral blood volume	μL/g	33.89	30 - 40	[Owman 1975]
Brain ISF	μL	116.67	-	-
Brain solid matrix	μL	272.22	-	-
Porosity ISF / (ISF+brain solid matrix)	-	0.30	-	-

Left ventricle	μL	2.05	2.0 $\pm$ 0.83	[Dorr 2008]
Right ventricle	μL	2.05	2.1 $\pm$ 0.5	[Dorr 2008]
Third ventricle	μL	1.28	1.3 $\pm$ 0.23	[Dorr 2008]
Aqueduct of Sylvius	nL	7.498	-	-
Fourth ventricle	μL	0.49	0.5 $\pm$ 0.1	[Dorr 2008]
Cerebral subarachnoid space	μL	13.91	-	-
Spinal subarachnoid space	μL	18.91	-	-
Total CSF	μL	38.71	$\sim$ 37	[Barten 2017]
Pressures of intracranial compartments: mean (min - max)				
Brain ISF	mmHg	3.82 (3.37 - 4.29)	4.11 $\pm$ 0.83	[Moazen 2016]
			3.73 $\pm$ 0.39	Intracathecal *in-vivo* measurements
Intracranium	mmHg	3.62 (3.04 - 4.17)	-	-
Left ventricle	mmHg	3.82 (3.24 - 4.38)	-	-
Right ventricle	mmHg	3.82 (3.24 - 4.38)	-	-
Third ventricle	mmHg	3.82 (3.25 - 4.37)	-	-
Aqueduct of Sylvius	mmHg	3.82 (3.46 - 4.38)	-	-
Fourth ventricle	mmHg	3.82 (3.47 - 4.39)	-	-
Cerebral subarachnoid space	mmHg	3.82 (3.49 - 4.36)	-	-
Spinal subarachnoid space	mmHg	3.82 (3.57 - 4.08)	-	-
Cerebrospinal fluid production and absorption				
ISF production by capillaries	μL/min	2.52	-	-
ISF absorption by venules	μL/min	2.17	-	-
CSF production by choroid plexus	μL/min	0.17	-	-
CSF production by ISF space	μL/min	0.36	-	-
net CSF production	μL/min	0.53	0.33	[Barten 2017]
CSF absorption through arachnoid villi	μL/min	0.50	-	-
CSF absorption by lymphatics	μL/min	0.03	-	-
Phase lag of the four fluid dynamics				
Arterio-venous delay	%CC	12.01	12 - 13	[Kim 2007] (humans)
			12.5 $\pm$ 8.06	[Ambarki 2007] (humans)
			13	[Linninger 2009] (humans)
Arterio-spinal CSF delay	%CC	9.50	5.35 $\pm$ 2.36	[Ambarki 2007] (humans)
Arterio-aqueduct CSF delay	%CC	32.48	22.17 $\pm$ 4.66	[Ambarki 2007] (humans)

Table 4.5: Validation of the computational results. From left to right columns we show: parameter, units, computational result, reference value and reference. Parameters shown in the computational results for the heart dynamics refers to the dynamics of the left ventricle. Arterio-venous delay was estimated as the lag in time between arterial and venous systolic flow peaks in the neck. Arterio-aqueduct CSF and arterio-spinal CSF delays were estimated as the lag in time between arterial systolic peak and CSF systolic peak in the aqueduct of Sylvius and in flow dynamics connecting cerebral and spinal subarachnoid space. CO, Cardiac output; ESPVR, end systolic pressure-volume relationship; EDPVR, end diastolic pressure-volume relationship; MAP, mean arterial pressure; ISF, interstitial fluid; CSF, cerebrospinal fluid.

4.3.1 Validation of the computational results against *in-vivo* measurements

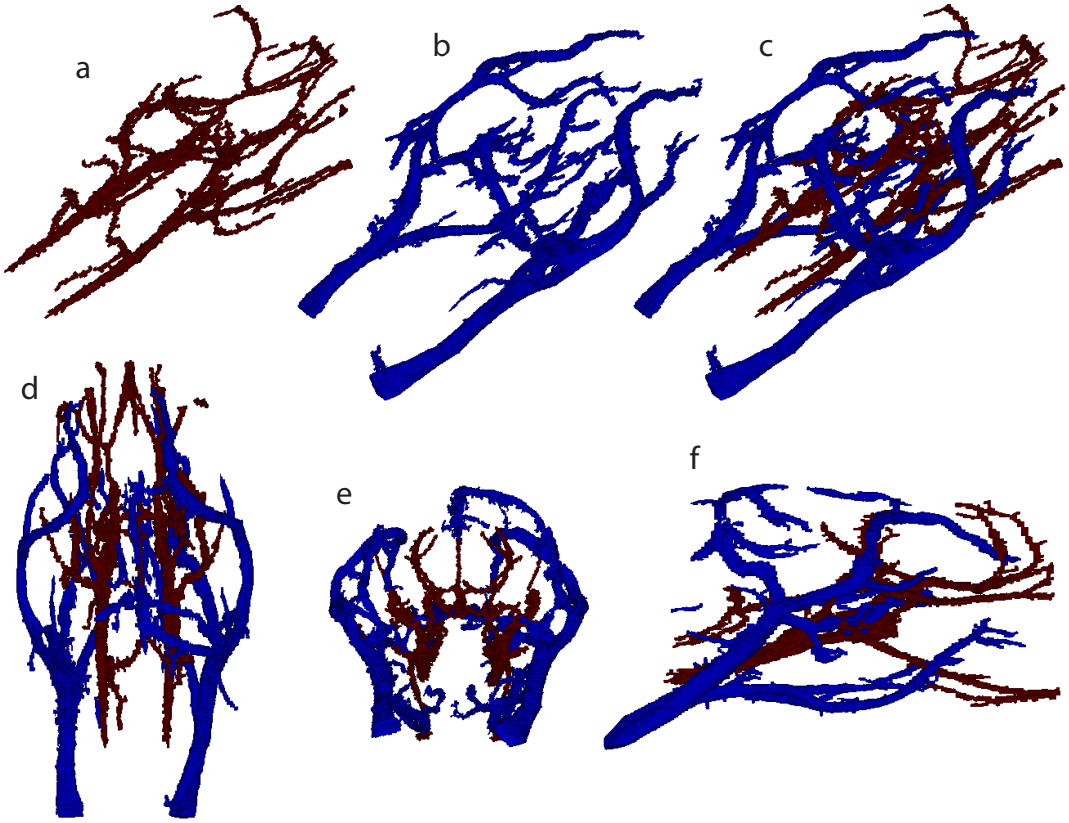

Figure 4.6: MRI segmentation of murine arterial and venous systems. a), b), c): Representative images of 3D segmentation of brain arterial a), venous b) and c) co-localization of a) and b). d), e), f): Representative images of 3D segmentation of c) in the axial d), coronal e) and sagittal f) view.

The MRI acquisition of the intracranial arterial, venous and ventricular systems are shown in Figs. 4.6, 4.7, 4.8. Major arteries and veins are visible through the MRI sequence. The geometrical parameters of the venous and arterial networks were estimated based on the MRI data.

The computational model gave satisfactory results as shown by the comparison with MR-flow measurements in Fig. 4.9. Computed flow rates of the ascending aorta, left/right common carotid arteries and left/right external jugular veins have the same order of magnitude of the MRI measurements. The computed flow rates of the left and right common carotid arteries are more oscillatory compared to those of the MRI acquisitions. This might be due to our assumption of purely elastic vessels [Matthys 2007a]. The computed waveform of the intracranial pressure is comparable to that of the range of in-vivo measurements.

The dynamics of the fluid systems are summarized in Table 4.5. The computed parameters of the heart dynamics agree with values reported in the literature. The order of magnitude of the peak Reynolds number ($\approx$ 195) agrees with 175 reported by Aslanidou et al. [Aslanidou 2015]

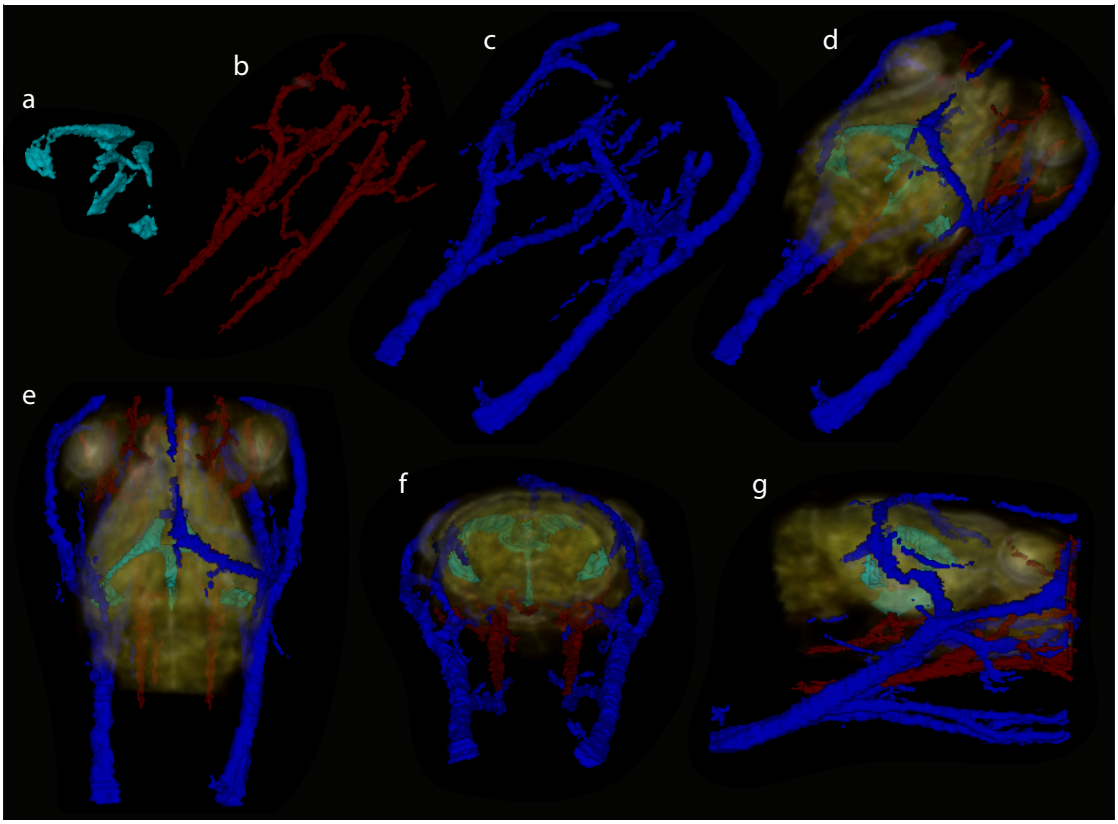

Figure 4.7: MRI segmentation of murine brain ventricular, arterial and venous systems. a), b), c), d): Representative images of 3D segmentation of brain ventricles a), arterial b) and venous c) systems and d) co-localization of a), b), c) with Maximum-Intensity-Projection (MIP) images of the murine brain parenchyma. e), f), g): Representative images of 3D segmentation of d) in the axial e), coronal f) and sagittal g) view.

and is reached at the ascending aorta. Throughout the network, the averaged Reynolds number is $\approx$ 1.4. The range of Womersley numbers confirms that the parabolic velocity profile ($\gamma = 2$, [Alastruey 2008]) is a good choice in our computational model. The apparent dynamic viscosity is in agreement with the value reported by Feintuch et al. [Feintuch 2006] of 3.5 cP and varies from ≈ 3.04 to ≈ 3.85 cP. The computed blood flow rates agree with our MRI measurements. The distribution of arterial blood agrees with the values reported by [Barakat 1997] for rabbits and by [Cuomo 2015], [Feintuch 2006] for mice. There are however some differences. The innominate artery has greater flow percentage compared to those of [Barakat 1997] and [Feintuch 2006]. Also, the percentage of flow in the right/left common carotid artery is slightly greater than the reference value. The flow distribution at the Celiac artery is $\approx$ 10 %CO and lies between the values reported by [Cuomo 2015] and [Barakat 1997]. According to Jacobson [Jacobson 1982], the averaged flow in humans through the celiac artery is 700 mL min^{-1}, which corresponds to $\approx 8.75\% - 17.5\%$ flow of the cardiac output in adults and agrees with our computational results. Blood velocities are slightly lower than those measured by Aslanidou et al. [Aslanidou 2015]. Our cardiac-averaged pressures agree in the measurements performed by the authors. However, the pressures slightly

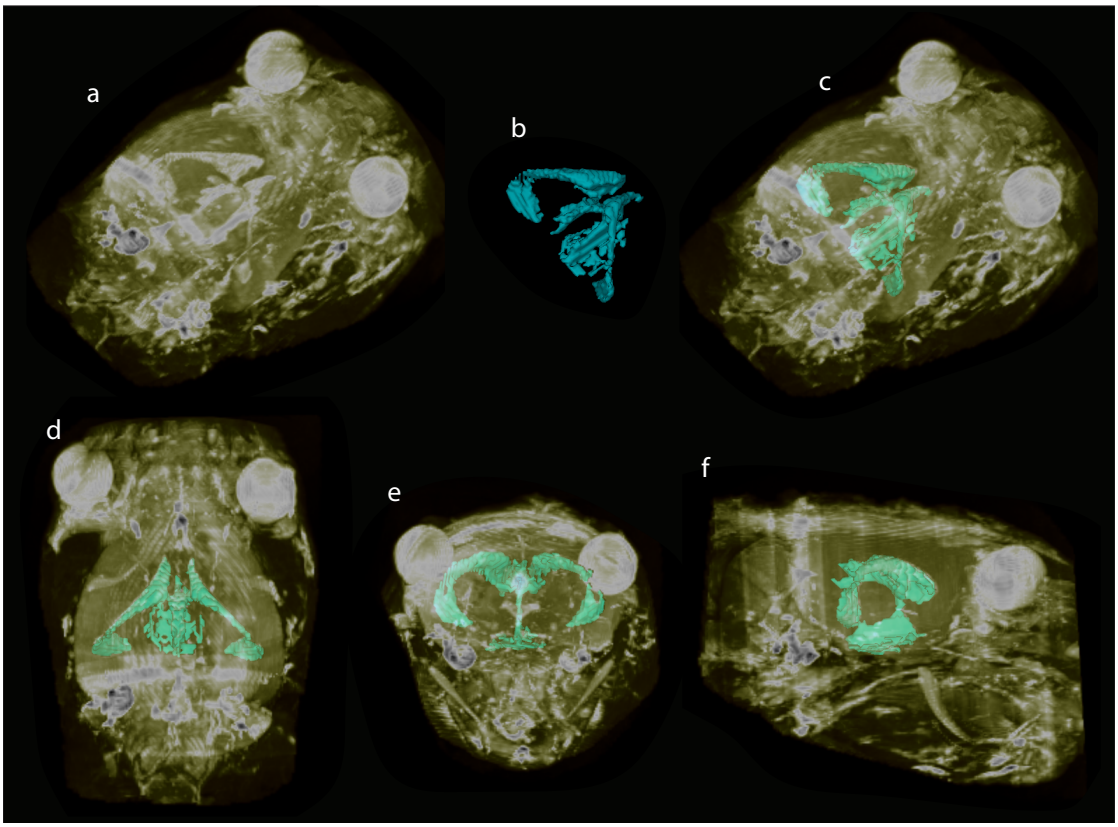

Figure 4.8: MRI segmentation of murine brain ventricular structure. a), b), c): Representative images of 3D segmentation of a) MIP image, b) brain ventricles and c) co-localization of a) and b). d), e), f) Representative images of 3D segmentation of the murine brain ventricles co-localized with MIP images in the axial d), coronal e) and sagittal f) view.

decrease towards the peripheral arterial vessels instead of increase as seen in the measurements. Although the reference cross-sectional area reduces towards the periphery arterial network, the geometrical source term of the tapering effect was neglected and might explain the decrement of the cardiac-averaged pressure. The computed intracranial volume agrees with the results reported by Kovacevic et al. [Kovačević 2005]. Also, the volumes of the ventricles agree with those reported by Dorr et al. [Dorr 2008]. The intracranial pressure agrees with our in-vivo measurements and with those reported by Moazen et al. [Moazen 2016]. The computed pulse pressure is ≈ 0.9 mmHg for each compartment and agrees with our in-vivo measurements (0.80 ± 0.17 mmHg). The CSF is produced by the imbalance of the ISF production/absorption and by the choroid plexus. The net CSF production is 0.53 μL min^{-1}, matches the CSF absorption by lymphatics and through arachnoid villi and is of the same order magnitude of 0.33. μL min^{-1} reported by Barten et al. [Barten 2017].

4.3.2 Dynamics of heart and peripheral vascular system

The computed heart and lung dynamics are illustrated at the top of Fig. 4.10. During systole, the left and right ventricles contract and cause the following chain of events: 1) the pulmonary and aortic valves open, causing the trans-valvular flow to increase; 2) the volumes of the left and right ventricles decrease and in the meanwhile the ejected blood into the ascending aorta spreads throughout the arterial network; 3) the pressures and volumes of the pulmonary arteries, capillaries and veins increase; 4) the right and left atria receive blood and increase in volume. During diastole, the right and left atria contract, leading the following events: 1) the tricuspid and mitral valves open, causing the trans-valvular flow to increase; 2) the volume of both right and left ventricle increase; 3) the pressure wave generated by the right atrial contraction propagates backwards into the venous network in the opposite direction of the bloodstream, contributing to the venous pressure waveform.

The computed dynamics of major arteries and veins are shown at the bottom of Fig. 4.10. The heart contractions determine the pressure waves which spread throughout the vascular system. The arterial pressure waveforms propagate in the arterial tree and change shape from the ascending aorta to peripheral arteries as there are reflected waves generated at the boundaries of the arterial network. The venous pressure waveform is generated by the right atrial contraction which propagates in the opposite direction to the bloodstream. The average arterial pressure is ≈ 93 mmHg and slightly decreases at distal ends, while the average venous pressure ranges from 1.0 mmHg in the right superior vena cava to 1.1 mmHg in the right external Iliac vein. These results show that venous and arterial systems are strictly coupled by the heart, the microcirculation and the pulmonary dynamics.

4.3.3 Dynamics of intracranial blood vessels

The computed intracranial pressure and flow dynamics for the main arteries and veins are shown in Fig. 4.11. The venous pressure waveforms change shape from the right atrium up to the superior sagittal sinus. The venous profile generated by the atrial contraction fades away moving towards the brain and is replaced by an arterial-like shape generated by the Monro-Kellie coupling. At $\approx 0.2\ s$, the arterial systolic blood enters the cranial cavity, slightly increases the intracranial volume and consequently the intracranial pressure, the external pressure of the dural sinuses. This sudden increase in the intracranial venous pressure causes the venous blood to be pushed back to the right atrium, contributing to the homeostasis of the intracranial fluids. The cardiac-averaged venous pressure decreases craniocaudally from ≈ 3.2 mmHg in the superior sagittal sinus to 1.0 mmHg in the right superior vena cava.

The space-time representation of two selected venous and arterial pathways are shown at the bottom of Fig. 4.11. At the beginning of the cardiac cycle, the waveform of the venous pressure shows an interesting characteristic: the pressure increases from the right atrium to a certain location on the distal side of the superior sagittal sinus (≈ 3 cm from the right atrium) and it decreases distally. This is in agreement with the suggestion of Mancini et al. [Mancini 2015] that blood flow might be bidirectional in the superior sagittal sinus of mice, in contrast with the unidirectional flow in the same venous location in humans. At the distance of ≈ 3 cm from the right atrium, the three venous peaks originated by the Monro-Kellie coupling can be appreciated. The space-time waveform of the arterial pressure is maintained from left ventricle up to intracranial cavity. These computational

results highlight that the intracranial fluids are coupled and that the arterial systolic wave greatly affects the intracranial dynamics.

4.3.4 Cerebrospinal fluid dynamics and its interaction with intracranial blood

The CSF dynamics is shown in Fig. 4.12. The pressure waveforms of all CSF compartments are strongly influenced by the arterial blood entrance in the cranial cavity. Except for the pressure dynamics of the spinal subarachnoid space, all CSF waveforms are characterized by three peaks: the percussion wave P_1, the tidal wave P_2 and the dicrotic wave P_3. P_1 is generated by the systolic arterial peak, while P_2 and P_3 come from the reflected waves generated at the periphery of the arterial tree. Classically, P_3 correlates with the dicrotic notch. However, in our computational results, P_2 occurs at the aortic valve closure time at $\approx$ 0.035 s (27 %CC).

The bottom panel of Fig. 4.12 shows the volumetric and flow interaction of CSF, arterial and venous blood. The intracranial fluid homeostasis is greatly maintained thanks to the dynamics of venous blood and intra/extra-cranial CSF. The venous and the CSF fluid act as a buffer when the arterial blood enters the cranial cavity. Indeed, during each systole, the inflow of arterial blood into the cranium is balanced by a craniocaudal movement of both CSF and venous blood. This is particularly evident at 0.019 s (16.0 %CC), where both volumes of CSF and venous blood decrease in correspondence of the peak aortic flow. The intracranial CSF volume reaches its minimum peak at $\approx$ 0.02 s (14.5 %CC) and is followed by the intracranial arterial and venous maximum volume peaks (0.051 s or 39.5 %CC and 0.062 s or 48.0 %CC). The peak flow of the aqueduct of Sylvius (1 = systolic peak = craniocaudal movement) occurs at 0.06 s (46.5 %CC), namely between the minimum CSF volume peak and the maximum venous volume peak, and is almost synchronous with the local minimum in the intracranial pressure between P_2 and P_3. During diastole, CSF from the spinal cavity returns back into the cranial subarachnoid space due to the decrement in the whole intracranial blood and occurs synchronously with the decrease in aqueduct CSF flow.

4.3.5 Interaction of heart, brain interstitial fluid and cerebrospinal fluid and the regulation of brain fluids

As illustrated in Fig. 4.13, during the cardiac cycle, the brain interstitial fluid compartment exchanges water with the CSF spaces. In particular, during systole, water moves from the *intracerebral CSF* compartments (lateral and third ventricles) into the ISF space, and at the same time, the ISF space ejects water into the *extracerebral CSF* compartments (fourth ventricle and cranial subarachnoid space). On the contrary, during diastole, the direction of water flow changes: the ISF space receives water from the extracerebral CSF compartments and releases water into the intracerebral CSF ones. Interestingly, the aqueduct of Sylvius divides the intracerebral CSF compartments from the extracerebral ones. The greatest water exchange occurs between the cranial subarachnoid space and the ISF, with a flow amplitude of ≈ 25 μL min^{-1}. Overall, there is a bidirectional water movement from the ISF space to the intracranial CSF compartments with a duration of about ≈ 61 %CC. Also, the brain ISF compartment exchanges water in both capillaries and venules through Starling forces. The capillary production and venous absorption of ISF are always positive during the cardiac cycle. However, water entrance from the capillary bed into the ISF compartment is only partially absorbed by venules during the cycle. This imbalance of ISF production and ISF

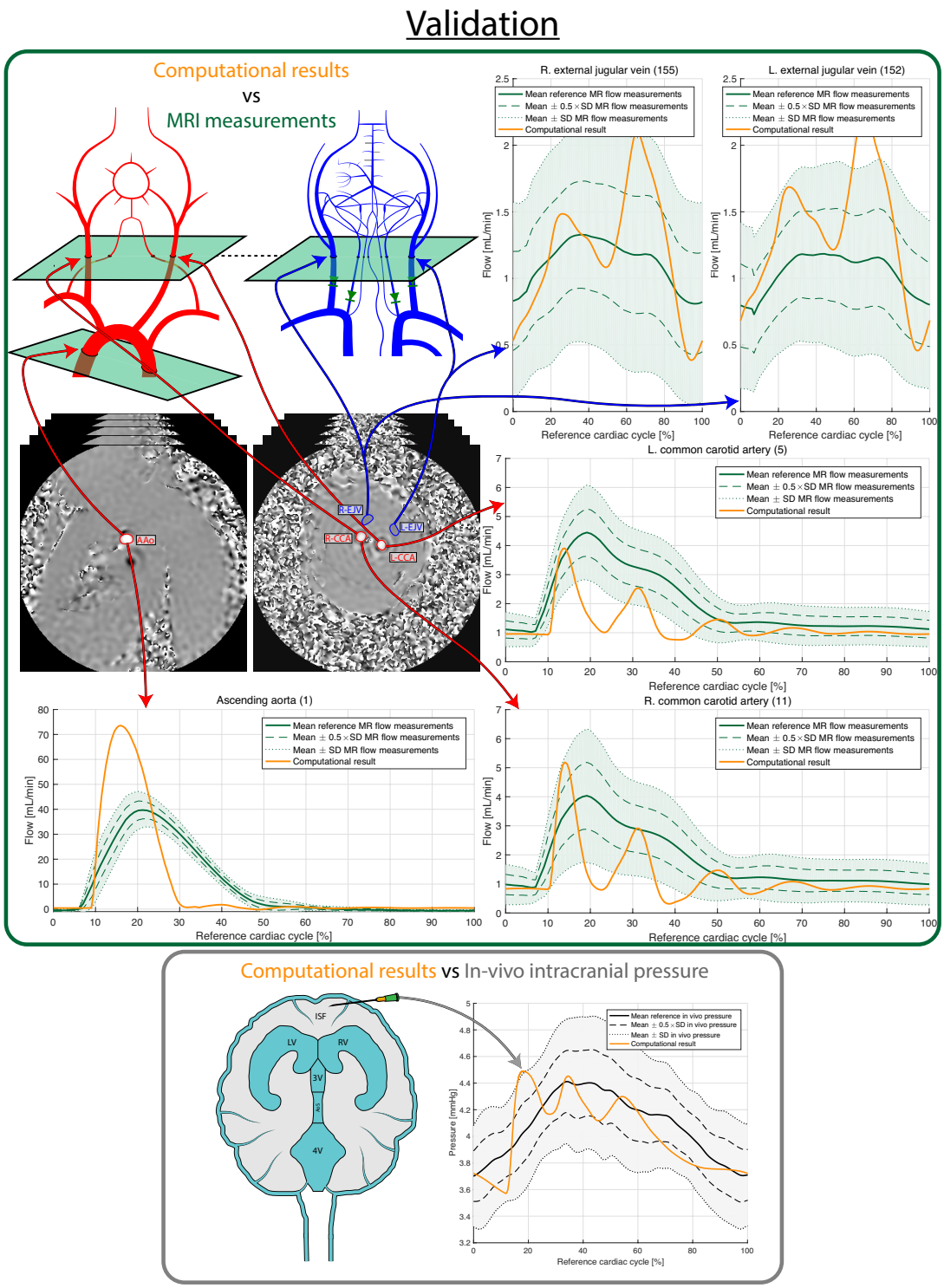

Figure 4.9: Validation of computational results against *in-vivo* flow and pressure measurements. Top: computational results (orange) compared with MR-flow measurements (green) for the right/left external jugular vein, right/left common carotid artery and the ascending aorta. The green slices illustrate the location at which the 2D slice of the MRI sequence was positioned. The SPCP MRI acquisition is shown at the centre ($n = 5$ animals). Bottom: computational results of the ISF pressure compared with in-vivo intracranial pressure measurements ($n = 4$ animals).

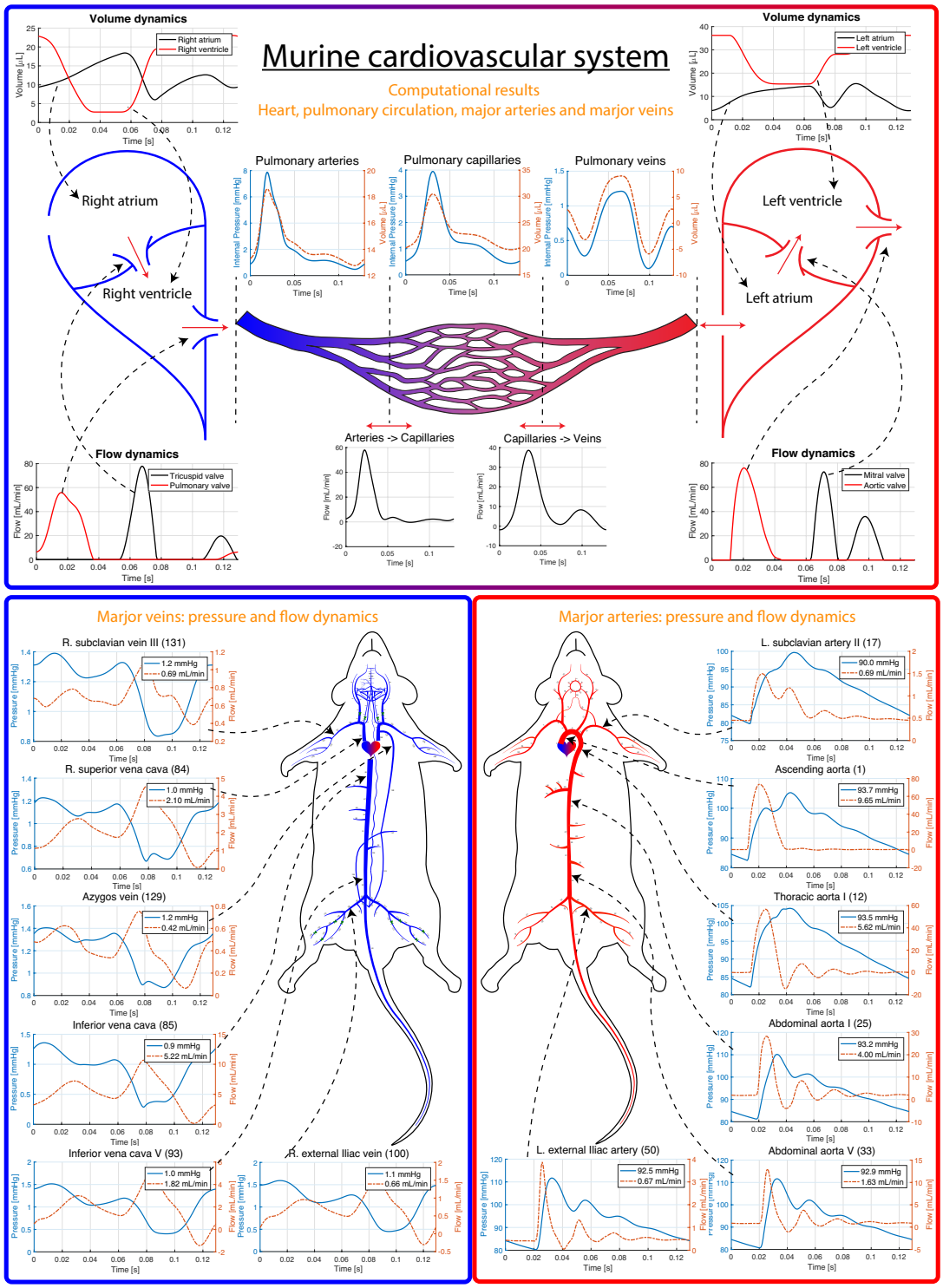

Figure 4.10: Computational results for heart, pulmonary circulation, major arteries and veins. Top: the computational results of volume and flow dynamics are shown for the left/right atrium and for the left/right ventricle. Pressure and volume dynamics for pulmonary circulation are shown at the centre. Bottom left and right: pressure and flow dynamics of major veins and arteries are shown. Cardiac-averages of pressure and flow are shown in the legends.

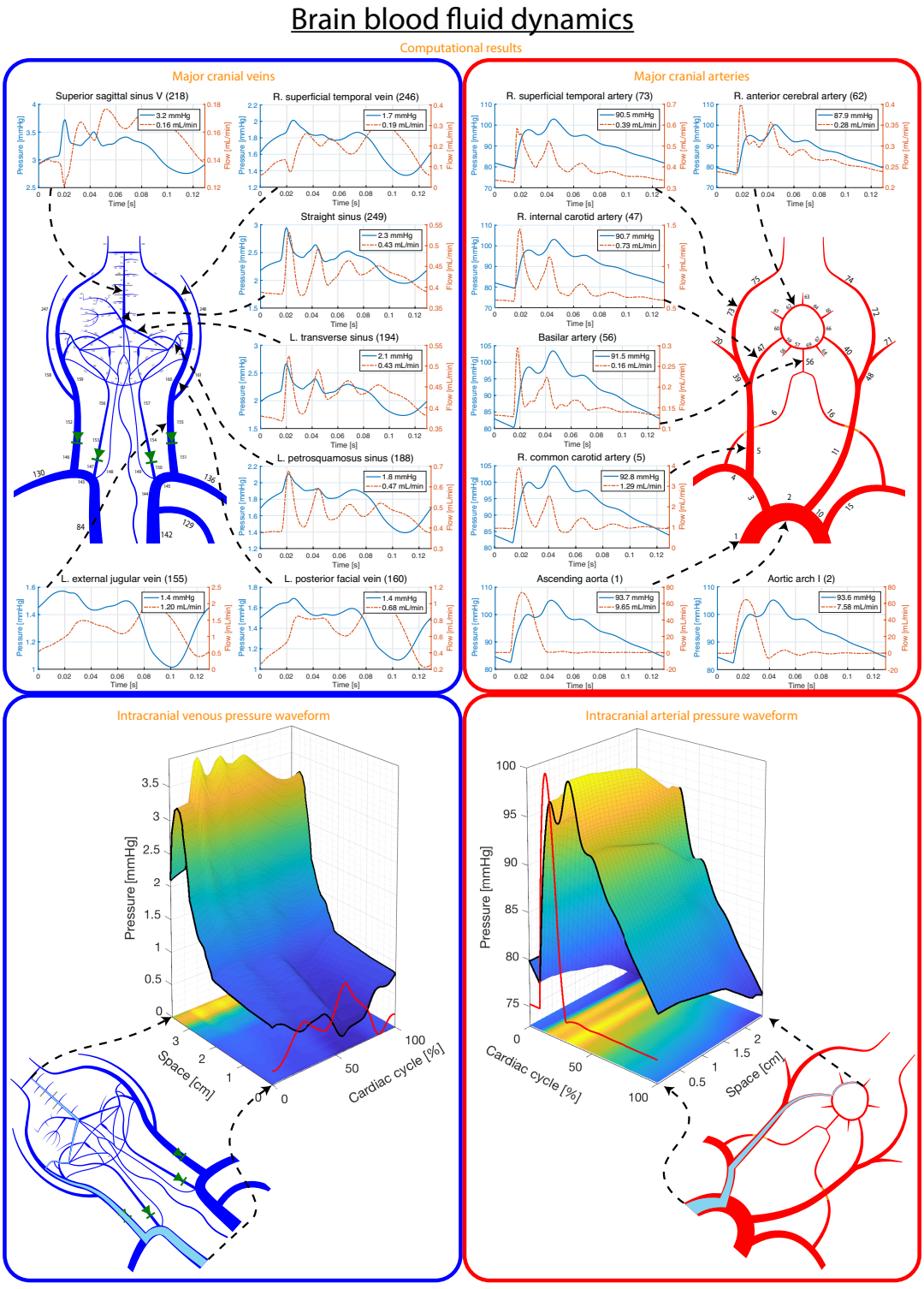

Figure 4.11: Computational results of brain blood fluid dynamics. Top left and right: results of the pressure and flow dynamics of major veins and arteries are shown. Bottom left and right: space-time representation of pressure waveform from the right atrium (left side) and left ventricle (right side) to intracranial vessels. The two selected paths are illustrated. The red curves in the space-time representation illustrate the non-dimensional flow profiles of the vessels adjacent to the right atrium (venous side) and to the left ventricle (arterial side).

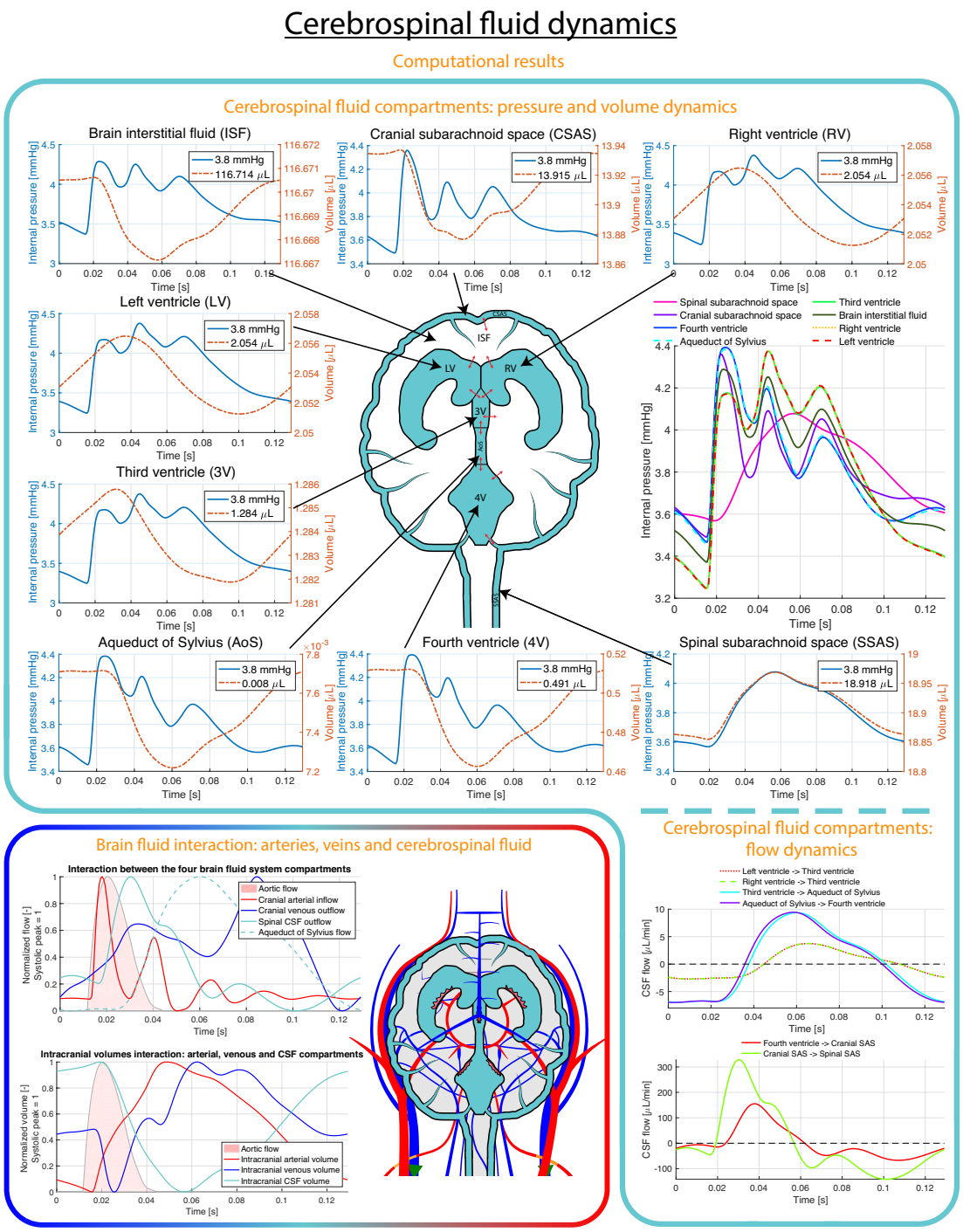

Figure 4.12: Interactive dynamics of cerebrospinal fluid, of arterial and of venous blood. Top: pressure and volume dynamics of cerebrospinal fluid compartments. Bottom right: cerebrospinal flow dynamics. Bottom left: CSF and blood normalized flow and volume analysis over a cardiac cycle. Cranial arterial inflow and venous outflow were calculated in the neck level (arteries No. 5, 11, 6, 16; veins No. 152, 155, 156, 157, 148, 149). Each flow profile was normalized between 0 and 1 such that all four systolic peaks correspond to 1. CSF, cerebrospinal fluid; ISF, interstitial fluid; LV, left ventricle; RV, right ventricle; 3V, third ventricle; AoS, aqueduct of Sylvius; CSAS, cranial subarachnoid space; SSAS, spinal subarachnoid space; SAS, subarachnoid space.

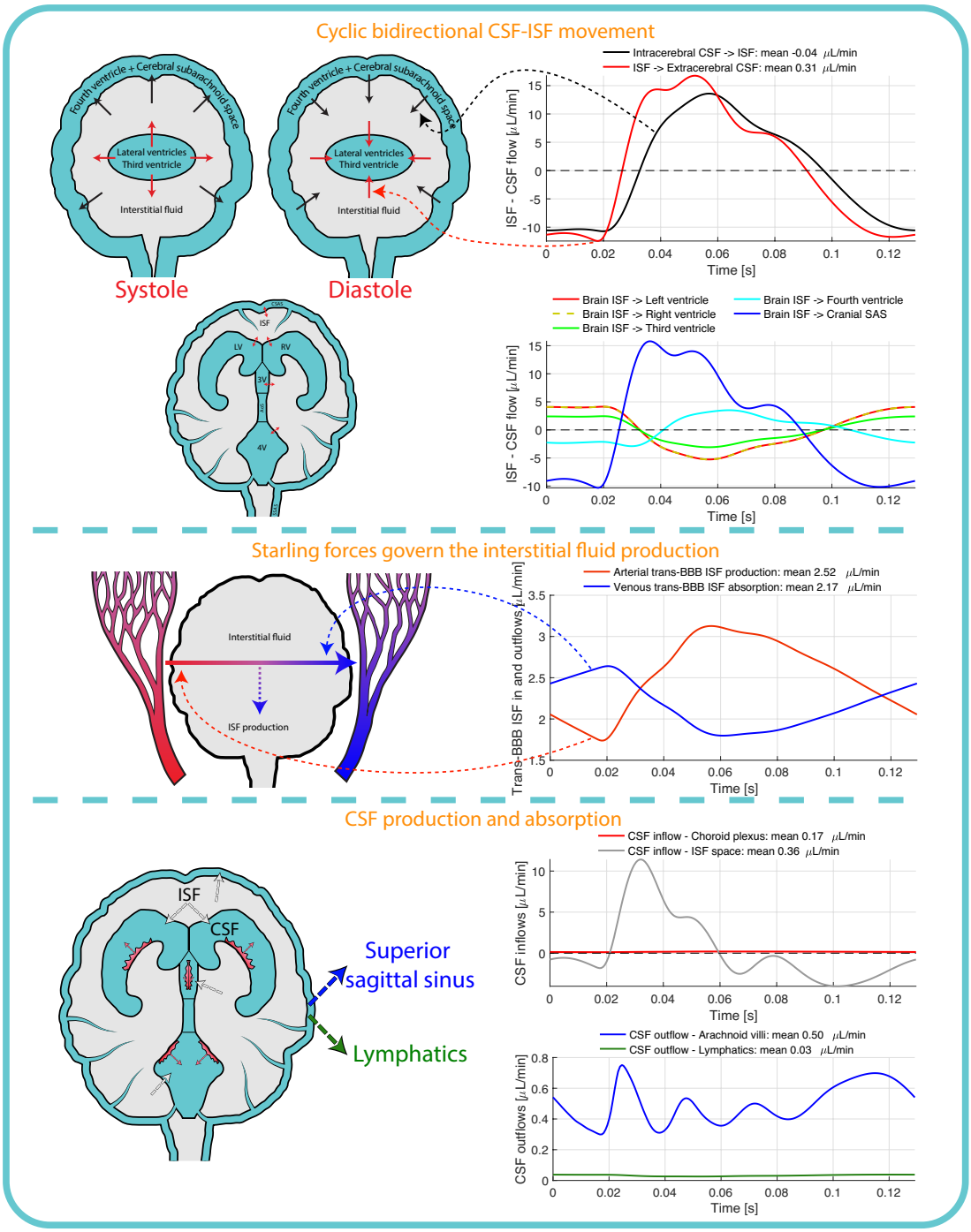

Figure 4.13: Dynamics of cerebrospinal fluid and brain interstitial fluid. Top: bidirectional CSF-ISF flow movement during systole and diastole. The *intracerebral CSF compartment* is formed by the lateral ventricles and third ventricle, while the *extracerebral CSF compartment* is formed by the fourth ventricle and the cranial subarachnoid space. Middle: ISF production and absorption through the blood-brain barrier in the capillary and venous level. Bottom: CSF production by the choroid plexus and by the ISF compartment, and CSF absorption, by lymphatics and through arachnoid villi. CSF, cerebrospinal fluid; ISF, interstitial fluid; SAS, subarachnoid space; BBB, blood-brain barrier.

absorption represents the net production of ISF during the cardiac cycle. Finally, the CSF compartment receives water from the ISF space and by the choroid plexus. This amount of volume is then absorbed through arachnoid villi and by lymphatics.

4.3.6 Alteration of CSF absorption, Starling forces, ISF-CSF permeability and the Monro-Kellie coupling: a mathematical study of the intracranial effect

Water movement in and out of the parenchyma is strictly connected with CSF absorption, with intracranial Starling forces, ISF-CSF permeability and the Monro-Kellie hypothesis. Through our computational model, we simulated various scenarios in which these dynamics have been altered. The effect in the intracranial fluid dynamics have been quantified and compared to the healthy control described in Sections 4.3.4, 4.3.5, 4.3.3, 4.3.2 and 4.3.1. The computational results are shown in Fig. 4.14.

When the CSF absorption was completely abolished, there were three major effects (Fig. 4.14a): 1) the ISF pressure increased by 54%, 2) the net ISF-CSF movement inverted its direction, leading to net water movement from the CSF space into the ISF one, and 3) the ISF absorption by venules increased, to compensate the increment in the ISF production from the CSF space. These results suggest that when the CSF absorption is abolished, solutes might not be attracted into the CSF space, but remain stuck in the parenchyma. The decrement in the ISF-CSF permeability did not greatly modify the CSF and ISF production/absorption (Fig. 4.14b). However, it remarkably decreased the flow amplitude of water entrance between the intra and extracerebral CSF compartments and the ISF space. The Monro-Kellie hypothesis is fundamental in the bidirectional CSF-ISF water movement. In our computational model, the Monro-Kellie coupling strictly depends on the compliance of the intracranial compartment. When the intracranial compliance has been increased by 100 times, the entrance of arterial volume in the cranium did not affect the remaining fluid systems (Fig. 4.14c). In particular, the intracranial arterial inflow did not induce a displacement of the CSF into the spinal subarachnoid space and consequently, the ISF was not subjected to a suction force, leading to a reduction of the flow amplitude ($\approx$ -96%) between the ISF and the CSF compartments. The main contribution of the intraparenchymal Starling forces is to create a continuous intraparenchymal water movement towards venules (Fig. 4.14d). The absence of the Starling forces completely abolished the net water movement from the ISF compartment into the CSF space, leading the CSF production to decrease by $\approx$ 63%.

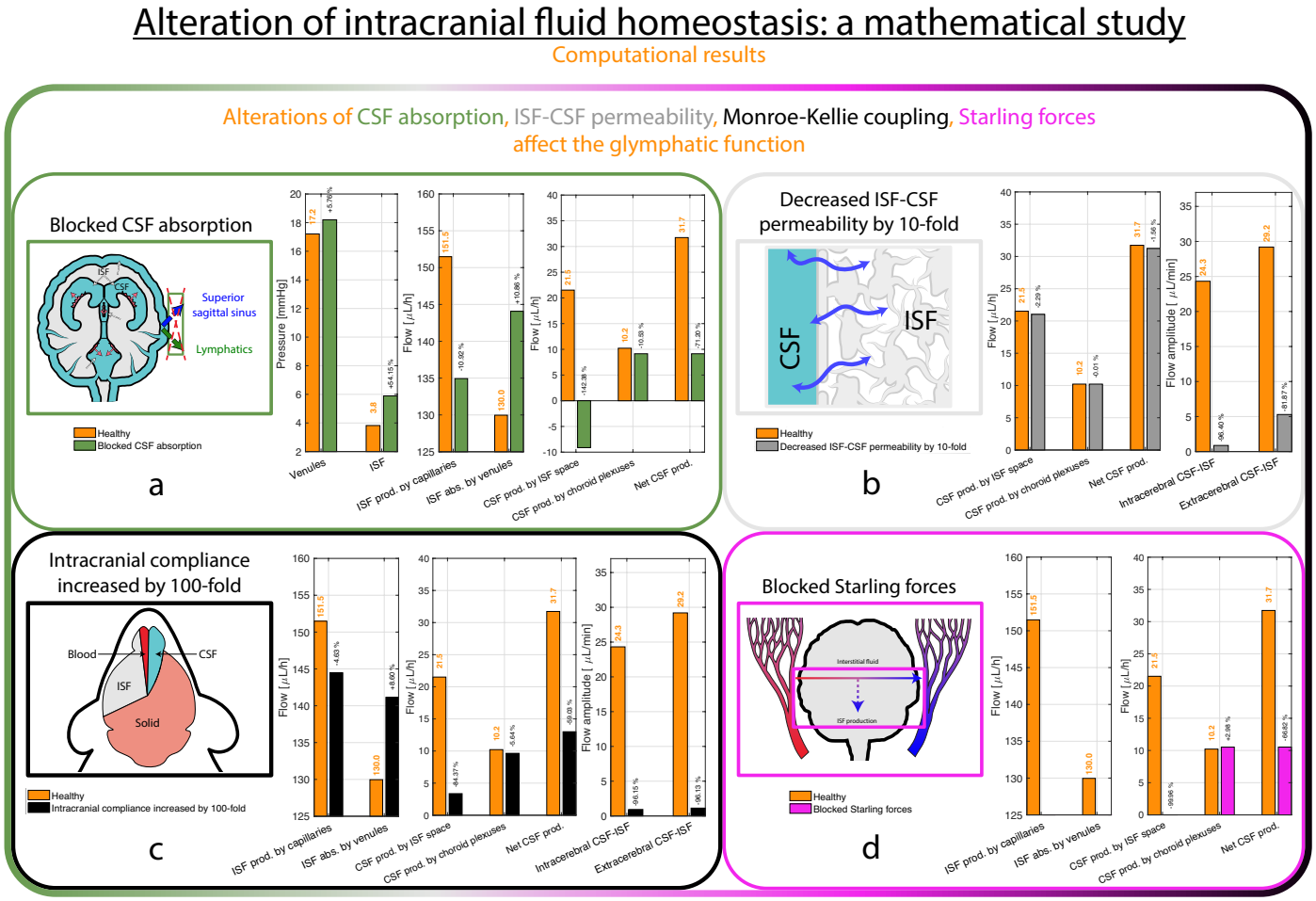

Figure 4.14: Alterations of CSF absorption, Starling forces, ISF-CSF permeability and the Monro-Kellie coupling affect the glymphatic function. Four different scenarios are presented. We completely blocked the CSF absorption by lymphatics and through arachnoid villi (a, top left), decreased by a factor of 10 the ISF-CSF water permeability (b, top right), increased by 100 times the compliance of the intracranial compartment $P_{intracranium}$ in Table 4.2 (c, bottom left) and blocked ISF production by intracranial capillaries and venules through Starling forces (d, bottom right). Bar plots show cardiac-averaged values.

4.3.7 Idiopathic intracranial hypertension and CSF-ISF alterations

Mice (C57BL/6J) with impairment of the intracranial venous outflow were modelled *in vivo* through a bilateral ligation of both petrosquamosus sinuses and *in silico* through a double stenosis of the 98% at the same locations. The location of the bilateral ligation is shown in Fig. 4.15. These *in-vivo* and *in-silico* mouse model aims to reproduce idiopathic intracranial hypertension, a neurological disorder characterized by an abnormal increase in intracranial pressure, related with intracranial venous drainage malfunctioning [Farb 2003] and which causes headache, tinnitus, papilledema with potentially progressive vision loss [Szewka 2012]. The intracranial pressure resulting from the mathematical model agrees well with that of the *in-vivo* intracranial pressure measurements (Fig. 4.15a), although the pulse pressure of the computational results is slightly higher (1.76 mmHg vs 0.58 $\pm$ 0.21 mmHg). The intracranial pressure waveform of the *in-silico* model is more oscillatory than that of the measurements. A possible explanation for this discrepancy could derive from the assumption of purely elastic pressure-volume relationships that we have made for each intracranial lumped model. The cardiac-averaged venous pressure increases greatly in the pathological case in the superior sagittal sinus compared to the healthy control (3.16 mmHg vs 5.47 mmHg), while there are no significant changes on venous cardiac-averaged pressures from the right atrium up to the location of the ligation (Fig. 4.15b). The intracranial blood volume is greater in the pathological case than in the healthy control (14.1 μL vs 14.18 μL) (Fig. 4.15c). This is consistent with the hypothesis in Agarwal et al. [Agarwal 2018] in which the additional blood stored in the cranium can be regarded as a pseudo-tumour which occupies volume in the cranium and permanently increases the ICP. Although the maximum CSF volumes in the healthy and pathological cases during the cardiac cycles do not differ significantly ($\approx$ 19.85 μL), the minimum CSF volume in the pathological case is lower than that of the healthy control (19.74 μL v 19.71 μL) and the amplitude of the volume variation during the cardiac cycle is larger (0.1 μL vs 0.14 μL). Likewise, the ISF volume has a lower minimum peak (116.667 μL vs 116.666 μL) and a larger amplitude of the volume variation during the cardiac cycle (3.48 nL vs 4.62 nL).

There are several changes in the ISF and CSF dynamics (Figs. 4.15d, 4.15e). As the ISF pressure increases by almost 50%, the ISF production is reduced by almost 45%. Although there is no significant change in the CSF production by choroids, the CSF production by the ISF compartment decreases by $\approx$ 45%. As the pressure in the superior sagittal sinus is greater, the drainage of CSF through arachnoid granulations decreases by 39%, while that through lymphatics increases by 74%. The total amount of CSF volume does not increase significantly (39.21 μL vs 39.63 μL), is redistributed between intra, extracerebral CSF spaces and the spinal subarachnoid space. These rearrangements of CSF lead the amount of CSF volume in the spinal subarachnoid space to increase by $\approx$ 2% (18.92 μL 19.35 μL). The bidirectional ISF-CSF flow amplitude increases in the pathological case (intracerebral CSF-ISF 24.32 μL min^{-1} vs 32.34 μL min^{-1}, extracerebral CSF-ISF 29.20 μL min^{-1} vs 40.05 μL min^{-1}).

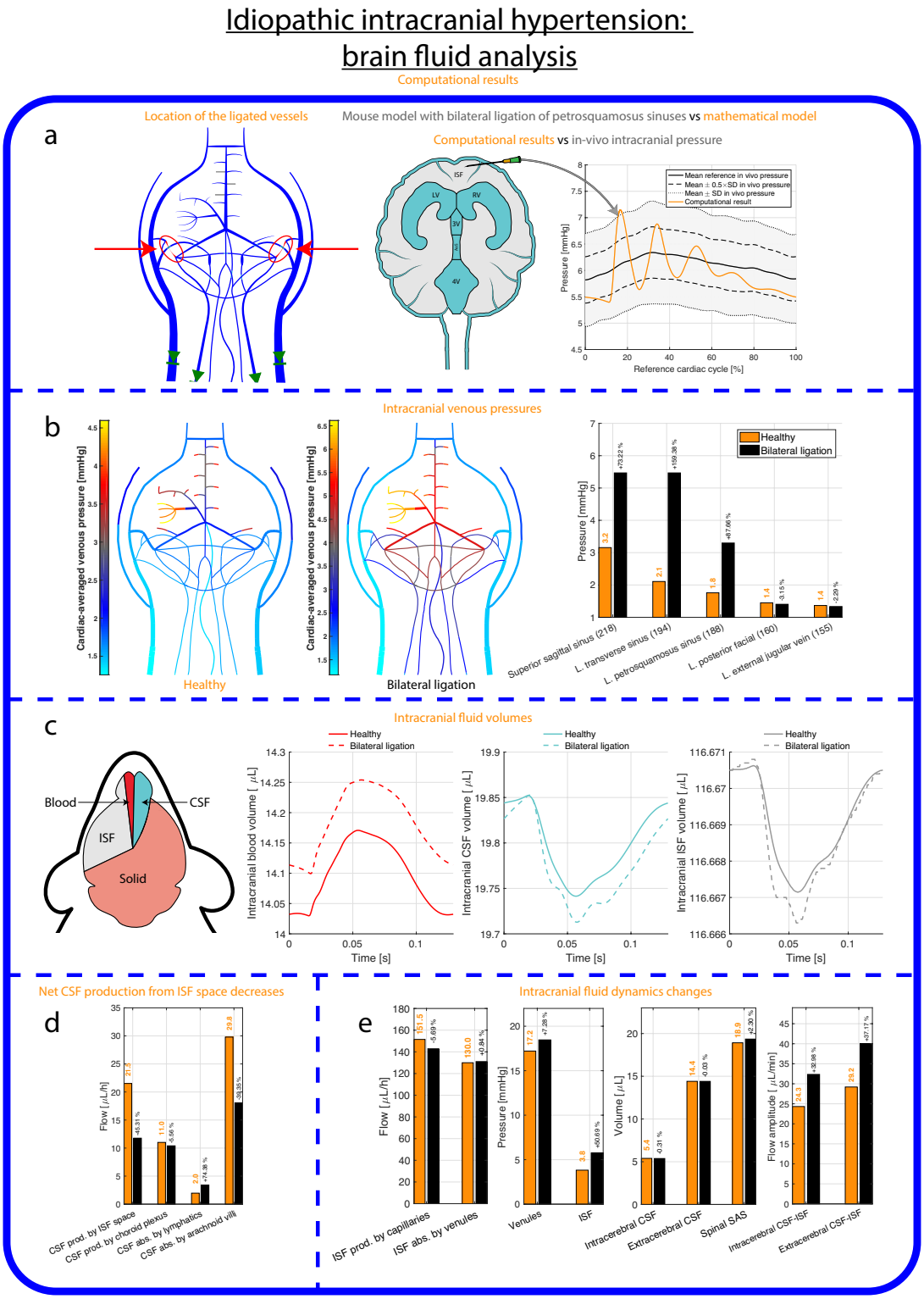

Figure 4.15: Cranial venous outflow impairment alters the intracranial fluid dynamics. Top, a): validation of the computational results against *in-vivo* measurements of a mouse model submitted to a bilateral ligation of both petrosquamosus sinuses. The bilateral ligation was modelled through a double stenosis of 98% at the same location of the ligation. Computational results of the ISF pressure compared with *in-vivo* intracranial pressure measurements ($n = 4$ animals). Middle top, b): cardiac-averaged venous pressure in the healthy (left) and in the bilateral ligation (right) cases. The bar plots show the cardiac-averaged venous pressure at chosen locations of the network. Middle bottom, c): Intracranial blood, intracranial CSF and ISF volume dynamics in the healthy and pathological cases. Bottom, d), e): Bar plots of ISF and CSF flow balance, of the pressure and volume in intracranial locations and the amplitude of flow variation the cardiac cycle.

4.4 Discussion

4.4.1 Mathematical models of the main murine fluid systems and comparison with the body of literature

The mathematical model presented here represents to the authors' knowledge the first attempt to theoretically describe and quantify the murine dynamics of the arterial, venous, CSF, ISF and lymphatic systems in a holistic, multi-scale framework. We built on previous works of the human circulation [Müller 2013b, Müller 2014, Mynard 2015, Strocchi 2017, Liang 2009a], of the murine circulation [Aslanidou 2015, Cuomo 2015] and took advantage of allometric scalings to estimate most of the murine parameters [Dawson 2014, Dawson 2005, Dawson 2001]. Our mathematical model incorporates a novel Monro-Kellie mathematical coupling, Starling resistors in cerebral veins, Starling forces through the blood-brain barrier and choroid plexus [Linninger 2017], and a simple model of lymphatic drainage of CSF.

Our computational results agree well with reported literature values for the murine fluid dynamics, as shown in Table 4.5. The validity of our results is also supported by our *in-vivo* intracranial pressure and MR-flow measurements. Previous mathematical models of the murine fluid systems have focused just on the arterial system using a one-dimensional approach [Aslanidou 2015] or a three-dimensional mathematical model [Cuomo 2015]. Cuomo et al. [Cuomo 2015] modelled the main murine arterial tree using a validated fluid-solid interaction code. The blood distribution of our computational results agrees well with the results of Cuomo et al., although some discrepancy has been observed in the level of the celiac artery. Aslanidou et al. [Aslanidou 2015] have proposed a one-dimensional model for the arterial tree, included the rheological properties of blood, modelled the visco-elastic nature of the arterial wall and used a three-element Windkessel model for the terminal segments. We incorporated the geometrical data of the arterial tree of Aslanidou et al. [Aslanidou 2015] collected through micro-CT on male C57BL/6J mice as well as the wave speed formula proposed by the authors.

Humans and mice are remarkably similar regarding the body fluid dynamics, as shown by our computational results. For instance the venous-heart-arterial interaction in mice is similar to that in humans. There are obviously some differences between mice and humans. Even though the arterial pressure does not differ between mice and humans, the murine intracranial pressure is somewhat lower than that of humans (mice: 3 - 5 mmHg vs humans: 7 - 18 mmHg [Steiner 2006]). Accordingly, the central venous pressure is lower in mice than in humans (mice: 0.3 - 1.5 mmHg [Scheuermann-Freestone 2001] vs humans: 3 – 8 mmHg [Klingensmith 2008]), allowing for CSF uptake into the venous system. There are also some discrepancies in terms of venous network geometry. In humans, the superior sagittal sinus drains proximally into the transverse sinuses and the majority of the venous drainage pathways is in most cases through the internal jugular veins. As described for mice by [Mancini 2015, Xiong 2017] and shown for rats in [Scremin 2015], in mice the superior sagittal sinus drains proximally into the transverse sinuses and distally through the rostral rhinal veins into the superficial temporal veins. Also, the principal venous drainage pathways in mice are the external jugular veins. Apart from possible differences between humans and mice, our computational results suggest that mathematical models together with allometric scaling can in principle be employed to model the dynamics of fluid systems of mammalians.

4.4.2 Intraparenchymal bidirectional water movement: the heart influence

How much do we know about the complex ISF-CSF dynamics induced by the pumping action of the heart during each cardiac cycle? The Monro-Kellie states that the increment of the intracranial arterial volume during systole must be balanced by a decrement of the venous and CSF intracranial volumes in order to maintain the homeostasis of intracranial fluid volume [Wilson 2016, Linninger 2016]. In fact, at each cardiac cycle, CSF moves towards the spinal subarachnoid space and venous blood is displaced into the right atrium. The natural question is: what happens to the brain interstitial fluid at every cardiac cycle? To the authors' knowledge, the CSF-ISF movement has not yet been evaluated through MRI measurements in neither human nor mice. Our computational results suggest that water continuously enters and exits the parenchyma during the cardiac cycle, creating a continuous mixing effect between ISF and CSF. In particular, during systole the intracerebral CSF compartments (lateral and third ventricles) release water into the parenchyma and at the same time, the parenchyma releases water into the extracerebral CSF compartment (fourth and cerebral subarachnoid space), while during diastole, the water direction inverts. The brain parenchyma effectively behaves like a sponge and allows for a continuous water movement [Penn 1984]. In this regard, intracerebral CSF compartments are fundamental to allow transparenchymal water movements. Alteration of the flow dynamics in the aqueduct of Sylvius or in the internal ventricles might affect this continuous bidirectional water movement. We speculate that a similar mechanism might occur in the spinal cord. The extracerebral CSF compartment would be the spinal subarachnoid space, while the spinal canal would represent the intracerebral CSF compartment. It would be interesting to understand if there is any correlation with alterations of our hypothesized dynamics of the spinal cord bidirectional CSF-ISF movement in relation to syringomyelia and Chiari malformation [Leung 2016].

4.4.3 Brain fluid homeostasis: modern view of CSF drainage

In the last couple of decades, CSF movement, production and absorption have been the subject of discussions [Brinker 2014, Miyajima 2015]. The old understanding of the CSF physiology sees the majority of the CSF production by the choroid plexus in the cerebral ventricles and the absorption at the level of the arachnoid villi [Brinker 2014]. However, this old but still traditional concept of CSF drainage must change in light of new knowledge regarding the brain lymphatic drainage [Louveau 2015, Zawieja 2008, Absinta 2017], glymphatic system [Iliff 2012, Jessen 2015], intramural peri-vascular ISF drainage within the basement membrane of arteries [Carare 2008, Weller 2008, Engelhardt 2016] and MR-flow measurements of CSF dynamics in humans [Beggs 2013, Kelly 2016].

A recent work of the group of Linninger [Linninger 2017] proposed a mathematical model which incorporates the main fluid components of the brain with water and species flux dynamics governed by the Hagen-Poiseuille flow (blood), Darcy flow (interstitial fluid transport), and Starling's law (transmembrane fluid exchange). The authors reviewed and reproduced some historical experiments on the dynamic changes of the intracranial pressure after intravenous or intracisternal infusion of mannitol, validating the *Bulat-Klarica-Orešković* hypothesis through their computational results. The *Bulat-Klarica-Orešković* hypothesis affirms that CSF exchange is present everywhere in the CSF system and is a consequence of water filtration between capillaries and ISF [Orešković 2017,

Linninger 2017].

In our computational model, we followed the mathematical model of Linninger [Linninger 2017] and adopted the *Bulat-Klarica-Orešković* hypothesis by incorporating Starling forces in the water dynamics through the blood-brain barrier and by the choroid plexus. However, we have assumed time-independent changes on solute concentrations. In summary, we are modelling the following fluid dynamics phenomena:

1. ISF production in capillaries through the blood-brain barrier (Starling forces).
2. Partial ISF absorption ($\approx 85\%$) by venules through the blood-brain barrier (Starling forces).
3. CSF production by the choroid plexus in cerebral ventricles (Starling forces).
4. CSF absorption by lymphatics and drainage towards subclavian veins.
5. CSF absorption through arachnoid villi into the superior sagittal sinus.
6. CSF and ISF exchange determined by hydraulic pressure forces without concentration gradients of small or large solutes.

In line with CSF human absorption knowledge, we assumed the presence of arachnoid villi, although existence has not yet been proved in mice [Ma 2017]. The zero osmotic pressure difference between the ISF and CSF compartments is motivated by the presence of large gap junctions in the pia and ependyma, providing a permeable molecular structure for CSF-ISF diffusion exchange [Spector 2015, Whish 2015].

Building on the work of Linninger [Linninger 2017], our mathematical model gives further insights into the heart-CSF-ISF dynamics, since all fluid systems are tightly coupled. Equipped with the previous hypotheses, our computational model gives the following results:

1. There is net production of ISF given by the imbalance of ISF production (capillaries) and ISF absorption (venules).
2. The Monro-Kellie coupling induces a bidirectional movement of CSF into the ISF compartment during each cardiac cycle.
3. There is net production of CSF from the ISF compartment during the bidirectional CSF-ISF cycles.
4. There is active production of CSF in the choroid plexus in cerebral ventricles.
5. CSF is absorbed through the arachnoid villi and through lymphatics.

These outputs gave us some hints on the possible mechanisms by which the so-called glymphatic system works.

4.4.4 A hypothesis on the working principles of the glymphatic system

Our results suggest that the glymphatic system depends on four mechanisms: 1) the Monro-Kellie coupling, 2) Starling forces governing the fluid exchange at the blood-brain barrier, 3) ISF-CSF bidirectional movement and 4) drainage of CSF through arachnoid villi and by lymphatics.

Fig. 4.16 summarizes our hypothesis on the working principles of the glymphatic system. During diastole, as ISF volume increases and recalls for fluids, the extracerebral CSF (cranial subarachnoid

space, fourth ventricle) enters into the ISF compartment. This causes solutes to be dragged from the para-arterial CSF compartment into the ISF space (Monro-Kellie coupling). The continuous water suction effect created by the Starling forces at the blood-brain barrier continuously attracts ISF towards blood-brain barrier of venules, transporting solutes through a slow water-current effect (Starling forces). Solutes likely move into the para-venous CSF compartment since 1) during the cardiac cycle there is net production of CSF from the ISF space and 2) during systole, the ISF rapidly moves into the extracerebral CSF compartments. Solutes remain into the para-venous CSF compartment since they cannot cross the blood-brain barrier (provided the integrity of the BBB). The low-venular pressure induces a continuous movement of water into venules and contrasts the suction ISF force during diastole, trapping solutes into the para-venous CSF compartments and preventing them to return back into the ISF compartment (Starling forces). The absorption of water through arachnoid granulations and by the lymphatic system and the continuous CSF movement generated by the Monro-Kellie coupling leads macromolecules to be transported into the cerebral subarachnoid space and finally drained by meningeal lymphatics.

Although our hypothesis is based on water movement and has yet to be validated experimentally, it suggests a possible explanation of the glymphatic system proposed by Iliff et al. [Iliff 2012] and consider the interactive effect of arteries, veins, CSF, ISF, lymph and heart.

4.4.5 Alterations of CSF absorption, ISF-CSF permeability, Monro-Kellie coupling and Starling forces affect the glymphatic system

Our hypothesis is based on water movement and suggests that the glymphatic system results from the combination of CSF absorption, ISF-CSF exchange and ISF-blood exchange. Our computational results suggest that alteration of these dynamics might affect the glymphatic system.

The CSF drainage is a key regulatory mechanism of the glymphatic system. As shown in Fig. 4.14, when the CSF uptake from both veins and lymphatics is completely blocked, the CSF production by the choroid plexus is balanced by a CSF absorption from the ISF compartment, which means that the net CSF-ISF movement changed direction compared to the healthy control. Also, the increase in ISF production is compensated by an increase in ISF absorption by venules. These results suggest that solutes can still be attracted towards venules. However, since there is no net force towards the para-venous CSF compartment, solutes might accumulate in the parenchyma.

The ISF-CSF communication is also a key regulatory mechanism. Nakata et al. [Nakada 2017] reviewed the water dynamics and the regulatory mechanisms of AQP-1 and AQP-4. In our model, we showed that a decrement in the permeability at the glial level decreases the amplitude of the CSF-ISF bidirectional flow, suggesting 1) an alteration of the mixing-diffusion properties of solutes and 2) a decrement in solutes uptake by para-venous spaces. This qualitatively agrees with the results shown by Iliff et al. [Iliff 2012], who showed a net reduction of CSF tracer influx into the parenchyma in AQP4-null compared to wild-type control mice.

The lack of the Monro-Kellie coupling leads to 1) a greatly reduced CSF flow dynamics in all compartments and 2) a greatly reduced bidirectional CSF-ISF movement. The lack of this cyclic water movement might affect the transport movement of solutes between the ISF compartment and both para-arterial and para-venous CSF spaces. Also, the absence of cyclic water movement might decrease the diffusion of solutes throughout the parenchyma. This suggests that the entrance of water from para-arterial and para-venous spaces and the ISF compartments strictly depends on

the intracranial blood entrance. Moreover, it suggests that impairments of the arterio-venous-CSF temporal dynamics might affect the glymphatic system by reducing bidirectional CSF-ISF exchange driven by the heart.

Osmotic and hydraulic pressures are key factors in the glymphatic mechanism. When we removed the Starling forces in the blood-ISF dynamics there were two main effects: 1) blocking of the continuous water movement from the arterial to the venous compartment and 2) the absence of a positive net water flow from the ISF to the CSF compartments. The bidirectional CSF-ISF movement was not greatly modified, suggesting that the diffusion capabilities of solutes driven by convection forces (advection and diffusion) are not modified and that injection of tracers in the CSF space with non-operating Starling forces can still penetrate in the parenchyma. However, the absence of the net CSF production from the ISF space might not lead solutes to be transported into the para-venous spaces but rather accumulate in the parenchyma. These results suggest that the Starling forces are fundamental in regulating the uptake of solutes from the parenchyma into the para-venous CSF spaces. Moreover, these results suggest that the bulk flow which leads solutes into the para-venous CSF space is the CSF production from the ISF compartment.

4.4.6 Impairment of intracranial venous outflow affects the glymphatic system

There have been several discussion on whether impairment of the intracranial vascular system can lead to accumulation of solutes in the brain [Di Marco 2015, Rivera-Rivera 2016, Simka 2015]. Our computational results, together with the hypothesized working principles of the glymphatic system, might explain the mechanisms by which solutes accumulate in the parenchyma when the intracranial vascular system is impaired. As shown in Fig. 4.15, the impairment of the venous outflow not only increases the intracranial pressure but also dramatically decreases the net motion of water from the ISF space into the CSF space. This comes from changes in the Starling forces at the capillary level, as the increased ISF pressure reduces the ISF production and leads to less CSF production from the ISF compartment. A reduction of the rate of CSF turnover might decrease the amyloid β clearance via arachnoid villi and lymphatics, as suggested by Simon et al. [Simon 2016]. More importantly, depending on the location of the venous stenosis (internal jugular veins, transverse sinus, torcula), only some portion of the parenchyma might suffer from alteration of Starling forces. Liu et al. [Liu 2014] concluded that a major fraction of patients with idiopathic Parkinson's disease appears to have abnormal venous anatomy on the left side of the brain and neck. Han et al. [Han 2015] observed that venous drainage obstruction of the transverse sinus, of the left brachiocephalic vein or of the bilateral internal jugular vein plays a significant role in the pathogenesis of transient global amnesia. Qualitatively, our results agree with these observations, suggesting that a local reduction of ISF production and CSF turnover caused by the increase in venous pressure might contribute to local accumulation of neurotoxins in the brain.

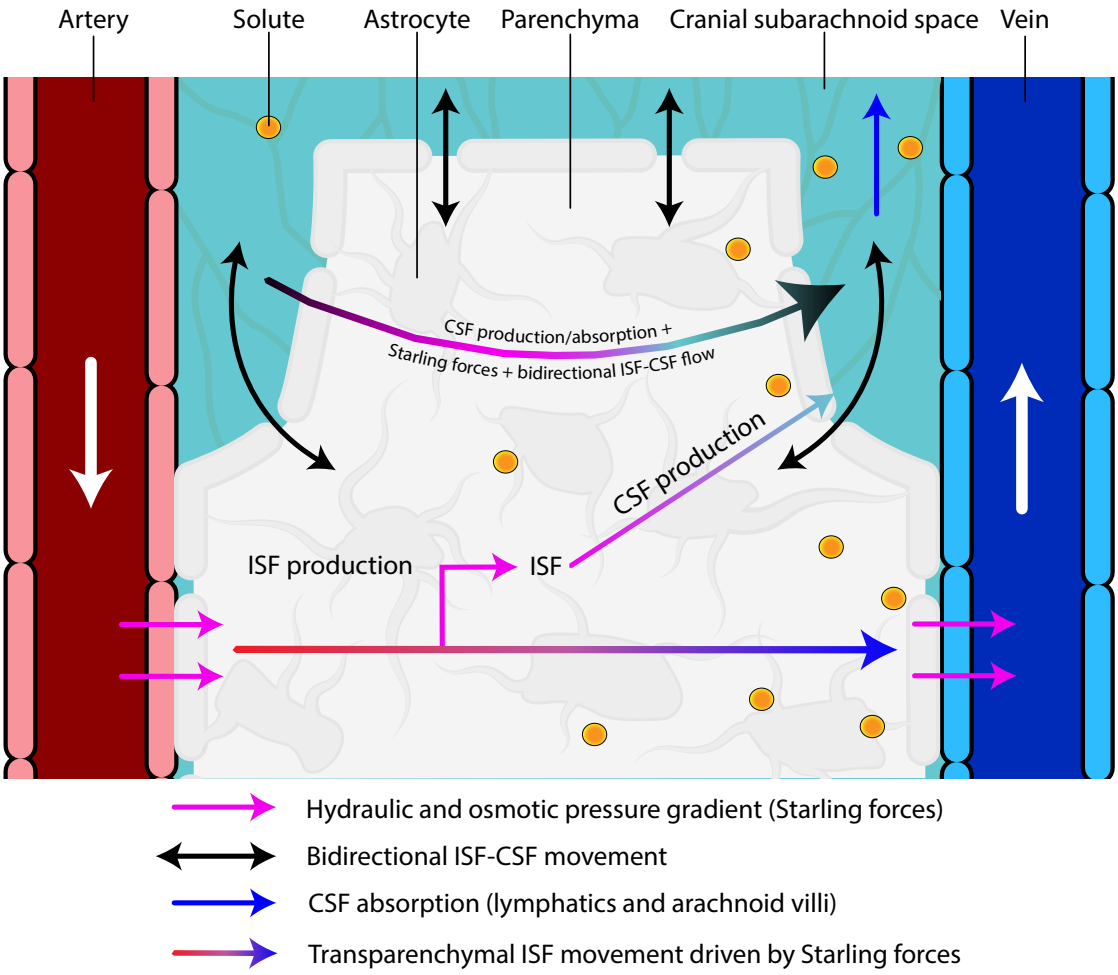

Figure 4.16: Schematic representation of our hypothesized working principles of the glymphatic system. Solutes are transported towards the venules by Starling forces. The imbalance between capillary production and venules absorption determines the net production of ISF. The net ISF movement into the CSF system transports solutes into the para-venous CSF spaces during the cardiac cycle. The cardiac contraction induces a trans-parenchymal and bidirectional CSF-ISF movement which helps solutes to diffuse in the brain tissue. The CSF absorption by lymphatics and through arachnoid villi contributes to the clearance of solutes by creating a low-pressure sink.

4.5 Conclusions

The mathematical model presented here represents to the authors' knowledge the first holistic, multi-scale mathematical model of the murine fluid systems, and includes: heart dynamics, major arteries and veins, microcirculation, pulmonary circulation, venous valves, CSF, brain interstitial fluid, intracranial Starling forces, Starling resistors, Monro-Kellie coupling, brain lymphatic drainage. Based on the recent works of Linninger et al. [Linninger 2017], Starling forces governed the Blood-ISF-CSF fluid exchange in the blood-brain barrier (Blood-ISF) and choroid plexus (Blood-CSF). Our computational results are validated against MR-flow measurements, literature values, and *in-vivo* pressure measurements acquired in healthy mice and in mice with impairment of the intracranial venous outflow.

Our computational results show that during the cardiac cycle there is an intraparenchymal bidirectional CSF-ISF movement which potentially helps to avoid localizations of stagnant water inside the brain. Based on the computational results, we propose that glymphatic system results from the following dynamics: 1) intraparenchymal bidirectional ISF-CSF movement induced by the Monro-Kellie hypothesis, 2) CSF drainage into the venous and lymphatic systems, 3) intracranial Starling forces. We also show that cerebral venous outflow decreases the ISF production and CSF turnover, potentially decreasing the brain-waste clearance and leading to accumulation of neurotoxins in the parenchyma.

Although our hypothesis has to be demonstrated through experimental measurements, it provides a possible explanation of the working principles of the glymphatic system and the mechanisms by which neurotoxins and waste products are removed. Also, it provides insights into the possible link between vascular and CSF pathologies with brain-waste clearance of parenchyma, help understanding the onset of neurological disorders [Louveau 2015, Bezerra 2018, Dissing-Olesen 2015, Tarasoff-Conway 2015, Zamboni 2015, Raper 2016, Engelhardt 2016] and possibly suggests new therapeutic treatments for enhancing the removal of macromolecules in the central nervous system [Louveau 2016].

4.6 Limitations and future development

Our mathematical model has several limitations. Some of the adopted computational parameters are based on allometric scaling and should be considered with caution. However, the validation of our computational results against *in-vivo* MR-flow measurements, intracranial pressures measurements and literature values gave us a degree of confidence on both output of the mathematical model and estimations of the computational parameters. We did not implement autoregulation, a key component of peripheral resistance and cerebral perfusion. Also, we did not take into account the viscoelastic behaviour of arteries and veins, which is known to greatly affect pressure waves [Matthys 2007a]. To the authors' knowledge, there are no available estimations of compliance and volume of intracranial lymphatic compartments. We estimated these values based on those of intracranial capillaries. Also, we assumed that CSF is mostly absorbed through arachnoid villi, and only a small percentage of it is absorbed by lymphatics ($\approx 15\%$). This was motivated by the experimental observation that brain lymphatics seem to regulate the solute homeostasis, rather than CSF volume, though some experimental observations have shown that obstruction of nasal

lymphatics might increase the intracranial pressure [Zawieja 2008, Mollanji 2002]. Classically, the brain is thought as a sponge [Linninger 2016]. To the authors' knowledge, there are no experimental measurements of the amount of CSF-ISF exchange during the cardiac cycle. Therefore, our results are more relevant to qualitatively understand the interactive dynamics of fluids, while the values of our computational results should be considered with caution. We did not model the transport of solutes in our model and consequently, oncotic pressures were assumed to be constant. Also, we assumed the *Bulat-Klarica-Orešković* hypothesis and supposed that both hydrostatic and oncotic pressure forces drive ISF production. This hypothesis has not yet been experimentally verified [Miyajima 2015]. Ultimately, our hypothesized working principles of the glymphatic system are based on water movement, which provides indications of the transport of solutes.

Chapter 5

Conclusions

5.1 Achievements

5.1.1 Insights into the glymphatic system and murine fluid dynamics

The mathematical model presented in this thesis represents, to the author's knowledge, the first multi-scale, closed-loop mathematical description of the main murine extracellular fluid systems. It includes: heart dynamics, arterial and venous circulation, microcirculation, pulmonary circulation, brain interstitial fluid (ISF), Starling resistors, venous valves and cerebrospinal fluid (CSF). We also incorporated the hypothesis of *Bulat-Klarica-Orešković* which states that blood-CSF and blood-ISF dynamics are regulated by Starling forces. Moreover, intracranial fluids are tightly coupled by a *relaxed* version of the Monro-Kellie hypothesis, which originally states that the sum of all fluid volumes in the cranial cavity is constant.

Our mathematical model represents a step forward in the understanding of brain fluid dynamics. Thanks to the capabilities of mathematical modelling, we have simulated healthy and pathological scenarios to understand the interactions of intracranial fluids and the consequences of abnormalities in a fluid compartment into the remaining compartments. Our computational results suggest that the glymphatic system depends on 1) a continuous bidirectional CSF-ISF movement induced by the Monro-Kellie hypothesis, 2) intraparenchymal Starling forces and 3) CSF turnover, which depends on both venous and lymphatic drainage. Although our hypothesis has to be experimentally demonstrated, it widens the understanding of brain fluid interactions, coupling arteries, veins, CSF, ISF, lymphatic drainage and heart pumping. Based on our hypothesis, intracranial vascular pathologies are closely coupled to neurological disorders. We show that impairment of cerebral venous drainage decreases the ISF production and CSF turnover, potentially decreasing the clearance of brain waste and leading to accumulation of neurotoxins in the parenchyma. Further studies are required in order to understand the intracranial ISF/CSF dynamics in both healthy and pathological situations.

5.1.2 Towards a multi-scale mathematical model for the human lymphatic system

Although a number of pathologies are known to be associated with malfunction of the lymphatic system, there is a considerable disparity in the understanding of the mechanisms that regulate the

lymphatic system compared to those of the cardiovascular system. Compared to arteries and veins, one of the driving forces that pushes lymph towards the venous system is the active contraction of lymphangions. Experimental observations have shown that occurrence of lymphatic contractions depends strongly on local fluid dynamics. One achievement of this thesis is the development of a mathematical model for collecting lymphatics in a one-dimensional framework coupled to a novel model for lymphatic contractions, which provides each lymphangion with the autonomous capability to trigger action potentials based on the local fluid-dynamical factors. This represents a desirable feature that a mathematical model for networks of collecting lymphatics should incorporate. In the longer term, our mathematical model could provide the basis for a more general holistic, multi-scale closed-loop mathematical model which includes networks of arteries, veins, lymphatics, lymph nodes and other relevant fluid districts.

5.1.3 High-order methods for networks of one-dimensional subdomains

High-order numerical methods are a fundamental tool for long-time evolution simulations because of their outstanding dissipation and dispersion properties and because they are more efficient compared to low-order methods when small errors are aimed for. One achievement of this thesis was the design a new implicit solver for the Junction-Generalized Riemann Problem (J-GRP), which is based on a recently proposed implicit method for solving the generalized Riemann problem for systems of hyperbolic balance laws. We use the new J-GRP solver to construct an ADER scheme that is globally explicit, locally implicit and with no theoretical accuracy barrier, in both space and time. The resulting ADER scheme is able to deal with stiff source terms and can be applied to non-linear systems of hyperbolic balance laws in domains consisting of networks of one-dimensional sub-domains. An application to a physical test problem consisting of a network of 37 compliant silicon tubes (arteries) and 21 junctions, reveals that in addition to high order in the interior of the one-dimensional subdomains, it is imperative to use high-order methods at junctions, in order to preserve the desired high order of accuracy in the full computational domain.

5.2 Future work

Mathematical models are a fundamental tool to understand the mechanisms and interactive dynamics of the body fluid systems. Our mathematical model of the murine extracellular fluid system was mainly used as a predictive tool to understand 1) the interaction of cardiac dynamics and cerebral fluids, 2) the effect of impairment of cerebral venous outflow on brain fluid dynamics. However, in principle, our mathematical framework could also be used to study pathologies of the central nervous system and the effect of treatment of the pathologies. For instance, one could employ our modelling framework to investigate CSF flow and pressure in hydrocephalus and analyse the effect of lumboperitoneal or ventriculoatrial shunt placements. Also, one could understand the effect of heart malfunctions in the dynamics of intracranial fluids.

There is a number of possible improvements that would significantly contribute to the mathematical framework of the murine extracellular fluid systems presented in this thesis. One of the primary goals of the vascular system is to provide nutrients, oxygen, carbon dioxide and blood cells to the body. A great improvement would be the incorporation of a model for the transport system in

a multi-scale framework. Other possible improvements include: autoregulation, baroreflex control of heart rate, a mathematical model for the spinal canal, spinal cord, spinal subarachnoid space and spinal microcirculation, a complete model of the lymphatic system and peripheral interstitial fluid and a respiratory model.

Bibliography

[Absinta 2017] Absinta M., Ha S. K., Nair G., Sati P., Luciano N. J., Palisoc M., Louveau A., Zaghloul K. A., Pittaluga S., Kipnis J. and Reich D. S. *Human and nonhuman primate meninges harbor lymphatic vessels that can be visualized noninvasively by MRI*. eLife, Vol. 6, oct 2017.

[Agarwal 2018] Agarwal N., Contarino C., Limbucci N., Bertazzi L. and Toro E. F. *Intracranial fluid dynamics changes in idiopathic intracranial hypertension: Pre and post therapy*. bioRxiv, page 245894, 2018.

[Alastruey 2006] Alastruey J. *Numerical modelling of pulse wave propagation in the cardiovascular system: Development, validation and clinical applications*. PhD thesis, University of London, 2006.

[Alastruey 2008] Alastruey J., Parker K. H., Pei O J. and Sherwin S. J. *Lumped Parameter Outflow Models for 1 - D Blood Flow Simulations : Effect on Pulse Waves and Parameter Estimation*. Communications in Computational Physics, Vol. 4, No. 4, pages 317–336, 2008.

[Alpini 2013] Alpini D. C., Bavera P. M., Di Berardino F., Barozzi S. and Cesarani A. *Bilateral sudden sensorineural hearing loss and chronic venous cerebrospinal insufficiency: A case report*. Phlebology, Vol. 28, No. 5, pages 231–233, 2013.

[Ambarki 2007] Ambarki K., Baledent O., Kongolo G., Bouzerar R., Fall S. and Meyer M. E. *A new lumped-parameter model of cerebrospinal hydrodynamics during the cardiac cycle in healthy volunteers*. IEEE Transactions on Biomedical Engineering, Vol. 54, No. 3, pages 483–491, mar 2007.

[Asgari 2016] Asgari M., De Zélicourt D. and Kurtcuoglu V. *Glymphatic solute transport does not require bulk flow*. Scientific Reports, Vol. 6, No. 1, dec 2016.

[Aslanidou 2015] Aslanidou L., Trachet B., Reymond P., Fraga-Silva R. A., Segers P. and Stergiopulos N. *A 1D model of the arterial circulation in mice*. ALTEX, Vol. 33, No. 1, pages 13–28, 2015.

[Baish 2016] Baish J. W., Kunert C., Padera T. and Munn L. *Synchronization and random triggering of lymphatic vessel contractions*. PLoS Computational Biology, Vol. 12, No. 12, page e1005231, dec 2016.

[Bales 2009] Bales P., Kolb O. and Lang J. *Hierarchical modelling and model adaptivity for gas flow on networks*. In International Conference on Computational Science, pages 337–346. Springer, Berlin, Heidelberg, 2009.

[Banda 2006] Banda M., Herty M. and Klar A. *Coupling conditions for gas networks governed by the isothermal Euler equations*. Networks and Heterogeneous Media, Vol. 1, No. 2, pages 295–314, mar 2006.

[Barakat 1997] Barakat A., Marini R. and Colton C. *Measurement of flow rates through aortic branches in the anesthetized rabbit.* Laboratory Animal Science, Vol. 47, No. 2, pages 184–9, 1997.

[Barten 2017] Barten D. M., Cadelina G. W. and Weed M. R. *Dosing, collection, and quality control issues in cerebrospinal fluid research using animal models*. In Handbook of Clinical Neurology, volume 146, pages 3–20. Elsevier, 2017.

[Bateman 2008] Bateman G. A. *Arterial inflow and venous outflow in idiopathic intracranial hypertension associated with venous outflow stenoses*. Journal of Clinical Neuroscience, Vol. 15, No. 4, pages 402–408, apr 2008.

[Bazigou 2013] Bazigou E. and Makinen T. *Flow control in our vessels: Vascular valves make sure there is no way back*. Cellular and Molecular Life Sciences, Vol. 70, No. 6, pages 1055–1066, aug 2013.

[Beggs 2013] Beggs C. B. *Venous hemodynamics in neurological disorders: An analytical review with hydrodynamic analysis*. BMC Medicine, Vol. 11, No. 1, 2013.

[Bertram 2011] Bertram C. D., Macaskill C. and Moore J. E. *Simulation of a chain of collapsible contracting lymphangions with progressive valve closure*. Journal of Biomechanical Engineering, Vol. 133, No. 1, page 011008, 2011.

[Bertram 2014a] Bertram C. D., Macaskill C., Davis M. J. and Moore J. E. *Development of a model of a multi-lymphangion lymphatic vessel incorporating realistic and measured parameter values*. Biomechanics and Modeling in Mechanobiology, Vol. 13, No. 2, pages 401–416, jun 2014.

[Bertram 2014b] Bertram C. D., Macaskill C. and Moore J. E. *Incorporating measured valve properties into a numerical model of a lymphatic vessel*. Computer Methods in Biomechanics and Biomedical Engineering, Vol. 17, No. 14, pages 1519–1534, 2014.

[Bertram 2016a] Bertram C. D., Macaskill C., Davis M. J. and Moore J. E. *Consequences of intravascular lymphatic valve properties: A study of contraction timing in a multi-lymphangion model*. American Journal of Physiology - Heart and Circulatory Physiology, Vol. 310, No. 7, page ajpheart.00669.2015, jan 2016.

[Bertram 2016b] Bertram C. D., Macaskill C. and Moore J. E. *Pump function curve shape for a model lymphatic vessel*. Medical Engineering and Physics, Vol. 38, No. 7, pages 656–663, jul 2016.

[Bertram 2017] Bertram C. D., Macaskill C., Davis M. J. and Moore J. E. *Valve-related modes of pump failure in collecting lymphatics: Numerical and experimental investigation*. Biomechanics and Modeling in Mechanobiology, Vol. 16, No. 6, pages 1987–2003, jul 2017.

[Bezerra 2018] Bezerra M. L. d. S., Ferreira A. C. A. d. F. and Oliveira-Souza d. R. *Pseudotumor cerebri and glymphatic dysfunction*. Frontiers in Neurology, Vol. 8, jan 2018.

[Blanco 2014] Blanco P. J., Watanabe S. M., Dari E. A., Passos M. A. R. F. and Feijóo R. A. *Blood flow distribution in an anatomically detailed arterial network model: Criteria and algorithms*. Biomechanics and Modeling in Mechanobiology, Vol. 13, No. 6, pages 1303–1330, 2014.

[Blanco 2015] Blanco P. J., Watanabe S. M., Passos M. A. R. F., Lemos P. A. and Feijóo R. A. *The ADAN model: An anatomically detailed arterial network model for hemodynamics simulations*. IEEE Transactions on Biomedical Engineering, Vol. 62, No. 2, pages 736–753, feb 2015.

[Borsche 2014a] Borsche R. and Kall J. *ADER schemes and high order coupling on networks of hyperbolic conservation laws*. Journal of Computational Physics, Vol. 273, pages 658–670, 2014.

[Borsche 2014b] Borsche R. and Klar A. *Flooding in urban drainage systems: Coupling hyperbolic conservation laws for sewer systems and surface flow*. International Journal for Numerical Methods in Fluids, Vol. 76, No. 11, pages 789–810, 2014.

[Borsche 2014c] Borsche R., Klar A., Kühn S. and Meurer A. *Coupling traffic flow networks to pedestrian motion*. Mathematical Models and Methods in Applied Sciences, Vol. 24, No. 2, pages 359–380, feb 2014.

[Borsche 2016] Borsche R. and Kall J. *High order numerical methods for networks of hyperbolic conservation laws coupled with ODEs and lumped parameter models*. Journal of Computational Physics, Vol. 327, pages 678–699, dec 2016.

[Breslin 2014] Breslin J. W. *Mechanical forces and lymphatic transport*. Microvascular Research, Vol. 96, pages 46–54, nov 2014.

[Bressan 2014] Bressan A., Čanić S., Garavello M., Herty M. and Piccoli B. *Flows on networks: Recent results and perspectives*. EMS Surveys in Mathematical Sciences, Vol. 1, No. 1, pages 47–111, 2014.

[Bretti 2007] Bretti G., Natalini R. and Piccoli B. *Numerical algorithms for simulations of a traffic model on road networks*. Journal of Computational and Applied Mathematics, Vol. 210, No. 1-2, pages 71–77, dec 2007.

[Brinker 2014] Brinker T., Stopa E., Morrison J. and Kinge P. *A new look at cerebrospinal fluid circulation*. Fluids and Barriers of the CNS, Vol. 11, No. 1, page 10, 2014.

[Brook 1999] Brook B., Falle S. and Pedley T. J. *Numerical solutions for unsteady gravity-driven flows in collapsible tubes: Evolution and roll-wave instability of a steady state*. Journal of Fluid Mechanics, Vol. 396, page S0022112099006084, 1999.

[Brouwer 2011] Brouwer J., Gasser I. and Herty M. *Gas pipeline models revisited: Model hierarchies, nonisothermal models, and simulations of networks*. Multiscale Modeling & Simulation, Vol. 9, No. 2, pages 601–623, apr 2011.

[Bruno 2014] Bruno A., Califano L., Mastrangelo D., De Vizia M., Bernardo B. and Salafia F. *Chronic cerebrospinal venous insufficiency in Ménière's disease: Diagnosis and treatment*. Veins and Lymphatics, Vol. 3, No. 3, dec 2014.

[Carare 2008] Carare R. O., Bernardes-Silva M., Newman T. A., Page A. M., Nicoll J. A. R., Perry V. H. and Weller R. O. *Solutes, but not cells, drain from the brain parenchyma along basement membranes of capillaries and arteries: Significance for cerebral amyloid angiopathy and neuroimmunology*. Neuropathology and Applied Neurobiology, Vol. 34, No. 2, pages 131–144, apr 2008.

[Castro 2008] Castro C. E. and Toro E. F. *Solvers for the high-order Riemann problem for hyperbolic balance laws*. Journal of Computational Physics, Vol. 227, No. 4, pages 2481–2513, 2008.

[Caulk 2015] Caulk A. W., Nepiyushchikh Z. V., Shaw R., Dixon J. B. and Gleason R. L. *Quantification of the passive and active biaxial mechanical behaviour and microstructural organization of rat thoracic ducts*. Journal of The Royal Society Interface, Vol. 12, No. 108, page 20150280, jun 2015.

[Caulk 2016] Caulk A. W., Dixon J. B. and Gleason R. L. *A lumped parameter model of mechanically mediated acute and long-term adaptations of contractility and geometry in lymphatics for characterization of lymphedema*. Biomechanics and Modeling in Mechanobiology, Vol. 15, No. 6, pages 1601–1618, apr 2016.

[Chou 2014] Chou D., Vardakis J. C. and Ventikos Y. *Multiscale modelling for cerebrospinal fluid dynamics: Multicompartmental poroelacticity and the role of AQP4*. Journal of Biosciences and Medicines, Vol. 02, pages 1–9, 2014.

[Chou 2016] Chou D., Vardakis J. C., Guo L., Tully B. J. and Ventikos Y. *A fully dynamic multi-compartmental poroelastic system: Application to aqueductal stenosis*. Journal of Biomechanics, Vol. 49, No. 11, pages 2306–2312, jul 2016.

[Chuang 2011] Chuang N., Mori S., Yamamoto A., Jiang H., Ye X., Xu X., Richards L. J., Nathans J., Miller M. I., Toga A. W., Sidman R. L. and Zhang J. *An MRI-based atlas and database of the developing mouse brain*. NeuroImage, Vol. 54, No. 1, pages 80–89, jan 2011.

[Cingolani 2011] Cingolani O. H. and Kass D. A. *Pressure-volume relation analysis of mouse ventricular function*. American Journal of Physiology - Heart and Circulatory Physiology, Vol. 301, No. 6, pages H2198–H2206, dec 2011.

[Coclite 2002] Coclite G. M. and Piccoli B. *Traffic flow on a road network*. SIAM Journal on Mathematical Analysis, Vol. 36, No. 6, pages 1862–1886, jan 2002.

[Colli Franzone 2014] Colli Franzone P., Pavarino L. F. and Scacchi S. Mathematical Cardiac Electrophysiology, volume 13. Springer International Publishing, 2014.

[Colombo 2008a] Colombo R. M. and Garavello M. *On the Cauchy problem for the p -system at a junction*. SIAM Journal of Mathematical Analysis, Vol. 39, No. 5, pages 1456–1471, 2008.

[Colombo 2008b] Colombo R. M., Herty M. and Sachers V. *On 2x2 conservation laws at a junction*. SIAM Journal on Mathematical Analysis, Vol. 40, No. 2, pages 605–622, 2008.

[Contarino 2016] Contarino C., Toro E. F., Montecinos G. I., Borsche R. and Kall J. *Junction-generalized Riemann problem for stiff hyperbolic balance laws in networks: An implicit solver and ADER schemes*. Journal of Computational Physics, Vol. 315, pages 409–433, jun 2016.

[Cooper 2016] Cooper L. J., Heppell J. P., Clough G. F., Ganapathisubramani B. and Roose T. *An image-based model of fluid flow through lymph nodes*. Bulletin of Mathematical Biology, Vol. 78, No. 1, pages 52–71, dec 2016.

[Cristini 2014] Cristini M. *Mathematical study of cerebral haemodynamics associated to malfunction of valves in internal jugular veins*. Master Thesis, Department of Mathematics, University of Trento, Italy, 2014.

[Cserr 1988] Cserr H. F. *Role of secretion and bulk flow of brain interstitial fluid in brain volume regulation.* Annals of the New York Academy of Sciences, Vol. 529, No. 1 Fourth Colloq, pages 9–20, jun 1988.

[Cuomo 2015] Cuomo F., Ferruzzi J., Humphrey J. D. and Figueroa C. A. *An experimental–computational study of catheter induced alterations in pulse wave velocity in anesthetized mice*. Annals of Biomedical Engineering, Vol. 43, No. 7, pages 1555–1570, feb 2015.

[Davis 2011] Davis M. J., Rahbar E., Gashev A. A., Zawieja D. C. and Moore J. E. *Determinants of valve gating in collecting lymphatic vessels from rat mesentery*. American Journal of Physiology - Heart and Circulatory Physiology, Vol. 301, No. 1, pages H48–H60, apr 2011.

[Davis 2012] Davis M. J., Scallan J. P., Wolpers J. H., Muthuchamy M., Gashev A. A. and Zawieja D. C. *Intrinsic increase in lymphangion muscle contractility in response to elevated afterload*. American Journal of Physiology - Heart and Circulatory Physiology, Vol. 303, No. 7, pages H795–H808, aug 2012.

[Davis 2016] Davis M. J. *Is nitric oxide important for the diastolic phase of the lymphatic contraction/relaxation cycle?* Proceedings of the National Academy of Sciences, Vol. 113, No. 2, pages E105–E105, dec 2016.

[Dawson 2001] Dawson T. *Similitude in the cardiovascular system of mammals.* Journal of Experimental Biology, Vol. 204, No. 3, pages 395–407, 2001.

[Dawson 2005] Dawson T. *Modeling of vascular networks*. Journal of Experimental Biology, Vol. 208, No. 9, pages 1687–1694, may 2005.

[Dawson 2014] Dawson T. *Allometric relations and scaling laws for the cardiovascular system of mammals*. Systems, Vol. 2, No. 2, pages 168–185, apr 2014.

[Di Marco 2015] Di Marco L. Y., Farkas E., Martin C., Venneri A. and Frangi A. F. *Is vasomotion in cerebral arteries impaired in Alzheimer's disease?* Journal of Alzheimer's Disease, Vol. 46, No. 1, pages 35–53, 2015.

[Dissing-Olesen 2015] Dissing-Olesen L., Hong S. and Stevens B. *New brain lymphatic vessels drain old concepts*. EBioMedicine, Vol. 2, No. 8, pages 776–777, aug 2015.

[Dorr 2008] Dorr A. E., Lerch J. P., Spring S., Kabani N. and Henkelman R. M. *High resolution three-dimensional brain atlas using an average magnetic resonance image of 40 adult C57Bl / 6J mice*. NeuroImage, Vol. 42, No. 1, pages 60–69, aug 2008.

[Dumbser 2007a] Dumbser M. and Käser M. *Arbitrary high order non-oscillatory finite volume schemes on unstructured meshes for linear hyperbolic systems*. Journal of Computational Physics, Vol. 221, No. 2, pages 693–723, feb 2007.

[Dumbser 2007b] Dumbser M., Käser M. and Toro E. F. *An arbitrary high-order discontinuous Galerkin method for elastic waves on unstructured meshes - V. Local time stepping and p-adaptivity*. Geophysical Journal International, Vol. 171, No. 2, pages 695–717, nov 2007.

[Dumbser 2008] Dumbser M., Enaux C. and Toro E. F. *Finite volume schemes of very high order of accuracy for stiff hyperbolic balance laws*. Journal of Computational Physics, Vol. 227, No. 8, pages 3971–4001, 2008.

[Dumbser 2014] Dumbser M. *Arbitrary-Lagrangian-Eulerian ADER-WENO finite volume schemes with time-accurate local time stepping for hyperbolic conservation laws*. Computer Methods in Applied Mechanics and Engineering, Vol. 280, pages 57–83, oct 2014.

[Elad 1991] Elad D., Katz D., Kimmel E. and Einav S. *Numerical schemes for unsteady fluid-flow through collapsible tubes*. Journal of Biomedical Engineering, Vol. 13, No. 1, pages 10–18, 1991.

[Engelhardt 2016] Engelhardt B., Carare R. O., Bechmann I., Flügel A., Laman J. D. and Weller R. O. *Vascular, glial, and lymphatic immune gateways of the central nervous system*. Acta Neuropathologica, Vol. 132, No. 3, pages 317–338, aug 2016.

[Farb 2003] Farb R. I., Vanek I., Scott J. N., Mikulis D. J., Willinsky R. A., Tomlinson G. and TerBrugge K. G. *Idiopathic intracranial hypertension: The prevalence and morphology of sinovenous stenosis*. Neurology, Vol. 60, No. 9, pages 1418–1424, may 2003.

[Feintuch 2006] Feintuch A., Ruengsakulrach P., Lin A., Zhang J., Zhou Y.-Q., Bishop J., Davidson L., Courtman D., Foster F. S., Steinman D. A., Henkelman R. M. and Ethier C. R. *Hemodynamics in the mouse aortic arch as assessed by MRI, ultrasound, and numerical modeling*. American Journal of Physiology - Heart and Circulatory Physiology, Vol. 292, No. 2, pages H884–H892, feb 2006.

[Formaggia 1999] Formaggia L., Nobile F., Quarteroni A. and Veneziani A. *Multiscale modelling of the circulatory system: a preliminary analysis*. Computing and Visualization in Science, Vol. 2, No. 2-3, pages 75–83, 1999.

[Formaggia 2001] Formaggia L., Gerbeau J. F., Nobile F. and Quarteroni A. *On the coupling of 3D and 1D Navier-Stokes equations for flow problems in compliant vessels*. Computer Methods in Applied Mechanics and Engineering, Vol. 191, No. 6-7, pages 561–582, dec 2001.

[Formaggia 2009] Formaggia L., Quarteroni A. and Veneziani A. Cardiovascular mathematics: modeling and simulation of the circulatory system. Springer, 2009.

[Fullana 2009] Fullana J. M. and Zaleski S. *A branched one-dimensional model of vessel networks*. Journal of Fluid Mechanics, Vol. 621, pages 183–204, feb 2009.

[Gadda 2015] Gadda G., Taibi A., Sisini F., Gambaccini M., Zamboni P. and Ursino M. *A new hemodynamic model for the study of cerebral venous outflow*. American Journal of Physiology - Heart and Circulatory Physiology, Vol. 308, No. 3, pages H217–H231, 2015.

[Gajani 2015] Gajani G. S., Boschetti F., Negrini D., Martellaccio R., Milanese G., Bizzarri F. and Brambilla A. *A lumped model of lymphatic systems suitable for large scale simulations*. In

2015 European Conference on Circuit Theory and Design, ECCTD 2015. Institute of Electrical & Electronics Engineers (IEEE), aug 2015.

[Garavello 2006] Garavello M. and Colombo R. M. *A well posed Riemann problem for the p–system at a junction*. Networks and Heterogeneous Media, Vol. 1, No. 3, pages 495–511, 2006.

[Gashev 2002] Gashev A. A., Davis M. J. and Zawieja D. C. *Inhibition of the active lymph pump by flow in rat mesenteric lymphatics and thoracic duct*. Journal of Physiology, Vol. 540, No. 3, pages 1023–1037, may 2002.

[Gashev 2004] Gashev A. A., Davis M. J., Delp M. D. and Zawieja D. C. *Regional variations of contractile activity in isolated rat lymphatics*. Microcirculation, Vol. 11, No. 6, pages 477–492, jan 2004.

[Gehlen 2017] Gehlen M., Kurtcuoglu V. and Schmid Daners M. *Is posture-related craniospinal compliance shift caused by jugular vein collapse? A theoretical analysis*. Fluids and Barriers of the CNS, Vol. 14, No. 1, feb 2017.

[Goetz 2013] Goetz C. R. and Iske A. *Approximate solutions of generalized Riemann problems for nonlinear systems of hyperbolic conservation laws*. Mathematics of Computation, Vol. 85, No. 297, pages 1–22, may 2013.

[Guo 2018] Guo L., Vardakis J. C., Lassila T., Mitolo M., Ravikumar N., Chou D., Lange M., Sarrami-Foroushani A., Tully B. J., Taylor Z., Varma S., Venneri A., Frangi A. and Ventikos Y. *Subject-specific multi-poroelastic model for exploring the risk factors associated with the early stages of Alzheimer's disease*. Interface Focus, Vol. 8, No. 1, page 20170019, 2018.

[Han 2014] Han E. E., Warnecke G. and Toro E. F. *On Riemann solutions to weakly hyperbolic systems: part 1. modelling subcritical flows in arteries*. SIAM Journal of Mathematical Analysis, 2014.

[Han 2015] Han K., Chao A. C., Chang F. C., Chung C. P., Hsu H. Y., Sheng W. Y., Wu J. and Hu H. H. *Obstruction of venous drainage linked to transient global amnesia*. PLoS ONE, Vol. 10, No. 7, page e0132893, jul 2015.

[Harten 1983] Harten A., Lax P. D. and Leer B.van . *On upstream differencing and Godunov-type schemes for hyperbolic conservation laws*. SIAM Review, Vol. 25, No. 1, pages 35–61, jan 1983.

[Harten 1987] Harten A., Engquist B., Osher S. J. and Chakravarthy S. R. *Uniformly high order accurate essentially non-oscillatory schemes, III*. Journal of Computational Physics, Vol. 71, No. 2, pages 231–303, 1987.

[Herrick 2008] Herrick A. *Diagnosis and management of scleroderma peripheral vascular disease*. Rheumatic Disease Clinics North America., Vol. 34, No. 1, pages 89–114, sep 2008.

[Hodgkin 1952] Hodgkin a. L. and Huxley a. F. *A quantitative description of membrane current and its application to conduction and excitation in nerve*. Journal of Physiology, Vol. 117, No. 4, pages 500–544, aug 1952.

[Holt 1981] Holt J. P., Rhode E. A., Holt W. W. and Kines H. *Geometric similarity of aorta, venae cavae, and certain of their branches in mammals.* American Journal of Physiology, Vol. 241, No. 1, pages R100–4, jul 1981.

[Hong 2011] Hong S. W. and Kim C. *A new finite volume method on junction coupling and boundary treatment for flow network system analyses.* International Journal for Numerical Methods in Fluids, Vol. 65, No. 6, pages 707–742, jan 2011.

[Iliff 2012] Iliff J. J., Wang M., Liao Y., Plog B. A., Peng W., Gundersen G. A., Benveniste H., Vates G. E., Deane R., Goldman S. A., Nagelhus E. A. and Nedergaard M. *A paravascular pathway facilitates CSF flow through the brain parenchyma and the clearance of interstitial solutes, including amyloid β.* Science Translational Medicine, Vol. 4, No. 147, page 147ra111, aug 2012.

[Iliff 2013] Iliff J. J., Wang M., Zeppenfeld D. M., Venkataraman A., Plog B. A., Liao Y., Deane R. and Nedergaard M. *Cerebral arterial pulsation drives paravascular CSF-interstitial fluid exchange in the murine brain.* Journal of Neuroscience, Vol. 33, No. 46, pages 18190–18199, nov 2013.

[Iliff 2014] Iliff J. J., Chen M. J., Plog B. A., Zeppenfeld D. M., Soltero M., Yang L., Singh I., Deane R. and Nedergaard M. *Impairment of glymphatic pathway function promotes tau pathology after traumatic brain injury.* Journal of Neuroscience, Vol. 34, No. 49, pages 16180–16193, dec 2014.

[Jacobson 1982] Jacobson E. D. *Physiology of the mesenteric circulation.* The Physiologist, Vol. 25, No. 5, pages 439–43, 1982.

[Jafarnejad 2015] Jafarnejad M., Woodruff M. C., Zawieja D. C., Carroll M. C. and Moore J. E. *Modeling lymph flow and fluid exchange with blood vessels in lymph nodes.* Lymphatic Research and Biology, Vol. 13, No. 4, pages 234–247, dec 2015.

[Jamalian 2016] Jamalian S., Davis M. J., Zawieja D. C. and Moore J. E. *Network scale modeling of lymph transport and its effective pumping parameters.* PLoS ONE, Vol. 11, No. 2, page e0148384, feb 2016.

[Jamalian 2017] Jamalian S., Jafarnejad M., Zawieja D. C., Bertram C. D., Gashev A. A., Davis M. J. and Moore J. E. *Demonstration and analysis of the suction effect for pumping lymph from tissue beds at subatmospheric pressure.* Scientific Reports, Vol. 7, No. 1, sep 2017.

[Janiczek 2011] Janiczek R. L., Blackman B. R., Roy R. J., Meyer C. H., Acton S. T. and Epstein F. H. *Three-dimensional phase contrast angiography of the mouse aortic arch using spiral MRI.* Magnetic Resonance in Medicine, Vol. 66, No. 5, pages 1382–1390, nov 2011.

[Jessen 2015] Jessen N. A., Munk A. S. F., Lundgaard I. and Nedergaard M. *The glymphatic system: A beginner's guide.* Springer, Vol. 40, No. 12, pages 2583–2599, may 2015.

[Kelly 2016] Kelly E. J. and Yamada S. *Cerebrospinal fluid flow studies and recent advancements.* Seminars in Ultrasound, CT and MRI, Vol. 37, No. 2, pages 92–99, apr 2016.

[Kesserwani 2008] Kesserwani G., Ghostine R., Vazquez J., Mosé R., Abdallah M. and Ghenaim A. *Simulation of subcritical flow at open-channel junction*. Advances in Water Resources, Vol. 31, No. 2, pages 287–297, feb 2008.

[Kim 2007] Kim J., Thacker N. A., Bromiley P. A. and Jackson A. *Prediction of the jugular venous waveform using a model of CSF dynamics*. American Journal of Neuroradiology, Vol. 28, No. 5, pages 983–9, may 2007.

[Kinmonth 1954] Kinmonth J. B. and Taylor G. W. *The lymphatic circulation in lymphedema*. Annals of Surgery, Vol. 139, No. 2, pages 129–136, feb 1954.

[Klingensmith 2008] Klingensmith M. E. The Washington manual of surgery. Wolters Kluwer Health/Lippincott Williams & Wilkins, 2008.

[Kotsikoris 2013] Kotsikoris I., Zygomalas A., Papoutsi S., Maras D., Pavlidis P., Papas T. and Bessias N. *Debating chronic cerebrospinal venous insufficiency in patients with multiple sclerosis*. Hellenic Journal of Surgery, Vol. 85, No. 3, pages 153–159, may 2013.

[Kovačević 2005] Kovačević N., Henderson J. T., Chan E., Lifshitz N., Bishop J., Evans A. C., Henkelman R. M. and Chen X. J. *A three-dimensional MRI atlas of the mouse brain with estimates of the average and variability*. Cerebral Cortex, Vol. 15, No. 5, pages 639–645, sep 2005.

[Kunert 2015] Kunert C., Baish J. W., Liao S., Padera T. and Munn L. *Mechanobiological oscillators control lymph flow*. Proceedings of the National Academy of Sciences, Vol. 112, No. 35, pages 10938–10943, aug 2015.

[LeFloch 2002] LeFloch P. G. Hyperbolic Systems of Conservation Laws. Springer Nature, 2002.

[Leung 2016] Leung V., Magnussen J. S., Stoodley M. A. and Bilston L. E. *Cerebellar and hindbrain motion in Chiari malformation with and without syringomyelia*. Journal of Neurosurgery: Spine, Vol. 24, No. 4, pages 546–555, apr 2016.

[Levick 2009] Levick J. R. An Introduction to Cardiovascular Physiology 5E, volume i. Butterworth-Heinemann, 2009.

[Levitt 2016] Levitt M. R., McGah P. M., Moon K., Albuquerque F. C., McDougall C. G., Kalani M. Y., Kim L. J. and Aliseda A. *Computational modeling of venous sinus stenosis in idiopathic intracranial hypertension*. American Journal of Neuroradiology, Vol. 37, No. 10, pages 1876–1882, may 2016.

[Li 2000] Li K.-J. J. *Scaling and invariants in cardiovascular biology*. Scaling in biology, pages 113–128, 2000.

[Liang 2009a] Liang F., Takagi S., Himeno R. and Liu H. *Biomechanical characterization of ventricular – arterial coupling during aging : A multi-scale model study*. Journal of Biomechanics, Vol. 42, No. 6, pages 692–704, apr 2009.

[Liang 2009b] Liang F., Takagi S., Himeno R. and Liu H. *Multi-scale modeling of the human cardiovascular system with applications to aortic valvular and arterial stenoses*. Medical and Biological Engineering and Computing, Vol. 47, No. 7, pages 743–755, feb 2009.

[Liang 2014] Liang F., Senzaki H., Kurishima C., Sughimoto K., Inuzuka R. and Liu H. *Hemodynamic performance of the Fontan circulation compared with a normal biventricular circulation: a computational model study*. American Journal of Physiology - Heart and Circulatory Physiology, Vol. 307, No. 7, pages H1056–H1072, jul 2014.

[Linninger 2009] Linninger A. A., Xenos M., Sweetman B., Ponkshe S., Guo X. and Penn R. *A mathematical model of blood, cerebrospinal fluid and brain dynamics*. Journal of Mathematical Biology, Vol. 59, No. 6, pages 729–759, feb 2009.

[Linninger 2016] Linninger A. A., Tangen K., Hsu C.-Y. and Frim D. *Cerebrospinal fluid mechanics and its coupling to cerebrovascular dynamics*. Annual Review of Fluid Mechanics, Vol. 48, No. 1, pages 219–257, jan 2016.

[Linninger 2017] Linninger A. A., Xu C., Tangen K. and Hartung G. *Starling forces drive intracranial water exchange during normal and pathological states*. Croatian Medical Journal, Vol. 58, No. 6, pages 384–394, dec 2017.

[Liu 2014] Liu M., Xu H., Zhong Y., Xia S., Utriainen D., Wang T. and Haacke E. M. *Patterns of chronic venous insufficiency in the major cerebral and extracranial draining veins and their relationship with white matter hyperintensities for patients with Parkinson's disease*. Journal of Vascular Surgery, Vol. Epub ahead, 2014.

[Louveau 2015] Louveau A., Smirnov I., Keyes T. J., Eccles J. D., Rouhani S. J., Peske J. D., Derecki N. C., Castle D., Mandell J. W., Lee K. S., Harris T. H. and Kipnis J. *Structural and functional features of central nervous system lymphatic vessels*. Nature, Vol. 523, No. 7560, pages 337–341, jun 2015.

[Louveau 2016] Louveau A., Da Mesquita S. and Kipnis J. *Lymphatics in neurological disorders: A neuro-lympho-vascular component of multiple sclerosis and Alzheimer's disease?* Neuron, Vol. 91, No. 5, pages 957–973, sep 2016.

[Louveau 2017] Louveau A., Plog B. A., Antila S., Alitalo K., Nedergaard M. and Kipnis J. *Understanding the functions and relationships of the glymphatic system and meningeal lymphatics*. Journal of Clinical Investigation, Vol. 127, No. 9, pages 3210–3219, sep 2017.

[Ma 2017] Ma Q., Ineichen B. V., Detmar M. and Proulx S. T. *Outflow of cerebrospinal fluid is predominantly through lymphatic vessels and is reduced in aged mice*. Nature Communications, Vol. 8, No. 1, nov 2017.

[Macdonald 2008] Macdonald A., Arkill K. P., Tabor G., McHale N. G. and Winlove C. P. *Modeling flow in collecting lymphatic vessels: One-dimensional flow through a series of contractile elements*. American Journal of Physiology - Heart and Circulatory Physiology, Vol. 295, No. 1, pages H305–H313, 2008.

[Mancini 2015] Mancini M., Greco A., Tedeschi E., Palma G., Ragucci M., Bruzzone M. G., Coda A. R. D., Torino E., Scotti A., Zucca I. and Salvatore M. *Head and neck veins of the mouse. A magnetic resonance, micro computed tomography and high frequency color Doppler ultrasound study*. PLoS ONE, Vol. 10, No. 6, page e0129912, jun 2015.

[Margaris 2012] Margaris K. N. and Black R. A. *Modelling the lymphatic system: challenges and opportunities*. Journal of The Royal Society Interface, Vol. 9, No. 69, pages 601–612, 2012.

[Matthys 2007a] Matthys K. S., Alastruey J., Peiró J., Khir A. W., Segers P., Verdonck P. R., Parker K. H. and Sherwin S. J. *Pulse wave propagation in a model human arterial network: Assessment of 1-D numerical simulations against in vitro measurements*. Journal of Biomechanics, Vol. 40, No. 15, pages 3476–3486, 2007.

[Matthys 2007b] Matthys K. S., Alastruey J., Peiró J., Khir A. W., Segers P., Verdonck P. R., Parker K. H. and Sherwin S. J. *Pulse wave propagation in a model human arterial network: Assessment of 1-D numerical simulations against in vitro measurements*. Journal of Biomechanics, Vol. 40, No. 15, pages 3476–3486, 2007.

[McHale 1975] McHale N. G. and Roddie I. C. *Effect of temperature on pumping activity in isolated bovine mesenteric lymphatic vessels*. Irish Journal of Medical Science, Vol. 144, No. 3, page 131, oct 1975.

[Mellor 2011] Mellor R. H., Tate N., Stanton A. W., Hubert C., Mäkinen T., Smith A., Burnand K. G., Jeffery S., Levick J. R. and Mortimer P. S. *Mutations in FOXC2 in humans (lymphoedema distichiasis syndrome) cause lymphatic dysfunction on dependency*. Journal of Vascular Research, Vol. 48, No. 5, pages 397–407, 2011.

[Miglio 2005a] Miglio E., Perotto S. and Saleri F. *Model coupling techniques for free-surface flow problems: Part I*. Nonlinear Analysis, Theory, Methods and Applications, Vol. 63, No. 5-7, pages e1885—-e1896, nov 2005.

[Miglio 2005b] Miglio E., Perotto S. and Saleri F. *Model coupling techniques for free-surface flow problems: Part II*. Nonlinear Analysis, Theory, Methods and Applications, Vol. 63, No. 5-7, pages e1897—-e1908, nov 2005.

[Mihara 2012] Mihara M., Hara H., Iida T., Todokoro T., Yamamoto T., Narushima M., Tashiro K., Murai N. and Koshima I. *Antegrade and retrograde lymphatico-venous anastomosis for cancer-related lymphedema with lymphatic valve dysfuction and lymphatic varix*. Microsurgery, Vol. 32, No. 7, pages 580–584, aug 2012.

[Miyajima 2015] Miyajima M. and Arai H. *Evaluation of the production and absorption of cerebrospinal fluid*. Neurologia medico-chirurgica, Vol. 55, No. 8, pages 647–656, 2015.

[Moazen 2016] Moazen M., Alazmani A., Rafferty K., Liu Z. J., Gustafson J., Cunningham M. L., Fagan M. J. and Herring S. W. *Intracranial pressure changes during mouse development*. Journal of Biomechanics, Vol. 49, No. 1, pages 123–126, jan 2016.

[Mollanji 2002] Mollanji R., Bozanovic-Sosic R., Zakharov A., Makarian L. and Johnston M. G. *Blocking cerebrospinal fluid absorption through the cribriform plate increases resting intracranial pressure*. American Journal of Physiology - Regulatory, Integrative and Comparative Physiology, Vol. 282, No. 6, pages R1593–9, jun 2002.

[Montecinos 2012a] Montecinos G. I., Castro C. E., Dumbser M. and Toro E. F. *Comparison of solvers for the generalized Riemann problem for hyperbolic systems with source terms*. Journal of Computational Physics, Vol. 231, No. 19, pages 6472–6494, aug 2012.

[Montecinos 2012b] Montecinos G. I. and Toro E. F. *Solver for the generalized Riemann problem for balance laws with stiff source terms: The scalar case*. In Hyperbolic Problems: Theory, Numerics and Applications, pages 576–583. World Scientific Pub Co Pte Lt, dec 2012.

[Montecinos 2014a] Montecinos G. I., Müller L. O. and Toro E. F. *Hyperbolic reformulation of a 1D viscoelastic blood flow model and ADER finite volume schemes*. Journal of Computational Physics, Vol. 266, pages 101–123, jun 2014.

[Montecinos 2014b] Montecinos G. I. and Toro E. F. *Reformulations for general advection-diffusion-reaction equations and locally implicit ADER schemes*. Journal of Computational Physics, Vol. 275, pages 415–442, 2014.

[Moore 2018] Moore J. E. and Bertram C. D. *Lymphatic system flows*. Annual Review of Fluid Mechanics, Vol. 50, No. 1, pages 459–482, jan 2018.

[Mortimer 2004] Mortimer P. S. and Pearson I. C. *Lymphatic function in severe chronic venous insufficiency*. Phlebolymphology, No. 44, pages 253–257, 2004.

[Müller 2012] Müller L. O., Montecinos G. I. and Toro E. F. *Some issues in modelling venous haemodynamics*. In Numerical Methods for Hyperbolic Equations, pages 347–354. CRC Press, 2012.

[Müller 2013a] Müller L. O., Parés C. and Toro E. F. *Well-balanced high-order numerical schemes for one-dimensional blood flow in vessels with varying mechanical properties*. Journal of Computational Physics, Vol. 242, pages 53–85, 2013.

[Müller 2013b] Müller L. O. and Toro E. F. *A global multi-scale mathematical model for the human circulation with emphasis on the venous system.* International Journal for Numerical Methods in Biomedical Engineering, Vol. 30, pages 681–725, 2013.

[Müller 2013c] Müller L. O. and Toro E. F. *Well-balanced high-order solver for blood flow in networks of vessels with variable properties*. International Journal for Numerical Methods in Biomedical Engineering, Vol. 29, No. 12, pages 1388–1411, 2013.

[Müller 2014] Müller L. O. and Toro E. F. *Enhanced global mathematical model for studying cerebral venous blood flow*. Journal of Biomechanics, Vol. 47, No. 13, pages 3361–3372, 2014.

[Müller 2015a] Müller L. O. and Blanco P. J. *A high order approximation of hyperbolic conservation laws in networks: Application to one-dimensional blood flow*. Journal of Computational Physics, Vol. 300, pages 423–437, 2015.

[Müller 2015b] Müller L. O., Toro E. F., Haacke E. M. and Utriainen D. *Impact of CCSVI on cerebral haemodynamics: a mathematical study using MRI angiographic and flow data*. Phlebology, Vol. 31, No. 5, pages 305–324, 2015.

[Müller 2016] Müller L. O., Blanco P. J., Watanabe S. M. and Feijóo R. A. *A high-order local time stepping finite volume solver for one-dimensional blood flow simulations: application to the ADAN model.* International Journal for Numerical Methods in Biomedical Engineering, Vol. 32, No. 10, page e02761, oct 2016.

[Munn 2014] Munn L. and Padera T. *Imaging the lymphatic system*. Microvascular Research, Vol. 96, pages 55–63, nov 2014.

[Munn 2015] Munn L. *Mechanobiology of lymphatic contractions*. Seminars in Cell and Developmental Biology, Vol. 38, pages 67–74, feb 2015.

[Mynard 2012] Mynard J. P., Davidson M. R., Penny D. J. and Smolich J. J. *A simple, versatile valve model for use in lumped parameter and one-dimensional cardiovascular models*. International Journal for Numerical Methods in Biomedical Engineering, Vol. 28, No. 6-7, pages 626–641, 2012.

[Mynard 2015] Mynard J. P. and Smolich J. J. *One-dimensional haemodynamic modeling and wave dynamics in the entire adult circulation*. Annals of Biomedical Engineering, Vol. 43, No. 6, pages 1443–1460, apr 2015.

[Nagumo 1962] Nagumo J., Arimoto S. and Yoshizawa S. *An active pulse transmission line simulating nerve axon*. Proceedings of the IRE, Vol. 50, No. 10, pages 2061–2070, oct 1962.

[Nakada 2017] Nakada T., Kwee I. L., Igarashi H. and Suzuki Y. *Aquaporin-4 functionality and virchow-robin space water dynamics: Physiological model for neurovascular coupling and glymphatic flow*. International Journal of Molecular Sciences, Vol. 18, No. 8, page 1798, aug 2017.

[Naresh 2016] Naresh N. K., Yang Y., Holmes J. W., Salerno M. and Epstein F. H. *High temporal-resolution phase-contrast MRI demonstrates impaired left-ventricular diastolic relaxation in mice fed a high-fat high-sucrose diet*. Journal of Cardiovascular Magnetic Resonance, Vol. 18, No. Suppl 1, page P50, 2016.

[Noel 2001] Noel A. A., Gloviczki P., Bender C. E., Whitley D., Stanson A. W. and Deschamps C. *Treatment of symptomatic primary chylous disorders*. Journal of Vascular Surgery, Vol. 34, No. 5, pages 785–91, nov 2001.

[Ohhashi 1980] Ohhashi T., Azuma T. and Sakaguchi M. *Active and passive mechanical characteristics of bovine mesenteric lymphatics*. American Journal of Physiology, Vol. 239, No. 1, pages H88–95, 1980.

[Olufsen 2000] Olufsen M. S., Peskin C. S., Kim W. Y., Pedersen E. M., Nadim A. and Larsen J. *Numerical simulation and experimental validation of blood flow in arteries with structured-tree outflow conditions*. Annals of Biomedical Engineering, Vol. 28, No. 11, pages 1281–1299, nov 2000.

[Orešković 2017] Orešković D., Radoš M. and Klarica M. *New concepts of cerebrospinal fluid physiology and development of hydrocephalus*. Pediatric Neurosurgery, Vol. 52, No. 6, pages 417–425, dec 2017.

[Owman 1975] Owman C., Edvinsson L. and Nielsen K. C. *Circadian rhythm in cerebral blood volume of mouse*. In Cerebral Circulation and Metabolism, pages 418–420. Springer Berlin Heidelberg, 1975.

[Pacher 2008] Pacher P., Nagayama T., Mukhopadhyay P., Bátkai S. and Kass D. A. *Measurement of cardiac function using pressure-volume conductance catheter technique in mice and rats*. Nature Protocols, Vol. 3, No. 9, pages 1422–1434, 2008.

[Penn 1984] Penn R. D. and Bacus J. W. *The brain as a sponge: A computed tomographic look at Hakim's hypothesis*. Neurosurgery, Vol. 14, No. 6, pages 670–675, jun 1984.

[Petrova 2004] Petrova T. V., Karpanen T., Norrmén C., Mellor R. H., Tamakoshi T., Finegold D., Ferrell R., Kerjaschki D., Mortimer P. S., Ylä-Herttuala S., Miura N. and Alitalo K. *Defective valves and abnormal mural cell recruitment underlie lymphatic vascular failure in lymphedema distichiasis*. Nature Medicine, Vol. 10, No. 9, pages 974–981, aug 2004.

[Plog 2018] Plog B. A. and Nedergaard M. *The glymphatic system in central nervous system health and disease: Past, present, and future*. Annual Review of Pathology: Mechanisms of Disease, Vol. 13, No. 1, pages annurev–pathol–051217–111018, jan 2018.

[Quarteroni 2016a] Quarteroni A., Lassila T., Rossi S. and Ruiz-Baier R. *Integrated heart – coupling multiscale and multiphysics models for the simulation of the cardiac function*. Computer Methods in Applied Mechanics and Engineering, Vol. 314, pages 345–407, feb 2016.

[Quarteroni 2016b] Quarteroni A., Veneziani A. and Vergara C. *Geometric multiscale modeling of the cardiovascular system, between theory and practice*. Computer Methods in Applied Mechanics and Engineering, Vol. 302, pages 193–252, apr 2016.

[Quarteroni 2017] Quarteroni A., Manzoni A. and Vergara C. *The cardiovascular system: Mathematical modelling, numerical algorithms and clinical applications*. Acta Numerica, Vol. 26, pages 365–590, may 2017.

[Rahbar 2011] Rahbar E. and Moore J. E. *A model of a radially expanding and contracting lymphangion*. Journal of Biomechanics, Vol. 44, No. 6, pages 1001–1007, apr 2011.

[Raper 2016] Raper D., Louveau A. and Kipnis J. *How do meningeal lymphatic vessels drain the CNS?* Trends in Neurosciences, Vol. 39, No. 9, pages 581–586, sep 2016.

[Rasmussen 2016] Rasmussen J. C., Aldrich M. B., Tan I. C., Darne C., Zhu B., O'Donnell T. F., Fife C. E. and Sevick-Muraca E. M. *Lymphatic transport in patients with chronic venous insufficiency and venous leg ulcers following sequential pneumatic compression*. Journal of Vascular Surgery: Venous and Lymphatic Disorders, Vol. 4, No. 1, pages 9–17, jan 2016.

[Reddy 1974] Reddy N. P. *A discrete model of the lymphatic system*. PhD thesis, Texas A&M University, 1974.

[Reigstad 2015] Reigstad G. a., Flåtten T., Haugen N. E. and Ytrehus T. *Coupling constants and the generalized Riemann problem for isothermal junction flow*. Journal of Hyperbolic Differential Equations, Vol. 12, No. 01, pages 37–59, mar 2015.

[Rivera-Rivera 2016] Rivera-Rivera L. A., Turski P., Johnson K. M., Hoffman C., Berman S. E., Kilgas P., Rowley H. A., Carlsson C. M., Johnson S. C. and Wieben O. *4D flow MRI for intracranial hemodynamics assessment in Alzheimer's disease*. Journal of Cerebral Blood Flow and Metabolism, Vol. 36, No. 10, pages 1718–1730, oct 2016.

[Roose 2012a] Roose T. and Swartz M. A. *Multiscale modeling of lymphatic drainage from tissues using homogenization theory*. Journal of Biomechanics, Vol. 45, No. 1, pages 107–115, jan 2012.

[Roose 2012b] Roose T. and Tabor G. *Multiscale modelling of lymphatic drainage*. In Multiscale Computer Modeling in Biomechanics and Biomedical Engineering, volume 14, pages 149–176. Springer Science + Business Media, oct 2012.

[Ruan 1999] Ruan X., Oliverio M. I., Coffman T. M. and Arendshorst W. J. *Renal vascular reactivity in mice: AngII-induced vasoconstriction in AT1A receptor null mice*. Journal of the American Society of Nephrology, Vol. 10, No. 12, pages 2620–2630, 1999.

[Sabine 2015] Sabine A., Bovay E., Demir C. S., Kimura W., Jaquet M., Agalarov Y., Zangger N., Scallan J. P., Graber W., Gulpinar E., Kwak B. R., Mäkinen T., Martinez-Corral I., Ortega S., Delorenzi M., Kiefer F., Davis M. J., Djonov V., Miura N. and Petrova T. V. *FOXC2 and fluid shear stress stabilize postnatal lymphatic vasculature*. Journal of Clinical Investigation, Vol. 125, No. 10, pages 3861–3877, sep 2015.

[Scallan 2012] Scallan J. P., Wolpers J. H., Muthuchamy M., Zawieja D. C., Gashev A. A. and Davis M. J. *Independent and interactive effects of preload and afterload on the pump function of the isolated lymphangion*. American Journal of Physiology - Heart and Circulatory Physiology, Vol. 303, No. 7, pages H809–H824, aug 2012.

[Scallan 2016] Scallan J. P., Zawieja D. C., Castorena-Gonzalez J. A. and Davis M. J. *Lymphatic pumping: Mechanics, mechanisms and malfunction*. Journal of Physiology, Vol. 594, No. 20, pages 5749–5768, aug 2016.

[Schain 2017] Schain A. J., Melo-Carrillo A., Strassman A. M. and Burstein R. *Cortical spreading depression closes paravascular space and impairs glymphatic flow: Implications for migraine headache*. Journal of Neuroscience, Vol. 37, No. 11, pages 2904–2915, feb 2017.

[Scheuermann-Freestone 2001] Scheuermann-Freestone M., Freestone N. S., Langenickel T., Höhnel K., Dietz R. and Willenbrock R. *A new model of congestive heart failure in the mouse due to chronic volume overload*. European Journal of Heart Failure, Vol. 3, No. 5, pages 535–543, oct 2001.

[Schmid-Schönbein 2003] Schmid-Schönbein G. W. *The second valve system in lymphatics*. Lymphatic Research and Biology, Vol. 1, No. 1, pages 25–31, jan 2003.

[Schwartzkopff 2002] Schwartzkopff T., Munz C.-D. and Toro E. F. *ADER: A high-order approach for linear hyperbolic systems in 2D*. Journal of Scientific Computing, Vol. 17, No. 1-4, pages 231–240, 2002.

[Schwartzkopff 2004] Schwartzkopff T., Dumbser M. and Munz C.-d. *Fast high order ADER schemes for linear hyperbolic equations*. Journal of Computational Physics, Vol. 197, No. 2, pages 532–539, jul 2004.

[Scremin 2015] Scremin O. U. *Cerebral vascular system*. In The Rat Nervous System, pages 985–1011. Elsevier, 2015.

[Secomb 2013] Secomb T. W. and Pries A. R. *Comptes rendus physique blood viscosity in microvessels: Experiment and theory*. Comptes Rendus Physique, Vol. 14, No. 6, pages 470–478, jun 2013.

[Seeley 1976] Seeley B. D. and Young D. F. *Effect of geometry on pressure losses across models of arterial stenoses*. Journal of Biomechanics, Vol. 9, No. 7, pages 439–448, jan 1976.

[Sherwin 2003a] Sherwin S. J., Formaggia L., Peiró J. and Franke V. *Computational modelling of 1D blood flow with variable mechanical properties and its application to the simulation of wave propagation in the human arterial system*. International Journal for Numerical Methods in Fluids, Vol. 43, No. 6-7, pages 673–700, 2003.

[Sherwin 2003b] Sherwin S. J., Franke V., Peiró J. and Parker K. *One-dimensional modelling of a vascular network in space-time variables*. Journal of Engineering Mathematics, Vol. 47, No. 3-4, pages 217–250, dec 2003.

[Shi 2011] Shi Y., Lawford P. and Hose R. *Review of zero-D and 1-D models of blood flow in the cardiovascular system*. BioMedical Engineering Online, Vol. 10, No. 1, page 33, 2011.

[Simka 2015] Simka M. *Recent advances in understanding the lymphatic and glymphatic systems of the brain*. Phlebological Review, Vol. 1, pages 69–71, 2015.

[Simon 2016] Simon M. J. and Iliff J. J. *Regulation of cerebrospinal fluid (CSF) flow in neurodegenerative, neurovascular and neuroinflammatory disease*. Biochimica et Biophysica Acta - Molecular Basis of Disease, Vol. 1862, No. 3, pages 442–451, mar 2016.

[Singh 2009] Singh A. V. and Zamboni P. *Anomalous venous blood flow and iron deposition in multiple sclerosis*. Journal of Cerebral Blood Flow and Metabolism, Vol. 29, No. 12, pages 1867–1878, 2009.

[Siviglia 2013] Siviglia A. and Toffolon M. *Steady analysis of transcritical flows in collapsible tubes with discontinuous mechanical properties: Implications for arteries and veins*. Journal of Fluid Mechanics, Vol. 736, pages 195–215, 2013.

[Smith 2017] Smith A. J., Yao X., Dix J. A., Jin B. J. and Verkman A. S. *Test of the 'glymphatic' hypothesis demonstrates diffusive and aquaporin-4-independent solute transport in rodent brain parenchyma*. eLife, Vol. 6, 2017.

[Spector 2015] Spector R., Robert Snodgrass S. and Johanson C. E. *A balanced view of the cerebrospinal fluid composition and functions: Focus on adult humans*. Experimental Neurology, Vol. 273, pages 57–68, nov 2015.

[Spiller 2017] Spiller C., Toro E. F., Vázquez-Cendón M. E. and Contarino C. *On the exact solution of the Riemann problem for blood flow in human veins, including collapse*. Applied Mathematics and Computation, Vol. 303, pages 178–189, jun 2017.

[Steiner 2006] Steiner L. A. and Andrews P. J. *Monitoring the injured brain: ICP and CBF*. British Journal of Anaesthesia, Vol. 97, No. 1, pages 26–38, jul 2006.

[Strocchi 2017] Strocchi M., Contarino C., Zhang Q., Passos M. A. R. F. and Toro E. F. *A global mathematical model for the simulation of stenoses and bypass placement in the human arterial system*. Applied Mathematics and Computation, Vol. 300, pages 21–39, may 2017.

[Sun 1995] Sun Y., Sjoberg B. J., Ask P., Loyd D. and Wranne B. *Mathematical model that characterizes transmitral and pulmonary venous flow velocity patterns*. American Journal of Physiology, Vol. 268, No. 1 Pt 2, pages H476–89, jan 1995.

[Sun 1997] Sun Y., Beshara M., Lucariello R. J. and Chiaramida S. a. *A comprehensive model for right-left heart interaction under the influence of pericardium and baroreflex.* American Journal of Physiology, Vol. 272, No. 3 Pt 2, pages H1499–H1515, mar 1997.

[Swartz 2001] Swartz M. A. *The physiology of the lymphatic system.* Advanced Drug Delivery Reviews, Vol. 50, No. 1-2, pages 3–20, aug 2001.

[Szewka 2012] Szewka A. J., Bruce B. B., Newman N. J. and Biousse V. *Idiopathic intracranial hypertension*. Journal of Neuro-Ophthalmology, Vol. 35, No. 3, page 1, may 2012.

[Tan 2010] Tan S. and Shu C.-W. *Inverse Lax-Wendroff procedure for numerical boundary conditions of conservation laws*. Journal of Computational Physics, Vol. 229, No. 21, pages 8144–8166, 2010.

[Tarasoff-Conway 2015] Tarasoff-Conway J. M., Carare R. O., Osorio R. S., Glodzik L., Butler T., Fieremans E., Axel L., Rusinek H., Nicholson C., Zlokovic B. V., Frangione B., Blennow K., Ménard J., Zetterberg H., Wisniewski T. and Leon M. J.de . *Clearance systems in the brain-implications for Alzheimer disease*. Nature Reviews Neurology, Vol. 11, No. 8, pages 457–470, jul 2015.

[Telinius 2015] Telinius N., Majgaard J., Kim S., Katballe N., Pahle E., Nielsen J., Hjortdal V., Aalkjaer C. and Boedtkjer D. B. *Voltage-gated sodium channels contribute to action potentials and spontaneous contractility in isolated human lymphatic vessels*. Journal of Physiology, Vol. 593, No. 14, pages 3109–3122, jul 2015.

[Titarev 2002] Titarev V. A. and Toro E. F. *ADER: Arbitrary high order Godunov approach*. Journal of Scientific Computing, Vol. 17, No. 1-4, pages 609–618, 2002.

[Titarev 2005] Titarev V. A. and Toro E. F. *ADER schemes for three-dimensional non-linear hyperbolic systems*. Journal of Computational Physics, Vol. 204, No. 2, pages 715–736, apr 2005.

[Toro 2000] Toro E. F. and Billett S. J. *Centred TVD schemes for hyperbolic conservation laws*. IMA Journal of Numerical Analysis, Vol. 20, pages 47–79, 2000.

[Toro 2001] Toro E. F., Millington R. C. and Nejad L. A. M. *Towards very high order Godunov schemes*. In Godunov Methods, pages 907–940. Springer, 2001.

[Toro 2002] Toro E. F. and Titarev V. A. *Solution of the generalized Riemann problem for advection-reaction equations*. Proceedings of the Royal Society A: Mathematical, Physical and Engineering Sciences, Vol. 458, No. 2018, pages 271–281, 2002.

[Toro 2009] Toro E. F. Riemann Solvers and Numerical Methods for Fluid Dynamics. Springer-Verlag Berlin Heidelberg, third édition, 2009.

[Toro 2011] Toro E. F. and Siviglia A. *Simplified blood flow model with discontinous vessel properties*. In Modeling of Physiological Flows, pages 19–39. Springer, 2011.

[Toro 2013] Toro E. F. and Siviglia A. *Flow in collapsible tubes with discontinuous mechanical properties: Mathematical model and exact Solutions*. Communications in Computational Physics, Vol. 13, No. 2, pages 361–385, feb 2013.

[Toro 2015a] Toro E. F. and Montecinos G. I. *Implicit, semi-analytical solution of the generalized Riemann problem for stiff hyperbolic balance laws*. Journal of Computational Physics, Vol. 303, pages 146–172, sep 2015.

[Toro 2015b] Toro E. F., Müller L. O., Cristini M., Menegatti E. and Zamboni P. *Impact of jugular vein valve function on cerebral venous haemodynamics.* Current neurovascular research, Vol. 12, No. 4, pages 384–397, sep 2015.

[Toro 2016] Toro E. F. *Brain venous haemodynamics, neurological diseases and mathematical modelling. A review*. Applied Mathematics and Computation, Vol. 272, pages 542–579, jan 2016.

[Toro 2018] Toro E. F., Borgioli F., Zhang Q., Contarino C., Müller L. O. and Bruno A. *Inner-ear circulation in humans is disrupted by extracranial venous outflow strictures: Implications for Ménière's disease*. Veins and Lymphatics, Vol. 7, No. 1, 2018.

[Ursino 1988] Ursino M. *A mathematical study of human intracranial hydrodynamics. Part 2 - Simulation of clinical tests*. Annals of Biomedical Engineering, Vol. 16, No. 4, pages 403–416, 1988.

[van Griensven 2006] Griensven A.van , Meixner T., Grunwald S., Bishop T., Diluzio M. and Srinivasan R. *A global sensitivity analysis tool for the parameters of multi-variable catchment models*. Journal of Hydrology, Vol. 324, No. 1-4, pages 10–23, jun 2006.

[Venugopal 2007] Venugopal A. M., Stewart R. H., Laine G. A., Dongaonkar R. M. and Quick C. M. *Lymphangion coordination minimally affects mean flow in lymphatic vessels*. American Journal of Physiology - Heart and Circulatory Physiology, Vol. 293, No. 2, pages H1183–H1189, mar 2007.

[Weller 2008] Weller R. O., Subash M., Preston S. D., Mazanti I. and Carare R. O. *Perivascular drainage of amyloid-b peptides from the brain and its failure in cerebral amyloid angiopathy and Alzheimer's disease*. Brain Pathology, Vol. 18, No. 2, pages 253–266, 2008.

[Whish 2015] Whish S., Dziegielewska K. M., Møllgård K., Noor N. M., Liddelow S. A., Habgood M. D., Richardson S. J. and Saunders N. R. *The inner csf-brain barrier: Developmentally controlled access to the brain via intercellular junctions*. Frontiers in Neuroscience, Vol. 9, feb 2015.

[Wiesmann 2000] Wiesmann F., Ruff J., Hiller K. H., Rommel E., Haase a. and Neubauer S. *Developmental changes of cardiac function and mass assessed with MRI in neonatal, juvenile, and adult mice.* American Journal of Physiology - Heart and Circulatory Physiology, Vol. 278, No. 2, pages H652–H657, feb 2000.

[Wilson 2015] Wilson J. T., Loon R.van , Wang W., Zawieja D. C. and Moore J. E. *Determining the combined effect of the lymphatic valve leaflets and sinus on resistance to forward flow*. Journal of Biomechanics, Vol. 48, No. 13, pages 3593–3599, oct 2015.

[Wilson 2016] Wilson M. H. *Monro-Kellie 2.0: The dynamic vascular and venous pathophysiological components of intracranial pressure*. Journal of Cerebral Blood Flow and Metabolism, Vol. 36, No. 8, pages 1338–1350, may 2016.

[Windberger 2003] Windberger U., Bartholovitsch A., Plasenzetti R., Korak K. J. and Heinze G. *Whole blood viscosity, plasma viscosity and erythrocyte aggregation in nine mammalian species: Reference values and comparison of data*. Experimental Physiology, Vol. 88, No. 3, pages 431–440, may 2003.

[Xiong 2017] Xiong B., Li A., Lou Y., Chen S., Long B., Peng J., Yang Z., Xu T., Yang X., Li X., Jiang T., Luo Q. and Gong H. *Precise cerebral vascular atlas in stereotaxic coordinates of whole mouse brain*. Frontiers in Neuroanatomy, Vol. 11, dec 2017.

[Zamboni 2008] Zamboni P., Galeotti R., Menegatti E., Malagoni A. M., Tacconi G., Dall'Ara S., Bartolomei I. and Salvi F. *Chronic cerebrospinal venous insufficiency in patients with multiple sclerosis*. Journal of Neurology, Neurosurgery and Psychiatry, Vol. 80, No. 4, pages 392–399, 2008.

[Zamboni 2015] Zamboni P. *The discovery of the brain lymphatic system*. Veins and Lymphatics, Vol. 4, No. 2, jun 2015.

[Zamboni 2017] Zamboni P., Tesio L., Galimberti S., Massacesi L., Salvi F., D'Alessandro R., Cenni P., Galeotti R., Papini D., D'Amico R., Simi S., Valsecchi M. G. and Filippini G. *Efficacy and safety of extracranial vein angioplasty in multiple sclerosis*. JAMA Neurology, Vol. 75, No. 1, page 35, jan 2017.

[Zawieja 1993] Zawieja D. C., Davis K. L., Schuster R., Hinds W. M. and Granger H. J. *Distribution, propagation, and coordination of contractile activity in lymphatics*. American Journal of Physiology, Vol. 264, No. 4 Pt 2, pages H1283–H1291, 1993.

[Zawieja 2008] Zawieja D. C., Weid P. Y.von der and Gashev A. A. *Microlymphatic biology*. In Microcirculation, pages 125–158. Comprehensive Physiology. John Wiley and Sons, 2008.

[Zawieja 2009] Zawieja D. C. *Contractile physiology of lymphatics*. Lymphatic Research and Biology, Vol. 7, No. 2, pages 87–96, jun 2009.